Characterisation and Modelling of Potassium-Ion Batteries

Shobhan Dhir

St Catherine's College
University of Oxford

A thesis submitted for the degree of Doctor of Philosophy

Hilary 2024

Abstract

Lithium-ion batteries (LIBs) are critical to decarbonisation, yet the future supply of of lithium-ion (Li-ion) critical minerals such as lithium, nickel, and copper face significant uncertainty and risk. Potassium-ion batteries (KIBs) are emerging as a promising alternative to LIBs due to their reduced dependency on critical minerals, and ability of K^+ to intercalate into graphite unlike sodium ions. KIBs may also present an opportunity for superior fast-charging due to the larger K^+ size and lower charge density, being speculated to result in faster electrolyte ionic transport.

Since there is no current viable potassium-ion (K-ion) electrolyte, a full-cell KIB rate model in commercial cell format is required to determine the fast-charging potential for KIBs and facilitate K-ion electrolyte and materials development. However, accurate characterisation of the fundamental electrolyte and material properties that determine rate performance has not yet been conducted. In this thesis the fundamental rate-determining properties of a K-ion electrolyte and leading K-ion electrode materials are characterised, and the first KIB Doyle-Fuller-Newman model is developed.

First, the ionic transport and thermodynamic properties of a K-ion electrolyte is fully characterised for the first time using state-of-the-art methods, characterising potassium bis(fluorosulfonyl)imide (KFSI) in 1,2-dimethoxyethane (DME) and comparing to the Li-ion equivalent. A K metal preparation protocol was developed enabling sufficient K metal stability for electrolyte characterisation. The results show the K-ion electrolyte displays significantly higher salt diffusivities and transference numbers than the Li-ion equivalent.

Second, the effective solid-state diffusivities and exchange current densities of the leading K-ion electrode materials—the graphite anode and potassium manganese hexacyanoferrate $K_2Mn[Fe(CN)_6]$ (KMF) cathode—are characterised, through a combination of optimised material design and state-of-the-art analysis. The results show both the ionic transport and particularly the charge-transfer kinetics are slower for the KMF compared to the graphite.

Finally, the first Doyle-Fuller-Newman model of a KIB full cell is presented in a hypothetical commercial cylindrical cell format, demonstrating ionic transport in the current leading K-ion electrolyte is too slow for even moderate rate performance using realistic electrode loading. Should a viable electrolyte be developed, the modelling shows K-ion could be competitive with the lithium iron phosphate (LFP) LIB in fast-charging capability.

Characterisation and Modelling of Potassium-Ion Batteries



Shobhan Dhir

St Catherine's College

University of Oxford

A thesis submitted for the degree of

Doctor of Philosophy

Hilary 2024

This thesis is dedicated to
Nani, Dadima, Dadaji and my parents Naresh and Bhanu Dhir
for all their hard work and sacrifice to give me every opportunity possible

Acknowledgements

First, I would like to thank my supervisor Professor Mauro Pasta for giving me this opportunity. I greatly appreciate his scientific rigour and critical mind, the brilliant organisation in the group, and for how he supported my career at key moments. I would also like to thank him for the world class facilities we have had access to. Thanks also to my industrial supervisor Dr Peter Klusener for his support and appreciation for my work. Thank you to EPSRC and Shell for their financial support.

It has been a privilege to work with such brilliant and kind colleagues in the Pasta Group. I would like to say a special thanks to a few group members in particular:

Ben Jagger, one of the greatest scientific minds I have come across, but more importantly a genuinely kind and good man, with a great sense of humour. It has been such a genuine pleasure to work with him, and I greatly appreciate all his support. I thoroughly enjoyed our many scientific discussions, achievements and collaborations, and look forward to watching the undoubtedly great science he will achieve in his career.

Maximilian Schart, his truly limitless kindness and friendship during these years has been unparalleled. An exceptional scientist, but always making the time to truly listen and help with my and everyone's research problems in the group. Right until the very end. I will never be able to thank him enough. All the good times and great food shared are cherished. Without him I would definitely not have made it to this point.

Lorenz Olbrich, one of the most impressive scientists I have had the pleasure of working with, but beyond that a truly great friend. I have thoroughly enjoyed all the random office conversations - scientific and very unscientific, the great times shared outside the lab, and always appreciated his thoughts on my research, his enthusiasm, and his exceptional critical mind.

Giulia Galatolo, for such wonderful friendship over these years, I appreciate all the great laughs and food shared, and the warmth and support, as well as the impressive blender skills. Brigita my number one for food recommendations, but also for being such a consistently kind person in the group.

Thanks to all those others I was able to work with including: Dr Isaac Capone for his mentorship and blender modelling, Dr Samuel Wheeler for the great perspective

collaboration and many interesting conversations, Professor Hyeon Jeong Lee for being so kind, for the many things she taught me and for always making time to help, John Cattermull and his excellent synthesis work, Christopher Doerrer for his CAD support, Yifan Chen for being a brilliant researcher to supervise, and Dr Soochan Kim for his schematic support, Dr Jack Fawdon for earlier help with transport, Junyi Zhao for being so kind and diligent, and Neil Cadman for his support and good humour.

I also want to thank others in the group who have helped me in numerous ways: Krish, Po-Yuan, Matthew, Yvonne, Johannes, Peng, Pranay, Souhardh, Sudarshan, Yi, Stephen Turrell, Jack, Liwei, Xinyao. All the laughs over group Linacre (and now Reuben) lunches have been a particular daily highlight.

Outside of the group I would like to thank first Andy and Steve at the PTCL workshop for all their brilliant help making countless cells. I would also like to thank: Marco Siniscalchi for his friendship and the laughs, Max Jenkins for his friendship and kindness, Mu for being such a great laugh and kind person, Ruihe Li for providing such great modelling feedback, Adam Lewis-Douglas for his modelling thoughts, Robert Timms for answering my many PyBaMM questions, Guillaume Matthews for his friendship and feedback, and Noël Hallemans for his impedance thoughts. I would also like to thank all those I shared Oxford Climate Society with particularly Nathan, Ellie and Alexis for all we achieved.

I feel very lucky to have such great friends to whom I am so grateful for their support: Dan for the laughs, great conversation and his incredible kindness (and legal prowess), Hamish being such a great listener and thoughtful friend, Antoine for the sass, laughs and for always being there for me, Timo for being the most loyal and true friend one could ever hope for, Ziski and Jake for being such wonderful friends to laugh, cook and play squash with, Jordi and Shev for being my shark companions and for some of the funniest and best times I've had, Brandon for the jams and frienship, Paula for her caring friendship, Claire for being such a unique and wonderful friend, Ioanna for the best day in Boston and her kindness, Sammy for the always hilarious times, Leo for the farming, laughs and his support, and finally, a special thanks to Lampros for all the hilarious and great times shared - from lockdown projector nights to Bugatsa and Psimeni, it is always so much fun when together and I appreciate his truly exceptional and thoughtful friendship, without him I'd never have made it.

I would also like to say a special thanks to Naomi Mowat-Amiet, who for the majority of this DPhil showed me kindness and support beyond what I knew possible, as well as being the best friend I could have ever hoped for. I am forever grateful.

Finally, I would like to say a very special thank you to my friend Markella Zormpa, the funniest person I know. Truly my heart in Oxford, the times living

together in our ‘flat’ with ‘Challenge’ were some of my favourite ever times. From discovering gravy, to half marathons and Welsh mountains, from shower and boiler outfits to Spanish villas and Athenian adventures, flooding ceilings to countless cinema dates and Sasi’s and cookies, I would never have made it through without all the laughs and wonderful times shared, and her unmatched love, originality and kindness.

Finally, and most importantly, I want to thank my family. To my grandparents Nani, Dadima and Dadaji, who worked so hard and sacrificed so much for us to have every opportunity possible. I am forever grateful. To my uncle Lil Mama for his limitless support and exceptional humour. And to my parents for their overwhelming love and support, and all the countless sacrifices they made to give me every opportunity I could ever hope for. There are no words which can express my gratitude. Thank you to my Dad, Bhanu, for always making me laugh, and being so calm and confident in me, and to my Mum, Naresh, for always being there for me, and for being such an infinite source of kindness, love, and support. Finally, thank you to the best younger sister in the world, Alishya, for being infinitely wiser and my number one source of advice, and for never failing to make me laugh. I will, hopefully, finally, be joining you as a Doctor soon.

Abstract

Lithium-ion batteries (LIBs) are critical to decarbonisation, yet the future supply of of lithium-ion (Li-ion) critical minerals such as lithium, nickel, and copper face significant uncertainty and risk. Potassium-ion batteries (KIBs) are emerging as a promising alternative to LIBs due to their reduced dependency on critical minerals, and ability of K^+ to intercalate into graphite unlike sodium ions. KIBs may also present an opportunity for superior fast-charging due to the larger K^+ size and lower charge density, being speculated to result in faster electrolyte ionic transport.

Since there is no current viable potassium-ion (K-ion) electrolyte, a full-cell KIB rate model in commercial cell format is required to determine the fast-charging potential for KIBs and facilitate K-ion electrolyte and materials development. However, accurate characterisation of the fundamental electrolyte and material properties that determine rate performance has not yet been conducted. In this thesis the fundamental rate-determining properties of a K-ion electrolyte and leading K-ion electrode materials are characterised, and the first KIB Doyle-Fuller-Newman model is developed.

First, the ionic transport and thermodynamic properties of a K-ion electrolyte is fully characterised for the first time using state-of-the-art methods, characterising potassium bis(fluorosulfonyl)imide (KFSI) in 1,2-dimethoxyethane (DME) and comparing to the Li-ion equivalent. A K metal preparation protocol was developed enabling sufficient K metal stability for electrolyte characterisation. The results show the K-ion electrolyte displays significantly higher salt diffusivities and transference numbers than the Li-ion equivalent.

Second, the effective solid-state diffusivities and exchange current densities of the leading K-ion electrode materials—the graphite anode and potassium manganese hexacyanoferrate $K_2Mn[Fe(CN)_6]$ (KMF) cathode—are characterised, through a combination of optimised material design and state-of-the-art analysis. The results show both the ionic transport and particularly the charge-transfer kinetics are slower for the KMF compared to the graphite.

Finally, the first Doyle-Fuller-Newman model of a KIB full cell is presented in a hypothetical commercial cylindrical cell format, demonstrating ionic transport in the current leading K-ion electrolyte is too slow for even moderate rate performance using realistic electrode loading. Should a viable electrolyte be developed, the modelling shows K-ion could be competitive with the lithium iron phosphate (LFP) LIB in fast-charging capability.

Contents

List of Figures **x**

List of Publications **1**

1 Introduction **3**
1.1 Context - Critical Minerals 4
1.2 Why Potassium-ion? 7
1.3 How Potassium-ion Batteries work 8
1.4 State-of-the-art Materials and Electrolytes for Potassium-ion Batteries 11
1.5 Techno-Economic Analysis 26
1.6 Critical Research Fronts for Potassium-ion Batteries 32
1.7 Doyle-Fuller-Newman Model 36
1.7.1 DFN Macroscopic Equations 36
1.7.2 DFN Microscopic Equations 40
1.8 Electrolyte Property Characterisation 42
1.8.1 Transference Number 43
1.8.2 Ionic Conductivity 44
1.8.3 Thermodynamic Factor 44
1.8.4 Salt Diffusivity 45
1.9 Electrode Material Property Characterisation 45
1.9.1 Solid-state Diffusivity 46
1.9.2 Exchange Current Density 49
1.10 Thesis Objectives 50

2 Methods **52**
2.1 Techno-Economic Analysis 53
2.2 Electrolyte Characterisation 56
2.2.1 Densitometry 56
2.2.2 Partial Molar Volumes 56
2.2.3 Hittorf Method - Transference Number 57
2.2.4 Restricted Diffusion - Salt Diffusivity 59
2.2.5 Concentration Cells - Thermodynamic Factor 62

2.2.6 Ionic Conductivity 64
2.3 Electrode Material Characterisation 65
2.3.1 Kang-Chueh GITT 65
2.3.2 PITT 67
2.3.3 Electrochemical Impedance Spectroscopy 68
2.3.4 Exchange Current Density 72
2.4 Other Electrochemical Techniques 73
2.4.1 Anode and Cathode Electrode Preparation 73
2.4.2 Coin Cell Assembly 73
2.4.3 Galvanostatic Cell Cycling 74
2.4.4 Three-electrode Cell 74
2.5 Error Analysis 75
2.6 Doyle-Fuller-Newman Modelling 76
2.7 Materials Characterisation Techniques 77
2.7.1 Scanning Electron Microscopy (SEM) 77
2.7.2 Powder X-ray Diffraction (XRD) 78
2.7.3 X-ray Photoelectron Spectroscopy (XPS) 78
2.7.4 Atomic force microscopy (AFM) 79

3 Characterising the Ionic Transport and Thermodynamic Properties of Potassium-ion Electrolytes 80
3.1 Introduction 80
3.2 Experimental 82
3.3 Results and Discussion 88
3.3.1 K Metal Electrode Preparation 88
3.3.2 Transference Number 93
3.3.3 Ionic Conductivity 95
3.3.4 Thermodynamic Factor 98
3.3.5 Property Parameterisation 103
3.3.6 Modelling 105
3.4 Conclusion 108

4 Characterising the Transport and Kinetic Properties of Potassium-ion Electrode Materials 110
4.1 Introduction 110
4.2 Experimental 112
4.3 Results and Discussion 115
4.3.1 Graphite Anode 115
4.3.2 Potassium Manganese Hexacyanoferrate Cathode 126
4.4 Conclusion 134

5 Modelling of Potassium-ion Batteries **136**
5.1 Introduction 136
5.2 Modelling details 137
5.3 Results and Discussion 138
5.3.1 Context - Lithium-ion NMC811 138
5.3.2 Potassium-ion Modelling 140
5.3.3 Comparison with LFP Lithium-ion 148
5.4 Conclusion 155

6 Conclusion and Future Work **158**
6.1 Conclusion 158
6.2 Future work 161

Appendices

A Appendix **165**

References **171**

List of Figures

1.1 Battery Critical Minerals and Metals Prices 5
1.2 Geographical distribution of the Global EV Battery Supply Chain . 6
1.3 Li^+, Na^+ and K^+ comparison 8
1.4 Example K-ion cell 10
1.5 Leading K-ion Cathode materials 13
1.6 Graphite Li^+, Na^+ and K^+ Intercalation properties 19
1.7 Techno-Economic Model of K-ion Batteries 27
1.8 Energy density and specific energy with Phosphorous anode 29
1.9 Mass and Volume fractions of modelled chemistries 30
1.10 Critical Research Fronts for K-ion Batteries. Adapted from Dhir *et al.*[1] 33
1.11 Doyle-Fuller-Newman Model schematic 37
1.12 Inconsistent diffusivity values reported in literature 47

2.1 Densitometric Hittorf cell 57
2.2 Designed Restricted Diffusion cell 60
2.3 Concentration cell 62
2.4 Concentration cell Measurement Window 63

3.1 K Electrode Preparation and Electrolyte Characterisation schematic 89
3.2 Potassium electrode stability and characterisation 90
3.3 AFM height maps K preparation comparison 91
3.4 OCV Restricted Diffusion Relaxation K Preparation comparison . . 91
3.5 Density correlations and Partial Molar Volumes 93
3.6 Transference Numbers and Ionic Conductivities 94
3.7 Cathodic and Anodic Hittorf Transference numbers 94
3.8 Cathodic chamber discolouration 95
3.9 Equivalent Conductance 96
3.10 Arrhenius plots 97
3.11 Activation energies for Ionic Conduction 97
3.12 Thermodynamic Factor 98
3.13 Representative Restricted Diffusion relaxation 100
3.14 Diffusivities 101

3.15 All Ionic transport and Thermodynamic electrolyte properties . . . 104
3.16 Doyle-Fuller-Newman (DFN) simulations 106

4.1 Graphite synchrotron XRD and SEM 115
4.2 Graphite SEM particle size analysis 117
4.3 Disc used to Model Graphite Particles 117
4.4 Graphite half-cell Galvanostatic Cycling 118
4.5 Graphite Kang-Chueh GITT Diffusivity characterisation 118
4.6 Example raw Graphite Kang-Chueh GITT 119
4.7 Graphite Nernst derivative and Dimensionless Pulse analysis 119
4.8 Graphite PITT and Kang-Chueh GITT Diffusivity comparison . . . 121
4.9 Graphite Exchange Current Density characterisation 123
4.10 Graphite EIS residual analysis 125
4.11 KMF Sychrotron XRD and SEM 126
4.12 KMF SEM particle size analysis 127
4.13 KMF half-cell Galvanostatic Cycling 128
4.14 KMF Kang-Chueh GITT Diffusivity characterisation 128
4.15 KMF Nernst derivative and Dimensionless Pulse analysis 129
4.16 Example raw KMF Kang-Chueh GITT 130
4.17 KMF PITT and Kang-Chueh GITT Diffusivity comparison 130
4.18 KMF Exchange Current Density characterisation 132
4.19 KMF EIS residual analysis 133

5.1 NMC811 Li-ion Simulations 139
5.2 K-ion Modelling Schematic 140
5.3 K-ion Full-cell DFN Simulations 142
5.4 K-ion Particle and Electrolyte Concentrations 144
5.5 Final overpotential components at increasing rate 145
5.6 Hypothetical LP57e electrolyte case 147
5.7 K-ion and LFP Li-ion Full-cell DFN Simulations 148
5.8 Final K-ion and Li-ion overpotential components 151
5.9 K-ion and LFP Particle and Electrolyte Concentrations 152

A.1 Median Electrode Material Diffusivities 166

List of Publications

This thesis is established based on the following articles:

1. Dhir, S., Wheeler, S., Capone, I., Pasta, M. Outlook on K-Ion Batteries. *Chem* **6**, 2442–2460 (2020).

2. Dhir, S., Jagger, B., Maguire, A., Pasta, M. Fundamental investigations on the ionic transport and thermodynamic properties of non-aqueous potassium-ion electrolytes. *Nature Communications* **14**, 3833 (2023).

3. Dhir, S., Cattermull, J., Jagger, B., Schart, M., Olbrich, L., Zhao, J., Sada, K., Goodwin, A., Pasta, M. Characterisation and Modelling of Potassium-ion Batteries. *Research Square* (2024) (*Preprint - Manuscript under review*)

   Other articles contributed to:

4. Zhao, J., Jagger, B., Olbrich, L., Ihli, J., Dhir, S., Zyskin, M., Pasta, M. Transport and Thermodynamic Properties of KFSI in TEP by Operando Raman Gradient Analysis *ACS Energy Letters* **9**, 1537-1544 (2024).

5. Narayanan, S., Burton, M., Jagger, B., Olbrich, L., Dhir, S., Shibata, M., Lain M., Astbury, R., Fumany, M., Favillier, H., Butcher, N., Copley, T., Pasta, M. Thin Lithium Metal Anodes for Solid-State Batteries: The Case for Scalable Evaporation *Manuscript in preparation*

6. Jagger, B., Aspinall, J., Dhir, S., Kotakadi, S., Cattermull, J., Pasta, M. Potassium alloy reference electrodes for potassium-ion batteries. *Manuscript in preparation*

7. Olbrich, L., Jagger, B., Dhir, S., Kakkanat, M., Pasta, M. Deconvolution of Li metal interphase formation processes *Manuscript in preparation*

8. Cattermull, J., Jagger, B., Dhir, S., Allan, P. K., Goodwin, A. L., Pasta, M. Mechanistic study of $K_2Mn[Fe(CN)_6]$ in a K-ion battery by *operando* characterisation. *Manuscript in preparation*

1 Introduction

Contents

1.1 Context - Critical Minerals 4
1.2 Why Potassium-ion? 7
1.3 How Potassium-ion Batteries work 8
1.4 State-of-the-art Materials and Electrolytes for Potassium-ion Batteries 11
1.5 Techno-Economic Analysis 26
1.6 Critical Research Fronts for Potassium-ion Batteries . 32
1.7 Doyle-Fuller-Newman Model 36
1.7.1 DFN Macroscopic Equations 36
1.7.2 DFN Microscopic Equations 40
1.8 Electrolyte Property Characterisation 42
1.8.1 Transference Number 43
1.8.2 Ionic Conductivity 44
1.8.3 Thermodynamic Factor 44
1.8.4 Salt Diffusivity 45
1.9 Electrode Material Property Characterisation 45
1.9.1 Solid-state Diffusivity 46
1.9.2 Exchange Current Density 49
1.10 Thesis Objectives 50

Some of the work of this chapter has been published in *Chem*:

1. Dhir, S., Wheeler, S., Capone, I., Pasta, M. Outlook on K-Ion Batteries. *Chem* **6**, 2442–2460 (2020).[1]

1.1 Context - Critical Minerals

To mitigate the most severe consequences of climate change requires a dramatic reduction in emissions, unprecedented in scale and speed[2,3]. It has been established that two of the most important solutions in terms of both emissions reduction potential and cost are the rapid scaling up of renewable energy supply and simultaneous electrification of a wide range of energy demand activities, such as road transport and heating[3,4]. Energy storage is critical in enabling this progress, first through storage of energy from intermittent and variable renewable generating sources to deliver power when required. Second through electrification of the road transport sector, one of the largest demand sources of emissions[5]. Hydro is the largest clean energy storage by current demand however, batteries are the the current leading geography-independent energy storage technology in terms of cost and capability. There is rapid rollout of grid-scale battery energy storage systems ongoing globally for this reason[6].

The transport demand sector is responsible for almost a quarter of all global energy-related emissions[5], with road transport responsible for around 75% of this[7]. Electrification of the majority of road transport is the current leading solution in terms of both cost and performance with batteries being the critical technology enabling this[3,4]. Hydrogen will play a role in heavy duty vehicles however in terms of cost and performance lithium-ion (Li-ion) battery electric vehicles (BEVs) are set to play the dominant role in road transport decarbonisation[4]. The leading battery chemistries for EVs are Li-ion nickel-rich metal oxide cathode chemistries, containing cobalt (60% cathode market share in 2022) matched with graphite anodes[8].

BEVs are reaching record sales and growth (14% of all new cars sold were electric in 2022 up from 9% in 2021)[8], and it is considered in many major economies EVs have already reached a tipping point where even without subsidies rapid rollout will continue[9]. One of the key drivers of this is that battery prices have dramatically decreased over the past decade, almost sixfold from 2013 to 2023[10]. Reaching 100 USD $kWh^{-}1$ is considered the critical goal where cost parity with internal

combustion engine (ICE) vehicles is reached, and widespread mass adoption of EVs will take place[11].

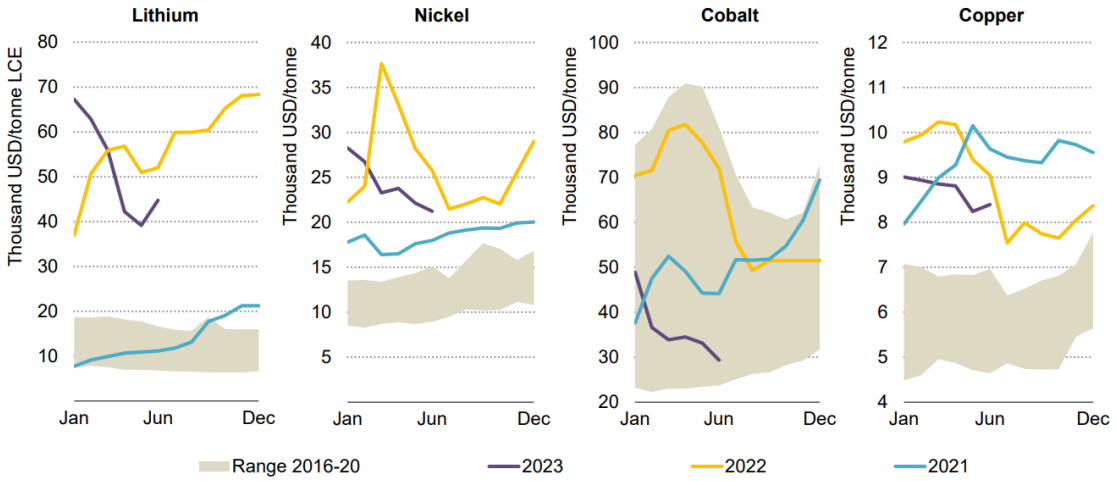


Figure 1.1 Battery critical minerals and metals price development. Reproduced from the IEA[12] under an Attribution 4.0 International (CC BY 4.0) license

.

However, the leading lithium-ion (Li-ion) chemistries meeting this demand are highly intensive in terms of critical minerals including lithium, nickel, cobalt, graphite and copper[13]. In critical pathways to meet net zero emissions by 2050, significant supply deficits are forecast for lithium, nickel, cobalt and copper in 2030[12], and new mines have lead times often over 10 years, making these supply gaps challenging to reduce in this timeframe[9]. In addition many of these critical minerals have experienced exceptional price volatility over recent years (Figure 1.1), posing significant uncertainty for their future security of supply[12,14,15]. For instance, in 2022 the trend of decreasing battery pack prices reversed with prices increasing for the first time in history and reversing a decade-long trend. The reason for this was the exceptional price rises of the critical Li-ion battery metals: lithium, nickel and cobalt. The lithium price increase over sevenfold from the start of 2021 to May 2022, nickel also reached price levels never seen before in this time[9]. These prices rises were caused by surging battery demand, supply chain disruption and supply underinvestment[9]. Since then the metal prices have dropped dramatically, particularly for lithium[12]. This is likely to again result in underinvestment in new supply with future supply consequences.

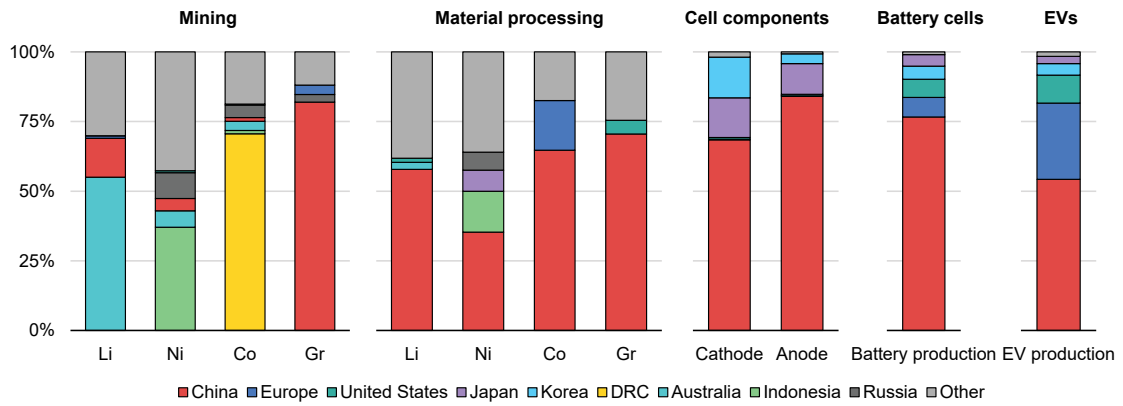


Figure 1.2 Geographical distribution of the global EV battery supply chain production and capacity 2021. Reproduced from the IEA[9] under an Attribution 4.0 International (CC BY 4.0) license

.

Coupled with this is the geographical concentration of battery critical mineral supply and processing. China dominates the entire downstream EV battery supply chain (Figure 1.2), being the dominant processor for all key critical minerals used in Li-ion[9]. The supply and processing of battery critical minerals is more concentrated than that for oil and gas[13]. This concentration means greater vulnerability to supply shocks, geopolitical shifts, and sudden policy changes. Restrictions on battery critical mineral exports have already occurred for instance Indonesia's nickel ore export ban from 2020 to develop a domestic processing industry, disrupting trade flows and global supply[16]. There are also significant environmental, social and governance (ESG) impacts with the mining of many of the critical Li-ion critical minerals, for instance human rights abuses associated with cobalt mining in the Democratic Republic of Congo[17,18], or intensive water usage from lithium mining where over half of lithium production is in areas of high water stress[13].

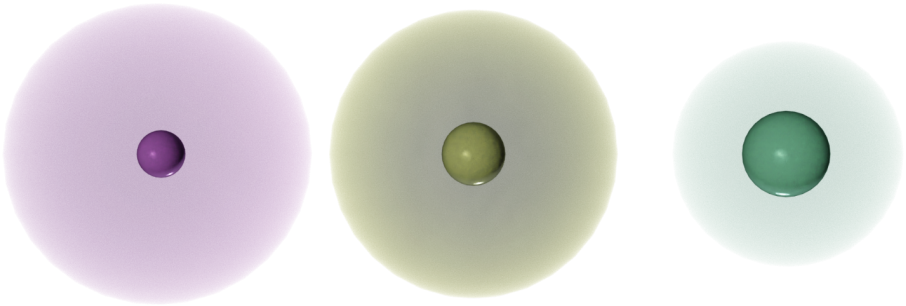
The level of price volatility, future supply deficits for net zero emissions pathways, geographical concentration, with its associated geopolitical risk, and significant ESG impacts of many Li-ion critical minerals is particularly concerning for future security of supply of critical minerals for Li-ion batteries (LIBs). Therefore, the case for alternative chemistries which can fulfil some LIB functions with reduced critical

mineral dependency is becoming increasingly important to ensure decarbonisation of the transport sector progresses unhindered[1,19–22].

1.2 Why Potassium-ion?

Potassium-ion (K-ion) presents several advantages over Li-ion, first potassium (K) is cheaper than Li, more abundant, and is significantly more globally distributed[1], particularly in comparison to the highly concentrated reserves of Li predominantly in South America and Australia[9]. In fact there is already an established industry for K as it is used as potash in fertilizer[23]. K-ion works the same as Li-ion so the LIB manufacturing processes developed over the past 30 years could easily be adapted[24]. In terms of other critical minerals the current leading cathode material for potassium-ion batteries (KIBs), the potassium manganese hexacyanoferrate $K_2Mn[Fe(CN)_6]$ (KMF), contains no critical minerals. Also, since K also does not alloy with aluminium, KIBs can also employ it as the anodic current collector, unlike for Li-ion, removing the requirement for any copper in the cell. Yet, most of these are advantages shared by sodium-ion (Na-ion) which is already making significant progress in commercialisation and scale-up[12]. However, KIBs present a critical advantage over sodium-ion batteries (NIBs) as K^+ can reversibly intercalate into the graphite electrodes used in LIBs[25,26], whereas Na^+ cannot, thus the anode for KIBs is already available at global industrial scale, unlike for NIBs[1].

Fast charging rates ($\sim$4C[29]) are also becoming increasingly important for batteries, particularly in electric vehicles (EVs) to be more competitive with ICE vehicles, however, conventional LIBs are inherently limited in their rate capability[30]. Critical challenges limiting accessible capacities at high rates in LIBs include slow electrolyte transport, Li metal plating and continuous solid electrolyte interphase (SEI) formation[29–31]. KIBs, however, may also present an advantage over LIBs and NIBs in terms of rate and power. The larger size of K^+ compared to Na^+ and Li^+ (Figure 1.3) results in a lower charge density, and thus weaker interactions with solvent molecules and a smaller Stokes radius[27], which is expected to facilitate faster ionic transport in the electrolyte[1]. Others have hypothesised this advantage



Alkali cation 'A'	Li^+	Na^+	K^+
Ionic radius	0.76 Å	1.02 Å	1.38 Å
Stokes radius in PC	4.8 Å	4.6 Å	3.6 Å
Ionic conductivity of 1 M AFSI in PC	6.8 mS cm^{-1}	7.8 mS cm^{-1}	9.9 mS cm^{-1}

Figure 1.3 Comparison of the ion size and Stokes radius in PC of Li^+, Na^+ and K^+, and the ionic conductivity of their corresponding FSI salts in PC[27,28]. Reproduced from Dhir *et al.*[1]

for K-ion from a smaller Stokes radius[32,33], however, there are also significant criticisms regarding the concept of a Stokes radius where for cases where the solvent molecules are similar size to the ions, the Stokes radius can lose physical meaning sometimes being smaller than the ion radius itself which is unphysical[34]. Though early data appears to show improved rate performance of K graphite compared to Li graphite half-cells[19,35]. Faster electrolyte transport would mitigate one of the critical limitations in fast charging rates. Therefore, this combination of having reduced critical mineral intensity, the advantage over Na-ion of being able to utilise graphite anodes, and the potential for faster charging make K-ion a particularly interesting and promising battery chemistry to research.

1.3 How Potassium-ion Batteries work

K-ion batteries work identically to Li-ion batteries. There are three primary components: the cathode (positive electrode), anode (negative electrode) and the electrolyte. The two electrodes are the primary reactive constituents where energy is stored as chemical potential energy. The two electrodes have their own electrochemical potential based on their chemical composition and the difference

between these determines the equilibrium cell voltage which is related to the Gibbs free-energy of the overall electrochemical reaction:

$$E = -\frac{\bar{\mu}_{cathode} - \bar{\mu}_{anode}}{zF} = -\frac{\Delta G}{zF} \tag{1.1}$$

Where E is the equilibrium cell voltage, $\mu_{cathode}$ and μ_{anode} are the electrochemical potentials of the cathode and anode, respectively, z is the charge of cation, F is Faraday's constant and ΔG is Gibbs free energy of the system.

The electrolyte is an ionically conductive, yet electronically insulating medium which separates the anode and cathode, comprising of a salt of the alkali cation in a solvent. The anode and cathode are electronically connected through an external circuit where power is drawn or supplied. During discharge an oxidation half-reaction occurs at the anode, while a simultaneous reduction half-reaction occurs at the cathode. Concurrently a positively charged cation (K^+) is released from the anode active material where oxidation occurs into the electrolyte and a negatively charged electron into the external circuit to maintain charge neutrality. The K^+ released from the anode migrates through the electrolyte to the cathode where the cathode active material is reduced with the electron supplied by the anode through the external circuit. As the cation and electrons are released or combined from or into the electrode, its electrochemical potential changes due to the oxidation or reduction. When fully charged, there is a large difference between the electrochemical potentials of the two electrodes providing a significant driving force for the reaction between the electrodes. If current is able to to flow the reaction will proceed spontaneously. During charging the process is reversed with current supplied and oxidation occurring at the cathode and reduction at the anode with electrons and the cations moving from the cathode to anode reversing the discharge reactions.

The cell voltage is the difference between the anode and cathode potentials. The energy and power density of a cell can be increased by increasing the difference between these potentials through optimised material selection. Capacity is also a critical measure of the amount of charge that can be stored by the cell in the

units Ah, with the capacity of an active electrode material typically compared per unit mass as specific capacity (or gravimetric capacity) with units mA h g^{-1}. The capacity of an electrode material refers to the amount of the alklai cation that can be stored in the material. Together the cell voltage and capacity determine how much energy can be stored and provided by the cell in units Wh, conventionally reported per unit mass or volume as specific energy (Wh $kg^{-}1$ often referred to as gravimetric energy density) or energy density (Wh $L^{-}1$). Rate capability of batteries is typically defined by its accessible capacity at increasing currents. The rate of discharge or charge is known as C-rate, which is a measure of the rate to fully charge or discharge the cell of known capacity. A C-rate of 1C refers to the current which will fully charge/discharge the cell in 1 hour, whereas a C-rate of 2C will charge/discharge the cell in 30 minutes. The C-rate can be determined by dividing the charge/discharge current by the cell capacity, or a desired C-rate multiplied by the capacity provides the required current.

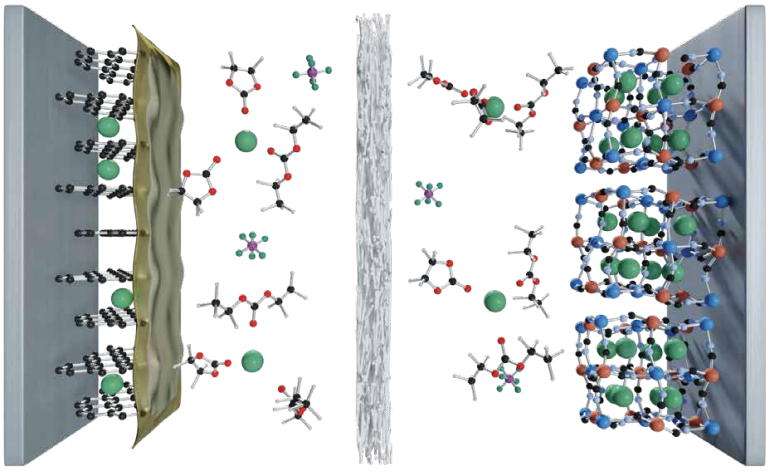


Figure 1.4 Example K-ion cell. Graphite anode on the left with the SEI formed, an ionic liquid electrolyte and separator in the middle and on the right a potassium manganese hexacyanoferrate $K_2Mn[Fe(CN)_6]$ cathode. The K^+ ion is shown in green. Adapted from Dhir *et al.*[1]

For Li-ion graphite is the leading anode where Li^+ is stored in the graphite via an intercalation mechanism, a reversible insertion into a layered structure. Layered metal oxides are the leading cathodes for Li-ion also storing the Li^+ through an

intercalation mechanism. K-ion batteries function just as Li-ion, but the leading materials for its electrodes and electrolytes differ from Li-ion. An example K-ion battery is depicted in Figure 1.4 with a graphite anode on the left, a potassium manganese hexacyanoferrate $K_2Mn[Fe(CN)_6]$ (KMF) cathode on the right separated by an electrolyte. The leading materials and electrolytes for K-ion are explored in further detail.

1.4 State-of-the-art Materials and Electrolytes for Potassium-ion Batteries

Cathodes

The larger size of K^+, compared to both Li^+ and Na^+ (Figure 1.3), causes significant challenges for KIB cathode development. Currently, the most researched cathodes are layered transition-metal oxides, Prussian Blue Analogues (PBAs), polyanionics and organic materials. Table 1.1 details a selection of the leading KIB cathode chemistries.

Layered Metal Oxides

Layered metal oxides with the general formula A_xMO_2 (A = alkali metals, M = transition metals) are the leading cathode material for LIBs and leading candidates for NIBs due to their high theoretical specific capacities and high crystal densities. However, they have shown limited performance for KIBs so far, exhibiting low operating voltages (<3 V vs. K^+/K), moderate specific capacities and limited cyclability (Table 1.1).

The layered metal oxide structure consists of edge sharing MO_6 octahedra forming two dimensional slabs with interslab layers which accommodate alkali metals (Figure 1.5a). Li^+, comparable in size to transition metals, exclusively occupy octahedral (O) sites, whereas Na^+ and K^+ occupy both octahedral and the larger prismatic (P) sites.[28] In fact, of the 3d transition metal K layered oxide materials only Cr and Sc can be synthesised in the stoichiometric form with the O3 structure, all others are

Table 1.1: Electrochemical properties of leading K-ion cathode chemistries. The three chemistries in bold were considered the leading chemistries in the PBA, metal oxide, and polyanionic material classes and were used in the techno-economic analysis.

Chemistry	**Material class**	**Capacity achieved** ($mA\,h\,g^{-1}$ **(theoretical))**	**Average voltage** (V)	**Rate (capacity** [$mA\,h\,g^{-1}$] **at current** [$mA\,g^{-1}$]**)**	**Initial coulombic efficiency (%)**	**Cyclability (capacity retention % (cycle number))**
$K_{1.75}Mn[Fe(CN)_6]_{0.93} \cdot 0.16\,H_2O$ (KMnFe-PBA)[36]	**PBA**	**141 (155)**	**3.8**	**108 at 1000** ($30\,mA\,g^{-1}$ **charge rate)**	**∼60**	**∼91 (100)**
$K_2Mn[Fe(CN)_6]$[35]	PBA	132 (155)	3.9	∼96 at 2C	80	∼95 (350)
$K_{1.89}Mn[Fe(CN)_6]_{0.92} \cdot 0.75\,H_2O$[37]	PBA	142 (155)	3.6	∼94 at 2C	∼70	∼73 (100)
$K_{1.91}Mn[Fe(CN)_6]_{0.97} \cdot 0.43\,H_2O$[38]	PBA	119 (155)	4.02	∼51 at 2C	80	∼87 (100)
$K_{1.64}Fe[Fe(CN)_6]_{0.89} \cdot 0.15\,H_2O$[36]	PBA	130	3.5	∼125 at 1000 ($30\,mA\,g^{-1}$ charge rate)	∼95 (70 on 2nd cycle)	∼86 (100)
P_2−$K_{0.65}Fe_{0.5}Mn_{0.5}O_2$ microspheres (KFeMnO)[39]	**Metal oxide**	**151**	**2.5**	**103 at 100**	**∼95**	**78 (350)**
P_3−$K_{0.7}Fe_{0.5}Mn_{0.5}O_2$ nanowires[40]	Metal oxide	178	2.25	∼60 at 1000	87.6	∼70 (45)
P_3−$K_{0.5}MnO_2$[41]	Metal oxide	100	2.6	72 at 100	∼50	70 (50)
K-birnessite $K_{0.77}MnO_2H_2O$[42]	Metal oxide	134	∼2.75	77 at 1000	-	80.5 (1000)
$K_3V_2(PO_4)_2F_3$ (KVPOF)[42]	**Polyanionic**	**104 (115)**	**3.7**	**83 at 100**	**∼65**	**95 (180)**
$KVPO_4F$[43]	Polyanionic	90 (131)	4.13	∼90 at 5C (2C charge rate)	∼68	97 (30)
Stoichiometric $KVPO_4F$[44]	Polyanionic	105 (131)	4.3	65 at 100	∼72	75 (30)
Amorphous $FePO_4$[45]	Polyanionic	156 (178)	2.64	-	-	70 (50)
Orthorhombic $KFeSO_4F$[46]	Polyanonic	100 (128)	3.6	∼88 at 2C (C/10 charge rate)	-	86 (100)
CuTCNQ[47]	Organic	244	2.8	125 at 1000	∼80	70 (50)
PAQS[48]	Organic	220	1.9	-	∼90	75 (50)

synthesised nonstoichiometric with less K per formula unit with P2 or P3 structures, an example being P2-K_xCoO_2[49]. In full cells, nonstoichiometric cathode materials would either significantly reduce the specific capacity or require prepotassiated anodes.

The large size of K^+ increases the interslab distance which reduces the screening of the K^+ charge from the slab layers. This increases the K^+ - K^+ repulsion leading to greater K^+/vacancy ordering within the layers[41,49]. The increased interslab

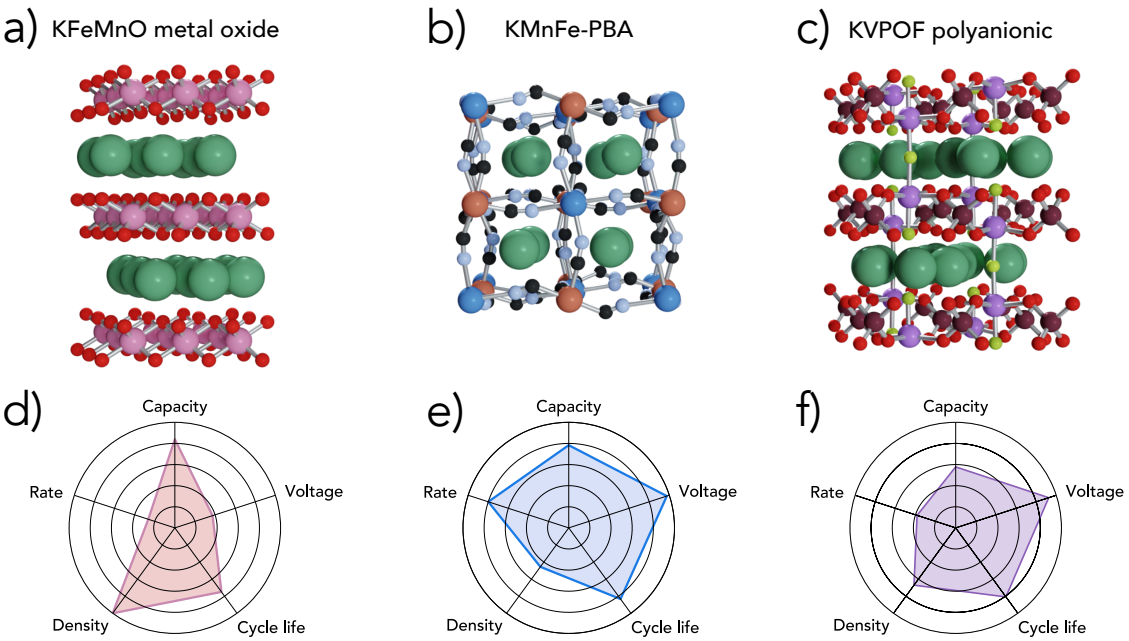


Figure 1.5 Crystal structures of the three leading K-ion cathode materials: (a) $K_{0.65}Fe_{0.5}Mn_{0.5}O_2$ (KFeMnO)[39]; (b) $K_{1.75}Mn[Fe(CN)_6]_{0.93} \cdot 0.16\,H_2O$ (KMnFe-PBA)[36]; (c) $K_3V_2(PO_4)_2F_3$ (KVPOF)[42]. Radar plot of electrochemical properties of the three leading K-ion cathode materials: (d) KFeMnO; (e) KMnFe-PBA; (f) KVPOF. Reproduced from Dhir *et al.*[1]

distance and greater K^+/vacancy ordering, coupled with transition metal charge ordering, leads to many stable intermediate phases being formed causing more phase transitions during cycling, limiting cyclability. This also results in many voltage plateaus and large voltage steps which increases the voltage range over which the material cycles and hence, reduces their average operating voltage. Phase transformations cause a voltage plateau because there is a mixture of two phases of constant composition during the transformation, with a changing share of each. Therefore, as the compositions do not change ΔG remains constant and from Equation 1.1 E is also constant, causing the voltage plateau.

In addition, the transition metal redox voltage is also lowered from weaker M-O bonds. Moreover, there are irreversible structural changes at high voltages/low K contents, limiting the maximum voltage cut-off and capacity to ensure adequate cyclability[41]. The larger interslab distance also enables water and oxygen intercalation which can lead to decomposition of the material and therefore requires inert atmosphere processing[50]. However, contrary to this, K-birnessite actually

shows improved performance from the intercalated water which acts as a pillar within the layer enabling faster K^+ diffusion and greater structural stability at low K content[42].

Developing compositions with multiple transition metals, including both redox active and inactive metals, is a vital strategy to: disrupt and alleviate the K^+/vacancy ordering and the corresponding voltage steps; stabilise the structure over a wider range of K content, increasing the capacity; and in some cases, increase the operating voltage. Morphology is also a crucial tool which has demonstrated success through nano scaling or using microspheres, resulting in improved electron/ion transport, reversible phase transformations, and higher capacity. For instance, $P_3{-}K_{0.7}Fe_{0.5}Mn_{0.5}O_2$ nanowires[40] and $P_2{-}K_{0.65}Fe_{0.5}Mn_{0.5}O_2$ (KFMO) microspheres[39] achieve specific capacities of 178 mA h g^{-1} and 151 mA h g^{-1} respectively, although at low operating voltages of <2.5 V vs. K^+/K. KFMO microspheres show notable cycling stability, maintaining 78% of initial capacity after 350 cycles (Figures 1a and d).

Prussian Blue Analogues

Prussian blue analogues (PBAs) have a cubic open-framework structure comprised of transition metals bridged by cyanide ligands (Figure 1.5b). They have the general formula $A_xM1\,[M2\,(CN)_6]_{1-y} \cdot wH_2O$ (abbreviated to AM1M2-PBA) where A is the insertion alkali metal cation, M1 and M2 are transition metals, y is the hexacyanometalate vacancy fraction, and w is the number of water molecules. M1 and M2 are octahedrally coordinated to six nitrogen and carbon atoms, respectively. They are synthesised through a low-cost aqueous coprecipitation procedure from abundant precursors[51]. The open-framework structure experiences minimal structural change during ion insertion, being stable over the full alkali-ion content range, and has wide diffusion channels that it is believed enable fast transport of large alkali cations such as Na^+ and K^+[51,52]. This leads to exceptional cyclability and high rate capability, although performance depends considerably on material composition and electrolyte. To reach the theoretical specific capacity

($155\,\mathrm{mA\,h\,g^{-1}}$ for KMnFe-PBA) the vacancy content must be minimised and both transition metals sites must be electrochemically active, ensuring a two-electron reaction and full utilisation of interstitial sites.

Currently, the best performing K-ion PBA cathode chemistries are KMnFe-PBA and KFeFe-PBA, having achieved high capacities in the range $130-142\,\mathrm{mA\,h\,g^{-1}}$[36,37]. Notably, KMnFe-PBA has a higher average discharge potential compared to KFeFe-PBA (Table 1.1), owing to the higher voltage $Mn^{3/2+}$ redox couple, and therefore, has received the most research attention. $K_{1.75}Mn[Fe(CN)_6]_{0.93} \cdot 0.16\,H_2O$ (Figures 1.5b and e) is one of the leading K-ion PBAs, having achieved a high specific capacity of $141\,\mathrm{mA\,h\,g^{-1}}$, an operating voltage of 3.8 V (vs. K^+/K), and good cyclability (∼91% after 100 cycles). However, it is currently limited by an impractically low coulombic efficiency (CE) of <95%[36]. Aluminium current collector corrosion and electrolyte decomposition are significant challenges at potentials >4 V. Using a concentrated KFSI electrolyte was shown to improve the cyclability of the KMnFe-PBA further (>90% capacity after 350 cycles)[35], however, the coulombic efficiency remains low at ∼95%. Employing a KFSI ionic-liquid electrolyte resulted in a higher average discharge voltage of 4.02 V (vs. K^+/K) for KMnFe-PBA with a high stable coulombic efficiency of 99.3%[38].

There are multiple possible mechanisms contributing to capacity fade and poor coulombic efficiency for the KMnFe-PBA. Remnant water in the structure from synthesis can be responsible for deleterious side reactions impacting electrochemical performance in non-aqueous electrolytes[51]. Therefore, synthesis methods which reduce the vacancy, and water, content must be developed as well as effective dehydration procedures. Dissolution of the material is also detrimental to cyclability, in particular for Mn-containing materials. Additionally, $Mn^{III}N_6$ octahedra undergo a Jahn-Teller distortion which leads to a phase transition from cubic to tetragonal as the material is oxidised, which lowers cyclability[36]. Fortunately, strategies to overcome these issues have been developed for the Na-analogue, NaMnFe-PBA, and are effective for KMnFe-PBA. For instance, citrate-assisted synthesis to produce low-vacancy and water content materials[38,53], and doping strategies to alleviate the

material dissolution and tetragonal phase transformation[54]. Furthermore, there is evidence that low-vacancy K-ion PBA cathodes exhibit much slower kinetics in non-aqueous electrolytes than their Na-ion counterparts, manifesting in reduced specific capacities for larger particle sizes and inferior rate capabilities[38,55]. However, the nature of this effect requires further investigation.

Nevertheless, the fundamental limitation of PBAs is their intrinsic low bulk density ($\sim$2.2 g cm^{-3} for stoichiometric KMnFe-PBA), limiting the achievable energy density. Another limitation of PBAs is their low electronic conductivity[51]. Carbon PBA composites are being developed for NIBs which may provide a solution, though at the expense of energy density[56,57].

Polyanionic Compounds

Polyanionic materials have framework structures composed of corner sharing MO_x (M = transition metals) and $[XO_4]^{n-}$ (X = P or S) polyhedra. Alkali ions, such as Li^+ or K^+, are hosted in interconnected interstitial sites, resulting in high stability and fast alkali cation bulk diffusion. Compared to PBAs, there are a greater diversity of polyanionic compounds, given the range of crystal structures and anion groups (phosphate, pyrophosphate, florophosphate, fluorosulphates etc.)[46]. Bulky anion groups lead to reduced specific capacities and crystal densities compared to layered oxide materials[50].

Lithium iron phosphate (LFP) a commercial LIB cathode is the most established polyanionic material. However, when the same material is cycled with potassium the structure loses crystallinity due to the larger size of K^+[46]. Nevertheless, amorphous or low crystallinity $KFePO_4$ displays stable reversible cycling, and presents high capacities (156 mA h g^{-1}), though with a low operating voltage (2.64 V)[45].

Open-framework structures with larger interstitial sites and wider diffusion channels are required for fast diffusion of the large K^+ and for reversible phase transformations, though inevitably this results in low density materials. KTP-type ($Pna2_1$) structures such as $KVOPO_4$[43], $KVPO_4F$[43], orthorhombic $KFeSO_4F$[58] display such properties and have proved successful. Among reported materials

only vanadium- and iron-based polyanionic materials have shown reasonable electrochemical activity as cathode materials, others appear to be inactive[46]. Vanadium-based polyanionic materials present the best electrochemical performance with high operating voltages (∼4 V) and reasonable capacities (∼100 mA h g^{-1})[42–44]. One of the leading materials is $K_3V_2(PO_4)_2F_3$ (KVPOF), having demonstrated impressive all round electrochemical performance (Figures 1.5c and f)[42]. However, vanadium is both expensive and toxic which limits the materials potential for application. Iron-based materials use the $Fe^{3/2+}$ redox couple which typically operates at low voltages. However, because of the strong inductive effect from SO_4^{2-} and F^- a moderate redox potential of 3.6 V vs. K^+/K was achieved by orthorhombic $KFeSO_4F$, which also has a KTP-type structure[46,58]. Future research should focus on developing high-voltage materials containing earth abundant elements, such as iron and manganese. To ensure high operating voltages and reversible potassium insertion, careful consideration of the anion groups and crystal structure is required.

Organic Materials

Organic materials do not require the high-temperature syntheses used for inorganic electrode materials, and therefore, present a potential low-cost option. Currently, organics have achieved high capacities but low operating voltages (2−2.5 V vs. K^+/K) and poor cyclability[28]. The best performing material, copper-tetracyanoquinodimethane (CuTCNQ), achieves a specific capacity of 244 mA h g^{-1}, an average discharge potential of 2.8 V (vs. K^+/K), and retains 70% of its initial capacity after 50 cycles[47]. However, organics suffer from three major challenges: a low bulk density leading to low energy densities; dissolution problems in the electrolyte; and the electrodes are synthesised without potassium in the structure.

Anodes

Graphite is indeed the leading KIB anode with impressive performance demonstrated, however, there is also considerable research into alternatives including hard and soft carbons, alloying, conversion, organics, polyanionics and other intercalation materials. Table 1.2 details a selection of the leading KIB anode chemistries.

Table 1.2: Electrochemical properties of leading K-ion anode chemistries. The graphite chemistry in bold was used in the techno-economic analysis.

Chemistry	**Material class**	**Capacity achieved ($mA\,h\,g^{-1}$ (theoretical))**	**Average voltage (V)**	**Rate (capacity $[mA\,h\,g^{-1}]$ at current $[mA\,g^{-1}]$)**	**Initial coulombic efficiency (%)**	**Cyclability (capacity retention % (cycle number))**
Graphite (SNO3 Carbon)[35]	**Graphite**	**260 (279)**	**0.3**	**250 at 5C**	**81.5**	**99.9 (300)**
Cellulose-derived hard carbon[59]	Hard carbon	290	≈0.5	-	≈81.5	95 (50)
Hard-soft carbon composite[60]	Hard/soft carbon	230	≈0.5	121 at 5C	67	93 (200)
Amorphous ordered mesoporous carbon[61]	Porous carbon	307.4	1.2	144.2 at 1000	63.6	64 (200)
Hollow carbon[62]	Porous carbon	340	≈0.25	105 at 2C	72.1	≈100 (150)
N-doped Graphene[63]	Graphene	350	≈0.4	50 at 200	≈55	≈78 (100)
Red phosphorous CNT composite[64]	Alloy	715.2	≈0.5	323.7 at 2000	59	≈59 (40)
Sn_4P_3-C[65]	Alloy	384.8	0.3	222 at 1000	≈64	≈80 (50)
Amorphous $FeVO_4$/C[66]	Conversion	350 (392)	≈1.7	180.3 at 2000	≈42	≈100 (2000)
K_2TP/SP[67]	Organic	260	≈0.6	185 at 1000	76.1	94.6 (500)
$K_2Ti_6O_{13}$[68]	Titanate	91	≈1.25	64 at 500	34	84 (1000) from 6th cycle
$KTi_2(PO_4)_3$@C[69]	Polyanionic	292.7	≈1.3	133.1 at 1000	35.3	75.7 (50)

Graphite

Graphite is comprised of sp2 hybridised graphene layers connected by weak Van der Waals forces of delocalised electron orbitals. This weak interaction between the layers is what enables the intercalation of ions into graphite through expansion of the interlayer distance and the formation of graphite intercalation compounds (GICs)[70].

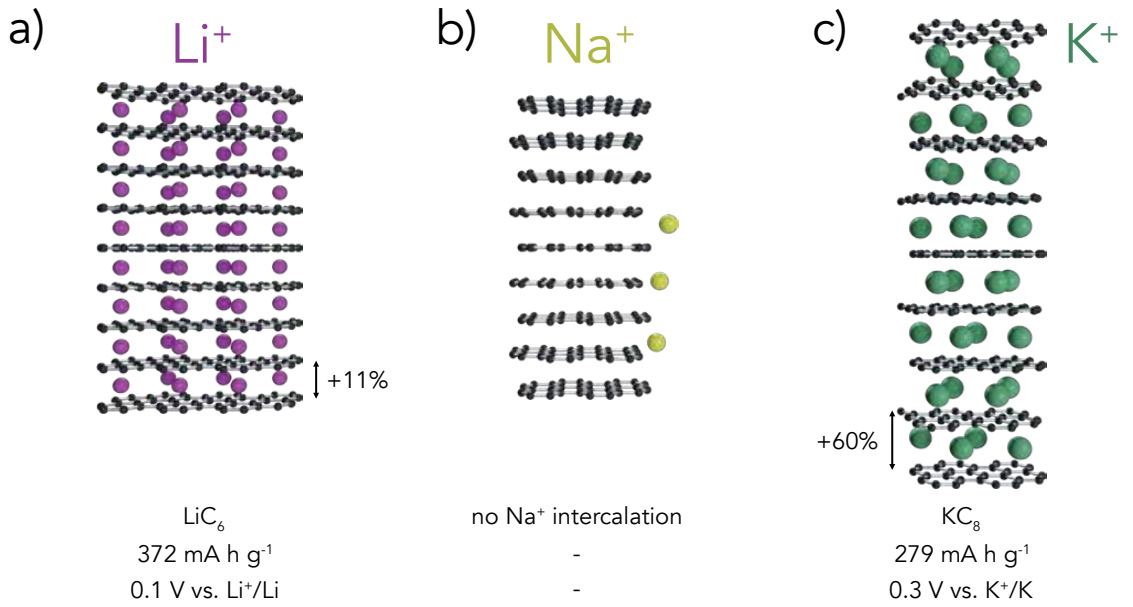


Figure 1.6 Comparison of the graphite intercalation properties of Li^+, Na^+ and K^+ including composition, theoretical specific capacity and operating voltage. Adapted from Dhir *et al.*[1]

The critical advantage of KIBs over NIBs is that K^+ electrochemically intercalates into graphite to form KC_8 (Figure 1.6)[25,26], whereas Na^+ does not intercalate. K^+ intercalation into graphite, compared to Li^+, occurs at a higher potential (0.3 V vs. K^+/K[26] compared to 0.1 V vs. Li^+/Li), results in a larger volume expansion (60% compared to 11%), and presents a lower theoretical specific capacity (279 mA h g^{-1} compared to 372 mA h g^{-1})[71]. Reversible capacities for K^+ intercalation into graphite ranging from 240−279 mA h g^{-1} have been achieved, essentially reaching the theoretical value. In addition, graphite has a relatively high density of 2.3 g cm^{-3}[25].

Interestingly, graphite may support superior rate performance in KIBs compared to LIBs. The diffusion coefficients of Li^+ and K^+ in graphite LiC_6 and KC_8 were calculated from density functional theory (DFT) modelling as 1.5×10^{-15} and 2.0×10^{-10} m^2 s^{-1}, respectively[72], though this should be evaluated experimentally. Additionally, there is a greater difference between the K^+ graphite intercalation potential versus the K-metal plating potential, in comparison to the Li equivalents i.e. $E_{K-graphite} - E_{K-plating} > E_{Li-graphite} - E_{Li-plating}$. This greater difference in potential allows larger overpotentials to be experienced without reaching the K plating potential thus reducing the risk of metal plating, a major degradation

mechanism[30], and dendrite formation, both which are major limitations for LIB charging rates[73]. Impressive rate performance has also been demonstrated experimentally. Komaba *et al.* maintained ∼96% capacity at the high rate of 5C[35].

Until recently, the primary concern was the volume change upon K^+ intercalation/deintercalation which damages the SEI and results in poor coulombic efficiency and cyclability. However, Komaba *et al.* achieved exceptional all-round electrochemical performance using a highly concentrated KFSI/DME electrolyte, achieving a specific capacity of 260 mA h g^{-1}, 81.5% first cycle CE, excellent rate capability (250 mA h g^{-1} at 5C) and cyclability (99.9% capacity retention after 300 cycles)[35]. In addition, excellent graphite electrochemical performance has been demonstrated by using a KFSI in ionic-liquid electrolyte, observing a specific capacity of 246 mA h g^{-1}, 99% capacity retention after 400 cycles and a stable coulombic efficiency of 99.94%[38]. Moreover, the choice of binder has been shown to significantly impact electrochemical performance. Komaba *et al.* found that using carboxymethyl cellulose (graphite with CMC), poly(sodium acrylate) (PANa), and polyvinylidene fluoride (PVDF) binders resulted in an initial coulombic efficiency of 89%, 79% and 59%, respectively[26]. The improved performance of CMC and PANa was attributed to the pre-formed SEI effect and avoiding deflourination as seen for PVDF. These studies highlight choosing the right electrolyte and binder is critical to realising high performance graphite anodes in KIBs.

Other Anodes

Other carbon materials have been reported to electrochemically intercalate K^+ including soft carbons[25,60], hard carbons[59,74], porous carbons[61,62,75] and graphene-based materials[63]. Soft carbons are graphitisable, and their degree of crystallinity and interlayer spacing is tunable by thermal treatment[76]. The expanded layers facilitate faster K^+ diffusion which, coupled with its high electronic conductivity, enables impressive rate capability. However, soft carbons typically display poor cyclability[25,60]. Conventional hard carbons are non-graphitisable and consist of disordered, randomly oriented graphitised microdomains without long

range order[74]. Compared to soft carbons they achieve superior cyclability as their structure can better tolerate potassium insertion[59,60]. Jian *et al.* concluded this was due to the nongraphitic structure with greater disorder along the c-axis[60]. However, hard carbons exhibit inferior rate capability compared to soft carbons[60]. The voltage profiles of both hard and soft carbons are more sloped and they have higher average potentials compared to graphite, and therefore lower energy density in a full cell. Both present specific capacities comparable to the theoretical capacity of graphite, however they have lower bulk densities ($\sim$1.5 vs 2.3 $\mathrm{g\,cm^{-3}}$) which results in inferior energy density compared to graphite. A hard/soft carbon composite has been synthesised in an attempt to realise both the hard carbon cyclability advantages and soft carbon rate advantages, however, the resulting capacity, cyclability and rate remain inferior to that achieved with graphite so far[60]. Porous carbons and graphene-based compounds have shown specific capacities significantly greater than that of graphite (300 - 420 $\mathrm{mA\,h\,g^{-1}}$), however, they also suffer from low tap densities, limiting achievable energy density, and some graphene-based materials have significantly higher costs of production than graphite, limiting their viability[61–63,75].

K alloys have been studied for KIBs because they store greater amounts of K than intercalation materials and can therefore, achieve considerably higher capacities. However, they display relatively high operating voltages, typically above 0.6 V (vs. $\mathrm{K^+/K}$)[77], exhibit large volume expansions, and have low electronic conductivities. Compared to their Li and Na counterparts, K alloying materials show lower specific capacities due to lower alkali metal content (KP compared to $\mathrm{Li_3P}$ and $\mathrm{Na_3P}$, for example)[28], higher operating voltages, and larger volume expansions for the equivalent amount of charged stored ($\sim$200% for KM and $\sim$500% for $\mathrm{K_3M}$)[28]. The volume expansion suffered by alloying materials during cycling is the most critical issue and may result in pulverisation of active materials possibly leading to loss of electrical contact; and SEI fracture leading to repeated electrolyte decomposition, resulting in lower coulombic efficiency and resultant capacity loss. Studies have achieved reversible capacities using K alloys with Group 15 elements such as Bi, Sb,

and P, and often carbon composites, in the range 400–715 mA h g^{-1}[64,78,79]. However, the significant volume expansion severely limits their cycle lives (<40 cycles) even at very low rate[64]. Nanostructured electrodes and modified electrolytes could present a solution to the volume change problem[28].

Conversion materials for KIBs are in their infancy, yet suffer the same volume expansion challenges as the alloy materials with the additional issues of a low energy efficiency from a large potential hysteresis between the charge and discharge processes, and extremely low initial CEs[66]. Organic anodes show promise in their ability to store the large K^+ but are limited by their low capacities, high operating voltages, low bulk density, and their low electronic conductivity[67,80]. Nevertheless, capacity, rate and cycle life results from organic carbon composites, such as $K_2C_8H_4O_4$/SP, are promising[67]. KTO chemistries, analogous to LTO ($Li_4Ti_5O_{12}$), have also been explored, however, they demonstrate poor performance including very low CEs, high voltages (0.8 – 1.6 V vs. K^+/K) and low capacities (<182 mA h g^{-1})[68,81,82]. More promising are Ti-based polyanionic compounds such as $KTi_2(PO_4)_3$@C achieved a high capacity 292.7 mA h g^{-1} yet, still a high operating voltage (1.3 V) and limited cyclability[28,69].

Electrolytes

As mentioned K^+ is larger in size than both Na^+ and Li^+ and, therefore, has a lower charge density which considerably influences its transport behaviour (Figure 1.3). Firstly, K^+ has the lowest energy of solvation/desolvation of the three as calculated by Okoshi *et al.*[83]. This enables a fast desolvation process at the electrode-electrolyte interface with beneficial effects on rate capability. In LIBs, Abe *et al.* demonstrated that one of the major rate-limiting processes of Li^+ intercalation into the graphite electrode is the desolvation process[32], suggesting KIBs may be more suitable for high power applications. Also K^+ in solution is expected to have have a smaller Stokes radius, due to weaker interactions with solvent molecules from the lower charge density, which facilitates higher ionic conductivity and faster transport.

This is supported by the findings of Barthel *et al.* who reported that the ionic conductivity of KPF_6/PC was highest compared to the Li and Na equivalents, which they concluded was due to the smaller Stokes radius of K^{+}[33]. Komaba *et al.* also evaluated the ionic conductivity of AFSI/PC (A = K, Li, Na) solution and found that KFSI/PC achieved the highest ionic conductivity of the three, although another study found KPF_6 in 50:50 EC:DMC showed the lowest ionic conductivity compared to its Li and Na counterparts[28,84,85]. The results suggest an optimised K^{+} electrolyte could achieve higher ionic conductivities than Li and Na optimised electrolytes. K^{+} solutions were also found to have lower viscosities than their Li and Na counterparts for both AFSI/PC and APF_6/EC:DMC solutions[84,85]. This low viscosity is highly advantageous for practical battery assembly as it facilitates wetting of the separator and electrodes thus expediting electrolyte filling and formation. Viscosity is often a critical overlooked parameter for viable electrolytes. However, one disadvantage is that potassium salts typically have lower solubilities as they have weaker bonds to solvent molecules.

The vast majority of KIB studies so far have utilised electrolytes comprised of KPF_6 and KFSI salts in organic solvents. KPF_6 is the most common as it prevents corrosion of the Al current collector at high potentials and shows increased ionic mobility and a higher dissociation constant compared to KFSI−based electrolytes[35]. Nevertheless, KPF_6−based electrolytes show an inferior coulombic efficiency at the anode due to the formation of an unstable SEI[71]. The choice of solvent was also found to play a significant role in performance. KPF_6 in EC:DEC experiences severe electrolyte decomposition at high and low potentials, however, KPF_6 in EC:PC has been shown to suppress these side reactions[43]. Zhao *et al.* found that, using KPF_6, the graphite electrodes reached over 200 cycles in EC:PC and EC:DEC electrolytes but suffered significant capacity degradation after 70 cycles in EC:DMC. In addition, EC:PC had the highest initial coulombic efficiency (66.5%), compared to 47% and 43% for EC:DEC and EC:DMC, respectively[71]. Ether-based electrolytes have been shown to cointercalate with potassium into graphite which raises the operating voltage and reduces the specific capacity[86].

KFSI−based electrolytes tend to cause corrosion of the Al current collector at potentials above 4 V (vs. K^+/K), which is a significant limitation. However, Hosaka *et al.* suppressed the corrosion in highly concentrated KFSI/DME and KFSI/y-butyrolactone electrolytes[35]. The high concentration prevents the dissolution of Al^{3+} by decreasing the activity of the solvent. In addition, the high concentration prevents the cointercalation of DME. Nevertheless, this is an expensive solution. Critically, KFSI-based electrolytes were found to be advantageous for full cells, where in a graphite||KMnFe-PBA full-cell the 7 mol kg^{-1} KFSI/DME achieved a higher coulombic efficiency and cyclability over 100 cycles, greater than in the 1 mol kg^{-1} KPF_6 EC:PC electrolyte. However, the coulombic efficiency and cyclability remain impractically low[35]. Komaba *et al.* showed using a mixture of KFSI and KPF_6 salts in carbonate solvents suppressed the aluminium corrosion whilst maintaining the SEI advantages from the FSI. They showed impressive cyclability in a full cell over 500 cycles, though still with impractical coulombic efficiencies.

Ionic liquid (IL) electrolytes are promising for KIBs because of their wider electrochemical stability window, compared to organic solvents. Hagiwara found that the IL K[FSI]−[C_3C_1pyrr][FSI] (C_3C_1pyrr = N-methyl-N-propylpyrrolidinium) presented a higher ionic conductivity 4.8 mS cm^{-1} and wider electrochemical window (5.72 V) than its Li and Na counterparts[87]. Our group has recently demonstrated cycling of KMnFe-PBA in a KFSI-based ionic-liquid electrolyte up to 4.3 V (vs. K^+/K) with minimal Al current collector corrosion and high coulombic efficiency[38]. ILs, and highly concentrated FSI-based electrolytes, are expensive, yet offer solutions to Al corrosion, form effective SEIs, and provide good chemical and electrochemical stability[38].

The SEI K^+ conductivity, uniformity and solubility is critical to anode performance. Zhang *et al.* compared SEI formation of alloy anodes Bi, Sb and Sn in KFSI/EC:DEC and KPF_6/EC:DEC electrolytes finding a clear difference after 10 cycles[88]. A thicker (10−30 nm) heterogeneous SEI grew on the electrode in the KPF_6−based electrolyte compared to the more uniform and thinner (5−10 nm)

SEI observed in KFSI, also resulting in a higher reversible capacity. Hui *et al.* evaluated the impact of a pretreated SEI on K^+ intercalation into few-layer graphene (FLG)[89]. They found the pretreated SEI enabled K^+ intercalation for 1000 cycles and exceptional rate performance of up to 360C, demonstrating that a suitable SEI significantly facilitates the kinetics of K^+ intercalation.

The FEC additive has been established to facilitate stable SEI formation in LIBs and NIBs[90], and has been found to improve the coulombic efficiency of KMnFe-PBA electrodes[36]. However, FEC actually reduced the reversible capacity and increased capacity degradation of K|graphite, possibly due to forming a highly resistive passivating layer on the graphite[36]. Therefore, it appears that FEC is incompatible with graphite anodes and is therefore unviable in KIBs.

There has however, been recent progress with electrolytes. Using a mixture of KPF_6 and KFSI salts has been shown to suppress the Al corrosion whilst enabling formation of a stable SEI[91] achieving good cyclability and being a potential low cost solution electrolyte. However, impractically low initial coulombic efficiencies are still experienced. Recently, KFSI in triethyl phosphate (TEP) electrolyte at moderately high concentrations ($\sim$ 2 - 2.5M) has become the leading K-ion electrolyte in the research community, achieving some of the best full cell performance to date and without the impractically high cost of ILs or highly concentrated electrolytes[92–94]. Deng *et al.* achieved negligible capacity decay after 300 cycles, however, still requiring graphite precycling to mitigate the poor initial coulombic efficiency during SEI formation[92]. Therefore, though a major step forward for KIBs, impractical coulombic efficiency electrolytes remain one of the most significant barriers to realising commercially viable KIBs.

Safety is a concern for KIBs given the high reactivity of K metal. However, when using a graphite anode the risk of plating K metal is lower in KIBs than plating Li in LIBs, due to the greater difference between the intercalation potential and plating potential for K compared with Li. This enables higher overpotentials to be experienced without reaching the K plating potential, thus reducing the risks of dendrite formation during high-rate operation and mitigating against the risks of

overcharging. In addition, due to the reactivity of K metal, any plated K is likely to quickly react with the electrolyte, before being able to form a short-circuit[28]. In the case of short-circuit forming, the melting point of K is low (63.4°C), therefore, the K metal would likely melt, cutting the short-circuit before severe thermal runaway occurs, acting as a fuse. The primary safety issue for KIBs is the use of organic electrolytes, which is the same for LIBs. Nevertheless, the safety of KIBs is currently speculative and significant research is required to verify their safety before manufacturing commercial batteries.

1.5 Techno-Economic Analysis

Though unconventional the techno-economic analysis conducted is presented here in the introduction as its results are required to make the conclusions on the state-of-the-art materials detailed in the next section. No techno-economic analysis had been published until this work evaluating if K-ion batteries can compete with Li-ion and Na-ion in terms of performance and cost. Therefore, the first concise techno-economic model was developed (Figure 1.7)[1], which provides initial answers to the following three questions:

1. Which K-ion chemistry is most promising in terms of energy and cost?
2. Beyond Li-ion: Is K-ion or Na-ion more competitive?
3. What use-cases are most addressable by K-ion batteries?

The model extends to the stack level, and is based on Hurlbutt *et al.*'s techno-economic model of PBAs[51], with values for many parameters taken from BatPaC 4.0 modelling software[95]. The performance and cost of the K-ion battery chemistries were modelled based on the top performing PBA, metal oxide, and polyanionic cathodes (Table 1.1)(Figure 1.5), and graphite anode (Table 1.2). Two LIB chemistries were chosen for comparison: NMC811||Graphite (G) as a leading LIB chemistry for EVs; and LFP||G as the leading cobalt-free LIB chemistry, identified for low-range EVs and grid-scale storage[96,97]. NMO||Hard carbon (HC) was also

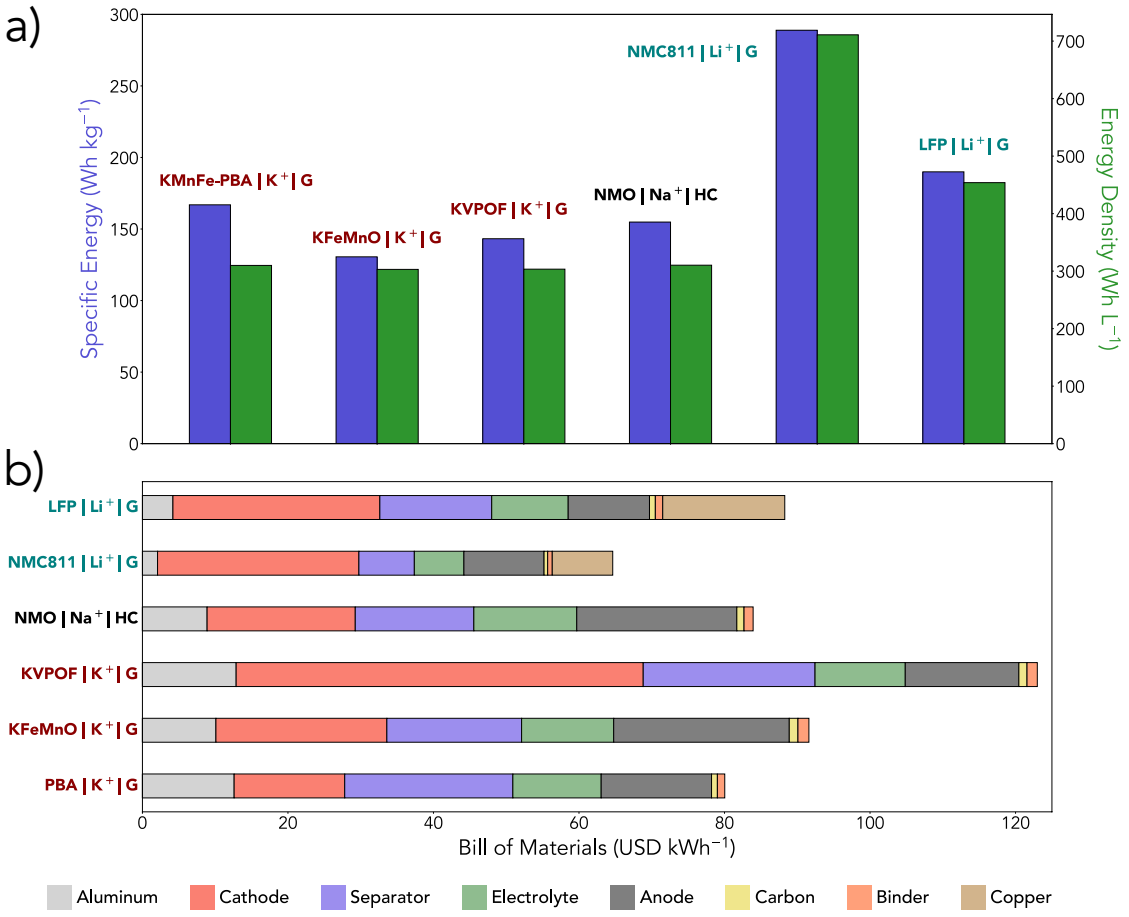


Figure 1.7 A concise techno-economic model of K-ion batteries. Three different KIBs (red) were modelled, as well as two LIBs (teal) and one NIB (black) for comparison at the stack level. The modelled chemistries are: $K_{1.75}Mn[Fe(CN)_6]_{0.93} \cdot 0.16\,H_2O$ (KMnFe-PBA)|K^+|graphite (G); $K_{0.65}Fe_{0.5}Mn_{0.5}O_2$ (KFeMnO)|K^+|G; $K_3V_2(PO_4)_2F_3$ (KVPOF)|K^+|G; sodium manganese oxide (NMO)|Na^+|hard carbon (HC); lithium nickel-manganese-cobalt oxide 811 (NMC811)|Li^+|G; lithium iron phosphate (LFP)|Li^+|G. Each system has a cathode of 80 µm thickness.
(a) The specific energy (blue bars, left axis) and energy density (green bars, right axis) are plotted for the six chemistries.
(b) The bill of materials in USD kWh^{-1} is plotted. The bar segments are colour coded according to the legend at the bottom. Reproduced from Dhir *et al.*[1]

chosen as a leading NIB chemistry for comparison[98,99]. Metal, raw material and electrode material prices from February 2020 were used in this analysis[95,100]. This techno-economic analysis was published in 2020[1]. Full details of the techno-economic model are detailed in Section 2.1.

Figure 1.7a compares the energy density and specific energy of the six chemistries. Comparing K-ion to Li-ion demonstrates that the three K-ion chemistries achieve

less than half of the energy density of the NMC811 Li-ion chemistry, indicating in high energy density applications K-ion is unlikely to ever compete. In terms of specific energy, the highest KIB, still only achieves 58% of the specific energy of the NMC811 LIB. This suggests that K-ion is also unlikely to ever rival Li-ion for long-range EVs. However, the PBA KIB exhibits a specific energy which is 88% that of the LFP LIB, demonstrating that the PBA KIB may be well placed to compete in low-range EV applications. Amongst the K-ion chemistries there is little difference in terms of energy density, however, the PBA KIB has the highest specific energy, whilst the KFeMnO KIB is the lowest. Interestingly, substituting the graphite anode for phosphorus in the PBA KIB leads to an increase of only 6% and 5% to the specific energy and energy density, respectively (Figure 1.8), despite using the theoretical specific capacity of phosphorus ($865\,\mathrm{mA\,h\,g^{-1}}$) which is 310% higher than graphite. The increase in specific capacity is almost entirely offset by its corresponding increase in anode voltage (0.8 V vs. K^+/K for phosphorus). KIB full-cell performance is primarily limited by the cathode, therefore, the superior capacities of alloying anodes will have only limited impact on increasing the energy of KIBs, unless cathode performance is significantly improved. Nevertheless, the most significant result is that all three K-ion chemistries are already comparable to Na-ion, whilst the PBA KIB actually presents a higher specific energy than the NIB (167 versus 155 Wh kg^{-1}), which is impressive given the comparatively little research attention K-ion has received.

Cost is where the significant difference between K-ion chemistries is most evident. Figure 1.7b depicts the bill of materials for the different chemistries, calculated from estimates of stack components and normalised by energy content. The PBA KIB is less expensive than the metal oxide and significantly less expensive than the polyanionic (80 versus 92 versus 123 USD kWh^{-1}, respectively). This is because the PBAs can be synthesized at room temperature from earth-abundant elements[101,102]. Whereas the high-temperature solid-state processing used for scalable production of metal oxides is energy intensive[103], and thus high cost, whilst, the polyanionic KVPOF ($K_3V_2(PO_4)_2F_3$) relies on both high-temperature processing for scalable

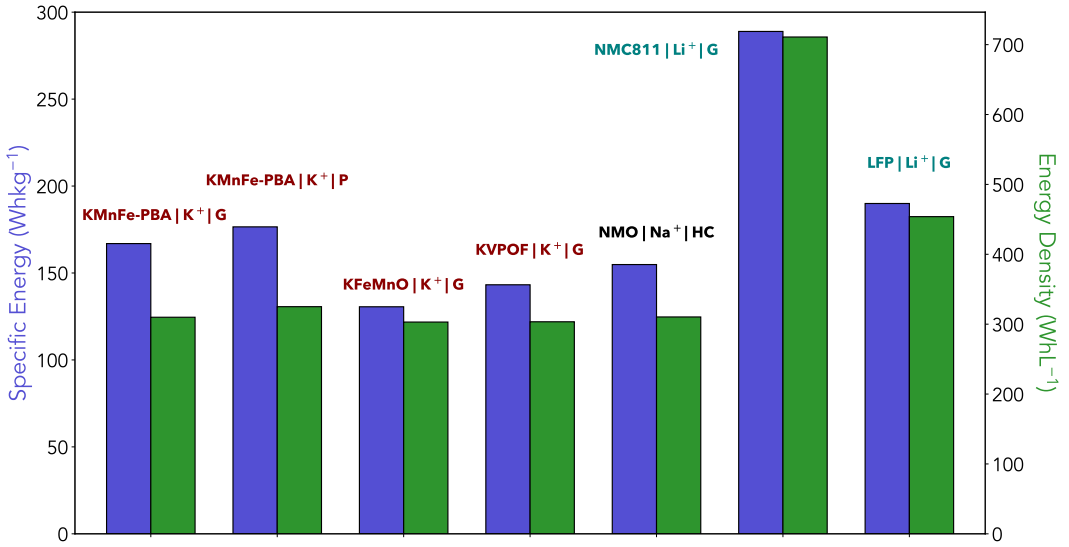


Figure 1.8 The specific energy (blue bars, left axis) and energy density (green bars, right axis) are plotted for four KIBs (red) including a KIB with a phosphorous anode, using its theoretical capacity, as well as two LIBs (teal) and one NIB (black) for comparison. The modelled chemistries are: $K_{1.75}Mn[Fe(CN)_6]_{0.93} \cdot 0.16\,H_2O$ (KMnFe-PBA)|K^+|graphite (G); KMnFe-PBA|K^+|phosphorous (P); $K_{0.65}Fe_{0.5}Mn_{0.5}O_2$ (KFeMnO)|K^+|G; $K_3V_2(PO_4)_2F_3$ (KVPOF)|K^+|G; sodium manganese oxide (NMO)|Na^+|hard carbon (HC); lithium nickel-manganese-cobalt oxide 811 (NMC811)|Li^+|G; lithium iron phosphate (LFP)|Li^+|G. Each system has a cathode of 80 µm thickness. Reproduced from Dhir *et al.*[1]

production, and expensive elements such as vanadium. In addition, KVPOF currently has no direct synthesis method – currently created from K-ion exchange with NVPOF – therefore, the calculated cost for KVPOF in this model is considered a minimum cost assuming a direct synthesis method is developed[42]. Other leading, similar, polyanionics, such as $KVOPO_4$ and $KVPO_4F$, which do have a direct synthesis method, result in a slightly lower cost ∼115 USD kWh^{-1} as they require less vanadium. However, they remain considerably more expensive than the other KIBs, and would offer inferior energy density and specific energy performance[43]. This demonstrates vanadium-based polyanionics are the least economically viable KIB chemistries. However, the most significant result is that the PBA KIB is cost competitive with the NIB (80 versus 84 USD kWh^{-1}) and achieves a higher specific energy.

It is also notable that the PBA KIB is comparable to LFP in terms of both cost (80 versus 88 USD kWh^{-1} for LFP) and specific energy. This indicates that

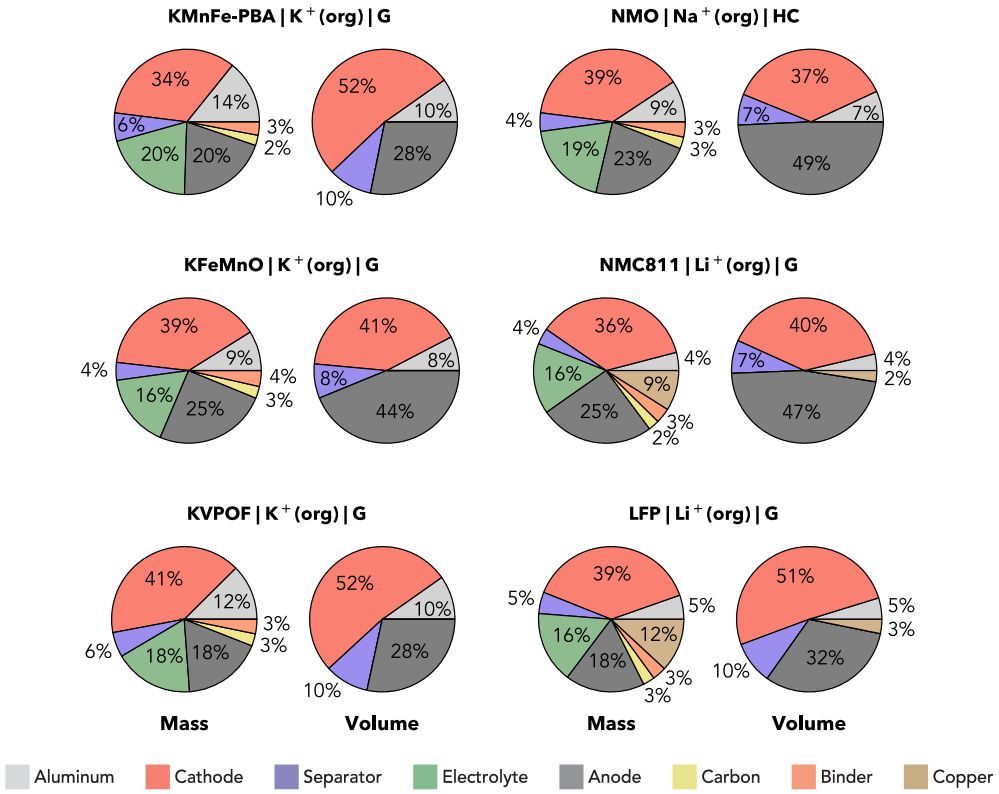


Figure 1.9 The mass fraction (left) and volume fraction (right) for the components of the six full cell chemistries. The slices in the charts are colour coded according to the legend. The two lithium-ion stacks also contain copper current collectors because lithium alloys with aluminium at low potentials. Reproduced from Dhir *et al.*[1]

low-range EVs and grid-scale storage are likely to be the most addressable use-cases for KIBs. The "per cycle" cost performance is more important when assessing grid-scale storage options[104]. However, there is currently no cycling data of full cell KIBs with realistic form factors. The potential higher rate capability of KIBs compared to LIBs would also support its application in grid-scale storage. The low cost and competitive specific energy of the PBA KIB suggest it could be a strong contender in the cobalt-free, low-range EV market.

Figure 1.9 shows the mass and volume fractions of the six full cell chemistries. Comparing the components of the PBA KIB and NIB, shows the PBA cathode is lower in mass proportion than the NMO (32% versus 39%) but is considerably greater in volume proportion (51 versus 37%) due to the lower bulk density of PBAs compared to metal oxides. The KVPOF cathode is similar to the PBA, whilst

the KFeMnO has similar fractions to the NIB due to metal oxides having higher densities.

It is important to note three aspects regarding the cost analysis. First, as mentioned, since this analysis battery metals particularly lithium have experienced exceptional price volatility, with the lithium price being over 700% higher in May 2022 than at the start of 2021 before dropping significantly since. Therefore, the cost picture will have changed considerably depending when taken during this time for the Li-ion chemistries. Second, this analysis used Li-ion cathode material costs per kg from BatPaC 4.0, and it was unexpected that the LFP chemistry results are more expensive than the NMC811 chemistry. In BatPaC 5.1, the cost difference per kg of these cathode materials has changed considerably, with NMC811 now three times more expensive than LFP[105] which would change the results likely making LFP cheaper per kWh which is more accurate. Finally, the results presented are only relevant if realistic cycling performance (>1000 cycles) can be demonstrated for the full cell PBA KIB which, as yet, has not been achieved. It is, also, recommended that more sophisticated techno-economic models are developed to extend the analysis further, for instance, to the pack level, incorporating rate capability, or to calculate the economics of lithium and cobalt recycling for additional comparison.

State-of-the-art Potassium-ion Cathode and Anode Materials Conclusion

In summary, the open-framework nature of PBAs and polyanion compounds provide improved K^+ diffusion and structural stability, resulting in improved cyclability and rate capability, though at the expense of lower bulk densities. On balance, the most promising KIB cathode to date is the KMnFe-PBA achieving both the highest specific energy and lowest cost of the K-ion chemistries evaluated in the techno-economic analysis, due to its high specific capacity, high operating voltage, and good cyclability, whilst being synthesizable by a low-cost and scalable process from abundant elements. Polyanionic materials offer some promise due to their diversity of structures, however, current leading vanadium-based polyanionic

compounds are impractically expensive due to their vanadium component, whilst also presenting inferior capacities to leading PBAs. Layered metal oxides, display poor performance in KIBs and they are unlikely to achieve the same success as with NIBs and LIBs, with low operating voltages, poor cyclability and moderate specific capacities achieved so far. The large size of K^+ leads to greater K^+ - K^+ interaction which results in limited K content in as-synthesised materials; numerous phase transitions during cycling, limiting cyclability; reduced average operating voltage; and structural instability at low K content.

Graphite presents the best overall electrochemical performance of any KIB anode and is unlikely to be surpassed. The K graphite capacity is high and close to theoretical capacity, cyclability and rate performance are excellent, and it provides a low operating voltage. Interestingly, early results indicate the kinetics of K graphite are superior to Li graphite, suggesting KIBs may be more suitable than LIBs for high power applications. Moreover, there is the critical advantage that graphite is already commercialised for LIB anodes, enabling KIBs to utilise the same global supply chains. Alloying materials present little opportunity for KIB full cell energy density and specific energy improvement unless cathode capacities and voltages are dramatically increased, which is highly unlikely.

1.6 Critical Research Fronts for Potassium-ion Batteries

The critical challenge for KIBs is that, at this point, impractical full-cell coulombic efficiencies are achieved. There is no electrolyte which simultaneously forms a stable SEI at the graphite anode, whilst avoiding aluminium corrosion and electrolyte decomposition at the high potentials of the leading KIB cathodes. Therefore, to realise commercially viable KIBs, the following five critical research fronts must be addressed (Figure 1.10).

Poor interfacial stability, characterised by low coulombic efficiency, is one of the most critical issues for the development of KIBs. Firstly, the large volume expansion of graphite exerts extra stress on the binder and

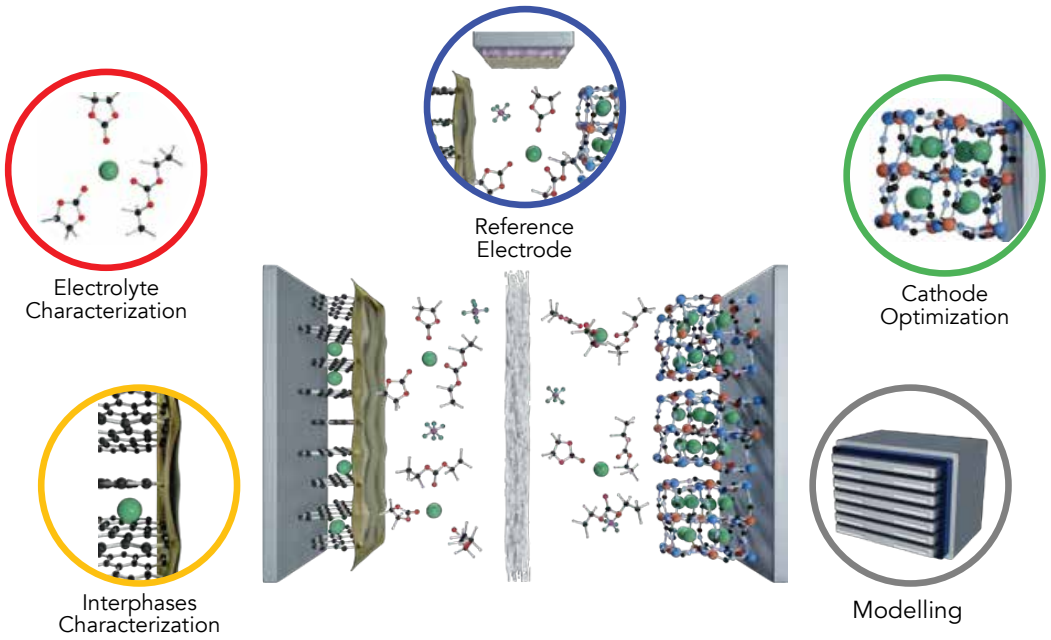


Figure 1.10 Critical Research Fronts for K-ion Batteries. Adapted from Dhir *et al.*[1]

protective SEI. Although some electrolytes form effective SEIs which enable efficient graphite cycling, there is no clear explanation as to why. Scientific insight into the composition and morphology which form effective graphite SEIs, and specific differences due to K, are required to design improved electrolytes. Secondly, current electrolytes are electrochemically unstable and some lead to aluminium corrosion at high potentials (>4 V vs. K^+/K), at which the best cathodes operate. Negligibly low Al solubility and intrinsically stable electrolytes, or electrolytes capable of forming passivating layers, are required to achieve acceptable coulombic efficiencies. Again, determining why K-ion electrolytes exhibit this poor behaviour, compared to high-voltage Li-ion electrolytes for example, must be explained. Crucially, at this point there is no practical electrolyte which simultaneously provides good graphite performance whilst achieving high coulombic efficiency[106] with a high-voltage KIB cathode, a critical problem for KIB development.

The lack of electrolyte options and comprehensive characterisation is limiting KIB progress. There have been relatively few electrolyte salt, solvent, and additive formulations characterised and critical properties, such as the transference number, cannot be easily measured. Most literature has focused on

a limited range of electrolytes comprised of KPF_6 and KFSI in organic solvents, however, these have not resulted in adequate electrode performance. A wider variety of electrolyte formulations should be investigated. There is speculation, and limited evidence, that K-ion electrolytes could have higher diffusivities and transference numbers than comparative Na and Li electrolytes. Measuring the transference number and diffusivities accurately for Li is already challenging, however, the reactivity of K metal poses significant additional challenges in metal symmetric cells, and K pulsed-field gradient NMR (pfg-NMR) probes are not common. Developing methodologies to understand K^+ solvation and characterise fundamental transport properties in K-ion electrolytes is critical in order to evaluate potential electrolyte performance and develop novel electrolytes. Commercially available separators have been optimized for Li-ion electrolytes and their influence on K-ion transport should also be investigated[107].

Potassium manganese hexacyanoferrate is the most promising high-performance low-cost KIB cathode material to date, but significant problems remain. The material undergoes multiple phase transformations during cycling (monoclinic – cubic - tetragonal) and suffers from material dissolution, both causing capacity fade. Strategies such as metal doping or surface coatings, like those developed for NaMnFe-PBA, should be utilised to minimise these capacity loss mechanisms. In addition, the material exhibits poorer electrode rate performance compared to Na analogues and KMnFe-PBA in aqueous electrolytes. The sluggish rate capability should be investigated to determine whether the cause is interfacial charge transfer reaction kinetics, diffusivity, or electronic conductivity.

K metal as prepared in literature is an inadequate reference electrode and an alternative must be developed. K is highly reactive forming thick and unstable surface layers that are highly dependent on both electrolyte and atmospheric compositions. This can create an unstable potential that leads to inaccurate evaluation of electrode materials[46]. Additionally, when employed as a counter-reference electrode in half-cells it exhibits large polarisation on K stripping/plating, much higher than Li or Na, thus severely affecting both rate and

voltage measurements. There can, also, be crosstalk effects in which decomposition products from the reactive K metal can interact with the working electrode material. Improving the stability of K metal as a reference or development of an alternative reference electrode which exhibits a stable rest potential, is chemically inert, and operates within the electrochemical stability window of the most commonly used electrolytes is important for reliable electrochemical measurements.

More advanced models are required to determine the viability and rate potential of K-ion batteries and their possible applications. Given the absence of current viable full-cells or electrolytes, models are even more critical to determine the potential of KIBs. Models must consider battery rate through bottom-up experimentally measured values, with critical properties including electrolyte salt diffusivity and transference number, electrode solid-state diffusivities, and exchange current densities to input into Doyle-Fuller-Newman (DFN)-type models developed for LIBs. Measuring these properties and conducting modelling is crucial to also understand what are the physical limitations in rate performance, guiding research to optimise these areas. The, speculated, faster K-ion rate in graphite and the electrolyte could result in superior rate-performance batteries or thicker electrodes (reducing cost). In addition, costs for K-ion battery raw materials, scale-up, and commercialisation have many assumptions and, therefore, a high degree of uncertainty. Higher confidence on these costs is important to more reliably determine the viability of KIBs.

From the critical research fronts identified, it is clear that critical properties for both the electrolyte and leading electrode materials for K-ion must be accurately characterised. This will inform electrolyte and electrode material optimisation research, and will enable predictive modelling of KIBs, which can further accelerate K-ion optimisation as well as demonstrate the true potential of KIBs in realistic cell formats, particularly for fast-charging.

1.7 Doyle-Fuller-Newman Model

The most established battery modelling framework is the Doyle-Fuller-Newman (DFN) model[108] (often referred to as the pseudo-two-dimensional (P2D) model), deriving from porous electrode theory. The DFN model is a physics-based model which is able to simulate the behaviour of a single anode-cathode pair at the cell level, providing sufficient complexity to capture much of the critical physics whilst maintaining enough simplicity for fast cell-level simulations[109,110]. This unique advantage is enabled by utilising a microscale one-dimensional domain with spherical symmetry to represent the particle behaviour in combination with the macroscale one-dimensional planar geometry representing the electrodes and separator. The microstructural simplification reduces computational complexity and expense compared to three-dimensional microstructure representations used in more complex models[110]. The DFN model comprises of a system of coupled partial differential equations containing over 20 parameters, which describe both the macroscale and microscale behaviour in the cell[109]. Impressive agreement between experimental measurement and DFN modelling has been demonstrated on the back of comprehensive and accurate characterisation of the critical DFN parameters coupled with some tuning[111–114].

Figure 3.16 shows a schematic of the DFN model for Li-ion. The typical DFN model is modelled with one macroscopic dimension, x being the distance across the cell, and one microscopic dimension, r being the distance within the active material particles. The complexity of the three-dimensional electrode microstructure is captured in averaged parameters and homogeneity is assumed in the y and z direction.

1.7.1 DFN Macroscopic Equations

The macroscopic DFN equations describe the electrolyte and electronic transport processes as well as charge and material conservation.

First, considering the macroscopic relations in the electrolyte. In defining liquid transport first, the molar flux of anions, N_e in a binary electrolyte is defined by

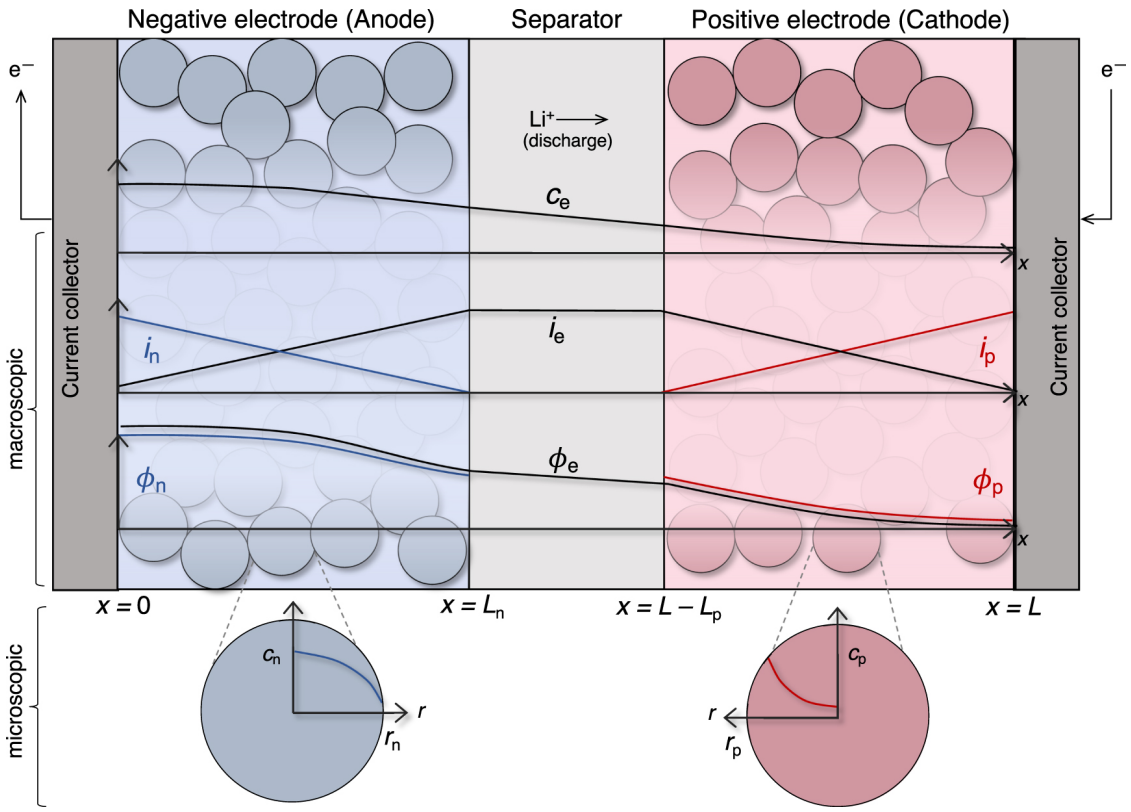


Figure 1.11 Schematic of the DFN model for Li-ion. The variables are defined in the following text. Reproduced from[109]

Equation 1.2. The DFN model is often defined in terms of anion balances since the electrodes are anion blocking which can provide numerical solution advantages[109].

$$N_e = -B_k D_e \frac{\partial c_e}{\partial x} + (1 - t_+^0)\frac{i_e}{F} + c_e v_0 \tag{1.2}$$

Where B_k is a transport efficiency, D_e is the salt diffusivity of the electrolyte in free liquid, c_e is the salt concentration of the electrolyte also equal to the anion and cation concentration due to electroneutrality, t_+^0 is the cation transference number, i_e is the ionic current density in the electrolyte, F is Faraday's constant and v_0 is the solvent velocity. Subscript k denotes the domain, either negative or positive electrode (n or p, respectively) or separator (s).

Equation 1.2 accounts for the flux contributions from diffusion, migration and convection. The diffusion flux is driven by concentration gradients, the migration flux by ionic current density and convection flux by the solvent velocity. In the DFN model convection is typically neglected. D_e defines rate of salt diffusion. t_+^0

defines the fraction of conductivity contributed by cation mobility, with the anion transference number $(1 - t_+^0)$ defining the same for the anion. B_k is a factor to account for the impact of the pore geometries and tortuosity which reduces D_e from its maximum value in free liquid to an effective diffusivity. B_k is defined in Equation 1.3 where τ_k is the pore tortuosity factor, which is often defined using the Bruggeman correlation ($\tau_k = \varepsilon_k^{1-b}$ where for effective transport in packed spherical beds the Bruggeman coefficient (b) is 1.5 and ε_k is the electrolyte volume fraction in the domain, equal to the porosity):

$$B_k = \frac{\varepsilon_k}{\tau_k} \tag{1.3}$$

This is coupled with Equation 1.4 a material balance ensuring continuity of electrolyte concentration:

$$\frac{\partial(\varepsilon_k c_e)}{\partial t} + \frac{\partial N_e}{\partial x} = 0 \tag{1.4}$$

There are then two more equations for the electrolyte comprising of a charge conservation and a constitutive relation:

$$\frac{\partial i_e}{\partial x} = b_k j_k \tag{1.5}$$

$$i_e = -B_k \kappa_e \left[\frac{\partial \phi_e}{\partial x} - \frac{2RT(1 - t_+^0)}{F} \left(1 + \frac{\partial \ln(f_\pm)}{\partial \ln(c)} \right) \frac{1}{c_e} \frac{\partial c_e}{\partial x} \right] \tag{1.6}$$

where b_k is the electrochemically active surface area per unit volume of pore network in domain k (Equation 1.7). j_k is the electrode-electrolyte interfacial current density describing the rate of the kinetics of the electrochemical (de)intercalation or (de)insertion reactions on the pore surfaces. κ_e is the electrolyte ionic conductivity, ϕ_e is the electrolyte potential, $\left(1 + \frac{\partial \ln(f_\pm)}{\partial \ln(c)}\right) = \chi_M$ which is the thermodynamic factor accounting for deviations from ideal Nernstian behaviour.

$$b_k = 4\pi r_k^2 \left(\frac{\varepsilon_{act,k}}{\frac{4}{3}\pi r_k^3} \right) \tag{1.7}$$

where r_k is the particle radius and $\varepsilon_{act,k}$ is the active material volume fraction.

Equation 1.5 details the electrolyte charge balance which comes from assuming that current density is all due to ion flux, following Faraday's law. Equation 1.6 is the MacInnes equation which is a modified form of Ohm's law, relating i_e to the gradient of electrolyte potential through κ_e but also including a concentration overpotential correction.

Two equations then define the solid electrode electronic conduction:

$$\frac{\partial(i_k + i_e)}{\partial x} = 0 \tag{1.8}$$

$$i_k = -\kappa_k \frac{\partial \phi_k}{\partial x} \tag{1.9}$$

where i_k is the electronic current density in the solid phase of domain k, κ_k is the effective electronic conductivity of the electrode and ϕ_k is the electrode potential. Equation 1.8 ensures charge conservation while Equation 1.9 defines the electron conduction is ohmic.

The macroscopic boundary and interface conditions are as follows:

$$i_n|_{x=0} = i_p|_{x=L} = i_{circuit}(t) \tag{1.10}$$

$$i_e|_{x=0} = i_e|_{x=L} = i_n|_{x=L_n} = i_p|_{x=L-L_p} = 0 \tag{1.11}$$

$$N_e|_{x=0} = N_e|_{x=L} = 0 \tag{1.12}$$

$$j_k(x) = \begin{cases} j_n & \text{if } 0 \leqslant x \leqslant L_n \\ 0 & \text{if } \mathrm{L}_n < x \leqslant L - L_p \\ j_p & \text{if } \mathrm{L}_p < x \leqslant L \end{cases} \tag{1.13}$$

1.7.2 DFN Microscopic Equations

In the microscopic dimension, there are two elements to consider. First the solid transport of the cation within the active material particles, for Li-ion either from the surface into the particle during lithiation or from within the particle to the surface during delithiation. Second, the rate of electrode-electrolyte interfacial reactions. This involves charge-transfer during (de)insertion or (de)intercalation, and in the DFN this rate of reaction and the electrode-electrolyte interfacial current density j_k is determined by the Butler-Volmer Kinetic rate laws:

$$j_k = j_{k0}\left(\exp\frac{\alpha_{ak}F\eta_k}{RT} - \exp\frac{\alpha_{ck}F\eta_k}{RT}\right) \tag{1.14}$$

$$j_{k0} = k_{k0}\left(1 - \frac{c_{\mathrm{ks}}}{c_{\mathrm{k,max}}}\right)^{\alpha_{\mathrm{ck}}}\left(\frac{c_{\mathrm{ks}}}{c_{\mathrm{k,max}}}\right)^{\alpha_{\mathrm{ak}}}\left(\frac{c_{\mathrm{e}}}{c_{\mathrm{e0}}}\right)^{\alpha_{\mathrm{ck}}} \tag{1.15}$$

$$\eta_k = \phi_k - \phi_e - U_k(c_{ks}) \tag{1.16}$$

Where j_{k0} is the exchange current density, c_{ks} is the cation concentration at the active material particle surface, c_{e0} is the initial cation concentration in the electrolyte, $c_{k,max}$ is the maximum cation concentration in the active material particle, η_k is the surface overpotential which is the difference between the electrolyte-electrode potential drop and the Nernst equilibirum potential U_k which is a function of c_{ks}, α_{ak} and α_{ck} are the anodic and cathodic direction charge transfer coefficients, respectively, k_{k0} is the reference current for the reaction. j_{k0} is a critical property, comparable to the rate constant from chemical kinetics. It describes the rate of electron transfer between the cation and the electrode in the absence of any surface overpotential. In a reaction with a high j_{k0}, both forward and backward reactions are fast. j_{k0} is the current measured at zero overpotential with no net charge transfer occurring[113,115].

Finally, determination of c_{ks} requires a microscopic transport model which calculates the distribution of the cation within the active material particles at every point in the macroscopic x dimension across the cell. So for Li-ion, the changing

concentration distribution of Li within the particles. This microscopic transport within particles occurs along the radial dimension r, where r is the radial position within a spherical active particle with radius r_k. The most common DFN assumption and model is the solid solution model within the particles where intercalated Li is in solid solution, and thus a nonlinear spherical diffusion equation is utilised. Studies have demonstrated this model is a good fit for experimental findings[113,114]. The solid solution microscopic transport equation is:

$$\frac{\partial c_k}{\partial t} = \frac{1}{r^2}\frac{\partial}{\partial r}(r^2 D_k)\frac{\partial c_k}{\partial r} \tag{1.17}$$

Where c_k is the cation concentration in the electrode particles, D_k is the cation solid-state diffusivity in electrode k. This is the material balance for the cation within the particles.

The DFN assumption that the electrode active material particles are spherical is a significant simplification, graphite for instance is highly nonspherical. However, it has not been clearly demonstrated that accounting for more complicated geometries improves outcomes whereas it becomes significantly more computationally intensive[109,116]. Alternative models of solid-state transport have been proposed to the spherical Fickian model most commonly used. These include shrinking core, and Cahn-Hilliard for where phase-transformation reactions may determine cation distribution rather than diffusion[117]. However, Cahn-Hilliard requires modelling or knowledge of of the change in free energy within the two-phase region which is is highly challenging to ascertain[118].

The microscopic initial and boundary conditions are as follows:

$$\frac{\partial c_k}{\partial r} = 0 \qquad \text{at} \quad r = 0 \tag{1.18}$$

$$-D_k\frac{\partial c_k}{\partial r} = \frac{j_k}{F} \qquad \text{at} \quad r = r_k \tag{1.19}$$

$$c_n|_{t=0} = c_{n0} \tag{1.20}$$

$$c_p|_{t=0} = c_{p0} \tag{1.21}$$

$$c_e|_{t=0} = c_{e0} \tag{1.22}$$

Equation 1.18 defines there is a finite cation concentration within the particle core while Equation 1.19 links the particle transport to the Butler-Volmer reaction kinetics, ensuring the cation flux entering the particle matches that leaving the electrolyte during lithiation and vise versa upon delithiation.

Therefore, again it is clear that accurate characterisation of the critical electrolyte and electrode material properties which determine rate performance is crucial to be able to utilise the DFN model for KIBs, and thus understand the fast-charging potential of K-ion in commercial cell formats, and what the rate limitations are.

The most critical material and electrolyte properties determining rate performance include, for the electrolyte, the salt diffusivity and transference number, and for the electrode materials, the solid-state diffusivity and exchange current density. These properties are notoriously difficult to measure accurately for even Li-ion[109,119,120] however, there are methods which are considered more accurate.

1.8 Electrolyte Property Characterisation

There are four critical electrolyte properties which define mass transport in the electrolyte and are required for the DFN model. These fundamental ionic transport and thermodynamic properties are the salt diffusivity (or salt diffusion coefficient) (D_e), the cation transference number (t_+^0), the ionic conductivity (κ_e), and the thermodynamic factor (χ_M)[109].

There are a growing number of studies which have fully characterised these properties for Li-ion electrolytes using a variety of electrochemical techniques[121–127]. Spectroscopic techniques, capable of determining these properties for Li-ion electrolytes through direct visualisation of concentration gradients, have also recently been developed. These include X-ray spectroscopy[128], Raman spectroscopy[129], or

magnetic resonance imaging (MRI)[130,131]. However, when determining transport properties directly from visualised concentration profiles requires fitting the gradient to a model and the results obtained are highly sensitive to the fitting model used, thus making the likelihood of errors high[109].

1.8.1 Transference Number

The cation transference number t_+^0 is the fraction of conductivity contributed by cation movement compared to anion movement, being essentially a power efficiency. t_+^0 can also be considered as the fraction of current carried by the cation in comparison the anion. It has been shown even increasing the transference number by 0.2 can significantly improve accessible capacity during non-aqueous Li-ion battery charge and discharge[132].

t_+^0 is difficult to measure accurately, and is often mischaracterised as the transport number t_+ using steady-state potentiostatic polarisation techniques such as the Bruce-Vincent method[133], relying on assumptions of electrolyte ideality and neglecting ionic species interaction which is known to be inaccurate in the concentrated electrolytes used in batteries[109,130]. There is also the current interrupt method first used by Ma *et al.* for a polymer electrolyte[134] and also implemented by others[123,124,126,135] where after a pulse the OCV is measured and related to t_+^0, D_e and $\frac{dV}{dlnc_e}$. Yet, this method is highly susceptible to error propagation, requiring independent measurement of D_e and $\frac{dV}{dlnc_e}$. The most direct and accurate method of characterising the transference number for concentrated electrolytes is the Hittorf method, which directly measures the change in moles of cations compared to anions with the passage of a set quantity of charge[109,136]. Hou and Monroe developed a densitometric Hittorf method which measures the change in densities of the electrolyte after polarisation to determine the concentration changes and hence t_+^0; they applied it to $LiPF_6$ in PC electrolyte[121]. The densitometric Hittorf method has also been subsequently used to measure t_+^0 for other liquid nonaqueous Li-ion electrolytes[130,137,138]. Full details of the densitometric Hittorf method methodology and theory are detailed in Section 2.2.3.

1.8.2 Ionic Conductivity

The ionic conductivity κ_e is a measure of the total mobility of ions in an electric field, without concentration gradients. It determines the ionic current in response to the electrochemical potential gradient. κ_e is a strong function of temperature and concentration. It increases with salt concentration and hence increasing mobile ions in the electrolyte however, it reaches a maximum before decreasing due to species-species interactions such as agglomerates and ion-pairing. Most commercial electrolytes use concentrations where their κ_e is maximum $\sim$ 1M. Measuring κ_e is simple and accurate using EIS in commercial conductivity probes. By using blocking electrodes and a known cell geometry, κ_e can be determined from the bulk resistance R_b from EIS. Full details of the ionic conductivity measurement methodology and theory are detailed in Section 2.2.6.

1.8.3 Thermodynamic Factor

The thermodynamic factor, χ_M $\left(1 + \frac{\partial \ln(f_\pm)}{\partial \ln(c)}\right)$, measures the non-ideality of an electrolyte and accounts for deviations from Nernstian behaviour, reflecting how the salt thermodynamic activity varies with concentration, which is determined by ion-ion and ion-solvent interactions. χ_M relates concentration changes in an electrolyte to the OCV drop across it, and it comes from the derivative of the chemical potential μ_e with respect to concentration. χ_M approaches a value of one at infinite dilution, as the electrolyte approaches ideality. Accurate characterisation of χ_M ensures more accurate determination of concentration overpotentials in DFN models and provides information on electrolyte ion-solvent and ion-ion interactions[109].

To measure χ_M accurately the leading method is the use of concentration cells. A concentration cell utilises symmetric metal electrodes and places two electrolytes with the same constituents but different compositions in chemical contact. χ_M can thus be determined by measuring the OCV that arises between them as a result of the difference in chemical potential from the different salt concentrations[109,137]. Full details of the concentration cells methodology and theory are detailed in Section 2.2.5.

1.8.4 Salt Diffusivity

The electrolyte salt diffusivity or salt diffusion coefficient, D_e, determines the contribution to ionic flux from electrolyte salt concentration gradients. Often pfg-NMR is used to characterise self-diffusivities however, it is important to note salt diffusivity is different and self-diffusion coefficients and experiments such as pfg-NMR do not directly relate to ionic transport in polarized electrolytes[139]. The restricted diffusion experiment, first developed by Harned and French, is the current most accurate and reproducible method of characterising D_e[121,134,140–142]. A concentration gradient is induced across a symmetric cell by galvanostatic or potentiostatic polarization, and the relaxation of the concentration gradient is measured between two points by tracking the OCV. D_e is determined from this exponential relaxation of OCV. This method is often used including a separator[121,142,143] which introduces errors from tortuosity estimation[121], therefore, it is most accurate without separators, in which case it must be vertically aligned with stripping occurring at the bottom of the cell to avoid natural convection effects[109]. Steady-state polarisation and long-term relaxation restricted diffusion has been identified to be more accurate than pulse polarisation methods due to reduced susceptibility to double layer relaxation effects[142]. Pulse polarisation methods, which are advantageous in terms of speed, often may decrease the robustness of the fit with short fitting times and increased noise in the OCV relaxation region, thus increasing the likelihood of errors compared with steady-state polarisation and long-term relaxation[143,144]. Bergstrom *et al.* also demonstrated the importance of choosing the fitting region correctly to reduce error in determination of D_e, an aspect which is often ignored in restricted diffusion experiments[122]. Full details of the restricted diffusion methodology and theory are described in Section 2.2.4.

1.9 Electrode Material Property Characterisation

Two of the most critical properties of the electrode materials for rate performance are the solid-state diffusivity, D_k, and the exchange current density, j_{k0}. Both are

difficult to measure accurately, particularly D_k where highly inconsistent results spanning several orders of magnitude have been reported in literature for the same material[109,119].

1.9.1 Solid-state Diffusivity

The solid state diffusivity, D_k, in the active material particles determines the cation transport from or to the surface of the active material where the electrochemical reaction takes place. If D_k is low at high rates there are steep cation concentration gradients formed within the active particle. The active particle surface can then become saturated with or depleted of the active cation, for instance Li^+, which prevents any further interfacial reaction taking place, leading to significant solid concentration overpotentials and to cutoff voltages being reached early with resultant inaccessible capacity[109,120].

D_k is measured using a variety of techniques including galvanostatic intermittent titration technique (GITT), the potentiostatic intermittent titration technique (PITT), electrochemical impedance spectroscopy (EIS), and cyclic voltammetry (CV). However, D_k characterised by these methods vary by even many orders of magnitude for the same material[119,120]. In GITT, a series of short constant current pulses are applied between OCV relaxation periods and D_k calculated from the changes in potential with time. In PITT a series of potential steps are applied and the current decay is used to characterise D_k. In EIS the low-frequency response is fitted as a Warburg diffusion element in an equivalent circuit. Finally, CV measures the current response to a potential sweep and if reversible the response can be fitted to determine D_k. However, all these techniques have their limitations in the characterisation of D_k. Most battery electrode materials display irreversible or quasi-reversible behaviour, therefore CV can only present qualitative information[109]. EIS has limitations in characterising D_k, one of the major being that battery electrochemical systems are changing and nonlinear yet conventional EIS assumes linearity. This assumption is reasonable in many cases using small perturbations and at high frequencies, however, characterising D_k requires long EIS times and low

frequencies where the system is more susceptible to change, reducing the accuracy of the D_k measurement. Also conventional EIS analysis involves a significant simplification of the system as there are many overlapping processes with similar time constants which are very difficult to distinguish. This oversimplification inevitably results in characterisation errors[145,146].

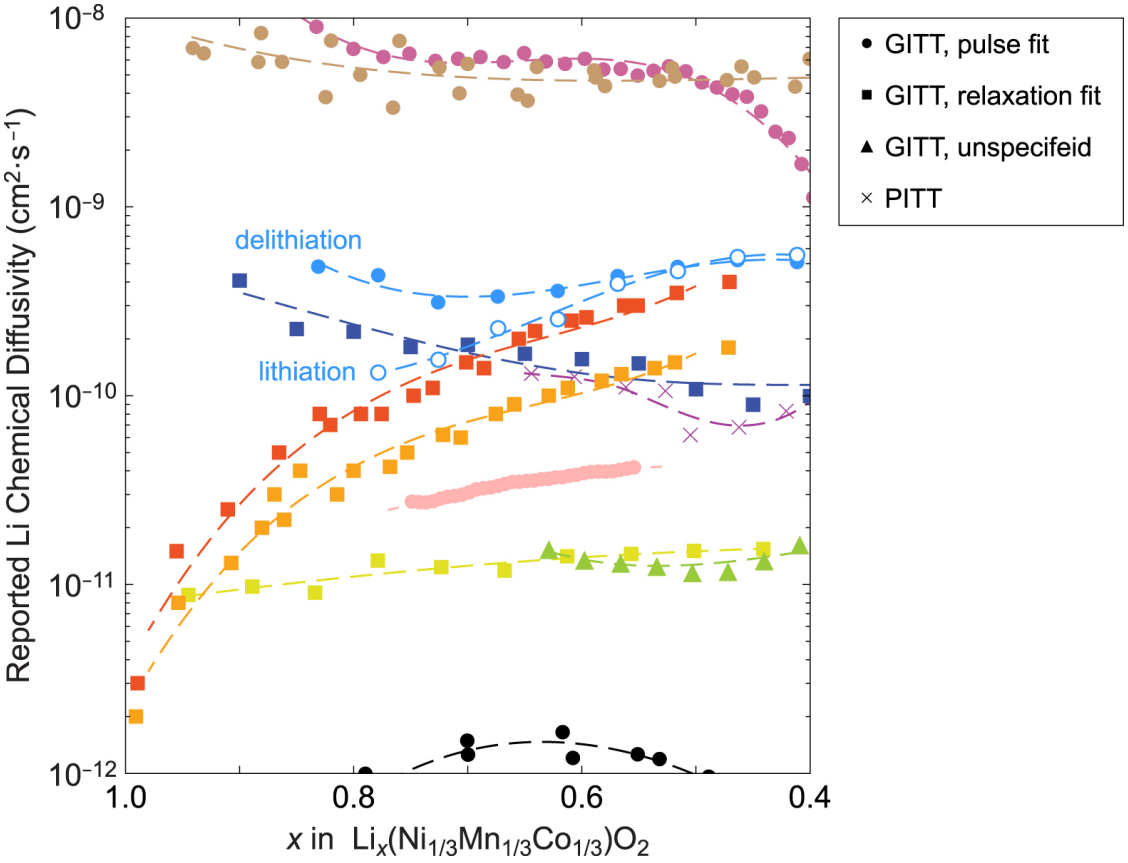


Figure 1.12 Inconsistent GITT and PITT diffusivity values reported in literature all for $Li_xNi_{1/3}Mn_{1/3}Co_{1/3}O_2$. Data from[147–152]. Reproduced from[119]

GITT and PITT are the most popular methods for characterising D_k, however, again, within just these methods D_k characterised for the same material vary by orders of magnitude Figure 1.12[119,147–152]. This is a result of a variety of sources of error including unsuitable experimental conditions, inaccurate analysis and high uncertainties of critical parameters. Both techniques were originally developed for dense, single-phase, planar bulk materials[153,154]. However, leading battery electrode materials today are multi-particle, often multiphase, porous materials, which poses significant additional challenges. One of the most critical sources of uncertainty for

both GITT and PITT applied to porous electrode materials is determination of the electrochemically active surface area or the diffusion length[119,120,155]. With a squared relation, the resulting D_k is highly sensitive to this parameter (Equations 2.19 and 2.22).

One issue with the leading methods of characterising D_k, including GITT, PITT, EIS and CV is that they all rely on Fick's law of diffusion and thus assume solid solution particles in single phase. Many of the leading battery electrode materials are multiphase and have clear two-phase regions, for instance LFP. The interphase boundary is not accounted for using these techniques and determination of an accurate chemical diffusivity of the phases in the two-phase regions is difficult, and instead an effective diffusivity ($\widetilde{D_k}$) is ascertained with contributions from the chemical diffusivities of the two stable phases as well as the movement of the interphase boundary[156,157]. There have been studies which try to take this into account in order to determine the chemical diffusivities in these two-phase regions with varying results[157–160] and alternative theories to solid solution Fickian behaviour based on phase field modelling and the Cahn-Hilliard equation which take phase change into account[117,161]. However, phase-field modelling methods often rely on assumptions regarding the change in free energy during the phase change[156]. A recent work by Bazant et al. was the first to ascertain this using machine learning of images, but again this is highly challenging[118]. Nevertheless, an investigation by Ceder *et al.* found conventional GITT and PITT are still highly accurate in determining D_k for phase transformation materials compared with that derived from phase field modelling, despite GITT and PITT being based on the Fickian model[156]. PITT has been found to be inferior to GITT for multiphase systems due to the insufficiently low potential step that can be applied in the two-phase potential plateaus and the inability to apply sufficient integration time[156,162]. PITT is also inherently limited compared to GITT due to there being no zero-current relaxation periods to separate current-related overpotentials[119].

Kang and Chueh recently conducted a systematic analysis of the sources of error in GITT application for battery materials, providing recommendations for improved

GITT experimental conditions and analysis, as well as determining an optimised modified fitting method for more accurate determination of D_k (method denoted herein as Kang-Chueh GITT). Details of the Kang-Chueh GITT methodology and analysis are described in Section 2.3.1.

1.9.2 Exchange Current Density

Reaction kinetics at the electrode-electrolyte interface for porous electrode materials are conventionally taken to follow the Butler-Volmer kinetic laws. The kinetic reaction rate is governed by the exchange current density j_{k0} according to the Butler-Volmer equation (Equation 1.14)[109]. By measuring the charge-transfer resistance, R_{ct}, using EIS, j_{k0} can be determined through linearising the Butler-Volmer equation, a reasonable assumption when applying a small excitation signal[163] (Full details in Section 2.3.4). By measuring j_{k0} at various stoichiometries, the plot of j_{k0} over composition can be fitted to a form of the Butler-Volmer equation (Equation 1.15) to determine the constant reference current for the reaction, k_{k0}, which can be utilised in the DFN model[109,111,113,164]. To isolate the R_{ct} and hence j_{k0} at a single electrode requires the use of three-electrode cells[109]. There are modifications to classical Butler-Volmer kinetics for multiphase materials that have been proposed recently from the work of Bazant *et al.* in multiphase porous electrode theory (MPET)[161] or coupled ion-electron theory (CIET)[165]. However, both models predict the exchange current densities for lithium iron phosphate (LFP) and graphite comparably to the values obtained using the classical Butler-Volmer model[118,166,167]. Therefore, similar to D_k, one of the most significant uncertainties in determining j_{k0} is also S, though it is less sensitive than D with an inverse rather than an inverse-square relation (Equation 2.29). Hence, again, improved homogeneous material design would improve the determination of j_{k0}.

The second challenge with characterising j_{k0} using conventional EIS is that the formation of passivation layers and SEI occurs at similar timescales and frequencies to charge-transfer. Therefore, disaggregating these to accurately identify R_{ct} is difficult. There are methods attempting to cause the charge transfer and

surface-layer formation to diverge such as using temperature[113] or preformation of SEI[168]. As with the case of using conventional EIS for characterisation of D_k, the same limitations apply using it for the characterisation of j_{k0} with assumptions of linearity and stationarity for an inherently nonlinear and changing electrochemical system[163]. Recent developments in nonlinear EIS offer significant promise for more accurate deconvolution of electrochemical processes, and characterisation and parameterisation of critical properties[163,169].

1.10 Thesis Objectives

With the case for alternative chemistries which can fulfil some Li-ion applications never being stronger, KIBs present a chemistry with significant promise, particularly due to its low critical minerals intensity, ability to intercalate into graphite anodes, unlike Na-ion, and with its potential for fast charging due to the lower charge density of K^+. However, to optimise the electrolyte and electrode materials, and to truly understand the potential of K-ion batteries, there is a clear gap of accurate characterisation of the critical electrolyte and electrode properties that determine rate performance. Knowledge of these critical properties not only facilitates electrolyte and electrode material development, it also enables simulations of KIBs using models such as the DFN model, which, in the current absence of a viable electrolyte, enables the fast-charging potential of K-ion to be investigated.

Therefore, the objectives of this thesis are to accurately characterise the fundamental electrolyte and electrode material rate-determining properties for K-ion. Then to combine these fundamental properties and develop the first DFN model of a full-cell KIB.

The detailed outline of the thesis' objectives are:

1. Characterising the Ionic Transport and Thermodynamic Properties of Potassium-ion Electrolytes (Chapter 3)

    - Develop the capability to apply the most accurate electrolyte characterisation techniques to K-ion electrolytes

- Fully characterise the ionic transport and thermodynamic properties of a K-ion electrolyte using the leading techniques, and characterise the Li-ion equivalent for comparison
- Simulate graphite potassium and lithium half-cell behaviour based on the electrolyte characterisation

2. Characterising the Transport and Kinetic Properties of Potassium-ion Electrode Materials (Chapter 4)

    - Identify accurate state-of-the-art methodologies of characterising the solid-state diffusivities and exchange current densities and develop strategies to improve accuracy and reduce error in K electrode material characterisation
    - Characterise the solid-state diffusivities for the leading K-ion graphite anode material and potassium manganese hexacyanoferrate cathode material and discuss implications for K-ion active material transport
    - Characterise the exchange current densities for the leading K-ion graphite anode material and potassium manganese hexacyanoferrate cathode material and discuss implications for K-ion charge-transfer kinetics

3. Modelling of Potassium-ion Batteries (Chapter 5)

    - Combine all the characterised fundamental electrolyte and electrode properties and develop a DFN K-ion full-cell model in commercial cell format
    - Model, evaluate and compare two DFN K-ion full cells with different electrolytes to understand rate capability and material rate limitations of K-ion in realistic cell formats
    - Develop a DFN model of an LFP Li-ion full cell in equivalent format to the K-ion cell with matched energies for possible comparison of K-ion rate capability with Li-ion

2
Methods

Contents

2.1 Techno-Economic Analysis 53
2.2 Electrolyte Characterisation 56
2.2.1 Densitometry 56
2.2.2 Partial Molar Volumes 56
2.2.3 Hittorf Method - Transference Number 57
2.2.4 Restricted Diffusion - Salt Diffusivity 59
2.2.5 Concentration Cells - Thermodynamic Factor 62
2.2.6 Ionic Conductivity 64
2.3 Electrode Material Characterisation 65
2.3.1 Kang-Chueh GITT 65
2.3.2 PITT 67
2.3.3 Electrochemical Impedance Spectroscopy 68
2.3.4 Exchange Current Density 72
2.4 Other Electrochemical Techniques 73
2.4.1 Anode and Cathode Electrode Preparation 73
2.4.2 Coin Cell Assembly 73
2.4.3 Galvanostatic Cell Cycling 74
2.4.4 Three-electrode Cell 74
2.5 Error Analysis 75
2.6 Doyle-Fuller-Newman Modelling 76
2.7 Materials Characterisation Techniques 77
2.7.1 Scanning Electron Microscopy (SEM) 77
2.7.2 Powder X-ray Diffraction (XRD) 78
2.7.3 X-ray Photoelectron Spectroscopy (XPS) 78
2.7.4 Atomic force microscopy (AFM) 79

Components of this chapter were published in the following articles:

1. Dhir, S., Wheeler, S., Capone, I., Pasta, M. Outlook on K-Ion Batteries. *Chem* **6**, 2442–2460 (2020).[1]

2. Dhir, S., Jagger, B., Maguire, A., Pasta, M. Fundamental investigations on the ionic transport and thermodynamic properties of non-aqueous potassium-ion electrolytes. *Nature Communications* **14**, 3833 (2023).[170]

3. Dhir, S., Cattermull, J., Jagger, B., Schart, S., Olbrich, L., Zhao, J., Sada, K., Goodwin, A., Pasta, M. Characterisation and Modelling of Potassium-ion Batteries *Research Square* (*Preprint - Manuscript under review*)[171]

2.1 Techno-Economic Analysis

A techno-economic model was developed to model novel K-ion chemistries and compare to Li-ion and Na-ion. The techno-economic model developed in this analysis was based on Hurlbutt *et al.*'s techno-economic analysis of PBA materials[51]. The data for the Li-ion chemistries and many other parameters were taken from BatPaC 4.0 modelling software[95]. The performance and cost of the K-ion battery chemistries were modelled based on the highest reported specific capacity, average discharge voltage, and bulk density data of the top performing PBA, metal oxide, and polyanionic cathodes, with cycle lives greater than 100 cycles at the time the paper was submitted for publication in 2020[1]. The cost of the K-ion and Na-ion cathode materials were calculated using the same method as in Passerini *et al.*'s cost analysis of Na-ion batteries[99]. The costs were derived from the cost of the lithium cathode with the most similar chemistry and synthesis in BatPaC, with the raw material cost recalculated and the processing costs kept constant; the raw material costs were calculated from the most recent market price information available at the time submitted for publication. Electrolyte costs were calculated based on the costs of the relevant salt, and assuming equivalent organic solvents.

Model

This model calculates the energy density and specific energy of a full cell based on specific capacity and average discharge voltage data for the cathode and anode active material, as well as the bulk density data for the active materials, carbon, binder, electrolyte and current collectors. Both the anode and cathode include carbon and binder, whilst the anode, cathode and separator include a void fraction. Each system has a cathode of 80 µm thickness kept constant, with the cathode loading altered. From this data the mass and volume of the cathode, anode, separator, and current collectors is calculated, as well as the mass of the electrolyte, carbon and binder. From these calculated mass and volumes, coupled with the specific capacity, voltage, and loading, the specific energy and energy density of the full cell is calculated. The specific capacity, average discharge voltage, and bulk density data was taken from literature for the KMnFe-PBA[36], KFeMnO[39], KVPOF[42], and NMO[98] cathode active materials. The data for the standard hard carbon anode was taken from Passerini et al's recent cost analysis of Na-ion batteries[99]. The cost of the full cell is calculated based on the mass and volumes of each component multiplied by its respective cost. The cost of materials for the copper, aluminium, carbon, binder, separator, graphite anode, and LIB cathodes were taken from BatPaC[95]. The KIB and NIB cathode costs were calculated as explained in the next section. The total cost of components for the full cell is then normalised by energy to determine a cost per kWh for each full cell chemistry.

KIB and NIB cathode costs

Currently there is no detailed information on the price of battery-grade potassium raw materials – potassium carbonate (K_2CO_3) – for the cathode. An estimate of 1000 USD tonne^{-1} for K_2CO_3 was included in a recent K-ion review[172]. From researching online, industrial scale prices of K_2CO_3 >99% purity, were identified as 800 - 1000 USD tonne^{-1} therefore, a price of 1000 USD tonne^{-1} for battery-grade (99.5%) potassium carbonate is assumed. The price of battery-grade sodium

carbonate is assumed to be 500 USD tonne^{-1} based on the sodium cost analysis by Passerini *et al.*[99]

The cost of the KFeMnO[39], KVPOF[42], and NMO[98] cathodes were derived from the cost of the lithium cathode with the most similar chemistry and synthesis method in BatPaC. The raw material cost was recalculated whilst the processing costs were kept constant. Using KFeMnO as an example, LMO was used as the closest lithium cathode. First, the cost of the lithium and manganese components in LMO were calculated and then replaced by the cost of the relevant amount of potassium, iron and manganese, based on wt%, to calculate the cost of the KFeMnO. This method was used for each cathode, keeping the processing costs constant. LMO was also used as the basis to calculate the NMO cost. LFP was used as the basis to calculate the cost of the KVPOF.

Since there is no PBA material in BatPaC, the cost of the KMnFe-PBA[36] cathode was calculated using a different method. First the costs of the raw material precursors were calculated using the method from Firouzi *et al.*[101] There is no information on the processing costs of PBA's at scale; previous studies have estimated the total price of PBA material at scale to be 5 USD kg^{-1}[51] and 10 USD kg^{-1}[99]. Therefore, our model assumes a cost of 7.5 USD kg^{-1} for the KMnFe-PBA active material including both raw material and processing costs.

Electrolyte costs

The price of the different electrolytes was calculated using the ratios of the cost of the respective K-, Na-, and Li-PF_6 salt from Sigma Aldrich of equivalent purity. The ratios matched the electrolyte costs in Pramudita *et al.*'s K review paper[173]. The KPF_6 salt is considerably cheaper than the others therefore, a higher purity for K than the Li and Na was used to provide a more conservative estimate in the salt ratio calculation. Using these ratios, and the fact that the $LiPF_6$ salt in organic solvent is responsible for approximately 21% of the total cost of the electrolyte solution[99], the salt component of the cost for Li organic electrolyte from BatPaC

was scaled, with the solvent component kept constant to provide a cost estimate for the K and Na electrolyte solution.

2.2 Electrolyte Characterisation

2.2.1 Densitometry

For higher precision in preparing electrolytes, electrolytes are prepared in a molal basis. However, it is important to determine the molar concentration for transport relations and the partial molar volumes which requires a density correlation. Using a high-precision density meter enables the molar electrolyte salt concentration, c_e, to be determined from the molal concentration, c_m which can also be stated as the salt mass fraction, ω, using the following relation.

$$c_e = \frac{\omega \rho}{M_e} \tag{2.1}$$

Where M_e is the molar mass of the salt, and ρ the electrolyte density. The densitometry results can then be used to determine the partial molar volumes of salt and solvent.

2.2.2 Partial Molar Volumes

The partial molar volumes of the salt, $\overline{V}_e$, and solvent, $\overline{V}_0$, describe the change in volume of a solution per mole of solvent or salt added. They are related to how the electrolyte density changes as a function of molar salt concentration c_e. $\overline{V}_e$ and $\overline{V}_0$ are calculated from the densitometry results using the following expressions:

$$\overline{V}_e = \frac{M_e - \frac{d\rho}{dc_e}}{\rho - c_e \frac{d\rho}{dc_e}} \tag{2.2}$$

$$\overline{V}_0 = \frac{M_0}{\rho - c_e \frac{d\rho}{dc_e}} \tag{2.3}$$

where M_0 is the molar mass of solvent, ρ is the electrolyte density, and $\frac{d\rho}{dc_e}$ is the slope of the density correlation.

2.2.3 Hittorf Method - Transference Number

The Hittof experiment design for K and Li was developed by myself and optimised by myself and Ben Jagger. Data was collected by myself, Ben Jagger and Alen Maguire. Hittorf analysis was conducted by myself and Ben Jagger. The Hittorf method is a technique which measures the change in moles of cations, compared to anions, across a cell with the passage of a set amount of charge. The transference number is determined from this ratio between this change in moles and charge passed. The densitometric Hittorf method developed by Hou and Monroe[121] uses the density changes to determine the change in concentration with the passage of charge to determine t_+^0 relative to the solvent velocity[121,130,137,138].

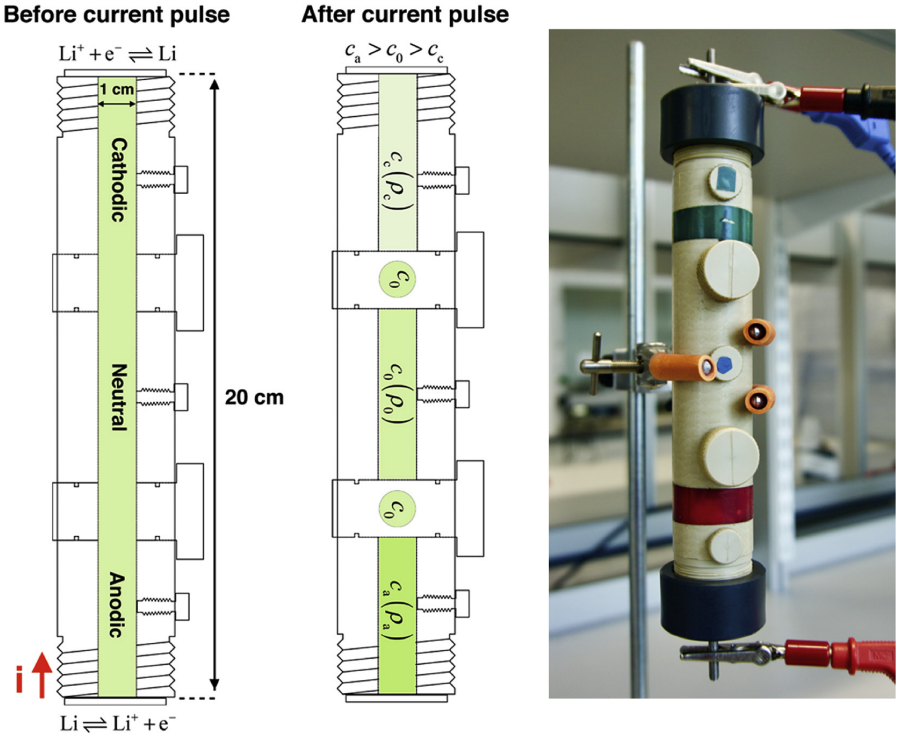


Figure 2.1 Densitometric Hittorf cell designed by Hou and Monroe. Reproduced from[121]

The densitometric Hittorf method utilises a custom densitometric Hittorf cell (Figure 2.1)[121], comprising of a large symmetric cell with a metal electrode on each end with a single long cavity, which can be split into three chambers using two stopcocks. There are also access ports to extract the electrolyte in each chamber.

The experiment involves first applying a polarisation to the cell for a set duration, then closing the two stopcocks to form three isolated chambers, before finally extracting the solutions, letting them equilbriate and measuring their densities using a high precision density meter to determine the concentration changes. The transference number is then determined via Equation 2.4. The cell must be oriented vertically with current applied so stripping occurs at the bottom of the cell. This ensures cation flux directly opposes the direction of gravity, preventing the effects of natural convection affecting the measurement due to density gradients[115]. The anodic chamber is at the bottom where stripping occurs, the neutral chamber in the middle, and the cathodic chamber at the top.

$$t_+^0 = 1 - \frac{FV_{chamber}|c_f - c|}{I_{pulse}t_{pulse}(1 - \overline{V}_e c)} \tag{2.4}$$

Where $V_{chamber}$ is the volume of the cathodic or anodic cell chamber, c_f is the concentration of the chamber after the experiment, c is the concentration of the neutral chamber, I_{pulse} is the current applied, t_{pulse} is the pulse duration, and $\overline{V}_e$ is the partial molar volume of salt, determined from densitometry. The selection of I_{pulse} and t_{pulse} is important, they should be set such that the concentration boundary layers remain within the anodic and cathodic chambers during the experiment whilst ensuring the passage of a sufficient amount of charge to produce a statistically significant density difference between the chambers[174]. Using much longer times would result in the concentration boundary layer extending beyond the anodic and cathodic chamber during the experimental period which would make the measurement void, estimated through the equation below where x_{max} is the maximum distance the concentration gradient can progress into the cell:

$$2\sqrt{D_e t_{pulse}} < x_{max} \tag{2.5}$$

The reason the Hittorf equation begins with '1-' is because when determining the cation t_+^0 from the method, in fact the anion t_+^0 is being directly measured since the electrodes are anion blocking, the concentration being measured is of the build up of anions during the passage of charge. If the cation t_+^0 was 1 then there would

be no build up of anions and no density difference measured as the cations would be responsible for all motion. The very large size of the Hittorf cell (15 cm long) also prevents error from diffusion once the current is stopped when closing the stopcocks which takes around 15 seconds when for this size cell based on the KFSI diffusivity the time constant is in the order of 1000 hours, thus any error from diffusion is negligible.

2.2.4 Restricted Diffusion - Salt Diffusivity

The Restricted Diffusion experiment design for K and Li and the cells were developed by myself, and the experiment was optimised by myself and Ben Jagger. Restricted Diffusion data was collected by myself, Ben Jagger, and Alen Maguire. Restricted diffusion analysis was conducted by myself and Ben Jagger. Steady-state galvanostatic polarisation and long-term relaxation restricted diffusion involves applying a polarisation for a set duration to a symmetric cell to induce formation of an electrolyte concentration gradient. After polarisation the cell is left to relax and the OCV is tracked. As the concentration gradients relate to the OCV via the MacInnes equation (Equation 1.6), D_e can be determined by its relaxation. The OCV relaxation displays exponential behaviour after a certain time reflecting the relaxation of the concentration gradient, and D_e can be determined from the linear time dependence of the logarithm of the OCV via Equation 2.6

$$\frac{d\ln(V)}{dt} = -\frac{\pi^2 D_e}{{L_s}^2} = -\frac{1}{\tau_{diff}} \tag{2.6}$$

Where V is the restricted diffusion cell OCV measured during relaxation, L_s is the bulk electrolyte thickness or interelectrode distance, t is time and τ_{diff} is the characteristic decay time $= \frac{{L_s}^2}{\pi^2 D}$.

The cell utilised for restricted diffusion should be designed so L_s is short enough to allow exponential diffusion relaxation to occur within a reasonable time, whilst also being long enough to ensure a more robust fit. Many recent studies use separators in restricted diffusion experiments[121,142,143] however, this introduces significant errors from tortuosity estimation and variability[121,137]. Without separators the cell must be

oriented vertically with stripping occurring at the bottom (positive current applied to working electrode at the bottom) to again suppress natural convection[115,121]. Newman and Thompson recommend that the linear fit in restricted diffusion experiments is conducted from $0.05\frac{L_s^2}{D_e}$ ($\approx 0.5\ \tau_{diff}$)[175].

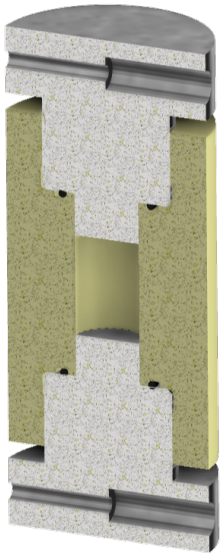


Figure 2.2 The designed restricted diffusion cell with polyether ether ketone (PEEK) chamber, stainless steel current collectors and perfluoroelastomer (FFKM) chemically resistant O-rings. Reproduced from Dhir *et al.*[170]

A custom restricted diffusion cell was designed (Figure 2.2) to ensure an airtight seal and the chamber is free of any geometric issues that can affect the concentration gradient. The cell geometry was designed to be longer than typically used for Li-ion restricted diffusion experiments due to the identified faster diffusion of K-ion electrolytes to enable sufficient time to observe the relaxation and enable a more robust fit. The cell went through a number of design iterations for restricted diffusion experiments before reaching this final design. This cell design ensures the PEEK inner is geometrically homogeneous on the inside and electrolyte is instead added at the top and the cell sealed by screwing in the current collectors until the O-rings form the seal.

Thermodynamic Diffusivity

The thermodynamic diffusivity, $\mathscr{D}$, describes diffusion with respect to the driving force of chemical potential gradients rather than concentration gradients. $\mathscr{D}$ is calculated from D_e, χ_M, total molarity, c_T, and partial molar volume of solvent, $\overline{V}_0$, according to Equation 2.7[109]:

$$\mathscr{D} = \frac{D_e}{c_T \overline{V}_0 \chi_M} \tag{2.7}$$

Stefan-Maxwell Diffusivities

The Stefan-Maxwell diffusion coefficients provide a more detailed understanding of the diffusional behaviour of each individual electrolyte species and their interactions with other species in solution. The Stefan-Maxwell formalism expresses transport laws through the thermodynamic forces which drive diffusion[121,137]. The coefficients are calculated from the characterised transport properties using the following expressions[115]:

$$\mathscr{D}_{0-} = \frac{z_+}{z_+ - z_-} \frac{\mathscr{D}}{t_+^0} \tag{2.8}$$

$$\mathscr{D}_{0+} = \frac{-z_-}{z_+ - z_-} \frac{\mathscr{D}}{1 - t_+^0} \tag{2.9}$$

$$\frac{1}{\mathscr{D}_{+-}} = -\frac{z_+ z_- c_T F^2}{RT\kappa_e} - \frac{z_+ - z_-}{z_+ \nu_+} \frac{c_0 t_+^0 (1 - t_+^0)}{c\mathscr{D}} \tag{2.10}$$

Where $\mathscr{D}_{0-}$ and $\mathscr{D}_{0+}$ are the Stefan-Maxwell diffusion coefficients between the solvent and the anion and cation, respectively. $\mathscr{D}_{+-}$ is the Stefan-Maxwell diffusion coefficient between the cation and anion. c_T is the total particle molarity, $c_T = c_0 + c_- + c_+$, where c_0 is the solvent molarity ($c_0 = \frac{1-\overline{V}_e}{\overline{V}_0}$), and c_- and c_+ are the cation and anion molarity, respectively. z_i and ν_i are the charge number and the number of ions of species i into which the salt molecule dissociates, respectively.

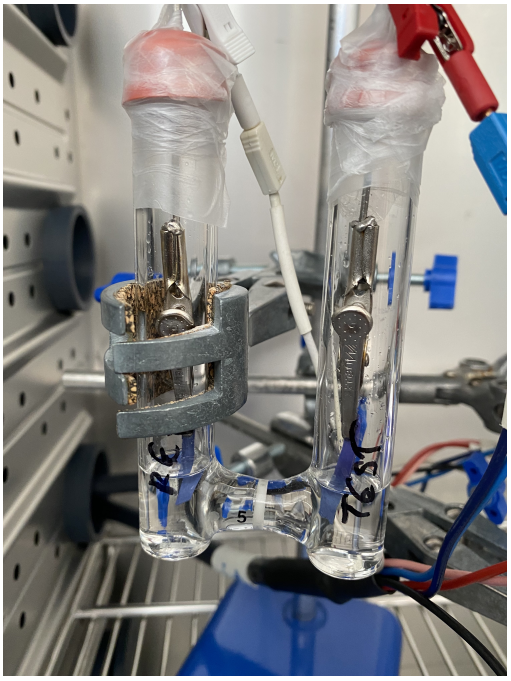


Figure 2.3 A concentration cell being utilised for K-ion electrolyte thermodynamic factor measurements

2.2.5 Concentration Cells - Thermodynamic Factor

The Concentration cell experiment design and cells for K and Li were developed and optimised by myself and Ben Jagger. Concentration cell data was collected by myself, Ben Jagger and Alen Maguire. Thermodynamic Factor analysis was conducted by Ben Jagger. A concentration cell (Figure 2.3) is a metal-metal cell which places two electrolytes with the same constituents but different compositions in chemical contact, and measures the OCV between them to determine χ_M. The cell involves two chambers, one for each electrolyte and metal electrode connected by a porous frit to enable electrochemical contact between the electrolytes but significantly slow interdiffusion. The cell is typically known as a H-cell. One chamber is filled with a 'reference' solution of constant concentration, while the other chamber contains a 'test' solution with a concentration that varies between experiments. The resultant OCV between the two electrolytes is measured after temperature stabilisation (Figure 2.4).

The change in the OCV across the concentration cell, V_c, with molar concentration, c_e, is related to χ_M and t_+^0 by Equation 2.11[109,121]:

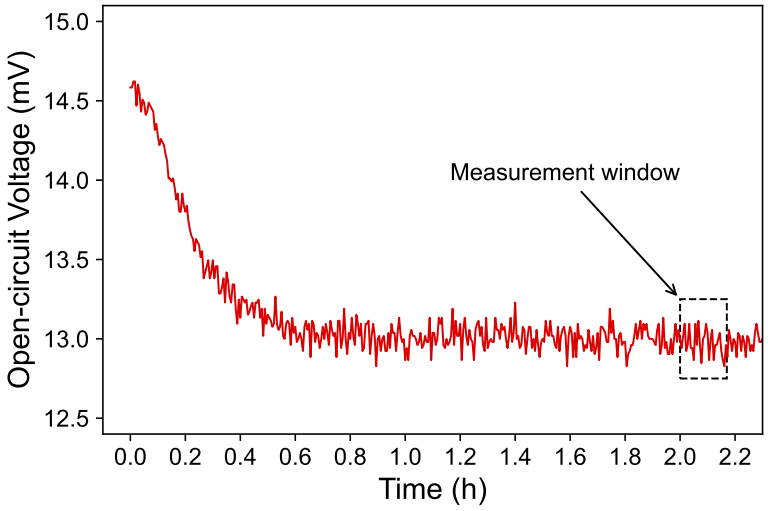


Figure 2.4 Open-circuit voltage (OCV) as a function of time for a representative concentration cell with a 1 m LiFSI in DME 'reference' concentration and a 1.5 m LiFSI in DME 'test' concentration at 20°C demonstrating the stabilisation of the OCV. The measurement window is visualised by the dashed box. Reproduced from Dhir *et al.*[170]

$$\chi_M = 1 + \frac{d\ln(f_\pm)}{d\ln(c_e)} = \frac{F}{2RT(1-t_+^0)}\frac{dV_c}{d\ln(c_e)} \tag{2.11}$$

Where $f_\pm$ is the mean molar activity coefficient, F is the Faraday constant, R is the gas constant and T is the absolute temperature. To determine χ_M therefore, also requires independent measurement of t_+^0. The solvent concentration, c_0, and the partial molar volume of solvent, $\overline{V}_0$, may be used to translate the thermodynamic factor to the molar basis from the molal basis in which it is defined[115,176]:

$$\chi_M = \frac{1}{c_0\overline{V}_0}\left(1 + \frac{d\ln(\gamma_\pm)}{d\ln(c_m)}\right) = \frac{F\frac{d\ln(c_m)}{d\ln(c_e)}}{2RT(1-t_+^0)}\frac{dV_c}{d\ln(c_m)} \tag{2.12}$$

Where $\gamma_\pm$ is the mean molal activity coefficient. From Debye-Hückel theory and taking into account that some electrolytes do not fully dissociate[115,137] leads to $\frac{dV_c}{d\ln(c_m)}$ being given by:

$$\frac{dV_c}{d\ln(c_m)} = \frac{2RT}{F\frac{d\ln(c_m)}{d\ln(c_e)}}(1-t_+^0)\frac{1}{c_0\overline{V}_0}\left(1 + A_1 c_m{}^{\frac{1}{2}} + A_2 c_m\right) \tag{2.13}$$

Where A_1 and A_2 are fitting constants. Equation 2.13 enables the OCV data with changing concentration to be fit. Once A_1 and A_2 are fit to the OCV data, χ_M can be calculated from Equation 2.14:

$$\chi_M = \frac{1}{c_0 \overline{V}_0}(1 + A_1 {c_m}^{\frac{1}{2}} + A_2 c_m) \tag{2.14}$$

There are also other forms of this equation which have also been suggested[137,176,177].

2.2.6 Ionic Conductivity

Ionic conductivity data collected by myself, Ben Jagger and Alen Maguire. Ionic conductivity analysis conducted by myself and Ben Jagger. Measuring the ionic conductivity, κ_e, of an electrolyte is relatively straightforward comparatively using commercial conductivity probes. The probe operates using EIS (described in detail in Section 2.3.3) and a cell comprised of blocking electrodes and the electrolyte of interest. From the high frequency intercept which is the series bulk electrolyte resistance, R_b, κ_e can be determined using the following expression using the known cell geometry:

$$\kappa_e = \frac{L_s}{R_b A} \tag{2.15}$$

where L_s is the inter-electrode distance, A is the geometrical electrode area.

The changes in ionic conductivity with concentration can fitted with the function proposed by Casteel and Amis (Equation 2.16)[178]:

$$\kappa_e(c_e) = \kappa_{max} \left(\frac{c_e}{c_{max}}\right)^{x_1} \exp\left(x_2(c_e - c_{max})^2 - \frac{x_1}{c_{max}}(c_e - c_{max})\right) \tag{2.16}$$

Where κ_{max} is the maximum ionic conductivity, c_{max} is the concentration at maximum ionic conductivity, and x_1 and x_2 are fitting constants.

Equivalent Conductance

Plotting the equivalent conductance, Λ, of an electrolyte can indicate to what degree it is a strong electrolyte - characterising its ability to dissociate salt. A linear dependence of conductance on the square root of concentration indicates a strong electrolyte[179]. Λ of an electrolyte can be calculated from the ionic conductivity, κ_e, and molar concentration, c, using Equation 2.17[137].

$$\Lambda = \frac{\kappa_e}{z_+ \nu_+ c_e} \tag{2.17}$$

Where z_+ is the cation charge number and ν_+ is the number of cations into which the salt molecule dissociates.

Activation Energy

The activation energy analysis was conducted by Ben Jagger. The activation energy, E_a, can be calculated as a function of concentration from the conductivity measurements at three temperatures using Equation 2.18[180]:

$$\kappa = \kappa_0 e^{-\frac{E_a}{kT}} \tag{2.18}$$

Where κ_0 is a constant and k is the Boltzmann constant.

2.3 Electrode Material Characterisation

2.3.1 Kang-Chueh GITT

In a conventional GITT experiment a short pulse of constant current is applied to a cell to electrochemically drive a surface composition change of the working electrode active material. After the pulse the cell is left to rest in open-circuit conditions as to approach equilibrium. The original method uses the potential change during the current pulse to ascertain the square-root time dependency which is expected for diffusion, and uses the relaxation period to determine the thermodynamic equilibrium potentials[109,153]. These current pulses are repeated

until the material is fully charged or discharged. The original equation to calculate D_k at each step is shown below:

$$D_k = \frac{4}{\pi}\left(\frac{IV_{\mathrm{m}}}{zFS}\right)^2\left[\left(\frac{\partial V_{\mathrm{eq}}}{\partial x}\right)/\left(\frac{dV_{pulse}}{d\sqrt{t}}\right)\right]^2 \tag{2.19}$$

where I is applied current, V_{m} is molar volume, F is the Faraday constant, z is the charge number, S is the electrochemically active surface area, $\frac{\partial V_{\mathrm{eq}}}{\partial x}$ is the derivative of the Nernst voltage with stoichiometry, V_{pulse} is voltage during the current pulse, t is time during the pulse.

However, as explained in the introduction, this original method has been poorly applied and utilised to characterise D_k for multi-particle, porous battery materials, resulting in orders of magnitude difference in D_k for the same materials[119,120]. The Kang-Chueh GITT method developed recommendations and an optimised fitting method to mitigate several of the key sources of error and improve accuracy of D_k characterisation in GITT application for battery materials. In the Kang-Chueh GITT analysis D_k is calculated according to Equation (2.20):

$$D_k = \frac{4}{\pi}\left(\frac{IV_{\mathrm{m}}}{zFS}\right)^2\left[\left(\frac{\partial V_{\mathrm{eq}}}{\partial x}\right)/\left(\frac{dV}{d(\sqrt{t_{\mathrm{relax}}+\tau}-\sqrt{t_{\mathrm{relax}}})}\right)\right]^2 \tag{2.20}$$

where V is voltage during relaxation, t_{relax} is relaxation time and τ is pulse duration.

Several of the key aspects of the Kang-Chueh GITT method are detailed here. First, the method employs relaxation-only analysis which circumvents the significant composition-dependent overpotential contribution errors associated with the original method when analysing the potential change during the pulse. Using large samples, large particles or even ideally dense pellets if the material allows, to increase the diffusion length ensures D_k limitation rather than any electrolyte transport limitation. Also using an appropriate pulse duration for the material size and assessing the impact of finite-size effects is important. Finally, the most significant modification is utilising their modified fitting variable $\left(\frac{dV}{d(\sqrt{t_{\mathrm{relax}}+\tau}-\sqrt{t_{\mathrm{relax}}})}\right)$ instead of $\frac{dV_{pulse}}{d\sqrt{t}}$ used in the original method to extract D_k. Contrary to other relaxation-only GITT analyses which have mathematical flaws[119], this fitting variable takes into

account the pulse length τ, which other relaxation analysis neglects. Not taking into account τ is shown to be inaccurate as the square-root time relaxation is not independent of τ since the current pulse determines the initial condition of relaxation. They show superior accuracy and fitting specificity using this modified relaxation fit compared to the conventional relaxation and pulse fits[119,181]. Again one of the most critical sources of error and uncertainty is the measurement of S, which is highly difficult to measure accurately for a porous material. Kang and Chueh recommend ideally a large bulk material sample dense enough to prevent electrolyte penetration, also making geometric area more accurate, however, this cannot be done for many battery materials and is also very difficult to check that the pellet does not allow any electrolyte penetration. Therefore, homogeneous material design of the active material particles can greatly improve the accuracy of S, through more accurate geometric analysis.

Other measures which improve GITT accuracy is the utilisation of three electrode cells to minimise overpotential contributions from the metal counter electrode[109,119,182]. Also electrodes for GITT should be made thin, with high porosity and low loading, to further minimise electrolyte transport limitations to ensure the sample is D_k limited[120,182].

2.3.2 PITT

PITT, first developed by Wen *et al.*, involves application of a series of constant voltage steps, where at each step the current response transient is measured. Each new potential step imposes a new activity and hence new cation concentration at the active material particle surface. This induces a concentration gradient within the particle which causes chemical diffusion of the cation until the cation concentration within the active particle material is homogeneous with the induced surface concentration. This generates a current transient which is a measure of the chemical diffusion flux over time[154]. Again based on Fickian diffusivity, the the current response data can be used to determine D_k. The original expressions were derived for a planar slab. During short time scales ($t << L^2/D_k$) in a semi-infinite

diffusion regime and where there are infinitely fast interfacial kinetics and neglibible ohmic resistance the Cottrell equation can be applied:

$$D_k = \pi t \left(\frac{i(t)}{FS(c_{ks} - c_{k0})} \right)^2 \tag{2.21}$$

However, infinitely fast kinetics are not a realistic assumption for many battery materials[183]. Montella et al developed a rigorous model using PITT to include finite reaction kinetics[184,185], however, the method requires complicated nonlinear fitting or EIS for key resistances, both versions which can provide another source of error, and the method is still designed for single phase materials. Levi et al developed a similar alternative[186–188].

PITT can also be conducted for long time scales ($t >> L^2/D_k$) in the finite diffusion regime where it is less susceptible to early kinetic overpotential contributions and errors. In this case the current relaxation becomes exponential and D_k can be determined by:

$$D_k = -\frac{4L^2}{\pi^2} \frac{dln(I)}{dt} \tag{2.22}$$

Similar to GITT electrodes used for PITT should be thin and as porous as possible to minimise electrolyte transport limitations affecting the current response from similar time constants[189]. Three electrode measurements again improve the accuracy of PITT measurements to minimise overpotential contributions from the metal counter electrode.

2.3.3 Electrochemical Impedance Spectroscopy

Electrochemical Impedance Spectroscopy (EIS) is an experimental technique which is able to determine information about a wide range of electrochemical processes occurring at various timescales for an electrochemical system. The underlying principle of EIS is the perturbation of a system through applying a sinusoidal signal (AC voltage or current) and measuring the sinusoidal response (current or voltage, respectively) to the perturbation signal over a range of frequencies[145,190]. EIS models the output response to the input perturbation signal through a transfer function

over a range of frequencies. Through this, it is able to discriminate between a wide variety of electrochemical, physical and electrical processes taking place due to the different time constants of the different processes. For instance in the context of a battery: the ohmic resistance of a liquid electrolyte, the charge-transfer kinetics of an electrode electrochemical reaction, or the mass transport of ions to the electrode surface all display different time constants.

If applying a potential signal and measuring the current response, there is the magnitude of the applied potential, E_0, and magnitude of the current response, I_0, and a resulting phase shift, ϕ between them. Since the time characteristics of the sinusoidal pertubation signal are described by the frequency f, this relates to the angular frequency (ω) through:

$$\omega = 2\pi f \tag{2.23}$$

The instantaneous value of the sinusoidal voltage perturbation signal and current response at time t are therefore, given by:

$$E(t) = E_0 \sin(\omega t) \tag{2.24}$$

$$I(t) = I_0 \sin(\omega t + \phi) \tag{2.25}$$

The electrochemical impedance, Z, is the form of resistance relating to AC circuits containing both magnitude and phase, and can thus be determined from Ohm's law. Z is a frequency-dependent complex number and represents the total opposition to current flow in an electrical circuit containing resistors (R), capacitors (C) and inductors (L)[190].

From the excitation voltage signal and current response signal for an electrochemical cell the impedance of the circuit at frequency, $Z(\omega)$, can be expressed:

$$Z(\omega) = \frac{\widetilde{E}(\omega)}{\widetilde{I}(\omega)} = |Z|exp(j\phi) = |Z|(\cos(\phi) + j\sin(\phi)) = Z' + jZ'' \tag{2.26}$$

where $\widetilde{E}(\omega)$ and $\widetilde{I}(\omega)$ and the Fourier Transform of $E(t)$ and $I(t)$, Z' is the real part representing the frequency-dependent resistance while Z'' is the imaginary part representing the frequency-dependent reactance with $j^2 = -1$. The vector at a fixed time, t, and angle, ωt, is a phasor (denoted with˜) which is a complex time-invariant number representing both the amplitude and phase of a sinusoidal signal.

The key requirements for conventional EIS are the following: (i) Causality - implying an exclusive cause-effect relationship between the input signal and output response of the system. This means the system response should be entirely dependent on the input perturbation. (ii) Linearity - The system should be linear meaning the input and output signals should have the same frequency (iii) Stability - The system is stable until excited by perturbation and should return to original state after perturbation finished.

However, in electrochemical systems current is a nonlinear function of potential. Therefore, linearity is achieved using a small input perturbation where the current is defined by the first term of its Taylor series expansion[146]. Nonlinear EIS is able to ascertain more information about electrochemical systems through access to other output frequency harmonics, however, it remains challenging to separate overlapping processes[163].

EIS data is typically plotted as a Nyquist plot (Example in Figure 4.9c) where the real component of the impedance is plotted on the x-axis and the negative imaginary part on the y-axis, while each data point is the EIS measurement at a single frequency. EIS data can also be displayed as a Bode plot which conventionally shows the change in the impedance magnitude or phase shift with frequency.

EIS data is usually analysed using equivalent circuits, where processes in the electrochemical system are represented by combinations of R, C and L and others, which have defined impedance behaviours. For instance, R has only a resistive real impedance component of value R and no imaginary part. Whereas C has an impedance of $\frac{1}{j\omega C}$. Other important elements of the equivalent circuits relevant for analysing battery systems include the Warburg element, Z_W, and the constant

phase element (CPE), CPE. Warburg elements represent low-frequency diffusion processes such as the transport of ions through the electrolyte to the electrode surface. Since perfect capacitive behaviour can only be achieved for perfectly flat surfaces, which is not the case for the majority of electrodes, a CPE is defined, which includes an α term which is a tunable parameter between 0 and 1. Surface roughness is the reason often attributed as the origin of the CPE, causing uneven distribution of resistances, capacitances and current densities on the electrode surface. The impedance of a CPE is $\frac{1}{Y_0(j\omega)^\alpha}$ where Y_0 is a coefficient. CPE can also be used as a nonideal Warburg element - an ideal Warburg element would have an α of 0.5 and a nonideal Warburg close to 0.5. Arranging these elements into a circuit using series and parallel formations then represents the electrochemical system and physical processes. An example equivalent circuit is shown in Figure 4.18b where the initial series resistance R_0 represents the ohmic resistance of the electrolyte and the other R and CPE circuits represent the charge transfer resistance and passivation layer growth, which typically occur at similar frequencies.

After determining the most relevant equivalent circuit the EIS data is fitted to the circuit using non-linear least squares regression to fit the data to the model. Reasonable starting values are required to converge to a reasonable solution. Adding too many circuit elements will often lead to overfitting of the data. Once a reasonable fit is achieved using elements representing the relevant physical processes, the values of each element can be extracted and thus associated to the relevant physical processes. EIS data should also be tested against the Kramers-Kronig relations which are derived assuming the system is causal, linear and stable. If the data is Kramers-Kronig compliant this indicates the key requirements for conventional EIS appear reasonably met, particularly causality and stability[146,191]. However, the Kramers-Kronig relations are more sensitive to stability violations than linearity which is why applying a small perturbation is critical[191].

2.3.4 Exchange Current Density

As stated the kinetics of interfacial reactions in porous electrodes are conventionally defined by the Butler-Volmer equations (Chapter 1), which relate the interfacial current density, j_k to the electrode surface overpotential, η_k. Measuring R_{ct} using EIS has been used to characterise j_{k0} through linearisation of the Butler-Volmer equation[111,113]. At small overpotentials around $\eta = 0$ the Butler-Volmer equation 1.14 may be linearised:

$$j_k = j_{k0}\frac{F\eta_k}{RT} \tag{2.27}$$

As η_k can be defined in terms of R_{ct} as:

$$\eta = j_k S R_{ct} \tag{2.28}$$

Combining equations 2.27 and 2.28 produces an equation for j_{k0} with respect to R_{ct}:

$$j_{k0} = \frac{RT}{SFR_{ct}} \tag{2.29}$$

From this the Butler-Volmer reference current for the reaction, k_{k0} can be determined using Equation 1.15

By measuring R_{ct} and thus j_{k0} at various compositions, the plot of j_{k0} over composition is fitted to a form of the Butler-Volmer equation (Equation (1.15). k_{k0} is the fitting parameter which can then be utilised in the DFN model to determine j_{k0} dependent on the electrolyte and electrode concentrations.

Since EIS requires a very small potential perturbation to ensure linearity, the linearisation of the Butler-Volmer equation is a reasonable assumption. To measure the impedance and hence j_{k0} at a single electrode requires three-electrode cells[109].

2.4 Other Electrochemical Techniques

2.4.1 Anode and Cathode Electrode Preparation

Active anode or cathode material must be mixed with other materials in a composite to improve their performance for the application in battery cells. PBA cathodes exhibit low electronic conductivity therefore, a significant quantity of fine powder carbon is added typically around 20 wt. %[1,38]. Graphite is already highly conductive so little if any carbon is added. The fine carbon is between the active material particles providing a conductive network to transport electrons between the active material particles and the current collector. Polymeric binder is also added to ensure the mixture is held together where the long polymer chains provide a film around the particles to hold them in place. The network of carbon and binder is often known and the carbon binder domain (CBD)[109]. The active material, carbon and binder are mixed well and dispersed in a solvent to create a slurry which is cast onto a current collector, before drying. If the electrodes are being made for energy density performance, then the casting is calendared to increase inter-particle contact and increase the electrode density. If power performance is more critical, there is less calendaring to maintain a greater degree of porosity to increase electrolyte penetration and electrochemically active area.

For many electrochemical characterisation techniques such as GITT and PITT, as high porosity as possible is desirable to minimise any electrolyte transport limitations. Therefore, minimal electrode calendaring is conducted to maintain high porosity. Finally the electrodes are punched and weighed for use in cells.

2.4.2 Coin Cell Assembly

To evaluate the electrochemical performance of the electrode materials half-cells are usually employed. These are cells with the active material anode or cathode as one electrode and with a metal reference/counter electrode, for instance Li of K metal acting as an infinite source of the active cation and the negative electrode. This makes it easier to evaluate the performance of a single electrode and removes the

challenges in balancing loading required in full-cells[109]. In lab-scale these half-cells are made in coin cells, comprised conventionally of a stainless steel base and cap which act as current collectors; they are separated and sealed by a plastic gasket. Inside the cell the cathode/anode is separated from the metal counter electrode by the electrolyte-soaked separator, which is typically made of glass fibre. There is also a steel spacer and spring to provide adequate pressure for electrolyte penetration into the porous electrodes and good electrical contact.

2.4.3 Galvanostatic Cell Cycling

The most established method of evaluating cell performance is through galvanostatic cycling. This involves applying a constant current to the cell and measuring the resultant cell potential response. Plotting the potential against the capacity provides the galvanostatic profile of the cell, where the shape of the profile is determined from the reactions of the active material. The current is set based on a desired charge/discharge rate in combination with the mass and hence maximum capacity of the active material. The current is typically set as a C-rate. The current may also be set simply as current per unit mass of active material (mA g^{-1}). The current is applied until the cell potential reaches the set upper or lower potential limit, in which the process is reversed. Galvanostatic cycling can assess multiple aspects of electrode material performance including accessible capacities at different rates or capacity retention over cycling.

2.4.4 Three-electrode Cell

A three-electrode cell separates the working electrode, counter electrode and reference electrode from each other contrasting to the combined reference/counter electrode used in a two-electrode cell such as a coin cell. This separation means that during an electrochemical measurement the current flows between the working and counter electrodes while the voltage is measured between the working and reference electrode. The reference electrode enables more accurate measurement of the potential of the working electrode since no current is flowing through the reference

electrode so its potential is more stable, as potential changes with polarisation. A reference electrode is used to remove contributions from kinetically slow processes at the counter electrode from the phenomena of interest (diffusion or reaction kinetics)[192]

In order to isolate impedance of the electrode of interest a three-electrode cell is required; separating the impedance contributions from each electrode in a two-electrode cell is not possible[109]. Additionally, for GITT and PITT experiments a three-electrode cell significantly improves accuracy by minimising overpotential contributions from the counter electrode[109,182]. A good reference electrode has a robust, stable potential with no current passing through to provide a stable datum to measure the changes in the working electrode potential against[193].

In the experiments in this thesis an EL-Cell ECC-ref was utilised for the three-electrode experiments.

2.5 Error Analysis

Unless specified otherwise the error bars in all figures represent the standard error in the mean, $\sigma_{\overline{x}}$, estimated from the sample standard deviation, σ_x, and the number of data points, n, using Supplementary Eq. 2.30:

$$\sigma_{\overline{x}} = \frac{\sigma_x}{\sqrt{n}} \tag{2.30}$$

Due to the high sensitivity of the calculated transference numbers to changes in solution densities, the limited resolution of the densitometer results in transference numbers with a non-negligible uncertainty. Each calculated transference number can take any value between $t^0_{+,min}$ and $t^0_{+,max}$, with equal probability, giving each measurement, i, an uncertainty variance, σ_i^2, of $\frac{1}{12}(t^0_{+,max} - t^0_{+,min})^2$. The error in the mean t^0_+, $\sigma_{\overline{x}}$, was then estimated by taking into account the sample standard deviation, σ_x, and the uncertainty variance, σ_i^2, for each of the n data points through Equation 2.31:

$$\sigma_{\overline{x}} = \sqrt{\frac{\sigma_x^2}{n} + \frac{1}{n^2}\sum_{i=1}^{n}\sigma_i^2} \tag{2.31}$$

Estimated errors in D and t_+^0 were then propagated through to χ_M, and the thermodynamic and Stefan-Maxwell diffusivities using the standard propagation rules given in Equation 2.32:

$$x = \frac{uv}{w}, \quad \sigma_x = x\sqrt{\left(\frac{\sigma_u}{u}\right)^2 + \left(\frac{\sigma_v}{v}\right)^2 + \left(\frac{\sigma_w}{w}\right)^2} \tag{2.32}$$

2.6 Doyle-Fuller-Newman Modelling

The DFN model was explained in detail in in the Introduction Section 1.7. For the DFN full cell modelling, the open-source python battery simulation package Python Battery Mathematical Modelling (PyBaMM)[194] and CasADi numerical solver[195] was used. The details of the DFN simulations are included in the respective results chapters. A high level overview follows here. Through characterisation of the relevant electrolyte and electrode material properties, these property values or concentration-dependent functions are utilised in a parameter set to be solved using PyBaMM to simulate the half- or full-cell model. For modelling comparisons, the total cell energy was matched by adjusting the electrode thicknesses while maintaining NP ratios, since the electrode capacity is linearly related to its thickness.

For the full-cell modelling the maximum concentrations in each electrode were determined using[109,113]:

$$c_{\mathrm{k}}^{\max} = \frac{\rho z}{M} \tag{2.33}$$

where ρ is the material crystal density and M is the molar mass of the active electrode material.

In the full-cell modelling the electrode capacities are initially matched by controlling electrode thicknesses based on each electrodes theoretical specific capacity or maximum K^+ concentration ($c_{\mathrm{k}}^{\max}$), in combination with the active material bulk density, and active material volume fraction as described in section 2.1 for the

techno-economic model. Then incorporating excess graphite capacity for the NP ratio. Since KMF can be fully depotassiated without irreversible crystal structure changes unlike many Li-ion cathode materials[109], it was assumed almost the full stoichiometry is used for the KMF in the models, leaving a very small fraction ($\sim$ 0.5%) to ensure the model runs. Therefore, the total cyclable K^+ was taken as this 99.5% of the KMF c_k^{max}. Since the initial conditions for PyBaMM are in the charged state, the graphite initial concentration is this total cyclable K^+ which defines its initial stoichiometry. As a check to ensure the cell is properly balanced the cell was cycled on PyBaMM twice since it has a feature to correct any imbalances. For charging simulations, the cell was first discharged at C/50 rate and this provides the initial conditions for the charging simulation. The formation cycle and any thermal effects were neglected for this analysis.

2.7 Materials Characterisation Techniques

2.7.1 Scanning Electron Microscopy (SEM)

SEM images were taken by Maximilian Schart and John Cattermull. SEM particle size analysis was conducted by myself. Scanning Electron Microscopy (SEM) is a powerful tool for evaluating material morphology at sub-micron length scales. Optical microscopes are limited in their resolution by the wavelength of visible light. SEM overcomes this through the use of a high energy beam of electrons with significantly shorter wavelengths than visible light[196]. This highly focused beam of electrons is scanned across the sample and this interaction results in a number of scattering and adsorption phenomena and thus three primary signals: secondary electrons, backscattered electrons and characteristic X-rays. Detection of secondary electrons, which are emitted from the sample from inelastic scattering, are the the primary mode of imaging, providing the highest resolution. The contrast generated from the electrons is determined by the steepness of the emitting surface providing rich morphological and topological information of the material surface. The resolution of SEM images is around 1 nm[197].

2.7.2 Powder X-ray Diffraction (XRD)

XRD experiments and analysis were conducted by John Cattermull. Powder X-ray Diffraction (XRD) is a technique which enables the identification of the atomic arrangement in the crystal structure of a material[198]. Diffraction occurs from scattering of the incident radiation from the atoms in the crystal structure of the material. The scattered waves can experience constructive or destructive interference, depending on their phase relationship. The constructive interference is defined by Bragg's law[199]:

$$n\lambda = 2dsin(\theta) \tag{2.34}$$

where λ is the radiation wavelength, d is the interplanar spacing, θ is the angle of incidence, and n is an integer. The number and position of the diffraction pattern peaks is determined by the unit cell parameters and space group of the crystal which set the interplanar spacing d. The intensity of the diffracted radiation is then plotted against the angle (2θ). Peaks are located where Bragg's law is met, confirming the existence of crystallographic planes separated by d. Therefore, it is possible to identify the crystalline phases in the material sample from the radiation diffracted.

2.7.3 X-ray Photoelectron Spectroscopy (XPS)

XPS experiments and analysis were conducted by Ben Jagger. X-ray Photoelectron Spectroscopy (XPS) is a highly surface-sensitive technique based on the photoelectric effect. The technique involves irradiating a material surface with low-energy X-rays. The incident X-ray photons undergo an interaction with the atoms on the material surface, leading to electron emission. The energy of the emitted electrons is determined by subtracting the electron binding energy from the incident photon energy with the binding energy determined by the bond of the material. From measurement of the energy and intensity of the emitted electrons, this enables insight into the elemental composition of the material, their chemical state, and even what other elements they are bonded to. XPS can be coupled with an ion

beam to etch away a surface to obtain depth-dependent information regarding the material[200].

2.7.4 Atomic force microscopy (AFM)

AFM experiments and analysis were conducted by Ben Jagger. Atomic force microscopy (AFM) is a high-resolution surface technique which operates by mechanically scanning the surface with a highly sensitive probe. The probe tip is attached to a cantilever and scans the surface using a continuous contact or tapping mode. AFM does not use any lenses or irradiation, enabling higher resolution less than 1 nm; it is also capable of producing a 3D surface profile[201].

3

Characterising the Ionic Transport and Thermodynamic Properties of Potassium-ion Electrolytes

Contents

3.1 Introduction 80
3.2 Experimental 82
3.3 Results and Discussion 88
3.3.1 K Metal Electrode Preparation 88
3.3.2 Transference Number 93
3.3.3 Ionic Conductivity 95
3.3.4 Thermodynamic Factor 98
3.3.5 Property Parameterisation 103
3.3.6 Modelling 105
3.4 Conclusion 108

3.1 Introduction

The work in this chapter has been published in *Nature Communications*:

1. Dhir, S., Jagger, B., Maguire, A., Pasta, M. Fundamental investigations on the ionic transport and thermodynamic properties of non-aqueous potassium-ion electrolytes. *Nature Communications* **14**, 3833 (2023).[170]

Fast charging rates ($\sim$4C[29]) are increasingly important for batteries, and slow electrolyte transport is one of the critical limitations in realising fast charging for LIBs[29,30]. Initial data appears to show improved rate performance of KIBs compared to LIBs[35], suggesting faster transport in non-aqueous potassium-ion (K-ion) electrolytes[83]. The larger ion size and thus lower charge density of K^+ compared to Na^+ and Li^+, results in weaker solvent interactions[27], which is anticipated to facilitate faster electrolyte ionic transport[1]. This is supported by the results from Landesfeind et al. who found improved transport properties of a nonaqueous sodium-ion (Na-ion) electrolyte compared to the lithium-ion (Li-ion) equivalent[143], given Na^+ is a larger ion than Li^+. It also appears from various data sources collated by Landesfeind et al. that aqueous K-ion electrolytes may show faster transport properties compared to Li- and Na-ion aqueous electrolytes[143]. K^+ has also been found to have the lowest desolvation activation energy of the three cations[32,83], showing promise for fast-charging capability.

Though studies suggest improved rate performance, a comprehensive understanding of mass transport in K-ion electrolytes can only be obtained through full and accurate characterisation of the fundamental ionic transport and thermodynamic properties: the salt diffusion coefficient (D_e), the cation transference number (t_+^0), the ionic conductivity (κ), and the thermodynamic factor (χ_M)[109]. However, there is currently no study which has fully characterised these properties for a K-ion electrolyte. Given these properties are challenging and time-consuming to obtain for Li-ion electrolytes, the added complication of the extreme reactivity of K metal provides significant additional challenges to K-ion electrolyte characterisation.

Therefore, the objective of this chapter is to characterise the fundamental transport and thermodynamic properties of a non-aqueous K-ion electrolyte, comparing with its Li-ion equivalent. The K-ion electrolyte investigated comprises of the potassium bis(fluorosulfonyl)imide (KFSI) salt and 1,2-dimethoxyethane (DME) solvent, which is compared to the Li-ion equivalent electrolyte (LiFSI in DME) over the concentration range 0.25–2 molal. A K metal preparation protocol is developed to ensure sufficient stability and data reproducibility to enable K-ion

electrolyte characterisation using the most accurate electrochemical characterisation techniques. FSI^- in DME is used as a model electrolyte system because of the ability of the FSI^- anion to more effectively passivate the K and Li metal surface[202–204] and due to the stability of ethers in contact with both K and Li metal[138,203]. The KFSI:DME electrolyte system has been shown to enable reversible plating and stripping of K metal due to formation of a more uniform solid electrolyte interphase (SEI) at the negative electrode, indicating an appropriate model electrolyte for the electrochemical measurements which require symmetric metal cells[203]. Moreover, Le Pham *et al.* have also investigated the solvation structure of K^+ in KFSI:DME electrolytes using operando XRD and Raman spectroscopy[205]. It is also important to note KFSI:DME is unlikely to be the electrolyte utilised in commercial KIBs due to its tendency for cointercalation into graphite[206], however, given its stability advantages with metals it provides a good model electrolyte to compare K-ion and Li-ion electrolyte ionic transport. Therefore, this chapter aims to fully characterise the critical transport and thermodynamic properties of the KFSI:DME K-ion electrolyte, comparing to the Li equivalent.

3.2 Experimental

Electrolyte Preparation and Electrochemical Measurements

All electrolytes were prepared and handled in an Ar-filled glovebox with O_2 and H_2O concentrations below 0.1 ppm. The electrolyte used was a solution of potassium bis(fluorosulfonyl)imide (KFSI, 99.9% Solvionic) or lithium bis(fluorosulfonyl)imide (LiFSI, battery grade, Fluorochem) in 1,2-dimethoxyethane (DME, 99.5% anhydrous, Sigma Aldrich). KFSI was dried under a high vacuum at 100°C for 48 hours and LiFSI at 70°C for 48 hours. DME was dried using 3 Å molecular sieves. All equipment was dried at 70°C under vacuum for a minimum of 24 hours before being used and brought into the glovebox. The H_2O content of the electrolyte solutions was determined by Karl Fischer titration, also performed in an argon-filled glovebox, and recorded to be below 10 ppm of H_2O. All restricted diffusion, Hittorf

and concentration cell experiments were conducted in a Binder Oven at 20°C (±0.3 K).

All electrochemical tests were carried out using a battery cycler (VMP3, Biologic). Electrochemical impedance spectroscopy (EIS) measurements were performed using a frequency response analyser (VMP3, Biologic), unless otherwise stated, over the frequency range of 200 kHz–500 mHz (6 measurement points per decade) with an applied potentiostatic signal of amplitude 10 mV. The spectra in Fig. 3.2b were gathered at OCV after a 1 h rest.

Electrode Preparation

For the potassium electrode preparation protocol, potassium electrodes were prepared from potassium chunks in mineral oil (98% trace metals basis, Sigma Aldrich). First the K chunks were removed and melted in a beaker on a hot plate in an argon-filled glovebox (< 0.1 ppm O_2 and H_2O). A spatula was then used to skim off and remove the visible impurity layers until the liquid K metal appeared clean. Then the liquid K metal was quenched into clean mineral oil forming spheres of clean K. These K spheres were then cleaned with hexane (95% anhydrous, Sigma Aldrich). Just before use the K was rolled to ∼0.6 mm thickness using an aluminium rolling pin with the K sandwiched between two sheets of weighing paper (Grade 2122, Whatman) coated in hexane and one metal surface was gently polished using a plastic blade to remove any oxide and provide a sticking surface. Electrodes were then punched into discs of required diameter using a wad punch. The K electrode was placed on the current collector (stainless steel) with the polished surface down. Next, for the active and exposed K surface, first the K was initially polished with the plastic blade, then followed by a second careful polish using a microtome blade (Epredia, Shandon), adapting a methodology developed for metallic lithium[207]. The microtome blade was used to form a mirror-like finish, resulting in an improved polished K surface free of surface irregularities. The active K metal surface was polished at the very end of cell setup, just before electrolyte

addition, so the polished surface was exposed to the glovebox environment for minimal time before the electrolyte was added.

For the standard preparation the same method was used from literature[202,208]. K metal was cut, washed in hexane, and rolled before punching into electrodes. Lithium (99.9% trace metal basis, Sigma Aldrich) electrodes were prepared for use by first initially brushing the Li metal surfaces using a plastic brush, then calendering the brushed Li to 0.3 mm thickness in a sample bag, before finally punching into electrode discs of required diameter using a wad punch. Stainless steel current collectors were also used for the Li cells.

Atomic Force Microscopy

Atomic force microscopy (AFM) was performed with a Bruker Dimension Icon AFM in an argon-filled glovebox ($<$ 0.1 ppm O_2 and H_2O). Surface height maps were gathered in the ScanAsyst imaging mode with ScanAsyst-Air probes (Bruker) at a scan rate of 0.25 Hz. Gwyddion software was used for data analysis[209].

X-ray Photoelectron Spectroscopy

X-ray photoelectron spectroscopy (XPS) was performed with an ULVAC PHI Versaprobe III XPS system generating monochromatic $Al_{K\alpha}$ X-rays (1486.6 eV, 15 kV anode voltage, 25 W beam power) under ultrahigh vacuum (UHV) conditions ($\sim 10^{-7}$–10^{-6} Pa). K metal samples were prepared in a glovebox and were immediately transferred into the XPS chamber using a vacuum transfer vessel (ULVAC PHI GmbH) to avoid contamination and ambient exposure. A 500 μm $\times$ 500 μm area from each sample was analysed. Survey scans were acquired at pass energies of 224 eV, and a lower pass energy of 55 eV was used for core-level spectra. In-built electron and low energy Ar^+ sources were utilized for charge neutralization. Depth-profiling was achieved with consecutive XPS analysis and Ar^+ sputtering (4 keV, 3 mm $\times$ 3 mm) for a total of 60 min. Acquired spectra were fitted with Voigt lineshapes, after application of a Shirley background, using CasaXPS software[210]. All spectra were charge referenced to adventitious C 1s peak at 285 eV[211].

Densitometry

For greater accuracy electrolyte concentrations were prepared gravimetrically rather than volumetrically, as using an analytical balance is more precise than a volumetric flask. In order to convert the gravimetric concentrations to volumetric (molality to molarity), high precision 5-digit density measurements were obtained using an Anton Paar DMA 4100 density meter in an argon-filled glovebox (< 0.1 ppm O_2 and H_2O). Each measurement was temperature controlled at 20°C. The density meter was rinsed with isopropanol ($\geq$ 99.9%, HPLC grade, Fisher Chemical) and DME (99.5% anhydrous, Sigma Aldrich) at least three times and dried in ambient argon between measurements. It was ensured that the density meter was completely clean and returned to reading the argon density between each measurement.

Hittorf Method

The sealed Hittorf cell was oriented vertically in the Binder Oven, and the current was applied so stripping occurred at the bottom electrode (anodic) and plating at the top electrode (cathodic), to prevent natural convection effects[115,121]. After an intial rest of 4 h, the current polarisation was applied for duration $t_{pulse} = 20$ h with the stopcocks open where the cell consists of a single cavity. Once finished, the two stopcocks were immediately closed creating three isolated chambers: anodic chamber at the bottom where stripping occurred, neutral chamber in the middle, and cathodic chamber at the top. The electrolyte solutions were then extracted through access ports. Extracted solutions from the three chambers were stirred for at least 1 h to ensure uniform concentration, after which their densities were measured using the Anton Paar DMA 4100 density meter at 20°C. The molarity of the solutions was calculated using the density correlation. The differences in concentrations of the anodic and cathodic chambers from the neutral chamber was used to calculate t_+^0. The current used for polarisation for all K-ion Hittorf experiments was 100 μA, except at 0.25 m where 50–100 μA was used. For the Li-ion Hittorf experiments 200 μA was used except at 0.25 m where 50 μA was used. I_{pulse} and t_{pulse} were set such that the concentration boundary layers remained within

the anodic and cathodic chambers during the experiment[174]. Three measurements were taken at each concentration for KFSI and LiFSI concentrations above 0.5 m. Two measurements were taken for LiFSI at 0.25 m and 0.5 m.

The conditions used were an optimum to form a detectable density difference with low error whilst preventing the concentration boundary moving out of the anodic and cathodic chambers. Due to the volatility of DME, the Hittorf was checked that evaporation did not have any impact over the experiment by running a test cell with no metal electrodes or current applied, filled with electrolyte and measuring the resultant density of the electrolyte before and in each chamber after. There was no change in density showing DME evaporation is not an issue.

Ionic Conductivity

For measurement of ionic conductivity, a commercial conductivity cell of known cell constant was used (CLR, 401-S-138C). The cell was filled with ∼0.5 mL electrolyte and tested with an impedance analyser (BioLogic MTZ-35 with ITS-e temperature chamber) at 15, 20 and 25°C. The ionic conductivity of the electrolyte was calculated by dividing the cell constant by the series resistance extracted from a Nyquist plot. The ionic conductivities in Fig. 3.6b were fitted with the function proposed by Casteel and Amis (Equation 2.16)[178].

Concentration Cell

For the concentration cell experiments a H-cell was designed including a Grade 5 frit to mitigate the faster diffusion from the K-ion electrolyte. A Grade 4 frit was found to be insufficient to suppress interdiffusion in the K-ion electrolyte, but gave reliable results with the Li-ion electrolyte. K and Li metal were prepared and cut into ∼5 mm × 20 mm strips. Each chamber of the H-cell was filled with 4 mL of electrolyte, with 1 m electrolyte used as the constant 'reference' concentration for both electrolyte systems. The electrodes were then lowered into the electrolyte and the cell was sealed and immediately brought into the Binder Oven. The OCV was tracked for 2 h to allow the cell to stabilise and reach the correct temperature and

the OCV was then averaged over the next 10 min, as shown in Figure 2.4. At least three repeat measurements were made for each concentration.

Restricted Diffusion

The cell used for the restricted diffusion cells (Figure 2.2) was designed to ensure an airtight seal and the chamber is free of any geometric issues that can affect the concentration gradient. The cell was designed to be longer than typically used for Li-ion restricted diffusion experiments due to the identified faster diffusion of K-ion electrolytes to enable sufficient time to observe the relaxation and enable a more robust fit. The distance between the current collectors was 12 mm and the distance between the electrodes, L_s, was measured using digital calipers for each cell due to the slightly varying thickness of K. The thickness of the K was measured once it had been placed on the cell current collector due to K being soft and easily compressed. For example, L_s was 10.8 mm with K metal electrodes of 0.6 mm thickness. No separators were used to improve accuracy errors introduced through separator variability and tortuosity estimation[121,137].

The experiment involved first a rest for 10 h where the OCV was tracked. Then a galvanostatic polarisation was applied for 20 h to induce the concentration gradient. The current was 35 μA for all Li-ion cells and 30 μA for K-ion cells from 1 m and higher concentration. 25 μA current was used for 0.25 and 0.5 m for K-ion. Finally, the current was switched off and the OCV recorded during relaxation. At least five cells were made for each K-ion diffusion concentration and at least three for Li-ion. The OCV values were adjusted by any V_{offset} from 0 V to ensure the OCV relaxed to 0 V so the linear behaviour of $\ln(V)$ vs time could be analysed[142,143]. The data was fit from the minimum time constant 0.5 τ_{diff} established by Newman and Thompson[175] for as long as it showed exponential relaxation behaviour, or until relaxation had completed. The $\ln(V)$ vs. time was plotted, with the gradient from the linear region used to obtain the salt diffusion coefficient.

Modelling

For the DFN modelling, the open-source battery simulation package Python Battery Mathematical Modelling (PyBaMM)[194] version 23.2 half-cell DFN model and CasADi numerical solver[195] was used. For determining the accessible capacity % at different C-rates, the baseline performance was determined from a C/50 charge rate (1C = 3.28 mA cm^{-2} for both). For both cells, the Li graphite maximum Li^+ concentration was used. For the KFSI and LiFSI:DME electrolytes the empirical concentration dependent functions characterised in this chapter were used. The 'Ai2020' pouch cell parameter set was used for the Li graphite and cell geometry base parameters[212]. The default metal electrode parameters were used[213] with a metal electrode thickness of 12.5 μm. Between the Li-ion and K-ion graphite, electrode parameters such as particle size, porosity, and graphite electrode geometries were kept constant as defined in the parameter set[212]. The graphite diffusivity function was also kept constant since the diffusivities of materials similar to K graphite characterised so far appear similar to that of Li graphite[109,214,215]. The exchange current density function was also kept constant as no K^+ graphite exchange current density has yet been characterised. The K graphite OCV profile was utilised for the K graphite simulation based on previously characterised data[38]. The lower voltage cut-off was set as 0.01 V vs. K^+/K or Li^+/Li below which metal plating would occur.

3.3 Results and Discussion

3.3.1 K Metal Electrode Preparation

The leading electrolyte transport and thermodynamic property characterisation techniques rely on metallic electrodes that are sufficiently chemically and electrochemically stable in the electrolyte under investigation. Metallic K reactivity is one of the main reasons why a thorough characterisation of a K-ion electrolyte has not yet been reported. Therefore, in this study a K electrode preparation protocol was developed to ensure sufficient K metal stability and data reproducibility. The

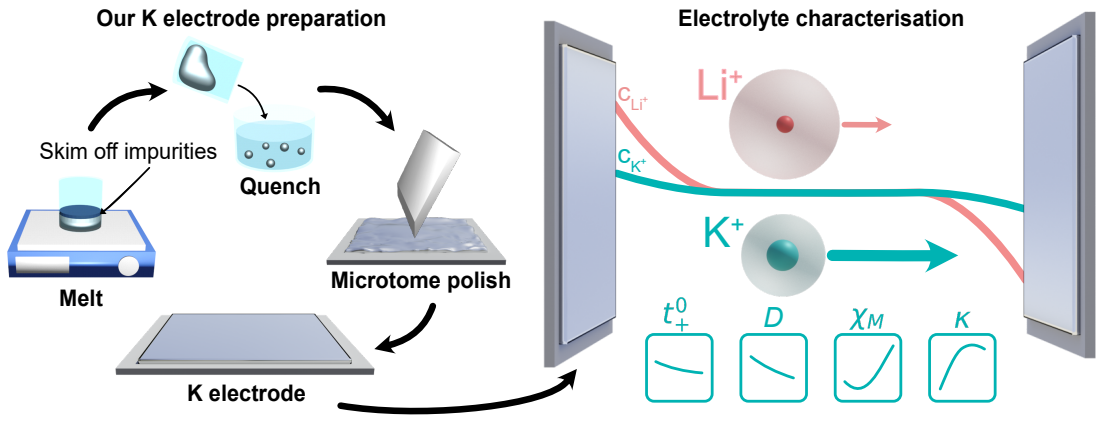


Figure 3.1 Potassium electrode preparation and electrolyte characterisation. Schematic of the K preparation protocol developed enabling K-ion electrolyte transport and thermodynamic property characterisation. The K metal preparation involves melting K metal chunks, skimming off impurities floating on the melt and quenching the clean metal. Clean K metal spheres are rolled, punched into discs and the surface polished using a microtoming technique adapted from a methodology developed for Li[207]. The K preparation enables characterisation of the K-ion electrolyte salt diffusion coefficient (D_e), the cation transference number (t_+^0), the ionic conductivity (κ), and the thermodynamic factor (χ_M). The higher D_e and t_+^0 of KFSI:DME compared to LiFSI:DME results in reduced concentration gradient formation, which is represented schematically. Reproduced from Dhir *et al.*[170]

first step involves melting K metal chunks in an Ar-filled glovebox (< 0.1 ppm O_2 and H_2O), skimming off impurities floating on the melt and quenching the clean metal. Right before cell assembly, a clean K metal sphere is rolled into a metal sheet (thickness ∼0.6 mm), punched into discs and the surface polished using a microtoming technique adapted from a methodology developed for metallic lithium (Figure 3.1)[207].

It has been shown that standard K metal preparation in literature, where K metal is cut, washed in hexane, rolled, and punched into electrodes[202,208], results in high open-circuit voltages (OCVs) in symmetric K cells, > 100 mV has been reported, which indicates K metal instability and an inhomogeneous distribution of impurities[202,216]. Figure 3.2a shows the low OCVs and superior reproducibility for K symmetric cells prepared using our K electrode preparation protocol compared to the standard preparation procedure reported in literature[202,208], demonstrating improved surface stability and homogeneity[216]. This is also supported by the considerably

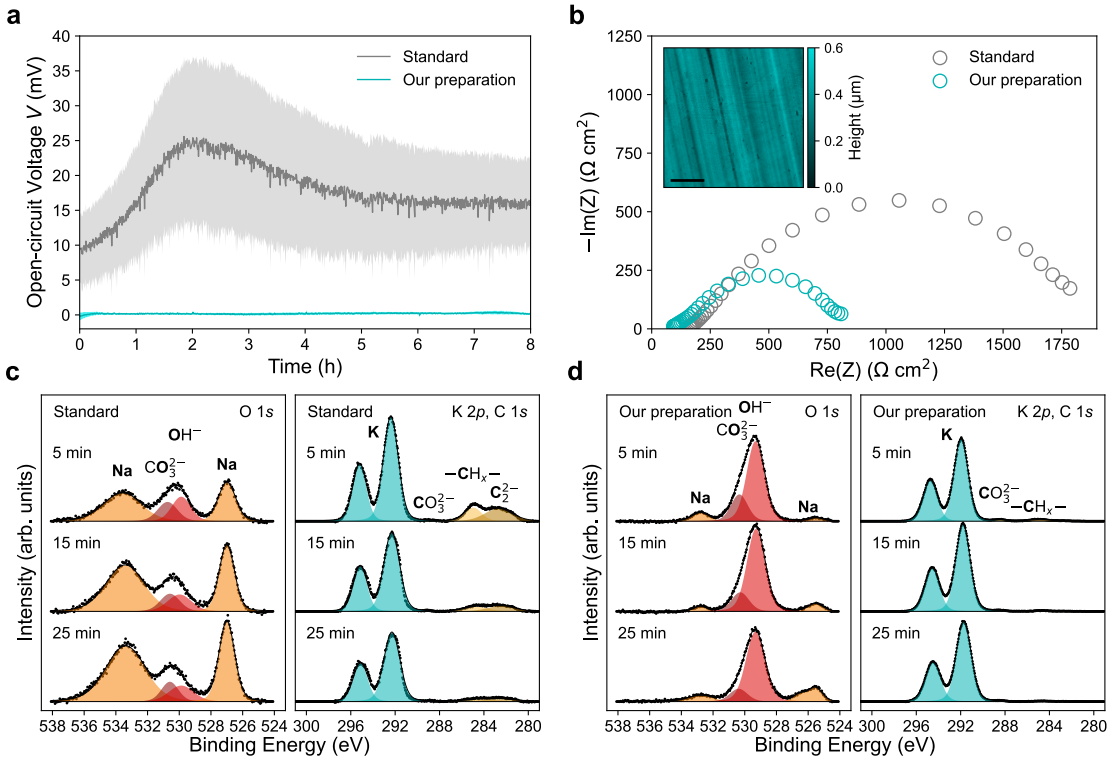


Figure 3.2 Potassium electrode stability and characterisation. Stability of K||K symmetric cells in 1 m KFSI:DME using our K preparation compared to standard K preparation at 20°C (**a**) Averaged initial OCV profiles for 8 h. Light shaded areas depict standard error in the mean, calculated from at least 5 cells (**b**) Complex impedance plots after 1 h rest at 20°C, inset shows AFM height map of pristine K metal electrode prepared with our method (scale bar, 20 μm). XPS depth profiles on K metal after 5, 15 and 25 min of Ar^+ sputtering (**c**) O 1*s*, K 2*p* and C 1*s* spectra from the standard preparation (**d**) O 1*s*, K 2*p* and C 1*s* spectra from our preparation. Reproduced from Dhir *et al.*[170]

reduced total impedance of cells prepared using our preparation compared to the standard method (Figure 3.2b). The inset in Figure 3.2b shows an atomic force microscopy (AFM) height map, which further highlights the surface uniformity we are able to achieve with our preparation protocol, showing that the as-prepared K surface is apparently flat with no visible contamination. The standard preparation method results in a surface with a much higher roughness (root mean square roughness of 253 and 33 nm for the surfaces prepared using the standard procedure and our preparation protocol, respectively) and greater nonuniformity, as evident in Figure 3.3).

Crucially, our K preparation protocol enables sufficient K stability for electrolyte

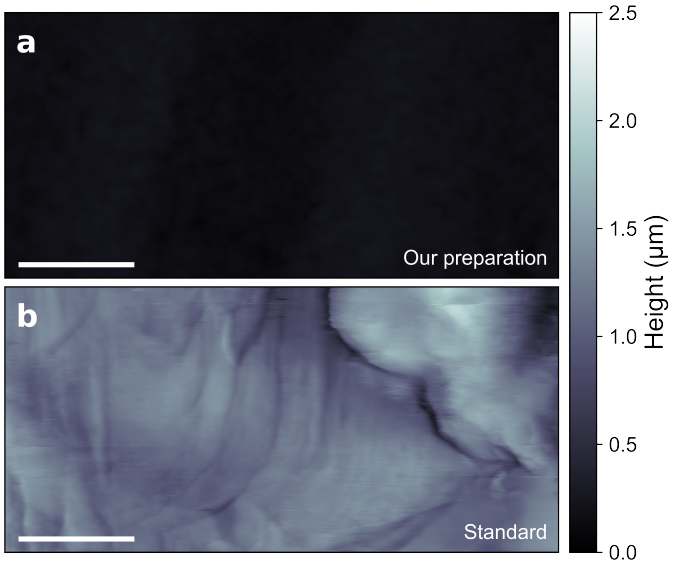


Figure 3.3 Comparison atomic force microscopy height maps of the surface of pristine K metal samples using (**a**) our preparation protocol (**b**) the standard procedure. Scale bars, 2 μm/. Reproduced from Dhir *et al.*[170]

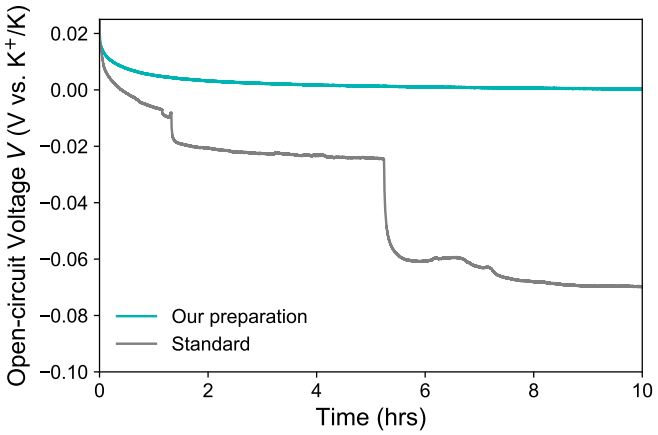


Figure 3.4 Diffusion open-circuit voltage relaxation profile after 10 h rest and 20 h galvanostatic polarisation in representative K||K symmetric cells in 1 m KFSI:DME in the restricted diffusion cell using our K preparation compared to standard K preparation at 20°C. Reproduced from Dhir *et al.*[170]

transport property characterisation. Characterising D_e using the restricted diffusion method requires exponential OCV relaxation after polarisation of symmetric metal cells. Figure 3.4 shows our K preparation results in exponential OCV relaxation in K symmetric cells, enabling the determination of D_e from its semi-log plot. The standard preparation cannot be used to determine D_e due to random OCV jumps, irreproducibility and erratic OCV behaviour, indicating side reactions and

K instability, matching similar findings occurring for Na-ion electrolytes[143]

X-ray photoelectron spectroscopy (XPS) with Ar^+ depth-profiling was utilised to examine the surfaces of K metal prepared using both the standard literature method and our preparation protocol to understand the improved stability. The O 1*s* spectra from the standard preparation in Figure 3.2c exhibits peaks at 533.6 and 527.0 eV as a result of Na KLL Auger electron emission[211] and Na is the main impurity species identified throughout the majority of the examined depth. However, Na is a minor impurity element in the electrode prepared with our method, as evidenced by the small Na KLL peaks in Figure 3.2d. This Na-rich surface may impede the transport of K^+ across the interface and be responsible for the large initial impedance observed (Figure 3.2b). Additionally, inhomogeneous distributions of impurity elements like Na could alter the activity of the K metal electrodes, leading to the non-zero OCV evident in Figure 3.2a[216].

The O 1*s* spectra from the electrode prepared with our preparation protocol are dominated by the KOH peak at 529.3 eV[211] in Figure 3.2d. Due to the high reactivity of K metal this KOH likely forms within the XPS as fresh K metal is exposed, suggesting the surface is rich in metallic K. In contrast, the hydroxide peak in Figure 3.2c has a relatively low intensity and appears at a binding energy of 529.9 eV, consistent with NaOH[211]. This suggests there is limited metallic K available at the surface of the standard preparation electrode.

The K 2*p* XPS spectra from the standard K electrode in Figure 3.2c show a decreasing K 2*p* doublet peak area with sputtering depth, while the K 2*p* doublet from our method remains intense during sputtering in Figure 3.2d[217]. There is also a C 1*s* peak indicative of a carbide species at the surface of the standard K electrode in Figure 3.2c. These results therefore demonstrate that our K electrode preparation process produces K-rich electrode surfaces with greater uniformity and reduced levels of impurity elements, allowing K metal electrodes to be prepared with greater reproducibility.

Therefore, K metal electrodes prepared with our preparation protocol enable us to apply and adapt the accurate electrochemical characterisation methods to measure the K-ion electrolyte t_+^0, κ, χ_M and D_e.

3.3.2 Transference Number

First the density correlations from densitometry for KFSI and LiFSI DME are shown in Figure 3.5a showing the linear relationship expected. Figure 3.5b then shows partial molar volume results determined from the density correlations. The results show the partial molar volumes of the salt and solvent for both KFSI and LiFSI electrolytes are constant with increasing concentration. The partial molar volumes are utilised to determine t_+^0.

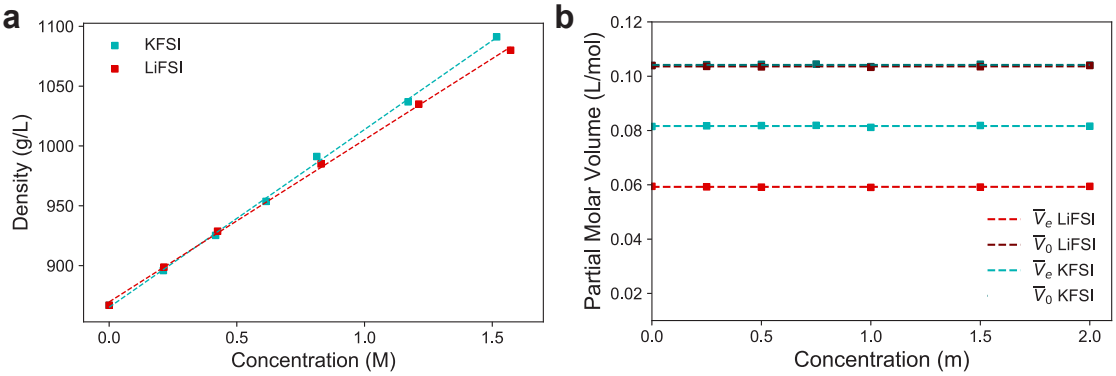


Figure 3.5 (**a**) Density correlations for KFSI and LiFSI in DME at 20°C (**b**) Partial molar volumes of salt, $\overline{V}_e$, and solvent, $\overline{V}_0$, for LiFSI and KFSI in DME at 20°C. Adapted from Dhir *et al.*[170]

Figure 3.6a shows the valid transference numbers from the Hittorf measurements for KFSI and LiFSI in DME. The results show the $t^0_{K^+}$ is significantly higher than $t^0_{Li^+}$ for the majority of the concentration range, though particularly at lower concentrations, for instance at 0.25 m (0.49 and 0.34, respectively). Though $t^0_{K^+}$ decreases with increasing concentration so that it is is only slightly higher than $t^0_{Li^+}$ from 1.5–2 m. $t^0_{K^+}$ and $t^0_{Li^+}$ appear to be trending to similar values suggesting that the lower charge density of K^+ delays some of the ion-ion and ion-solvent interaction effects of increasing concentration. $t^0_{K^+}$ decreases from around 0.49 to 0.38 over the concentration range indicating increasing ion-ion and ion-solvent interactions are

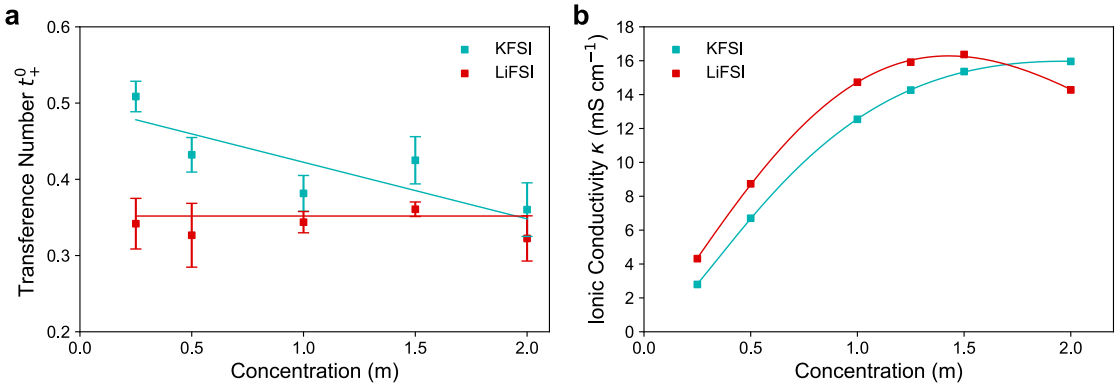


Figure 3.6 KFSI and LiFSI in DME concentration-dependent transference number and ionic conductivity. Transference numbers and ionic conductivities of KFSI and LiFSI in DME at 20°C (**a**) Cation transference number t_+^0 measured by Hittorf experiments. Error bars for t_+^0 depict error in the mean. Fits described in Section 3.3.5 (**b**) Ionic conductivity κ measured with a conductivity cell, fit with the Casteel-Amis equation (Section 2.2.6) Reproduced from Dhir *et al.*[170]

acting to bind up K^+ more strongly than FSI^-. Whereas for Li^+ these interactions appear to have become significant at concentrations below those measured as $t^0_{Li^+}$ remains constant in this concentration range. The $t^0_{K^+}$ results are similar to those reported for $NaPF_6$:EC:DEC by Landesfeind et al., though it is important to note their study treats the cosolvent as a single entity, assuming identical velocity of the two solvents, which is an assumption that has recently been shown to be untrue by Wang et al. and to have an impact on transference number measurements[138].

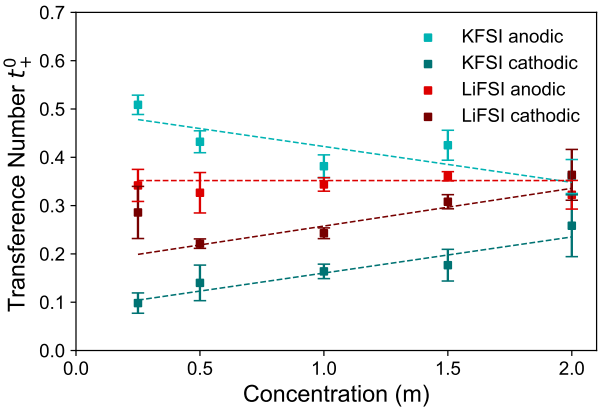


Figure 3.7 LiFSI and KFSI cation transference numbers determined from the Hittorf anodic and cathodic chambers in DME at 20°C. Error bars depict error in the mean. Reproduced from Dhir *et al.*[170]

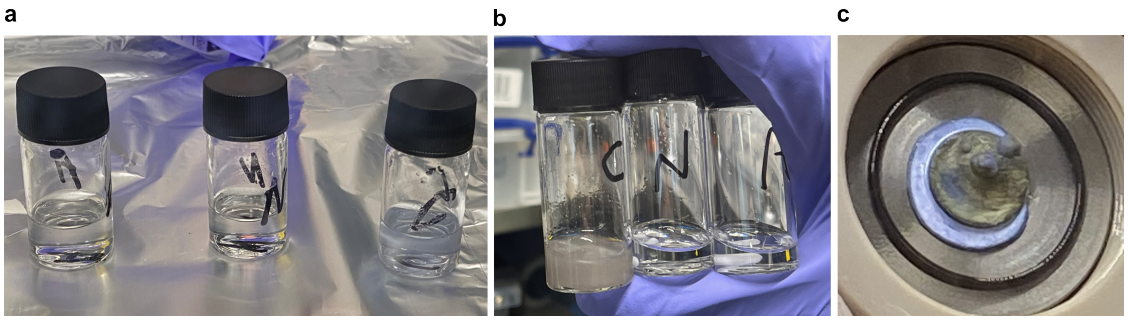


Figure 3.8 Cathodic chamber discolouration after Hittorf experiment in DME at 20°C. The cathodic, neutral and anodic solutions are labelled as C, N and A, respectively (**a**) KFSI cathodic solution with neutral and anodic solutions for comparison (**b**) LiFSI cathodic solution with neutral and anodic solutions for comparison (**c**) Cathodic Hittorf K electrode after 1 m KFSI:DME Hittorf experiment showing nonuniform plating. Reproduced from Dhir *et al.*[170]

Figure 3.7 shows the anodic and cathodic chamber t_+^0 measurements, with $t_{K^+}^0$ exhibiting significant deviation between them. The cathodic data was discounted due to evidence of nonuniform K deposition and cathodic electrolyte discolouration in both systems (Figure 3.8). These high surface area K metal deposits result in the continuous formation of SEI and significant electrolyte consumption. Therefore, given the highly sensitive density measurements, the cathodic transference numbers are likely underestimated. There is evidence in the literature of nonuniform K deposition in the same electrolyte at even much higher concentrations (5 M) and at lower current densities than can be used in our investigation (Section 2.2.3)[203]. Significant discolouration was also observed in the cathodic solution for many of the Li- and K-ion experiments, further supporting the nonuniform Li/K deposition as mossy Li/K formed during plating can become electronically disconnected from the electrode, a phenomenon known as 'dead' metal formation[30]. Similar discolouration was found in the study by Hou and Monroe using metallic Li and their cathodic data was also discounted[121].

3.3.3 Ionic Conductivity

Figure 3.6b shows the ionic conductivities over the concentration range. LiFSI displays slightly higher κ from low concentrations through until ~1.5 m, after which its κ decreases significantly, matching previous findings[218]. KFSI, however, continues

increasing and appears to plateau at 2 m. It has been shown to decrease after this point[35]. This indicates there is likely greater species-species interaction for the LiFSI electrolyte compared with the KFSI electrolyte above ∼1.5 m. The trend matches that found by Hosaka et al. for KPF_6 and $LiPF_6$ in EC:DMC where the K-ion electrolyte conductivity was lower than the Li-ion electrolyte below 1.5 m. However they also found KFSI:PC had significantly higher conductivity than LiFSI:PC at all concentrations tested[19]. This shows the importance of the combination of salt and solvent for optimum ionic conductivities for K-ion electrolytes. Since the χ_M for KFSI is closer to ideality than LiFSI at lower concentrations (Figure 3.12), indicating less ion-ion interaction than for Li^+, it appears that the lower ionic conductivity for KFSI for the majority of the concentration range could be due to lower KFSI salt dissociation[19].

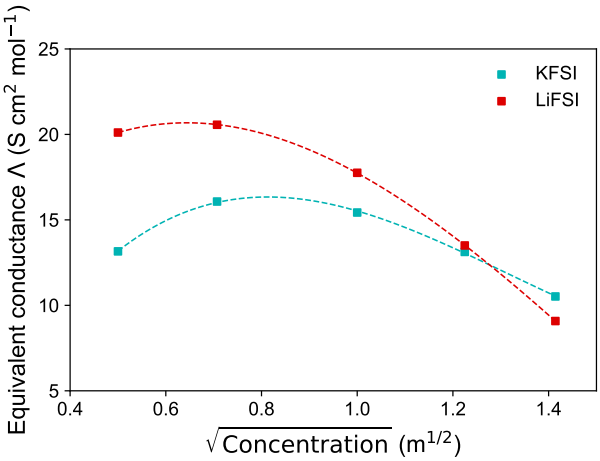


Figure 3.9 Equivalent conductance of KFSI and LiFSI in DME at 20°C. Reproduced from Dhir *et al.*[170]

Plotting the equivalent conductance over concentration also indicates that both are weak electrolytes with their non-linear dependence of conductance on the square root of concentration[137,179] (Figure 3.9). Though KFSI:DME is more non-linear than LiFSI:DME, again indicating lower salt dissociation for KFSI. At higher concentrations above 1.7 m, the drop in conductivity for LiFSI is likely due to the greater ion-solvent and ion-ion interaction for Li^+, where it is dragging more solvent than the K^+ due to its higher charge density and thus stronger solvation, while the

stronger coulombic interaction of the Li^+ also results in greater ion-ion association, forming aggregates that increase the electrolyte viscosity[218,219]. Aggregates have been shown not to form in KFSI:DME until concentrations above this range (> 3 M)[205]. High ionic conductivities are reached in the DME electrolytes, 16 mS cm^{-1} for KFSI:DME at 2 m and 15 mS cm^{-1} for LiFSI:DME at 1.5 m. The κ reached here are higher than that for carbonate equivalents due to the lower viscosity of DME[220], matching previous findings[35,61].

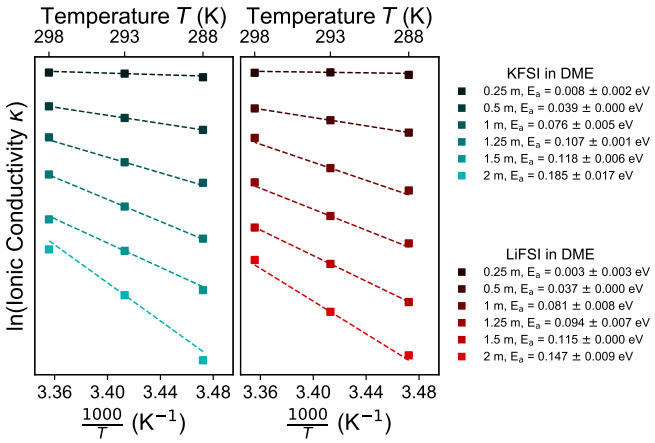


Figure 3.10 Arrhenius plots used to calculate the activation energy as a function of concentration. The different concentrations are shifted along the y-axis for clarity. Reproduced from Dhir *et al.*[170]

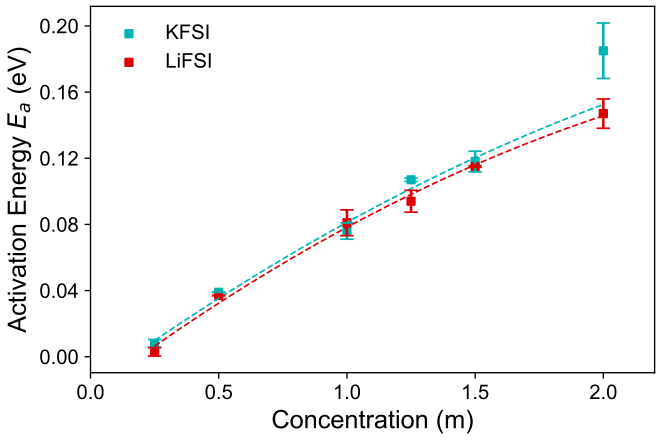


Figure 3.11 Activation energies for ionic conduction for KFSI and LiFSI in DME. Error bars depict the standard error in each activation energy determined from the linear fits in Figure 3.10. Reproduced from Dhir *et al.*[170]

Figures 3.10 and 3.11 show that the activation energies of ionic conduction of

KFSI and LiFSI in DME are very similar and increase with concentration as a result of increasing ion-solvent interactions[180].

3.3.4 Thermodynamic Factor

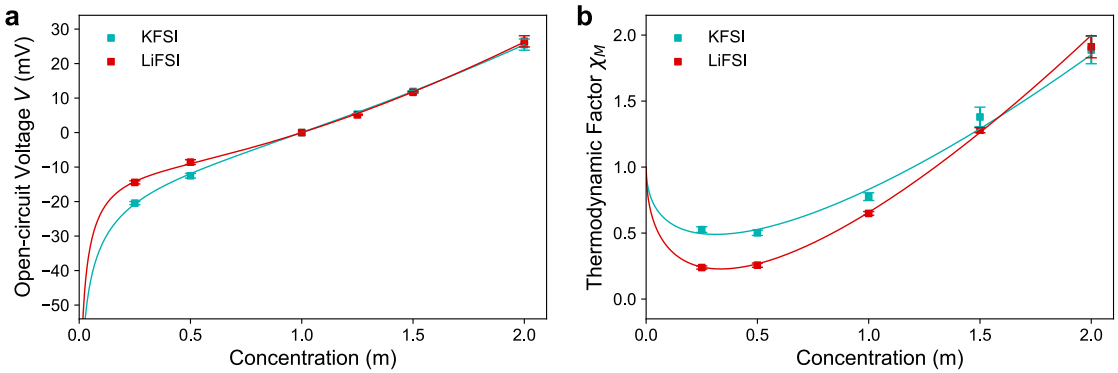


Figure 3.12 KFSI and LiFSI in DME concentration-dependent thermodynamic factor. Concentration cell and thermodynamic factor data for KFSI and LiFSI in DME at 20°C (**a**) Concentration cell open-circuit voltage V (**b**) Thermodynamic factors χ_M. Error bars depict the standard error in the mean for V, and the propagated t_+^0 error for χ_M. The fits are described in Section 3.3.5. Reproduced from Dhir *et al.*[170]

Figure 3.12a shows the expression derived in Section 2.2.5 is a good fit to the concentration cell OCV data. Therefore, from this Figure 3.12b shows how the resultant thermodynamic factor changes with concentration. The χ_M trends match those found for other nonaqueous electrolytes[109,121,129,137]. With increasing concentration, first coulombic ion-ion interactions decrease the salt free energy relative to the DME, reducing the salt activity coefficient and hence causing a drop in χ_M. As the concentration increases further, ion-solvent interactions increase, resulting in DME being increasingly bound, decreasing solvent vapour pressure, hence increasing the salt activity coefficient and χ_M[137,221]. The results show the decrease in χ_M at lower concentrations for KFSI is significantly less than for LiFSI. This can be attributed to the following two factors. First the larger size and thus lower charge density of K^+ compared with Li^+, resulting in weaker K^+ coulombic ion-ion interactions, hence the smaller reduction in χ_M. Second, from Debye-Hückel theory the gradient of the χ_M decrease at lower concentrations for both LiFSI and KFSI in DME should be equal as it is determined by the dielectric constant, ε, of

the solvent[115]. As Debye-Hückel theory assumes fully dissociated electrolytes, the lower KFSI gradient magnitude could further suggest poorer salt dissociation[137], which is also indicated by the lower ionic conductivity (Figure 3.6b) and more non-linear equivalent conductance (Figure 3.9) at low concentrations. The low ε of DME also provides minimal electrostatic screening, thus having a limited effect on reducing ion-ion interactions[222].

At higher concentrations, the increase in χ_M with increasing concentration is also higher for LiFSI than for KFSI. This is again due to the reduced charge density of K^+ resulting in weaker interactions with solvent molecules and thus a smaller solvation shell of K^+ compared to Li^+. The weaker K^+ solvation results in more free DME compared to Li^+ at higher concentrations, and therefore, the salt activity coefficient and χ_M increase with increasing salt concentration at a reduced rate for KFSI. This is the same trend identified by Landesfeind et al. comparing $NaPF_6$ and $LiPF_6$ in EC:DMC[143]. Le Pham et al. found a constant solvation number for KFSI:DME from Raman characterisation across this concentration range, supporting this increased binding of solvent increasing χ_M[205]. A similar study also found significant ion-pairing and solvent binding in LiFSI:DME[218]. χ_M is below unity until relatively high concentrations for both LiFSI and KFSI ($\sim$1.4 m) indicating the point where ion-ion and ion-solvent interactions are equal.

Further experiments could characterise χ_M over a wider concentration range with greater accuracy using the shifting-reference concentration cell technique developed by Wang et al.[137]. Given the narrow concentration range, this was not deemed necessary for this study.

Salt Diffusivity

The longer custom designed restricted diffusion cell enabled longer polarisation and relaxation times (20 h for polarisation and up to a maximum of 60 h for relaxation) to ensure less noisy relaxation and a more robust fit for both KFSI and LiFSI, similar to Wang et al.[130]. This was significantly longer than the shorter relaxation times ($\leq$ 3 h) in many recent studies[122,142,143]. Contrary to many recent

studies[121,142,143], no separators were used in the restricted diffusion experiments to improve accuracy, due to the errors introduced through separator tortuosity estimation and variability[121,137].

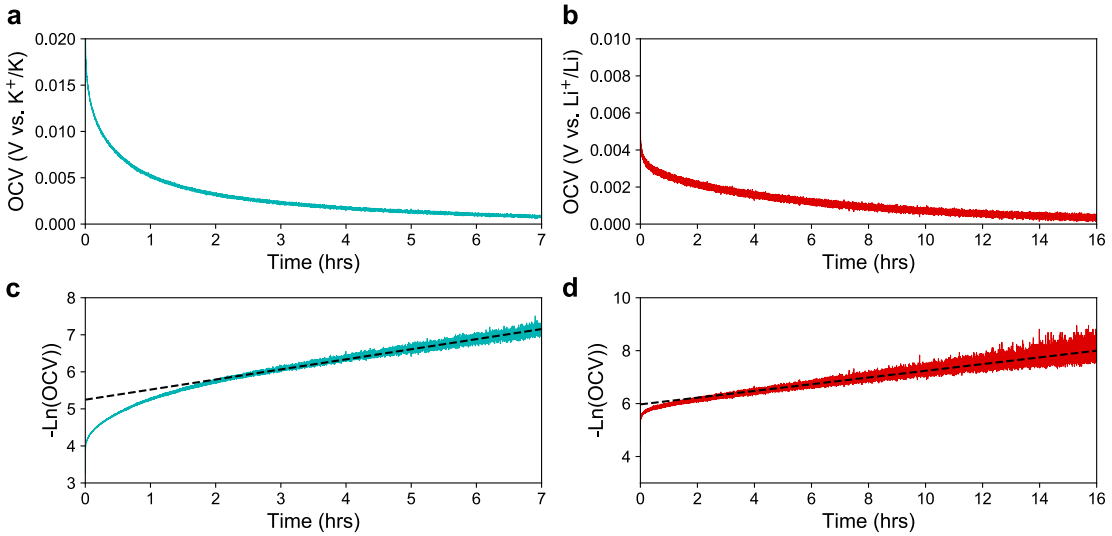


Figure 3.13 Representative restricted diffusion open-circuit voltage relaxation data for 1 m in DME at 20°C (**a**) KFSI (**b**) LiFSI. Open-circuit voltage data adjusted for V_{offset}. Semi-log plot with fitted linear decay region (black dashed line) used to determine salt diffusion coefficient (**c**) KFSI (**d**) LiFSI. Reproduced from Dhir *et al.*[170]

Example relaxation profiles and the resultant linear time dependence of the logarithm of the OCV from which D_e is determined are shown in Figure 3.13 for both KFSI and LiFSI.

Figure 3.14a shows D_e is significantly higher for KFSI than for LiFSI at all concentrations at 20°C. At 1 m D_{KFSI} is over 50% higher than D_{LiFSI} (7.6×10^{-10} m^2 s^{-1} and 5.0×10^{-10} m^2 s^{-1}, respectively). The difference is most significant at low concentrations where D_{KFSI} is almost double that for D_{LiFSI} (9.6×10^{-10} m^2 s^{-1} and 5.2×10^{-10} m^2 s^{-1}, respectively at 0.25 m).

With increasing concentration the difference between D_{KFSI} and D_{LiFSI} becomes smaller (5.2×10^{-10} m^2 s^{-1} and 4.8×10^{-10} m^2 s^{-1}, respectively at 2 m). This appears again to be due to increasing ion-ion and ion-solvent interactions occurring for K^+ at higher concentrations having a greater relative impact compared to minimal interaction at lower concentrations, matching the same trend observed for t_+^0. Both D_{KFSI} and D_{LiFSI} appear to be trending to similar values with increasing

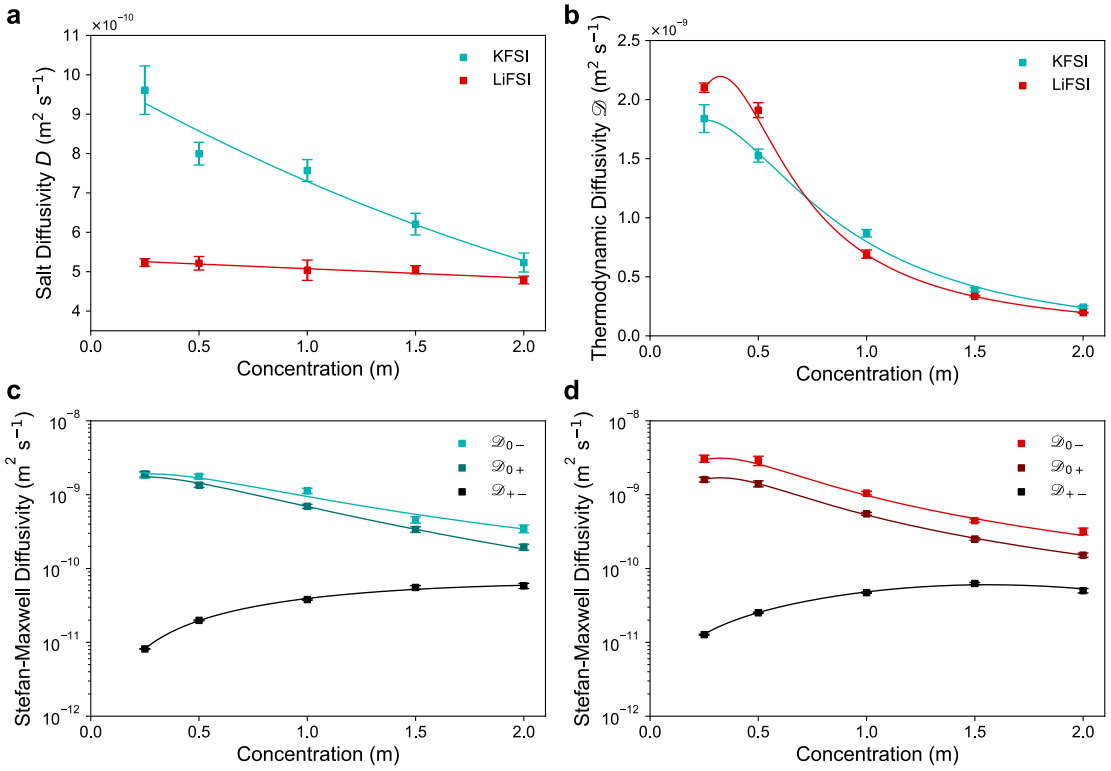


Figure 3.14 KFSI and LiFSI in DME concentration-dependent diffusivities. Diffusion coefficients of KFSI and LiFSI in DME at 20°C measured by steady-state galvanostatic restricted diffusion (**a**) Salt diffusion coefficient D_e. Error bars depict the standard error in the mean. Fits described in Section 3.3.5 (**b**) Thermodynamic diffusion coefficient $\mathscr{D}$ calculated using the measured thermodynamic factor (Fig. 3.12b). Stefan-Maxwell diffusion coefficients $\mathscr{D}_{ij}$ (**c**) KFSI (**d**) LiFSI. Errors bars in $\mathscr{D}$ and $\mathscr{D}_{ij}$ depict the propagated D_e, t_+^0 and χ_M errors. Fits obtained by combining all parameterised transport and thermodynamic properties (Section 3.3.5). Reproduced from Dhir *et al.*[170]

concentration, again matching the trends for t_+^0 and supporting the argument that the lower charge density appears to delay some of the ion-ion and ion-solvent interaction effects of increasing concentration. The higher D_{KFSI} also matches the trend observed by Landesfeind et al. with $NaPF_6$ showing higher D_e than $LiPF_6$[143]. However, the difference is much more significant for the K-ion electrolyte. D_{KFSI} is also significantly higher than those of Li-ion and Na-ion electrolytes characterised, with 2.9×10^{-10} m^2 s^{-1} found for 1 M $NaPF_6$:EC:DEC at higher temperature of 25°C[143], and with D_e for the majority of $LiPF_6$-based electrolytes coalescing around 2–3 $\times 10^{-10}$ m^2 s^{-1} at 1 M at 25°C[109,121,137,142]. The values obtained for D_{LiFSI} here are also higher than most Li-ion carbonate electrolytes characterised and this is attributed to the significantly lower viscosity of the DME solvent used compared to

carbonate solvents[222].

In D_e analysis using the restricted diffusion method, there is some dependence of the resulting diffusion coefficient on the time window it is fit[122]. Newman and Thompson demonstrated that exponential decay after polarisation occurs for times greater than $0.05\frac{L_s^2}{D_e}$ ($\approx 0.5\ \tau_{diff}$), regardless of the initial concentration profile indicating this is the point from which the data should be fit[175]. Therefore, in this analysis the data was fit from this minimum time constant $0.5\ \tau_{diff}$ for as long as it showed exponential relaxation behaviour, or until relaxation had completed. Due to the significantly higher diffusivity of KFSI than LiFSI, this was on average 11 h for KFSI and 33 h for LiFSI. For K-ion electrolytes, due to the reactivity of the K metal, very long analysis time windows occasionally resulted in significant OCV data noise levels or random jumps in potential, similar to what was found for the Na-ion electrolyte $NaPF_6$:EC:DEC[143]. This is attributed to the continued reformation of the SEI on the freshly plated K metal affecting local ion concentration and increasing side reactions.

Figure 3.14b shows D_e converted into the thermodynamic diffusion coefficient, $\mathscr{D}$, using χ_M and Equation 2.7, reflecting the diffusion coefficient with respect to salt chemical potential gradients instead of concentration gradients. The $\mathscr{D}$ trend matches those in literature[121,124,129,137]. The initial increase in $\mathscr{D}$ is due to increasing ion association due to the effective merging of two species into a single species resulting in lower resistance to the single species motion[137]. $\mathscr{D}_{\mathrm{LiFSI}}$ shows a greater initial increase due to greater ion-ion interaction for Li^+ than for K^+ as indicated by χ_M. At higher concentrations $\mathscr{D}_{\mathrm{KFSI}}$ is only slightly higher than $\mathscr{D}_{\mathrm{LiFSI}}$, but shows almost the same trend, demonstrating that the most significant difference in diffusion behaviour is related to concentration gradients rather than chemical potential gradients.

The Stefan-Maxwell diffusion coefficients express the mobility of each electrolyte species relative to each other in terms of the thermodynamic forces driving diffusion, providing deeper understanding of diffusional behaviour (Section 2.2.4). The Stefan-Maxwell coefficients for the KFSI and LiFSI electrolytes are shown in Figure

3.14c and 3.14d, respectively. The coefficients are relatively similar for both KFSI and LiFSI and this is due to their similar thermodynamic diffusivities. Both of the solvent-ion coefficients, $\mathscr{D}_{0+}$ and $\mathscr{D}_{0-}$, for LiFSI and KFSI decrease by about an order of magnitude over the concentration range, demonstrating the drag from the DME solvent becomes stronger on both cation and anion with increasing salt concentration. $\mathscr{D}_{0-}$ is higher than $\mathscr{D}_{0+}$ across the concentration range for LiFSI, indicating weaker interaction of the FSI^- with the DME compared with the Li^+ interaction with DME. However, for KFSI, $\mathscr{D}_{0-}$ and $\mathscr{D}_{0+}$ are much closer and at low concentrations are almost the same. This is due to t_+^0 being ∼0.5 for K^+ at 0.25 m indicating K^+ and FSI^- are carrying the same amount of current. With increasing concentration, the difference between $\mathscr{D}_{0-}$ and $\mathscr{D}_{0+}$ increases, matching the falling $t^0_{K^+}$ as ion-solvent interactions increase. The ion-ion diffusivity $\mathscr{D}_{+-}$ for both LiFSI and KFSI is approximately two orders of magnitude lower than the solvent-ion diffusivities, particularly at lower concentrations demonstrating ion-ion interaction is somewhat significant for both, similar to that found for $LiPF_6$:PC[121], but not as significant as the five orders of magnitude difference found for $LiPF_6$:EMC, indicating substantial ion-ion interaction[137]. For both KFSI and LiFSI the maximum in $\mathscr{D}_{+-}$ matches their maximum ionic conductivity, suggesting the greater cation/anion interaction is occurring due to lack of free DME at a lower concentration for Li^+, corresponding to its stronger solvation interactions.

3.3.5 Property Parameterisation

Finally, Figure 3.15 shows all four fundamental transport and thermodynamic properties characterised for KFSI and LiFSI:DME together.

All transport and thermodynamic properties characterised were parameterised by fitting functions to the data points. If the functional form was known then non-linear least squares fitting was used. Otherwise, least squares polynomial fits were used, with inverse variance weighting for the case of t_+^0. The parameterised forms of t_+^0, κ, χ_M and D are given as a function of concentration (either molar, c_e, or molal, c_m) for LiFSI and KFSI in DME, respectively. All fits are from data

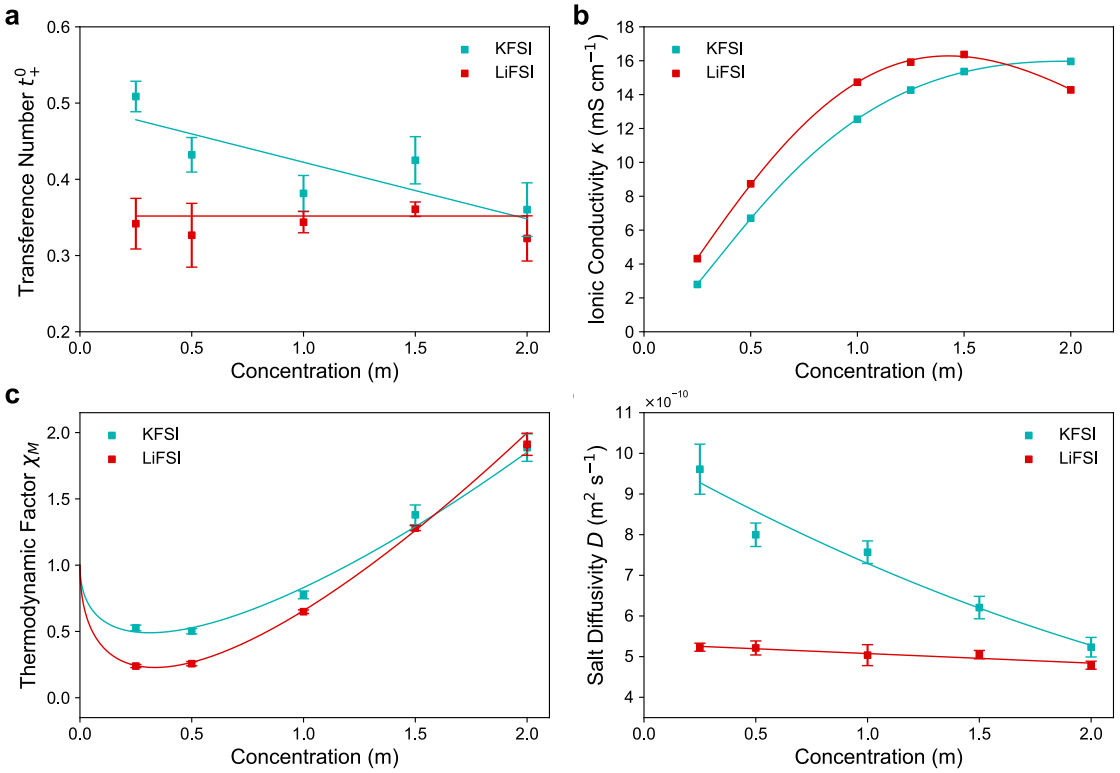


Figure 3.15 KFSI and LiFSI in DME concentration-dependent transport and thermodynamic properties Measured at 20°C (**a**) Transference number t_+^0 (**b**) Ionic conductivity κ (**c**) Thermodynamic Factor χ_M (**d**) Salt diffusivity D_e. Error bars depict the standard error in the mean. Adapted from Dhir *et al.*[170]

gathered in the concentration range 0.25–2 m. Approximate conversions between molal and molar concentrations are also provided.

LiFSI in DME

Cation transference number, t_+^0:

$$t_+^0 = 0.352 \tag{3.1}$$

Ionic conductivity, κ (mS cm^{-1}):

$$\kappa = 16.286 \left(\frac{c}{1.158}\right)^{1.085} \exp\left(-0.426(c-1.158)^2 - \frac{1.085}{1.158}(c-1.158)\right) \tag{3.2}$$

Thermodynamic factor, χ_M:

$$\chi_M = (1 + 0.052c_m)(1 - 2.663{c_m}^{\frac{1}{2}} + 2.287c_m) \tag{3.3}$$

Salt diffusivity, D (m^2 s^{-1}):

$$D = 5.312 \times 10^{-10} - (2.358 \times 10^{-11})c_m \tag{3.4}$$

Concentration conversion:

$$c_e = 0.873c_m - 0.043{c_m}^2 \tag{3.5}$$

KFSI in DME

Cation transference number, t_+^0:

$$t_+^0 = 0.497 - 0.074c_m \tag{3.6}$$

Ionic conductivity, κ (mS cm^{-1}):

$$\kappa = 15.970 \left(\frac{c}{1.493}\right)^{1.620} \exp\left(0.023(c - 1.493)^2 - \frac{1.620}{1.493}(c - 1.493)\right) \tag{3.7}$$

Thermodynamic factor, χ_M:

$$\chi_M = (1 + 0.071c_m)(1 - 1.833{c_m}^{\frac{1}{2}} + 1.608c_m) \tag{3.8}$$

Salt diffusivity, D (m^2 s^{-1}):

$$D = 1.003 \times 10^{-9} - (3.104 \times 10^{-10})c_m + (3.633 \times 10^{-11}){c_m}^2 \tag{3.9}$$

Concentration conversion:

$$c_e = 0.859c_m - 0.051{c_m}^2 \tag{3.10}$$

3.3.6 Modelling

To provisionally understand the impact of the differences in the electrolyte transport and thermodynamic properties on cell performance together with the different graphite OCV profiles, DFN[108,109] simulations of the charging behaviour of model K-ion and Li-ion graphite half-cells with KFSI and LiFSI:DME electrolytes were conducted. The four fundamental properties characterised in this chapter (D_e, t_+^0, κ and χ_M) are all of the electrolyte properties required for electrolyte DFN cell

modelling, therefore, this is the first time K-ion has been simulated using the DFN model. The cells were modelled using the battery modelling package PyBaMM[194] in combination with the empirical transport and thermodynamic property relationships of the KFSI and LiFSI:DME electrolytes characterised (Section 3.3.5). Since graphite is the negative electrode of choice for both Li-ion and K-ion[1,223,224] and is the limiting factor in realising fast charging in Li-ion batteries[223,225], the graphite half-cell was deemed the most appropriate comparison. 1 M electrolyte concentration was utilised for both chemistries. Full details of the model are described in the Experimental section.

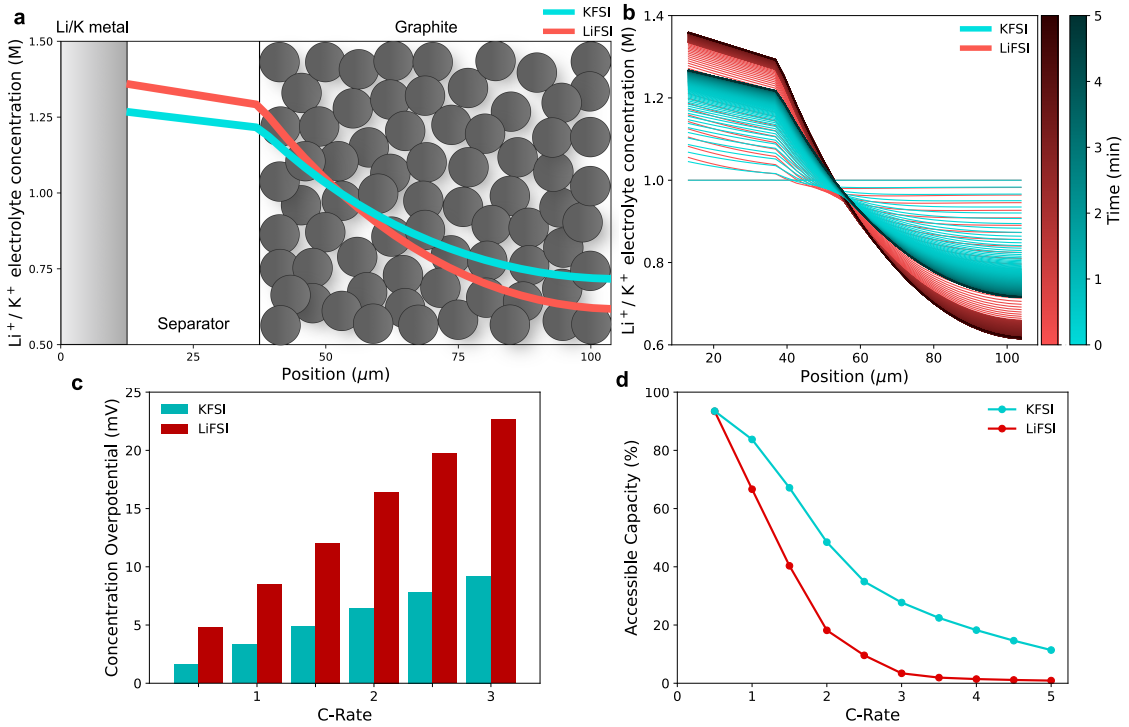


Figure 3.16 Doyle-Fuller-Newman (DFN) simulations. DFN simulations of K||graphite and Li||graphite cells during charge with 1M KFSI and LiFSI in DME electrolytes using the transport and thermodynamic property relationships characterised (Section 3.3.5). Modelled using PyBaMM[194] (**a**) Simulated metal||graphite cells after 5 min of 2C constant current charge (1C = 3.28 mA cm^{-2} for both) including Li^+/K^+ electrolyte concentration gradient. (**b**) Li^+/K^+ electrolyte concentration gradient over time during 2C charge (**c**) Concentration overpotentials for the metal||graphite cells with increasing C-rate (**d**) Accessible capacity for the metal||graphite cells with increasing C-rate. Reproduced from Dhir *et al.*[170]

Figure 3.16a depicts the graphite half-cells being modelled and shows the reduced electrolyte concentration gradient formation for the KFSI cell compared to the

LiFSI cell after 5 minutes of charging at 2C (1C = 3.28 mA cm^{-2} for both). The LiFSI cell reaches the lower cut-off voltage of 0.01 V very shortly after this due to overpotentials, below which Li metal plating would start to occur[225]. Figure 3.16b shows the concentration gradient formation over time at the same charging rate, again showing reduced electrolyte concentration gradient formation for the KFSI cell and demonstrating the clear advantages of the higher t_+^0 and D_e for the KFSI electrolyte. Figure 3.16c shows that the reduced concentration gradient formation results in lower concentration overpotentials (∼60% lower for the KFSI compared to the LiFSI cell at the charging rates 1–3C) again emphasising the importance of t_+^0 and D_e. Finally, Figure 3.16d illustrates the fast charging cell performance, demonstrating that the KFSI cell can achieve higher accessible capacities at higher charging rates (48% vs. 18% at 2C for the KFSI cell compared to the LiFSI cell, respectively), showing improved high-power capability for the KFSI cell. The Li-ion concentration overpotentials cause the LiFSI cell to reach the lower cut-off voltage, and hence the Li plating potential, faster than for the KFSI cell, limiting the accessible capacity. The KFSI cell can experience higher overpotentials due to the higher graphite intercalation potential of K^+ before reaching the cut-off voltage (Figure 1.6. Therefore, this improved accessible capacity for the KFSI cell is due to a combination of both faster transport and greater ability to experience overpotentials. From the reduced K^+ electrolyte concentration gradient formation in Figure 3.16a and 3.16b, the electrolyte K^+ concentration at the back of the graphite electrode near the current collector is considerably higher than that for Li^+, also enabling greater accessible K^+ for graphite intercalation and hence greater accessible capacity. Even at the high charging rate of 4C the KFSI cell can access 19% capacity whilst the LiFSI cell only 1%. The faster electrolyte transport properties, particularly t_+^0 and D_e, combined with the higher potential of K^+ intercalation into graphite[1,26], enables improved high-power charging performance of the K-ion chemistry compared to Li-ion.

Nevertheless, this is only a provisional indicative model to demonstrate the potential impact on cell performance of the faster K-ion electrolyte transport

properties and different intercalation potentials. Full cell high-power K-ion performance may only be achieved if a suitable electrolyte is developed which provides both a stable SEI for the graphite anode and stability at the high operating voltages of the leading cathodes[1]. Also a more accurate and sophisticated full cell model is needed, where advanced characterisation should be conducted of critical electrode material properties such as the solid-state diffusivities and exchange current densities.

3.4 Conclusion

In summary, the work of this chapter has fully characterised the ionic transport and thermodynamic properties of a K-ion electrolyte system for the first time and compared them to the Li-ion equivalent. A K metal preparation protocol was developed which enabled sufficient stability for electrolyte characterisation. The results show the salt diffusion coefficient and cation transference number of the KFSI:DME electrolyte is significantly higher than that of the LiFSI electrolyte for all concentrations below 2 m. Higher salt diffusion coefficients and cation transference numbers reduce ionic concentration gradient formation and the associated concentration overpotentials, thus substantiating the potential of KIBs to deliver improved rate capability and low-temperature performance based on this faster electrolyte transport with all else being equal. The ionic conductivities were found to be similar, with LiFSI slightly higher until $\sim$1.7 m, appearing due to inadequate KFSI salt dissociation. The thermodynamic factor behaviour with concentration appears to indicate weaker solvent and ion-ion interactions of K^+ compared to Li^+ again evidencing the advantages of K^+ for faster transport. DFN simulations of K-ion and Li-ion graphite half-cells, using the electrolyte property relationships characterised here and the OCV profiles, demonstrates superior charging rates for the K-ion cell due to the combination of faster K-ion electrolyte transport and the ability to experience larger overpotentials. Overall this study proves that the increased cation size and lower charge density of K^+, and thus weaker solvent and ion-ion interactions result in faster ion transport in K-ion

electrolytes, which is promising for faster charging all else being equal, however, further investigation of the electrode materials is required to understand whether full-cell K-ion fast charging is possible. Full characterisation of the K-ion electrolyte has provided a more accurate understanding of K-ion electrolyte mass transport and thermodynamics, laying the foundations for further K-ion electrolyte development and optimisation.

4

Characterising the Transport and Kinetic Properties of Potassium-ion Electrode Materials

Contents

4.1 Introduction 110
4.2 Experimental 112
4.3 Results and Discussion 115
4.3.1 Graphite Anode 115
4.3.2 Potassium Manganese Hexacyanoferrate Cathode 126
4.4 Conclusion 134

4.1 Introduction

A significant proportion of the work in this chapter was published in the following preprint article which is currently under review:

1. Dhir, S., Cattermull, J., Jagger, B., Schart, S., Olbrich, L., Zhao, J., Sada, K., Goodwin, A., Pasta, M. Characterisation and Modelling of Potassium-ion Batteries *Research Square* (*Preprint - Manuscript under review*)[171]

Building on the work of Chapter 3 where the critical electrolyte properties determining rate behaviour were characterised for a K-ion electrolyte. This chapter

now focuses on characterising the two critical electrode material properties which determine rate performance: the the solid state diffusivity, D_k, and the exchange current density, j_{k0}.

Accurate characterisation of D_k is particularly challenging as detailed in the Introduction Section 1.9.1. GITT has been shown to be more accurate than PITT particularly in multiphase systems as explained in Section 1.9.1[119,156,162]. Kang and Chueh recently conducted a systematic study of critical errors sources in GITT application for battery materials[119], as well as determining an optimised modified fitting method for more accurate determination of D_k (Kang-Chueh GITT detailed in Section 2.3.1). Important sources of error in conventional GITT include composition-dependent overpotentials during conventional pulse analysis, finite-size effects due to inappropriate pulse conditions or particle size, convolution of electrolyte transport limitation with D_k, or counter electrode overpotential contributions in two-electrode cells[119]. Utilising accurate Kang-Chueh GITT relaxation-only analysis, large particles and appropriate pulse conditions to minimise finite-size effects, low sample mass loading with high porosity to ensure that the potential relaxation profile is governed by D_k, and three-electrode cells, mitigate these key sources of error[119,120]. However, one of the most critical sources of uncertainty for both GITT and PITT applied to porous electrode materials is the determination of the electrochemically active surface area, S, or the diffusion length, L[119,120,155,158]. With an inverse-square relation, the resulting D is highly sensitive to this parameter (Equation 2.20). This ambiguity in S results in orders of magnitude difference in D_k alone. Therefore, the accuracy of D_k could be substantially improved with the design of a material with greater morphological homogeneity.

Characterising j_{k0} accurately is also difficult as detailed in the Introduction (Section 1.9.2) however, through linearising the Butler-Volmer equation and using EIS in three-electrode cells is able to provide a reasonable measure of j_{k0} (Section 2.3.4). Similar to D_k, one of the most significant uncertainties in determining j_{k0} is also S, though it is less sensitive than D_k with an inverse rather than an

inverse-square relation (Equation 2.29). Hence, again, improved homogeneous material would also improve the determination of j_{k0}.

Therefore, in this Chapter the effective solid-state diffusivities and exchange current densities of the leading K-ion electrode materials: the graphite anode and $K_2Mn[Fe(CN)_6]$ (KMF) cathode are characterised. Since both materials are multiphase the effective solid state diffusivity ($\widetilde{D_k}$) is characterised here (Section 1.9.1). To mitigate the critical source of uncertainty and error of S, for the determination of $\widetilde{D_k}$ and j_{k0}, a highly homogeneous and monodisperse KMF cathode material was synthesised enabling a considerably more accurate determination of S, while the active area of a commercial synthetic graphite is analysed. To determine $\widetilde{D_k}$ of these materials, the state-of-the-art Kang-Chueh GITT technique and analysis is applied to mitigate key sources of error from conventional GITT application[119,181]. j_{k0} is characterised for both materials for the first time using EIS. KFSI in triethylphosphate (TEP) was utilised as the electrolyte as it has achieved the most impressive K-ion full-cell performance[92] as to ensure the greastest possible electrolyte stability for the characterisation experiments.

4.2 Experimental

KMF synthesis

A highly crystalline, monodisperse sample of $K_2Mn[Fe(CN)_6]$ was synthesised to ensure accurate approximations could be made about surface area and diffusion length. The synthesis was a citrate-assisted co-precipication in aqueous media. $MnSO_4$ (Sigma-Aldrich, 0.5 mmol) was dissolved in an aqueous solution of potassium citrate (Sigma-Aldrich, 1 M, 50 mL). $K_4Fe(CN)_6$ (Sigma-Aldrich, 0.5 mmol) was dissolved in a separate aqueous solution of potassium citrate (Sigma-Aldrich, 1 M, 50 mL). These solutions were added simultaneously, dropwise (2 mL min^{-1}), to a stirring round bottom flask containing a 100 mL solution of 1 M potassium citrate at 20°C. The mixture was stirred for 24 h before the precipitate was isolated by centrifugation and washed with a 50:50 water/ethanol mixture in order to prevent

the solid dispersing. The solid was dried in air at 70°C overnight and then under vacuum at 70°C. The KMF material was synthesised by John Cattermull.

Synchrotron XRD

Synchrotron X-ray diffraction (XRD) measurements were performed on the I11 beamline of the Diamond Light Source operating with an X-ray wavelength of 0.824385 Å. The position-sensitive detector was used to collect diffraction patterns in capillary transmission geometry. All Rietveld refinements were carried out using the TOPAS-Academic software.[226]

SEM

Particles were dispersed in acetone and then mounted on an aluminium stub. These particles were imaged using a Zeiss Merlin scanning electron microscope (SEM) equipped with a field emission gun, operated at an accelerating voltage of 3 kV and a probe current of 100 pA. The particle size distribution was determined by measuring at least 100 particles from SEM images using Feret's mean diameter and Fiji ImageJ software.

Electrode preparation

The electrode loadings were low with high porosity to minimise any electrolyte transport limitations, and ensure solid D_k limitations. The graphite (SGP5, SEC Carbon) electrodes were composed of 92 wt.% active material and 8 wt.% Carboxymethyl cellulose (CMC) binder (Sigma Aldrich) using highly purified deionised water as the solvent. The KMF electrodes were prepared using the mass ratio 7:2:1 active material:carbon:binder using Super P carbon additive, polyvinylidene fluoride (PVDF) binder (Sigma Aldrich) and NMP solvent. The electrodes were cast onto carbon-coated aluminium current collector. All electrodes were dried first in air at room temperature for 24 h followed by vacuum drying at 100°C for 24 h. The graphite electrodes were not calendered to ensure as high a

porosity as possible. The KMF electrode was lightly calendered to ensure good electrical contact due to the low electronice conductivity of PBA materials[1].

Electrochemistry

Three-electrode EL ECC-Ref cells (EL-CELL) were utilised for all Kang-Chueh GITT, PITT and EIS experiments using a K metal reference electrode prepared using the K metal preparation protocol detailed in Chapter 3[170]. Glass microfiber separators were used (grade GF/F, Whatman). 2 m KFSI in TEP electrolyte was utilised for the Kang-Chueh GITT, PITT and EIS experiments. All Kang-Chueh GITT, PITT and EIS experiments were conducted in a Binder Oven at 20°C (± 0.3 K). CR2032 coin cells were assembled to assess electrochemical performance. Aluminium-coated bases were used for the KMF cells due to the high operational voltages and steel cell parts for the graphite cells (MTI).

All electrochemical tests were carried out using a battery cycler (VMP3, Biologic). Electrochemical impedance spectroscopy (EIS) measurements were performed using a frequency response analyser (VMP3, Biologic), over the frequency range of 200 kHz–100 mHz (6 measurement points per decade) with an applied single sine potentiostatic signal of amplitude 10 mV.

Exchange current density

All EIS experiments were conducted in three-electrode ECC-Ref EL-cells to isolate the impedance and R_{ct} of the working electrode. The cells were cycled once before conducting the EIS measurements over stoichiometry on the second cycle. EIS analysis was conducted using impedance.py[227] and the Kramers-Kronig analysis was conducted using the using the Lin-KK method from impedance.py[227].

Kang-Chueh GITT

All Kang-Chueh GITT experiments were conducted in three-electrode ECC-Ref EL-cells using a K metal reference electrode prepared using the K metal preparation protocol detailed in Chapter 3[170]. Kang-Chueh GITT experiments were conducted

after one formation cycle at C/20. The Kang-Chueh GITT experiments were performed using C/20 15 min pulses and 2 h relaxations with application of current between to obtain a high-resolution OCV profile. The Kang-Chueh GITT pulse duration was selected to minimise finite-size effects[119,181]. At least two cells were utilised to determine the error. The OCV profile was determined from the Nernst potential points at the end of each relaxation step[119,153,181]. The Kang-Chueh GITT analysis uses relaxation-only analysis to avoid any overpotential errors according to Equation (2.20)[119,181].

PITT

The long-time PITT experiments were performed in three-electrode ECC-Ref EL-cells. The PITT experiments were conducted using 5 - 20mV steps.

4.3 Results and Discussion

4.3.1 Graphite Anode

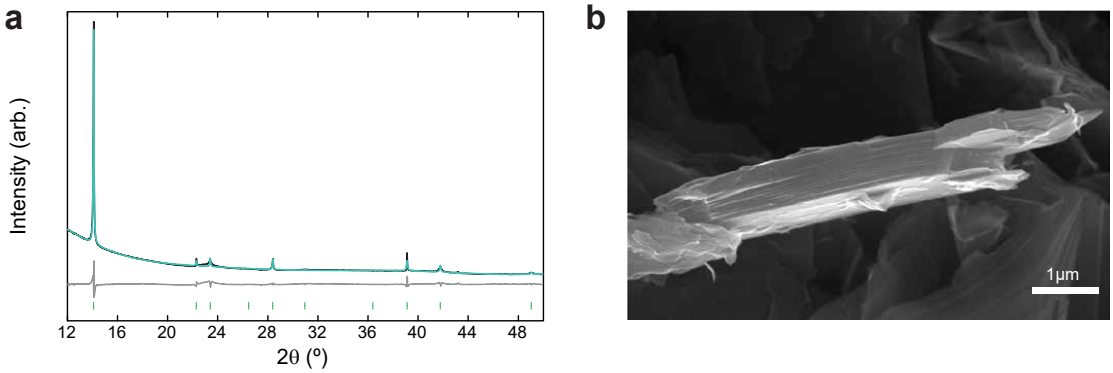


Figure 4.1 Graphite Sychrotron XRD and SEM (**a**) Pawley refinement of graphite synchrotron XRD pattern (data in black, fit in teal, data-fit difference in grey, and reflection positions below in green) (**b**) SEM image of a single graphite particle. Adapted from Dhir *et al.*[171]

High-crystallinity synthetic graphite exhibits superior capacity retention to low-crystallinity graphite in K-ion cells[228]. Therefore, a commercial, highly crystalline, synthetic graphite was utilised (SGP5, SEC Carbon). A larger particle size was utilised to minimise finite-size effects in the Kang-Chueh GITT

measurements[119]. Pawley refinement of synchrotron X-ray diffraction (XRD) data confirms the highly crystalline, phase-pure nature of the synthetic graphite (Figure 4.1a). Graphite particles comprise of highly oriented layers, shown in a single graphite particle in the the SEM image Figure 4.1b, where the basal planes are parallel to the graphene layer while the edge planes expose the end faces of the graphene layers[70]. Intercalation of K^+ into graphite is similar to Li^+ and only occurs through these edge planes where graphene layers are exposed as shown clearly in Figure 4.1b, with the diffusion process advancing into the particle centre along the basal plane[70,229–231]. Therefore, the electrochemically active area S, where intercalation occurs, of the graphite particles is only this edge area (Figure 4.1b). Figures 4.2a and b show other SEM images of the graphite particles in powder and in a cast electrode, respectively, showing the flake-like morphology expected. The graphite average particle size and thickness distributions from SEM analysis is shown in Figure 4.2c and d, with an average graphite particle size of 5.28 µm and thickness of 0.17 µm, respectively.

Adsorption methods such as Brunauer-Emmett-Teller (BET) are most commonly used to characterise S. Though this adsorption area correlates with electrochemically active area[232] it is highly uncertain to map between them[119]. It is also unclear whether the very fine pores measured by BET are wetted by the electrolyte[182]. BET is particularly unsuitable for determining S of graphite as it would include the large area of inactive basal plane regions of the graphite particles. Based on the active edge area and the SEM average particle size and thickness geometric analysis, the graphite particles were approximated as discs (Figure 4.3) with S determined from this disc edge geometric shaded area through which K^+ intercalation occurs. Levi *et al.* and Yang *et al.* also accounted for this edge intercalation area in graphite in their determination of Li graphite $\widetilde{D_k}$[229,230]. The graphite reversible capacity is close to the theoretical capacity (260 vs. 279 mA h g^{-1}, respectively, shown in Figure 4.4), this indicates there is very little inactive material of the cast graphite electrode, supporting this method of S estimation. However, it is important to note a source of error with this approximation of this edge area of a disc neglects any roughness

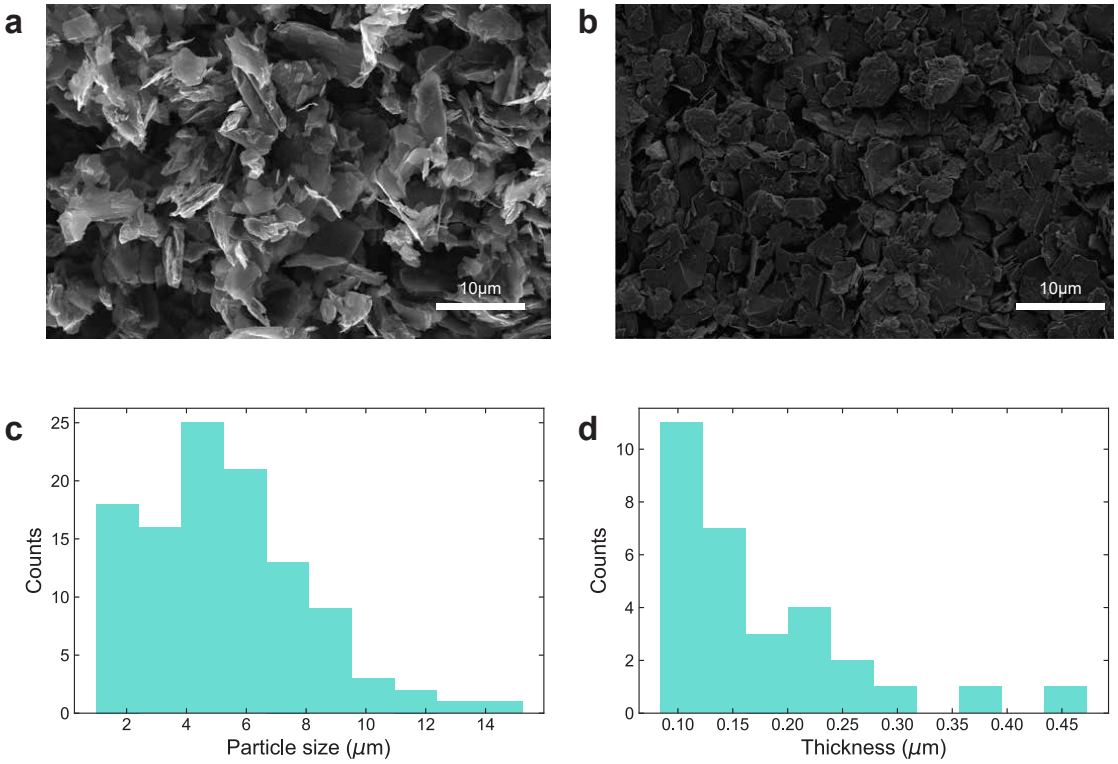


Figure 4.2 Graphite SEM particle size analysis **(a)** Pristine graphite **(b)** Cast graphite electrode (**c**) Graphite particle size distribution (**d**) Graphite particle thickness distribution. Adapted from Dhir *et al.*[171]

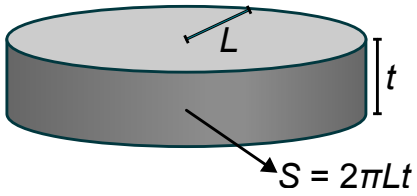


Figure 4.3 Disc used to model graphite particles. Shaded edge area represents the active area for intercalation. Adapted from Dhir *et al.*[171]

which will be present at the particle edges, thus somewhat underestimating the area.

Figure 4.5a shows the OCV profile of the graphite and Figure 4.5b shows the effective $\widetilde{D}_g$ results over stoichiometry from the Kang-Chueh GITT and determined S (example raw GITT data is shown in Figure 4.6). The median $\widetilde{D}_g$ from both potassiation and depotassiation is 2.32×10^{-13} cm^2 s^{-1}. This appears to be two to three orders of magnitude lower than the values reported for Li^+ in graphite[111,113,229],

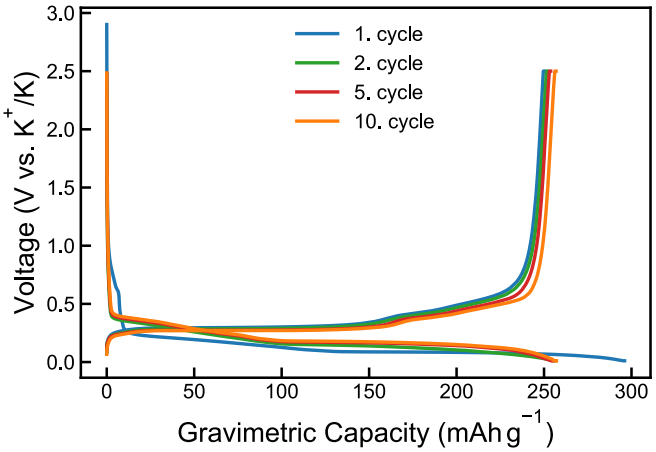


Figure 4.4 Galvanostatic cycling at C/20 of K|graphite half-cell with 2 m KFSI TEP electrolyte at 30°C. Adapted from Dhir *et al.*[171]

suggesting slower diffusion for K^+ in graphite. However, the Li^+ $\widetilde{D}_g$ should also be measured using the Kang-Chueh GITT for a more meaningful comparison.

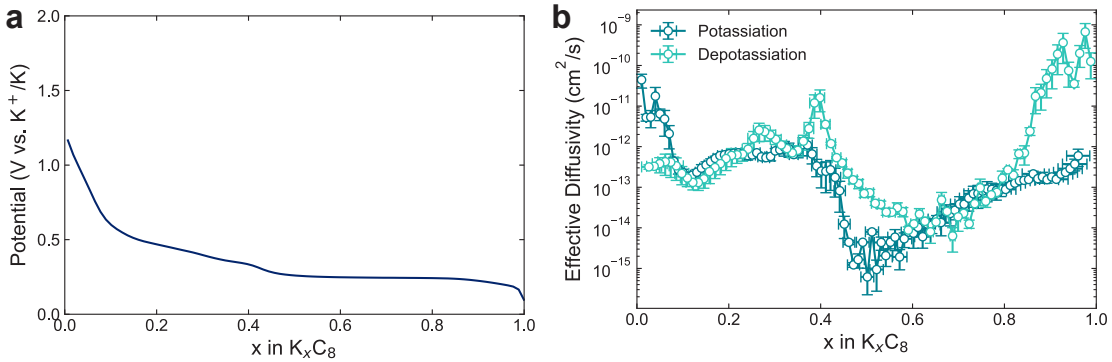


Figure 4.5 Graphite Kang-Chueh GITT results at 20°C (**a**) Example OCV profile during depotassiation (**b**) Effective diffusivity over composition. Error bars depict the standard error in the mean. Adapted from Dhir *et al.*[171]

Studies have shown using operando XRD and Raman[215,233] that K^+ intercalation into graphite progresses through several two-phase transformations and Onuma et al. proposed the staging evolution in Eq. (4.1)[233]:

$$\text{Graphite} \rightarrow \underset{\text{Graphite–KC}_{96}}{\text{Disorderly stacked high stage}} \rightarrow \underset{\text{KC}_{96}\text{–KC}_{24}}{\text{Stage 4L–3L}} \rightarrow \underset{\text{KC}_{28}\text{–KC}_{24}}{\text{Stage 2L}} \rightarrow \underset{\text{KC}_8}{\text{Stage 1}} \tag{4.1}$$

Stages 4L, 3L and 2L exhibit "liquid-like" in-plane potassium distributions and Daumas-Hérold defects are generated during the phase transformations. The

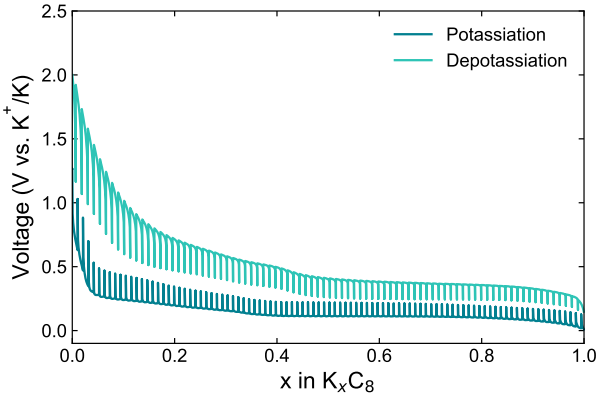


Figure 4.6 Example raw Graphite Kang-Chueh GITT data at 20°C

phases therefore have variable compositions and a high concentration of defects, causing their potentials to change during intercalation and explaining the lack of clear plateaus in Figure 4.5a for $x < 0.4$. In contrast, stage 1 forms with a fixed composition through the complete filling of the graphene layers with potassium, eliminating Daumas-Hérold defects and resulting in a constant potential, as evident by the flat voltage plateau for $x \sim 0.4$ to 0.8 in Figure 4.5a as KC_8 forms. This appears to coincide with a two to three orders of magnitude drop in the effective $\widetilde{D}_g$ between $x \sim 0.4$ to 0.8 (Figure 4.5b). However, caution should be exercised in analysing regions where $\frac{\partial V_{eq}}{\partial x}$ approaches zero (Figure. 4.5a), which in turn leads to $\widetilde{D_k} \sim$ zero (Equation 2.20), which is not physical[158].

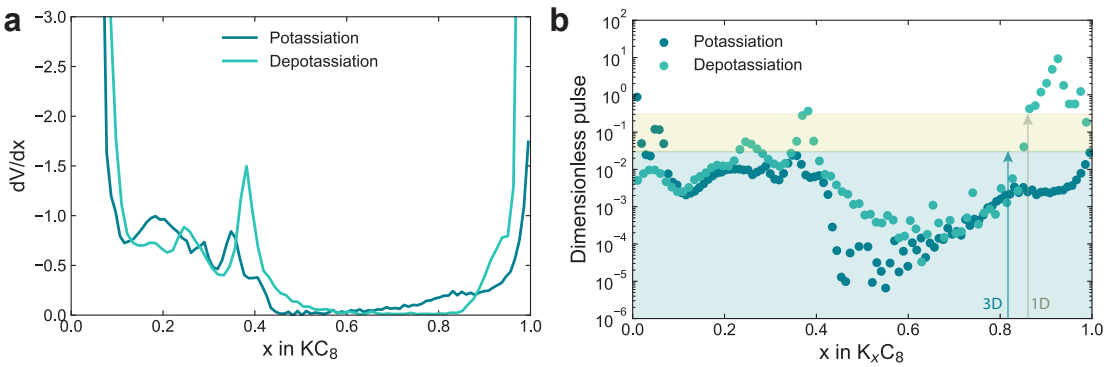


Figure 4.7 (**a**) Example Kang-Chueh GITT graphite derivative of the Nernst potential ($\frac{\partial V_{eq}}{\partial x}$) over stoichiometry at 20°C (**b**) Example dimensionless pulse $\hat{\tau}$ for graphite electrode over stoichiometry from Kang-Chueh GITT in three-electrode cell at 20°C. Coloured region indicates the ideal valid range for the semi-infinite assumption in planar (1D) and spherical (3D) geometries. Adapted from Dhir *et al.*[171]

Onuma et al. further observed hysteresis between the intercalation and deintercalation processes, with a stage 2 (KC_{16}) structure able to form from KC_8 initially before Daumas-Hérold defects are again necessary for further deintercalation[233]. These differences may explain the directional difference in $\widetilde{D}_g$ profile during potassiation and depotassiation, particularly since composition-dependent overpotentials are avoided here through relaxation-only Kang-Chueh GITT analysis[119]. However, autocatalysis effects may also contribute to direction-dependencies therefore, it is advisable to refrain from assigning excessive physical meaning to the direction-dependency[119].

Moreover $\widetilde{D}_g$ appears to be significantly greater at low x during potassiation and at high x during depotassiation, which is not expected physically. Both of these inflated regions correspond to the first few pulses after switching the current direction, which may be caused by SEI formation. Although the GITT measurements were performed with the current leading K-ion electrolyte (KFSI:TEP), continuous SEI formation is still a common issue, even after numerous cycles[92,93]. A recent study further evidences that the SEI is partially soluble[234] and its composition can change dynamically during cycling[31,235]. Therefore, there may be a restructuring of the SEI that takes place when the direction of the current pulse is changed, consuming capacity until a sufficiently passivating structure is formed. This is supported by evidence that the SEI composition on graphite in K-ion cells changes considerably between charge and discharge[217]. The necessarily short current pulses applied here mean that this may influence the $\widetilde{D}_g$ results over several pulses. We therefore believe the potassiation data to give a more reliable $\widetilde{D}_g$ for $x \sim 1$, and depotassiation for $x \sim 0$. This also affects the determination of the composition x due to capacity contributions from SEI formation. However, it is not possible to know exactly SEI formation is occuring, therefore it is assumed that the decomposition is spread evenly over the composition in the determination of x.

An alternative hypothesis however, is that as the inflated $\widetilde{D}_g$ correspond to the first pulses after changing current direction, that not enough time had been given for the cell to equilibrate before changing direction and therefore, there is

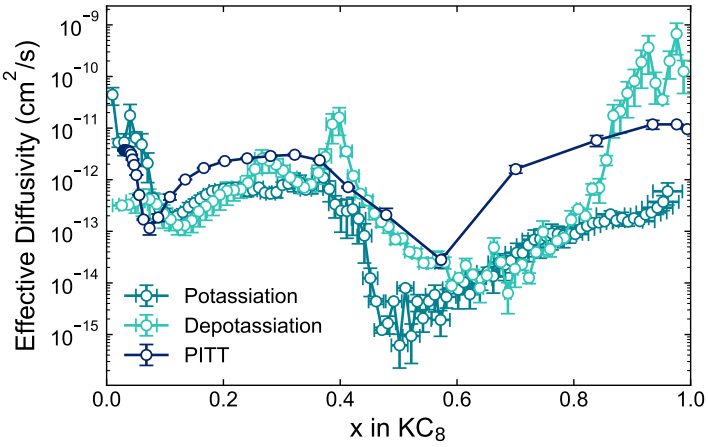


Figure 4.8 Long-time PITT during potassiation compared to Kang-Chueh GITT effective diffusivity during depotassiation and potassiation (GITT labelled depotassiation and potassiation) for graphite at 20°C. Adapted from Dhir *et al.*[171]

still a residual concentration gradient which with the change of current direction facilitates the potential decay making the apparent $\widetilde{D}_{\mathrm{g}}$ appear higher. Based on the average particle size and the median diffusivity, the time constant is in the order of 80 hours for the graphite whereas the cell was only left for an hour to equilibrate before changing current direction. Therefore, it appears that the cells were not left to rest for long enough which causes the inflated $\widetilde{D}_{\mathrm{g}}$ for the initial current pulses upon changing direction.

The impact of finite-size effects on the modifed GITT $\widetilde{D}_{\mathrm{g}}$ can be assessed through evaluating the dimensionless pulse time ($\hat{\tau} = \widetilde{D}\tau/L^2$)[119]. Figure 4.7b shows both the dimensionless pulse time for the majority of the graphite GITT data is within the ideal valid semi-infinite region for 3D geometries, minimising finite-size effects[119,181]. Diffusion in graphite particles can also be considered 2D along the graphene planes, providing further mitigation against finite-size effects.

For an additional characterisation and comparison PITT during potassiation was also utilised to characterise $\widetilde{D}_{\mathrm{g}}$. For the long-time PITT analysis, which is less susceptible to short-term reaction kinetic overpotential errors, the diffusion length term, L is required. To determine the graphite L (L_g), again from the approximated disc geometry (Figure 4.3), L_g was taken to be the the disc radius using the average particle size (Figure 4.2c). Figure 4.8 shows the $\widetilde{D}_{\mathrm{g}}$ evaluated using PITT agrees

reasonably well with the Kang-Chueh GITT results. There is also a drop in $\widetilde{D}_{\mathrm{g}}$ during the flat potential plateau from $x \sim 0.4$ to 0.8, though not as significant as for GITT. However, PITT cannot obtain the high resolution composition dependence possible using GITT in the potential plateau two-phase regions which is one of the major limitations of PITT, that an insufficiently small potential step can be applied in order to produce a measurable current response, and therefore, the composition change can be large during a single potential step[156,162]. Markevich et al also showed in a comparison of GITT vs PITT that PITT was less accurate as it is more susceptible to parasitic current contribution than GITT[162], also finding the PITT D_k results were overestimated and particularly the D_k minima were shallower than those for GITT matching the findings for $\widetilde{D}_{\mathrm{g}}$ values for PITT here. They concluded GITT is superior particularly when phase transitions are involved[156,162] as in this case. Also the long-time PITT is derived for planar geometry and is occuring out of a region where the semi-infinite assumption is valid, therefore, there is more geometric error compared to the GITT semi-infinite analysis. Since there can also be no zero-current current response transient in PITT the current-related overpotential errors are inherent therefore, the Kang-Chueh GITT method has a significant advantage with the relaxation-only analysis mitigating any overpotential error[119]. Therefore, given all these advantages of the GITT method the Kang-Chueh GITT results are taken as more accurate.

Three other studies have attempted to characterise $\widetilde{D}_{\mathrm{g}}$ for similar materials to K graphite using conventional GITT[214,215,236]. Though all studies are limited by some of the previously described limitations with conventional GITT and are not analogous. One measured the D_k of the DEGDME K^+ cointercalation complex in graphite[214] which is not comparable. Another study characterised the D_k of K^+ in graphite foam[215] which is a different material. Finally, another measures D_k of K^+ in a recycled LIB graphite anode treated by pyrolysis[236] so again is not directly comparable. However, all studies show the similar qualitative drop in $\widetilde{D}_{\mathrm{g}}$ in the large Stage 2-1 two-phase region.

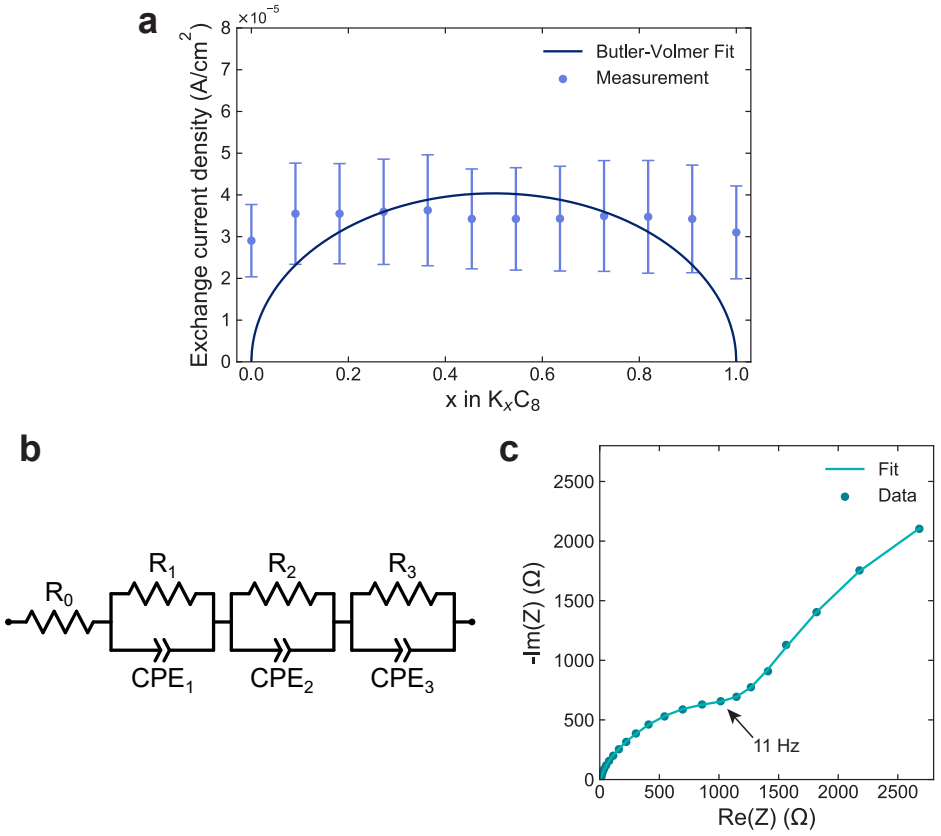


Figure 4.9 Graphite exchange current density characterisation in 2m KFSI TEP at 20°C (**a**) Exchange current density over composition. Error bars depict the standard error in the mean. (**b**) Equivalent circuit used to fit graphite impedance data (**c**) Example K graphite impedance spectra in three-electrode cell > 0.5 Hz. Adapted from Dhir *et al.*[171]

Figure 4.9a shows $j_{0,g}$ of the graphite over stoichiometry in 2 m KFSI in triethyl phosphate (TEP) electrolyte fitted to the Butler-Volmer equation (Equation 1.15). The mean $j_{0,g}$ over the composition is 3.42×10^{-5} A cm^{-2}. $j_{0,g}$ is similar to that found for Li graphite[111,164] indicating similar charge-transfer reaction kinetics between Li^+ and K^+ and graphite. A critical challenge with accurately determining R_{ct} from EIS is the fact that constantly evolving SEI and passivation layer formation occur at similar frequency ranges to charge transfer[237]. The equivalent circuit used to determine R_{ct} and an example impedance spectra for K graphite is shown in Figures 4.9b and c, respectively. R_{ct} was represented by R2 in the equivalent circuit, with R1 representing the SEI due to evidence that SEI impedance has a higher characteristic frequency than R_{ct}[238,239] and due to evidence that the impedance from SEI formation is significantly larger than for charge transfer[240] as is the case here (Table A.1).

Figure 4.10a shows that the model describes the data well as the EIS residuals are low and randomly distributed in the frequency range relevant for charge transfer. The higher percentage residuals at higher frequencies are likely due to the small magnitude of the impedance at these frequencies and may be due to the limited instrument resolution or noise effects. The absolute residuals plotted in Figure 4.10b show that the residuals at these high frequencies are small and unlikely to be of concern. The data also satisfies the Kramers-Kronig relations with exceptionally low residuals as shown in Figure 4.10c, indicating the stability, causality and linearity requirements for conventional EIS are reasonable assumptions for the data. Even though x errors between experiments were negligible it is important to recognise that it is not possible to measure the EIS at 100% potassiation. Since EIS requires a small perturbation, at a fully potassiated state this would lead to K plating and thus not being able to measure the actual $j_{0,\mathrm{g}}$ at $x = 1$. The same is true in reverse for $x = 0$ where no more K can be removed, thus there is inherent error in the x values at these points.

From the Butler-Volmer fit (Equation (1.15)) the reference current for the reaction $k_{0,\mathrm{g}}$ is 8.07×10^{-5} A cm^{-2}. The poor Butler-Volmer fit for the graphite $j_{0,\mathrm{g}}$ matches the findings of Ecker et al. and Schmalstieg et al. for Li graphite[111,241], though O'Regan achieved a good fit for Li graphite[164]. These results indicate that the SEI interferes with the impedance measurements for the graphite anode. Overlapping time constants for SEI formation and charge-transfer at the graphite anode may make it difficult to correctly isolate R_{ct} and thus very accurately determine $j_{0,\mathrm{g}}$, however, this provides a reasonable order of magnitude for $j_{0,\mathrm{g}}$, as required for the model.

Three-electrode cells were utilised for the EIS measurements which is critical to isolate the impedance of the working electrode from the counter electrode. However, many three-electrode cells using point-like references electrodes suffer from measurement artifacts during EIS due to the electrochemical and geometric asymmetry effects[242]. Ideally the reference electrode should be a mesh reference electrode to minimise these artifacts[242], though this can also block ionic current

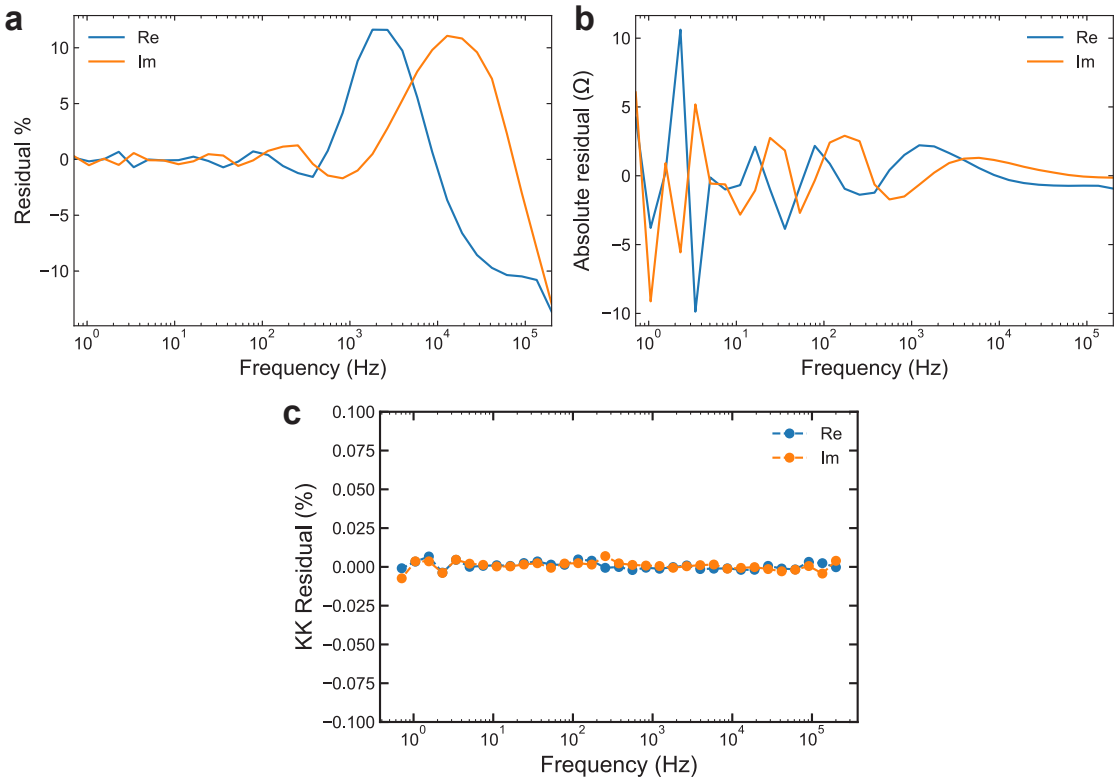


Figure 4.10 Graphite EIS residual analysis (**a**) Percentage residuals between example graphite EIS model and data (**b**) Absolute residuals between example graphite EIS model and data (**c**) Kramers-Kronig residuals from example graphite EIS spectra

flow between the electrodes[243]. However, a mesh reference is almost impossible to create with K metal due to the softness and stickiness of K. Therefore, a K metal needle reference electrode in the EL ECC-Ref cell was utilised prepared using the K metal preparation protocol described in Chapter 3 however, needle reference electrodes have been shown to be susceptible to these asymmetry issues[242]. Thus this is another source of error with the EIS and j_0 results obtained. In addition, though the K metal stability was improved using our K preparation protocol[170], K metal is still not completely stable and is not an ideal reference electrode. Therefore, the development of a truly stable, reliable reference electrode is critical to improve the accuracy of not only the EIS, but also the three-electrode GITT and PITT experiments further[1].

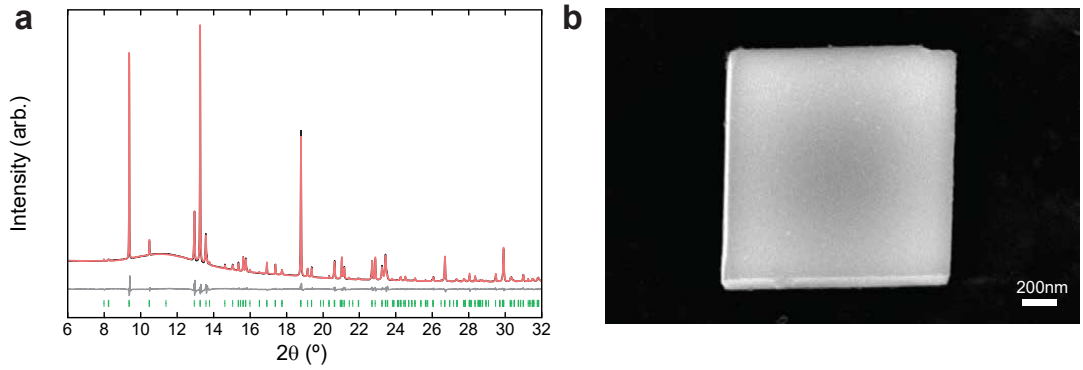


Figure 4.11 (**a**) Rietveld refinement of KMF synchrotron XRD pattern (data in black, fit in peach, data-fit difference in grey, and reflection positions below in green) (**b**) SEM image of a single KMF particle. Adapted from Dhir *et al.*[171]

4.3.2 Potassium Manganese Hexacyanoferrate Cathode

Figures 4.11a and b show the large, highly-crystalline, non-agglomerated and cuboid KMF material—synthesised via a citrate-assisted co-precipitation. Figures 4.12a and b show further SEM images in powder and cast electrode, respectively, demonstrating the material is homogeneous and non-agglomerated. Synchrotron XRD measurement of the KMF sample confirmed that the high degree of crystallinity achieved through more traditional synthesis had been retained (Figure 4.11a). Further, Rietveld refinement revealed that a near identical structure and high potassium concentration (1.871(3) per formula unit) compared to previous studies was produced[38,171,244]. Elemental analysis by inductively coupled plasma mass spectrometry (ICP-MS) also indicated a low-vacancy/high potassium content with a Fe:Mn ratio of 0.98(5), giving a chemical formula of $K_{1.871(3)}Mn[Fe(CN)_6]_{0.98(5)}$. The material was synthesised to have as large particles as possible while maintaining performance to minimise finite-size effects and ensure D_k limitation in the Kang-Chueh GITT measurements. From SEM analysis the average KMF particle size was identified as 1.02 µm (Figure 4.11c), significantly larger than other KMF materials synthesised[38,92].

There has been a historical mischaracterisation of $\widetilde{D_k}$ for Prussian blue analogue (PBA) materials, with many studies characterising in the order of 10^{-8} to $10^{-11}\,cm^2\,s^{-1}$,[155]. This is due to several sources of error. First, as PBAs are frequently synthesised as agglomerated nanoparticles, the active surface area (S)

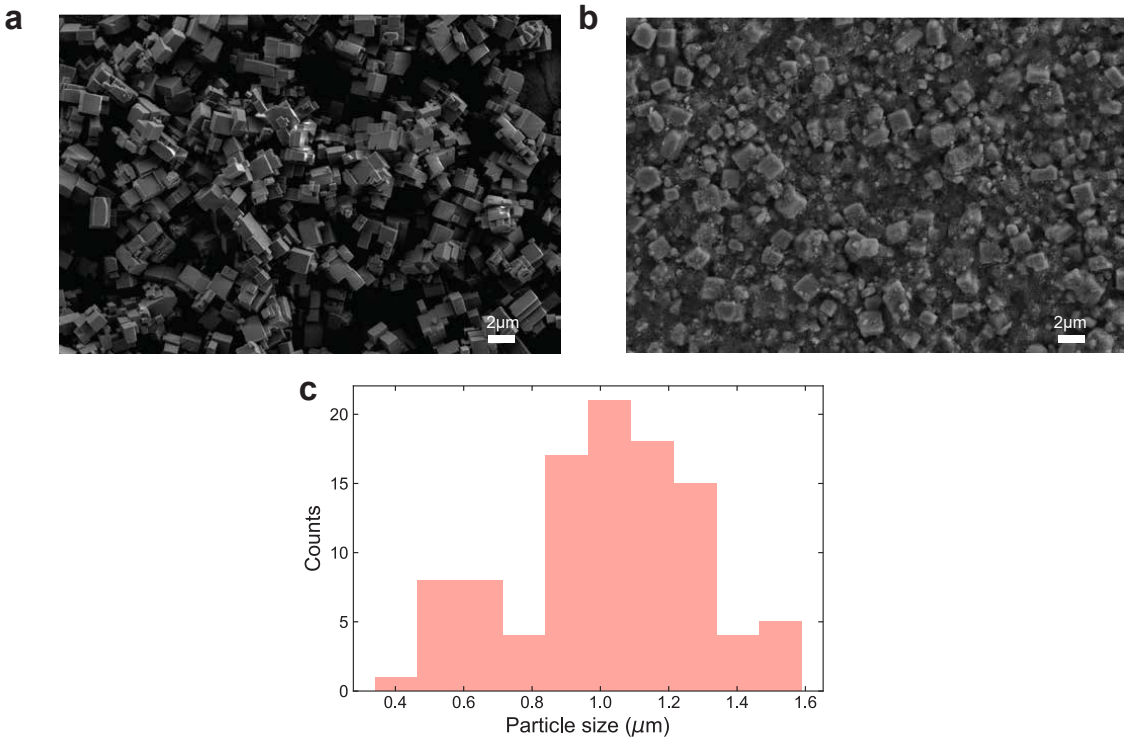


Figure 4.12 KMF SEM particle size analysis **(a)** Pristine KMF **(b)** Cast KMF electrode (**c**) KMF particle size distribution. Adapted from Dhir *et al.*[171]

or diffusion length (L) ($L \propto \frac{nV_m}{S}$ for a cube, where n is the number of moles) is often mischaracterised based on the agglomerate rather than the primary particle size (or for electrodeposited PBA films the film thickness rather than the individual nanoparticle size) resulting in significant overestimates of $\widetilde{D_k}$ since $\widetilde{D_k}$ is inversely proportional to S^2 or proportional to L^{2},[155]. Inhomogeneous material, poor morphological characterisation and poor diffusivity analysis has also led to mischaracterisation[155]. However, recently Komayko et al. conducted a detailed analysis of several PBA materials[155] using PITT analysis and improved characterisation of the materials, finding $\widetilde{D_k}$ of various PBA materials assessed was in fact around four orders of magnitude lower than conventionally measured and of the order 10^{-12} to $10^{-15}\,\mathrm{cm^2\,s^{-1}}$,[155]. However, they did not characterise $\widetilde{D_k}$ for the KMF material.

The highly uniform morphology and lack of agglomeration of the KMF synthesised here enables significantly increased accuracy in the determination of the active surface area S, which has been a significant source of error in the

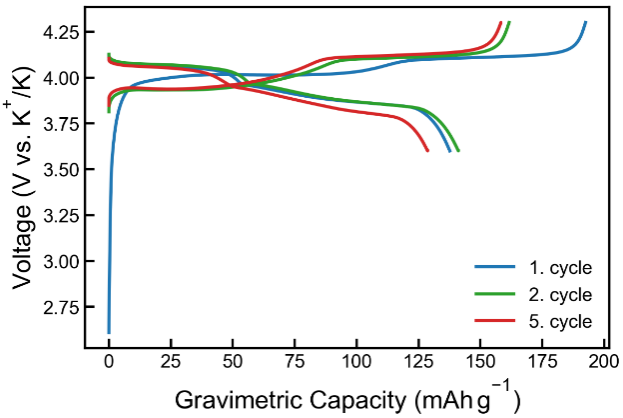


Figure 4.13 Galvanostatic cycling at C/20 of K|KMF half-cell with 2 m KFSI TEP electrolyte at 30°C. Reproduced from Dhir *et al.*[171]

determination of $\widetilde{D_k}$ in the past[155]. Due to this morphological homogeneity, and the cubic crystal structure of PBAs enabling K^+ insertion through all exposed facets[245], the geometric surface area of the KMF particle is a good measure of S. Given the reversible capacity is very close to the theoretical capacity (141 vs. 155 mA h g^{-1}) (Figure 4.13), this indicates there is very little inactive region of the cast KMF electrode, supporting our method of estimation of S.

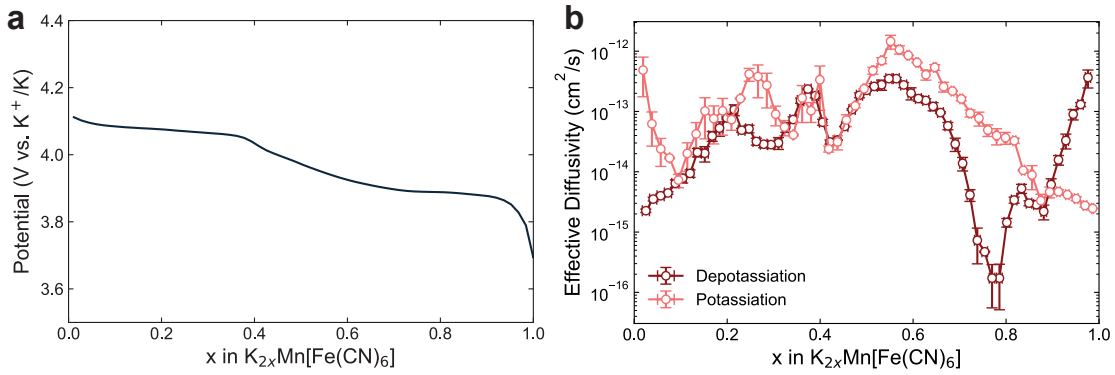


Figure 4.14 KMF Kang-Chueh GITT results at 20°C (**a**) Example OCV profile during depotassiation (**b**) Effective diffusivity over composition. Error bars depict the standard error in the mean. Adapted from Dhir *et al.*[171]

The OCV profile in Figure 4.14a shows the two well-defined plateaus, which are characteristic of the low-vacancy KMF. Multiphase behaviour in PBA cathodes is a consequence of maximising the theoretical capacity by reducing the vacancy content,

which induces highly correlated distortions in the structure[245]. From previous in-situ XRD studies it is understood that there is three dominant phases; the Jahn-Teller distorted ($x = 0$) and slide distorted ($x = 1$) phases with an apparently undistorted phase at the intermediate $x = 0.5$ composition[36]. The results from the Kang-Chueh GITT experiment are rationalised in this context. The results from the Kang-Chueh GITT (Figure 4.14b), show a median $\widetilde{D}_{\mathrm{KMF}}$ from both potassiation and depotassiation of 5.50×10^{-14} cm^2 s^{-1}, therefore, $\widetilde{D}_{\mathrm{KMF}}$ is $\sim$ four times lower than the $\widetilde{D}_{\mathrm{g}}$, indicating slower K^+ transport in the KMF. The drops in $\widetilde{D}_{\mathrm{KMF}}$ appear to align with the two plateaus between $x \sim 0.95$ to 0.75 and $x \sim 0.4$ to 0.1, the former of which corresponds to an apparent drop of three to four orders of magnitude in the effective $\widetilde{D}_{\mathrm{KMF}}$. However, again it is important to exercise caution in analysing regions where $\frac{\partial V_{eq}}{\partial x}$ approaches zero (Figure 4.15a), and without reliable quantification of the phase behaviour from in-situ structural techniques one cannot comment further on this result. An example raw GITT data is shown in Figure 4.16).

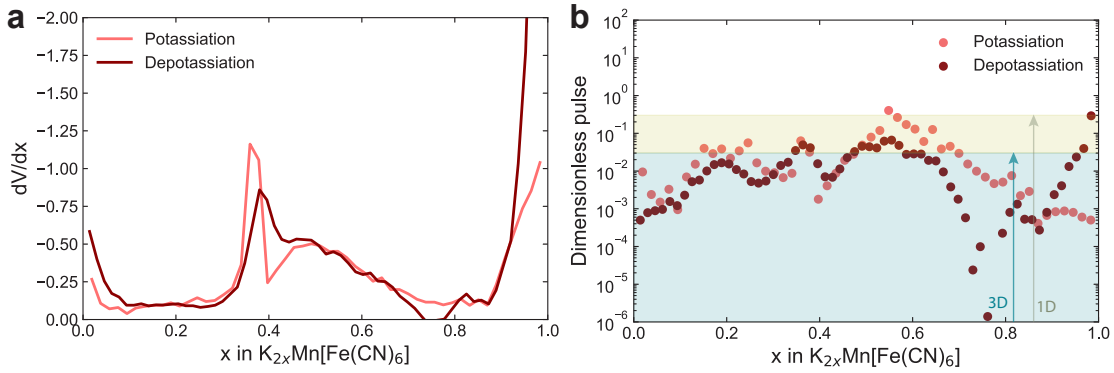


Figure 4.15 a Example Kang-Chueh GITT KMF derivative of the Nernst potential ($\frac{\partial V_{eq}}{\partial x}$) over stoichiometry at 20°C **b** Example dimensionless pulse $\hat{\tau}$ for KMF electrode over stoichiometry from Kang-Chueh GITT in three-electrode cell at 20°C. Coloured region indicates the ideal valid range for the semi-infinite assumption in planar (1D) and spherical (3D) geometries. Adapted from Dhir *et al.*[171]

The $\widetilde{D}_{\mathrm{KMF}}$ results obtained here are within the lower range identified by Komayko *et al.* for other PBA materials evaluated with improved materials and analysis[155], thus supporting the accuracy of the $\widetilde{D}_{\mathrm{KMF}}$ results ascertained here. Moreover, the PBA particle homogeneity, lack of agglomeration and monodisperse nature of

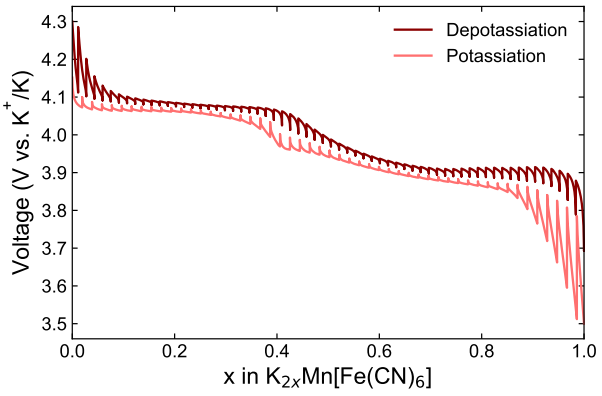


Figure 4.16 Example raw KMF Kang-Chueh GITT data at 20°C.

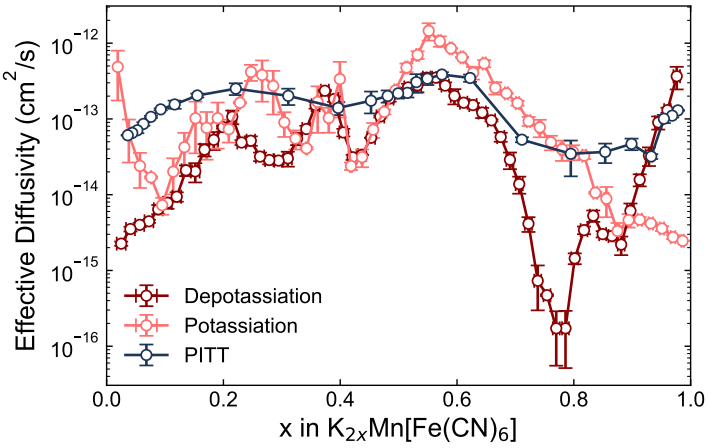


Figure 4.17 Long-time PITT during depotassiation compared to Kang-Chueh GITT effective diffusivity during depotassiation and potassiation for KMF (GITT labelled depotassiation and potassiation). Adapted from Dhir *et al.*[171]

the KMF synthesised here is a further improvement to that achieved in the study by Komayko et al., further strengthening the assessments of S and hence D_{PBA}. Using the Kang-Chueh GITT relaxation analysis also avoids the current-related overpotential errors from PITT analysis in their study[119,155]. Authors He and Nazar found that the KMF analogue $K_2Fe[Fe(CN)_6]$ (KFF) displayed notably inferior rate capability to its sodium equivalent when their crystallites are micron-sized[55]. This suggests that K^+ diffusion is slower for K-PBA materials compared with Na equivalents.

Similar to the graphite case, $\widetilde{D}_{\mathrm{KMF}}$ appears to also be enhanced for the first few pulses after the direction of the current pulse is changed, which could also

indicate regions where cathode electrolyte interphase (CEI) formation is influencing the results. Therefore again it appears that the the potassiation data provides a more reliable $\widetilde{D}_{\mathrm{PBA}}$ for $x \sim 1$, and depotassiation for $x \sim 0$. Given this and the evidently poor coulombic efficiency for the KMF shown in Figure 4.13, it is again important to note that the determination of the stoichiometry may also be affected, as electrolyte decomposition contributes to capacity. It is impossible to know when the most decomposition is occuring, therefore, it is again assumed that the decomposition is spread evenly across the composition in the determination of x. This yet again emphasises the requirement for more stable K-ion electrolytes. However, again similar to the graphite case from the time constant for the KMF particle based on its average size and median diffusivity, the time constant is in the order of 10 hours so again the 1 hour rest was not enough to allow full equilibration. Therefore, this also may explain the enhanced $\widetilde{D}_{\mathrm{KMF}}$ values in the first initial pulses after change of current direction. Figure 4.15b assesses the dimensionless pulse time for the KMF, also showing the majority of data is within or close to the ideal valid semi-infinite region for 3D geometries, again minimising finite-size effects[119,181]. The range of data within this region is considerably larger than that for many Li cathode materials reported[119].

Again long-time PITT during depotassiation was also conducted for the KMF material. L_{KMF} was determined from the average particle size (Figure 4.12c) and cuboid geometry, with an equivalent volume sphere modelled with L_{KMF} being its radius. Figure 4.17 shows the PITT $\widetilde{D}_{\mathrm{KMF}}$ results showing they match the Kang-Chueh GITT results in general trend and average magnitude quite well. Again the minima are more shallow from the PITT results compared to the Kang-Chueh GITT results as was the case for graphite and matching the findings of Markevich *et al*[162]. However, again the PITT depicts significantly less compositional resolution compared to the Kang-Chueh GITT for the multiphase material. The drop in $\widetilde{D}_{\mathrm{KMF}}$ during the two-phase slide-distorted and undistorted region between $x \sim 0.95$ to 0.75 is captured by PITT however, the two-phase undistorted and Jahn-Teller distorted region between $x \sim 0.4$ to 0.1 is not. Again, due to the inherent limitations

with PITT compared to GITT described previously, the Kang-Chueh GITT results are taken as more accurate.

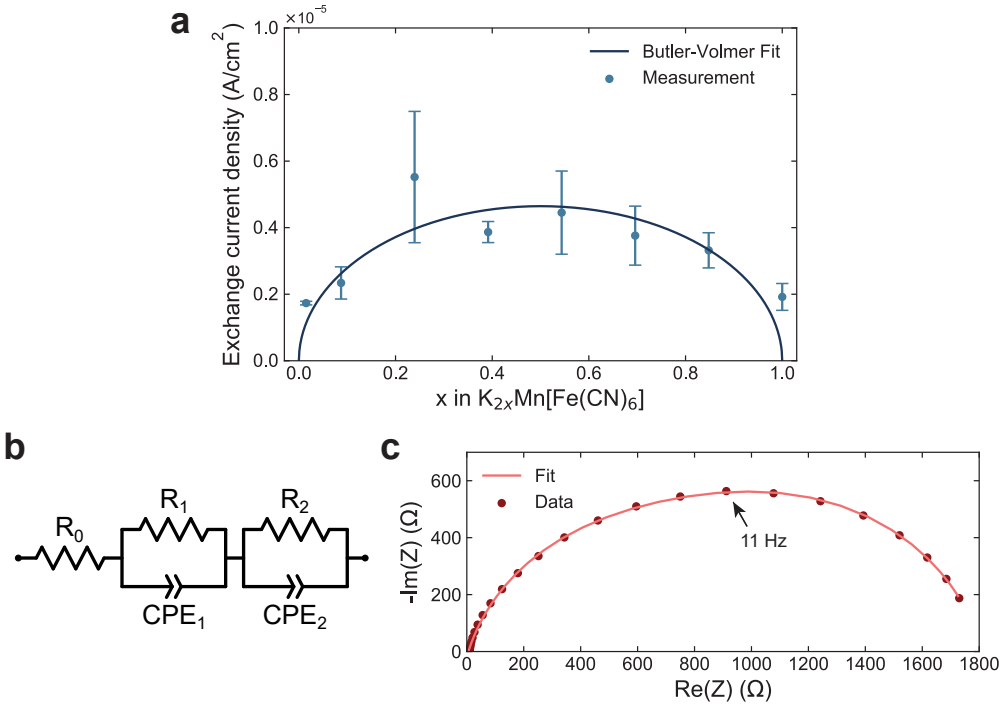


Figure 4.18 KMF exchange current density characterisation in 2m KFSI TEP at 20°C (**a**) Exchange current density over composition. Error bars depict the standard error in the mean. (**b**) Equivalent circuit used to fit graphite impedance data (**c**) Example KMF impedance spectra in three-electrode cell > 0.5 Hz. Adapted from Dhir *et al.*[171]

Figure 4.18a shows the KMF exchange current density, $j_{0,\mathrm{KMF}}$, over stoichiometry in 2 m KFSI TEP electrolyte, measured in a three-electrode cell, and again fitted to a form of the Butler-Volmer (Equation 1.15). The data fits the Butler-Volmer trend well matching other studies of j_{k0} for Li-ion NMC materials[111,241]. For the fits the charge-transfer coefficients (α_a and α_c) are maintained as 0.5, as is conventionally assumed[109,111,241]. O'Regan *et al.* allow α_a and α_c to be a free fitting parameter to improve the Butler-Volmer fit[164]. However, since α_a and α_c are highly difficult to measure accurately and validate[109], and as 0.5 gave a good fit for the KMF, this conventional assumption was maintained. From the Butler-Volmer fit (Equation 1.15) $k_{0,\mathrm{KMF}}$ was determined as 0.93×10^{-5} A cm^{-2}. The equivalent circuit used to determine the KMF R_{ct} and an example KMF impedance spectra is shown in Figures 4.18b and 4.18c, respectively. Again, R_{ct} is represented by R2 in the

equivalent circuit as R2 results in $j_{0,\mathrm{KMF}}$ clearly fitting the Butler-Volmer trend, and also due to evidence that passivation layer formation occurs at higher frequencies than R_{ct}[239] (Table A.2). The results show a mean $j_{0,\mathrm{KMF}}$ of 0.34×10^{-5} A cm^{-2} over the composition which is an order of magnitude lower than $j_{0,\mathrm{g}}$, indicating notably faster kinetics for the graphite anode. Again the low residuals in the frequency range relevant for charge transfer show the model describes the data well (Figure 4.19)a. The higher percentage residuals at high frequencies again appear to be due to the low impedance and instrument resolution limitations as again the absolute residual values are low at these high frequencies (Figure 4.19b). Again the data very well satisfies the Kramers-Kronig relations showing the causality, linearity and stability requirements for conventional EIS are reasonable assumptions for the data (Figure 4.19)c. The same is true for the KMF as the graphite regarding it not being possible to measure the EIS at true 100% and 0% potassiation, and there being slight x error in these points.

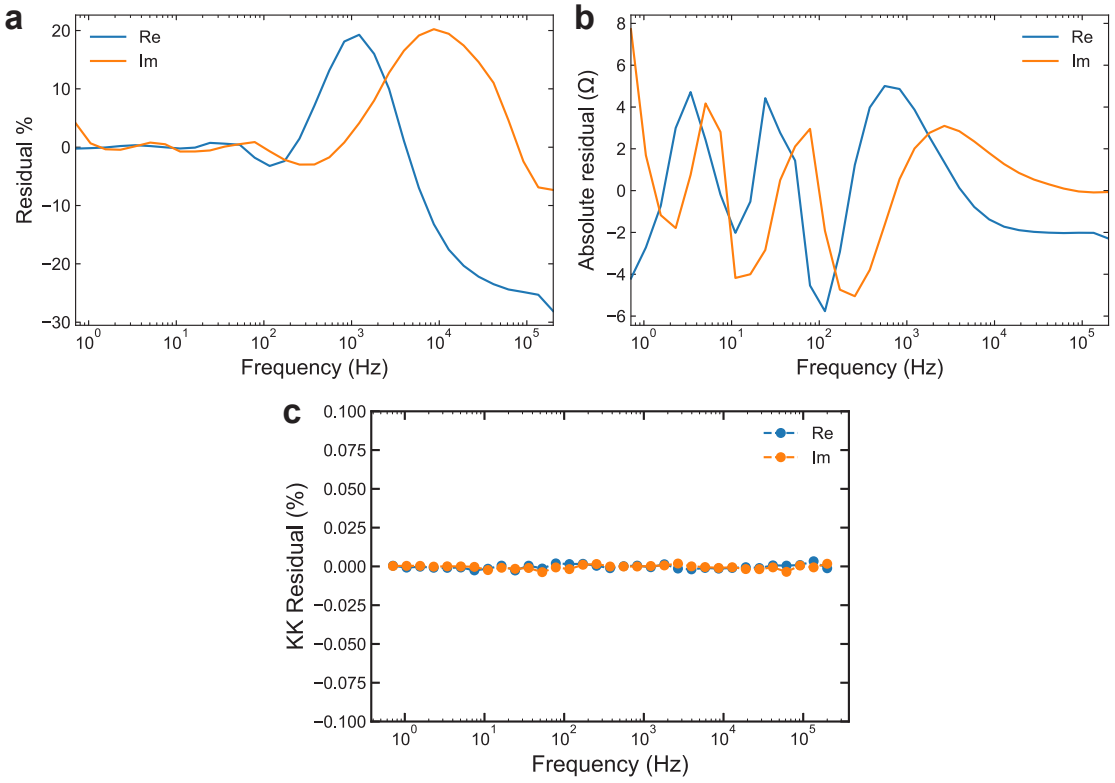


Figure 4.19 KMF EIS residual analysis (**a**) Percentage residuals between example KMF EIS model and data (**b**) Absolute residuals from example KMF EIS model and data (**c**) Kramers-Kronig residuals from example KMF EIS spectra

The sluggish $j_{0,\mathrm{KMF}}$ charge-transfer kinetics identified could finally explain the poor rate capability found by other studies assessing the KMF electrochemical performance[38,55], where the underlying cause had not been identified[1]. For context $j_{0,\mathrm{KMF}}$ is almost two orders of magnitude lower than that found for lithium nickel manganese cobalt oxide (NMC) cathode materials indicating significantly less efficient reaction kinetics to the high energy density Li-ion metal oxides[111,164,241]. However, the $j_{0,\mathrm{KMF}}$ appears around half an order of magnitude higher than LFP (from 4.7–16.7$\times10^{-7}$ A cm^{-2}) determined from fitting to commercial LFP electrode experimental data[246] and to other models validated to experimental LFP testing[247]. Another study estimated LFP j_{k0} similar to the value determined here for KMF[248]. Therefore, the kinetics appear to be similar or slightly better than that for LFP. Given LFP Li-ion is actually the competitor for K-ion, rather than the high energy density high nickel cathodes, the comparable j_0 for KMF to LFP is promising for the competitiveness of K-ion.

4.4 Conclusion

In summary, the work in this chapter has characterised the effective solid state diffusivities, $\widetilde{D_k}$, and exchange current densities, j_{k0}, of the leading K-ion electrode materials, the graphite anode and KMF cathode. By synthesising highly homogeneous and non-agglomerated KMF particles the electrochemically active surface area S, one of the greatest sources of uncertainty in characterising $\widetilde{D_k}$, was determined more accurately. The state-of-the-art Kang-Chueh GITT method and analysis was applied to determine $\widetilde{D_k}$ more accurately and compared to long-time PITT characterisation, showing good agreement, though the Kang-Chueh GITT obtains superior compositional resolution. The median $\widetilde{D}_{\mathrm{KMF}}$ is over four times lower than $\widetilde{D}_{\mathrm{g}}$ and $j_{0,\mathrm{KMF}}$ is an order of magnitude lower then $j_{0,\mathrm{g}}$, showing the KMF cathode displays slower ionic transport and in particular slower reaction kinetics than the graphite anode. The Butler-Volmer equation fits the composition-dependent $j_{0,\mathrm{KMF}}$ well but not for $j_{0,\mathrm{g}}$ likely due to overlapping SEI formation. Further research should investigate why the KMF kinetics are limited and attempt to develop material

modifications to improve the kinetics to match that of the graphite. Characterising the exchange current density in different electrolytes is also important to identify whether this is a specific issue with KFSI:TEP.

5

Modelling of Potassium-ion Batteries

Contents

5.1 Introduction 136
5.2 Modelling details 137
5.3 Results and Discussion 138
5.3.1 Context - Lithium-ion NMC811 138
5.3.2 Potassium-ion Modelling 140
5.3.3 Comparison with LFP Lithium-ion 148
5.4 Conclusion 155

5.1 Introduction

A significant proportion of the work reported in this chapter was published in the following preprint article which is currently under review:

1. Dhir, S., Cattermull, J., Jagger, B., Schart, S., Olbrich, L., Zhao, J., Sada, K., Goodwin, A., Pasta, M. Characterisation and Modelling of Potassium-ion Batteries *Research Square* (*Preprint - Manuscript under review*)[171]

The K-ion electrolyte and electrode material characterisation in Chapter 3 and Chapter 4 indicate the potential fast charging capability of K-ion. However, as detailed in the Introduction, there is currently no electrolyte which provides

practical coulombic efficiencies for K-ion. Therefore, to understand the potential of K-ion fast-charging in commercial cell formats once a suitable electrolyte has been developed requires full-cell Doyle-Fuller-Newman (DFN)[108,109] modelling of K-ion. However, until this work the characterisation of the critical rate-determining electrolyte and electrode material properties required by the DFN model had not been reported. Now, by bringing together these characterised fundamental properties from the previous chapters in a DFN K-ion model in a commercial cell format, a bottom-up approach to understanding the rate potential and rate limitations of K-ion may be ascertained. Therefore, the work of this chapter conducts the first ever full-cell DFN modelling of a KIB, exploring multiple cases and comparing to LFP Li-ion. This work both helps to more accurately understand the fast charging potential of K-ion as well as identify the critical material and electrolyte property rate limitations that research should focus on addressing. Finally, this work provides the foundation for further K-ion DFN modelling to accelerate the development and optimisation of new K-ion materials and electrolytes.

5.2 Modelling details

DFN Modelling

For the DFN full cell modelling, the open-source battery simulation package Python Battery Mathematical Modelling (PyBaMM)[194] version 23.5 full cell DFN model and CasADi numerical solver[195] was used. Full details of the parameters used are detailed in Table A.3. For determining the accessible capacity % at different C-rates, the baseline performance was determined from a C/50 discharge (1 C = 1.91 mA cm^{-2} for the K-ion cells and 2.24 mA cm^{-2} for the LFP Li-ion cells). For the KFSI and LiFSI:DME electrolytes the empirical concentration-dependent functions characterised in our previous work were used[170]. The PyBaMM 'Chen2020' parameter set was used for the LG M50 cylindrical cell geometries and Li^+ graphite material parameters[113]. For the K graphite electrode, the Li graphite electronic conductivity was used[113]. For the KMF cathode the Li-ion LFP electronic conductivity was used[248]. In order to achieve model convergence the graphite particle

size of 1 µm was used; a commercial size (Table A.3) yet smaller than typical Li-ion and likely required in reality. The crystal density for the KMF cathode used in the modelling was derived from the unit cell volume determined from the refinement in combination with the KMF stoichiometric M. Thermal effects were neglected in the models.

Due to the structure of PBAs, KMF can be fully depotassiated without causing irreversible crystal structure changes unlike for many Li-ion cathode materials such as NMCs[109]. Therefore, almost the full stoichiometric capacity is utilised for the KMF in the models, and a very small K^+ concentration is kept as a minimum in the KMF to ensure the model converges. The capacities of the graphite and KMF electrodes were matched and then an excess of graphite capacity used using a 1.1 negative to positive electrode capacity ratio (NP ratio) as standard in commercial Li-ion cells to avoid plating and overcharging risks[105,109]. The voltage limits were set using the half-cell OCV profiles ensuring during charging the negative electrode potential did not reach 0V vs. K^+ to prevent K metal plating.

5.3 Results and Discussion

5.3.1 Context - Lithium-ion NMC811

First, for context, a leading Li-ion cell was modelled. There have been recent comprehensive teardown and parameterisation analyses of the LG M50 21700 cylindrical NMC811 Li-ion cell[113,164], and NMC811 is one of the leading Li-ion high energy density cell chemistries[14]. Therefore, this cell was modelled during charging at different rates using PyBaMM[194] to understand its rate capability and its the rate limiting overpotentials. Figure 5.1a displays the accessible capacity at increasing rate and corresponding final overpotential contributions when the upper cut-off voltage is reached. The results demonstrate the electrolyte concentration overpotential and negative electrode reaction overpotential are the most significant sources of overpotential at high rates >3C, drastically limiting the accessible capacity. Therefore, electrolyte properties such as t_+^0 and D_e, which determine concentration gradient formation and electrolyte concentration overpotentials are

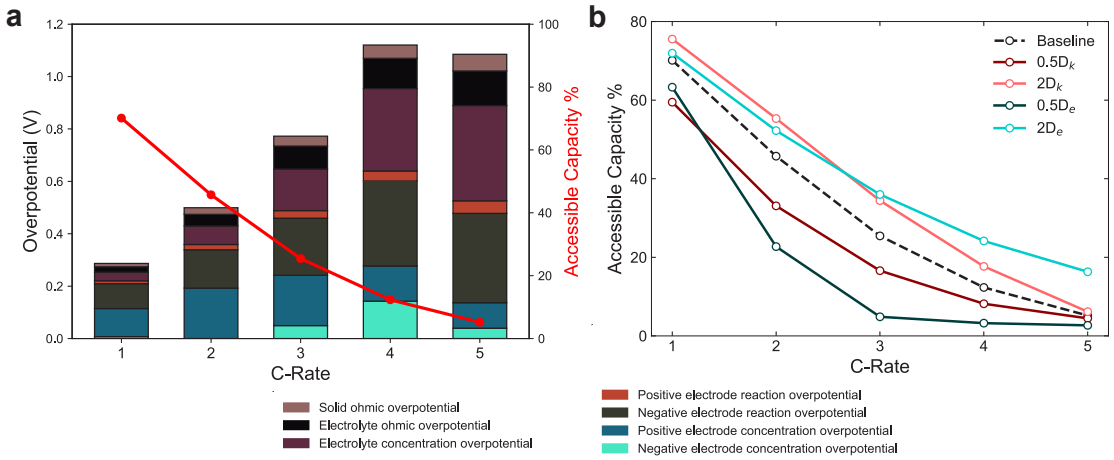


Figure 5.1 NMC811 Li-ion simulations. Full-cell Doyle-Fuller-Newman (DFN) simulation of a commercial LG M50 cylindrical NMC811 Li-ion cell. Modelled using PyBaMM[194] at 25 °C. (**a**) Final overpotential components when the upper cut-off voltage is reached (**b**) Sensitivity analysis comparing the impact of doubling or halving the electrolyte salt diffusivity (D_e) compared to the diffusivity of the active materials

critical limitations. The limiting graphite reaction overpotential is determined by the area available for reaction and $j_{0,\mathrm{g}}$. Since the graphite and NMC particles are similar size ($\sim$ 5 μm radius), the significantly faster charge transfer kinetics of the NMC ($\sim$ one order of magnitude faster than the graphite), result in the reaction kinetics limitation for the graphite electrode in rate capability[113,164]. To mitigate the electrolyte rate limitations, higher electrode porosities could be utilised while smaller graphite particles could be used to address the graphite kinetic limitations, though this higher surface area will exacerbate parasitic reactions, increasing electrolyte consumption and SEI formation in the formation cycle, decreasing formation cycle coulombic efficiency. At lower rates (<3C) the graphite reaction kinetics are still one of the largest source of overpotential but also the positive electrode concentration overpotential. This is due to the $\sim$ order of magnitude slower D_{NMC} than D_g[113]. To illustrate the electrolyte importance further, Figure 5.1b shows the sensitivity of the accessible capacity of the NMC811 cell at increasing rates to the electrolyte salt diffusivity D_e or active material solid state diffusivities D_k. Both anode and cathode active material D_k were scaled simultaneously when scaling D_k. The results

show the NMC811 cell rate performance is significantly more sensitive to D_e, again emphasising the importance of electrolyte transport. Halving D_e is detrimental to rate performance, while doubling D_e provides the greatest rate benefit.

5.3.2 Potassium-ion Modelling

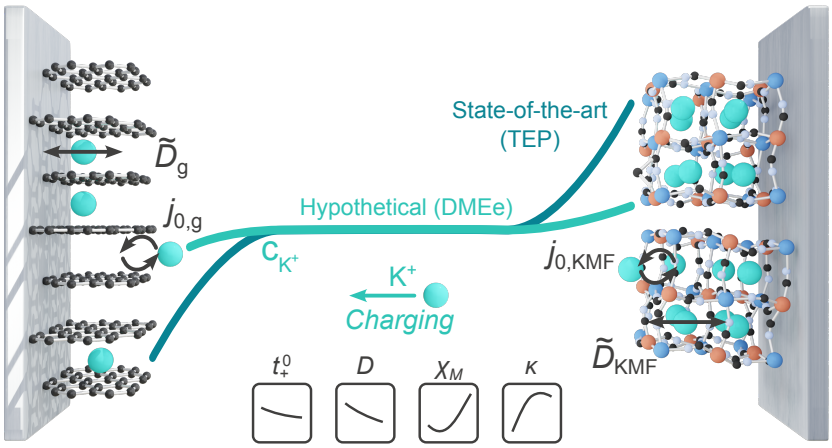


Figure 5.2 K-ion Modelling Schematic Schematic of the leading K-ion chemistry characterised and modelled. The graphite anode (left) and the potassium manganese hexacyanoferrate (KMF) cathode (right). The K-ion model brings together the effective solid-state diffusivities and exchange current densities characterised in Chapter 4 in combination with the electrolyte transport properties of a hypothetical electrolyte with equivalent transport properties of the KFSI:DME (DMEe) electrolyte characterised in Chapter 3[170] or the current state-of-the-art K-ion electrolyte in the K-ion research community KFSI:TEP (TEP)[171]. Adapted from Dhir *et al.*[171]

To understand the potential of KIBs for fast-charging, a KIB full-cell DFN model in a hypothetical commercial LG M50 21700 cylindrical cell format was modelled[113,164]. A schematic of the K-ion chemistry modelled is shown in Figure 5.2. As mentioned, since there is no current K-ion electrolyte which provides practical coulombic efficiencies, two K-ion cells were modelled with alternative electrolytes. First, using a hypothetical electrolyte with equivalent properties to KFSI:DME (DMEe), the only K-ion electrolyte fully characterised by this research, with the results in Chapter 3[170]. Second, using KFSI:TEP, which is recently considered the current leading K-ion electrolyte in the K-ion research community[92], and is also the electrolyte used to characterise the electrode material properties in Chapter 4. KFSI:DME properties were used as a model electrolyte to indicate

full-cell K-ion performance once a potential suitable electrolyte has been developed and optimised. It is important to note KFSI:DME will not be the electrolyte utilised in commercial KIBs unless additives are developed which mitigate its tendency for cointercalation into graphite[206]. Both electrolytes were utilised at 2m concentration for fair comparison due to evidence of greater stability at moderately high concentrations for KFSI:TEP[92,93]. The K-ion models were developed using the electrode properties characterised in Chapter 4 ($\widetilde{D}_{\mathrm{g}}$, $j_{0,\mathrm{g}}$, $\widetilde{D}_{\mathrm{KMF}}$ and $j_{0,\mathrm{KMF}}$) in combination with the relevant electrolyte properties. For the KFSI:DME electrolyte, the transport properties and concentration relationships fully characterised in Chapter 3 (Section 3.3.5) were utilised[170]. For the KFSI:TEP electrolyte, the four critical transport and thermodynamic properties were recently characterised for a single concentration, 2 m, for this work using the same methods used in Chapter 3 by Junyi Zhao[171] (Table A.3). The cells were modelled using the battery modelling package PyBaMM[194]. The total energy of each K-ion cell was simulated to be 7.3 Wh by adjusting the electrode thicknesses. The half-cell OCV profiles for the graphite anode and KMF cathode determined here were implemented in the model (Figure 4.5a and 4.14a, respectively). All electrode properties, including cathode and anode material particle size and electrode porosities were kept constant for both cases, and the NP ratios were set to be 1.1 as typical in commercial Li-ion cells[105]. The cells simulated use power-cell electrode porosities of 0.35[105]. The median $\widetilde{D}_{\mathrm{g}}$ and $\widetilde{D}_{\mathrm{KMF}}$ (Figure A.1a and b) are being used in the model as a conservative representation of the Kang-Chueh GITT data characterised in the regions where potassiation and depotassiation match, whilst minimising exposure to the extreme values—the high values where SEI/CEI formation and finite-size effects are likely to have some impact due to being above the ideal semi-infinite regime (Figure 4.7b and 4.15b), and also avoiding impact from the the potential plateau regions when $\frac{\partial V_{\mathrm{eq}}}{\partial x}$ approaches zero (Figure 4.7a and 4.15a) as mentioned previously. In commercial LFP LIBs, LFP particles need to be nanosized to increase the surface area available for reaction and decrease the diffusion length due to the substantially lower j_{k0} and D_k of LFP than Li graphite. In the K-ion cell, $\widetilde{D}_{\mathrm{KMF}}$ is approximately

four times lower than $\widetilde{D}_{\mathrm{g}}$, and $j_{0,\mathrm{KMF}}$ is around one order of magnitude lower than $j_{0,\mathrm{g}}$. Consequently, the KMF particles must also be nanosized to match the faster kinetics of the graphite anode. One of the advantages of PBA synthesis is that the particle size can be easily controlled[38]. In the model, the KMF particle sizes are set to 500 nm, consistent with the commercial LFP particle size[105]. The graphite particle size utilised is 1 µm - a commercial size but smaller than conventional Li-ion due to the lower $\widetilde{D}_{\mathrm{g}}$ (Chapter 4) and thus challenges with the K-ion cell model converging at larger sizes. Full details of the model parameters used in the K-ion DFN simulations are detailed in Table A.3.

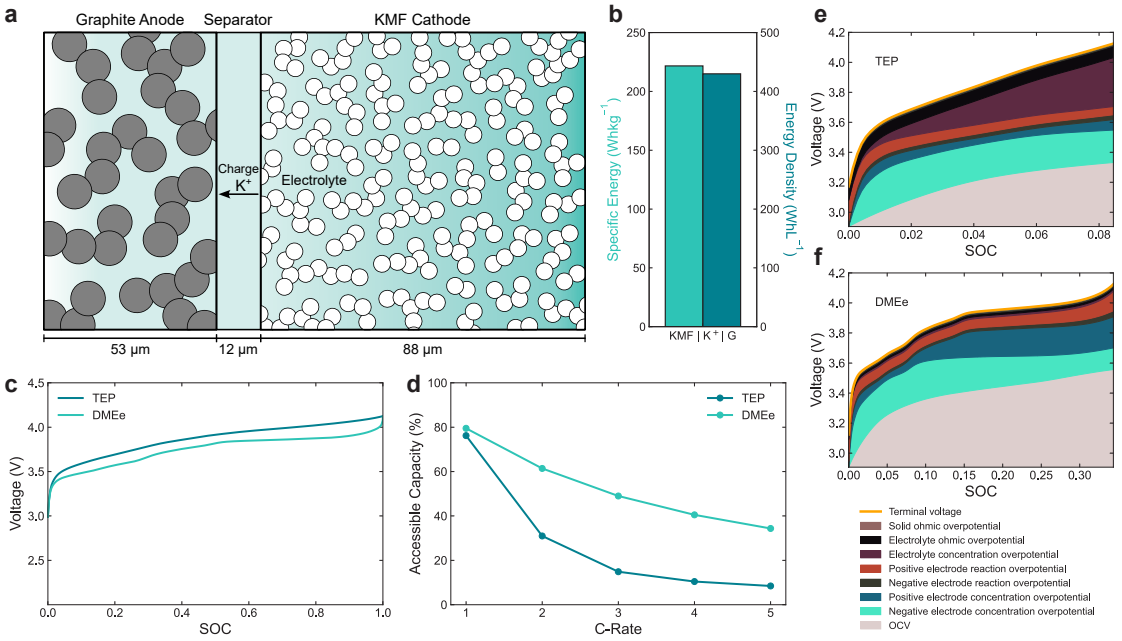


Figure 5.3 K-ion full-cell Doyle-Fuller-Newman (DFN) simulations. Simulations of two K-ion full-cells with different electrolytes in commercial LG M50 21700 cylindrical cell format. The state-of-the-art modelled K-ion cell is $K_2Mn[Fe(CN)_6]$ (KMF) | | graphite (G) with 2 m KFSI TEP electrolyte (denoted as TEP)[171]. The other cell is a hypothetical electrolyte case using the characterised electrolyte properties of the 2 m KFSI:DME characterised in Chapter 3[170] to simulate K-ion performance with an equivalent electrolyte (DMEe). The cell energies are 7.3 Wh. NP ratios were kept constant at 1.1 with constant electrode porosities, and properties for both chemistries. Modelled using PyBaMM[194] at 20 °C. (1C = 1.91 mA cm^{-2} for both) (**a**) Schematic of simulated K-ion cell (**b**) Energy density and specific energy of the K-ion chemistry at the stack-level using the stack-level technoeconomic model developed and used in the Introduction described in Section 2.1[1] (**c**) Simulated galvanostatic profiles for the K-ion cells (**d**) Accessible capacities at increasing C-rate (**e**) TEP cell overpotential components during a 5 C charge (**f**) DMEe cell overpotential components during a 5 C charge. Reproduced from Dhir *et al.*[171]

Figure 5.3a depicts the K-ion cell being modelled with the two electrolytes. The KMF cathode is 66% thicker than the graphite anode due to the lower specific capacity and bulk density of the KMF material[1]. Figure 5.3b shows the specific energy and energy density of the K-ion chemistry based on the anode and cathode theoretical capacities and the simulated galvanostatic profile (Figure 5.3c) using the stack-level technoeconomic model developed and used in the Introduction described in Section 2.1[1]. Figure 5.3c displays the DFN simulated galvanostatic profiles of the two chemistries during a 1C charge, demonstrating the higher overpotentials experienced by the TEP cell. Finally, Figure 5.3d shows the fast-charging performance comparison for the two K-ion chemistries, demonstrating the DMEe shows significantly higher rate capability than the TEP cell, achieving significantly higher accessible capacities at all rates simulated. Even at the fast-charging rate of 5C the DMEe cell can access 34% capacity compared to 8% for the TEP cell. To understand the reasons for the significant difference in rate capability, Figure 5.3e and f plot the overpotential components for each K-ion chemistry during a 5C charge until the upper cut-off voltage is reached, beyond which point metal plating could start to occur resulting in dramatic capacity losses[30]. Figure 5.3e shows the electrolyte concentration overpotentials are exceptionally high and growing quickly for the TEP K-ion cell early in the charge cycle at SOC < 0.1, causing the upper-cutoff voltage to be quickly reached. This is the result of significantly larger electrolyte concentration gradient formation in the TEP cell compared to the DMEe cell (Figure 5.4f and c, respectively) due to the lower salt diffusivity of the TEP electrolyte ($\sim$ one order of magnitude lower than DMEe (Table A.3)[170,171]), thus limiting the transport of K^+ to the graphite anode during charge. The ionic conductivity of the TEP electrolyte is also five times lower than that of the DMEe electrolyte (Table A.3)[170,171], resulting in larger electrolyte ohmic overpotentials. The significantly slower electrolyte transport properties are a result of highly viscous nature of the TEP electrolyte (for context around five times higher viscosity than a commercial Li-ion carbonate electrolyte LP30[93,249]). Figure 5.5 plots the final overpotential components at the point the upper cut-off voltage is reached

with increasing C-Rate also showing the electrolyte concentration overpotential is the largest contribution for all rates for the TEP cell, whilst a minor component for the DMEe cell, thus the slow transport of the TEP electrolyte limits accessible capacity at all rates. Therefore, though KFSI:TEP is the current leading electrolyte for the K-ion research community using low loading in coin cells, this electrolyte is unsuitable for even moderately high charge rates using commercial cell electrode thicknesses and loading, and an electrolyte with faster transport properties must be developed.

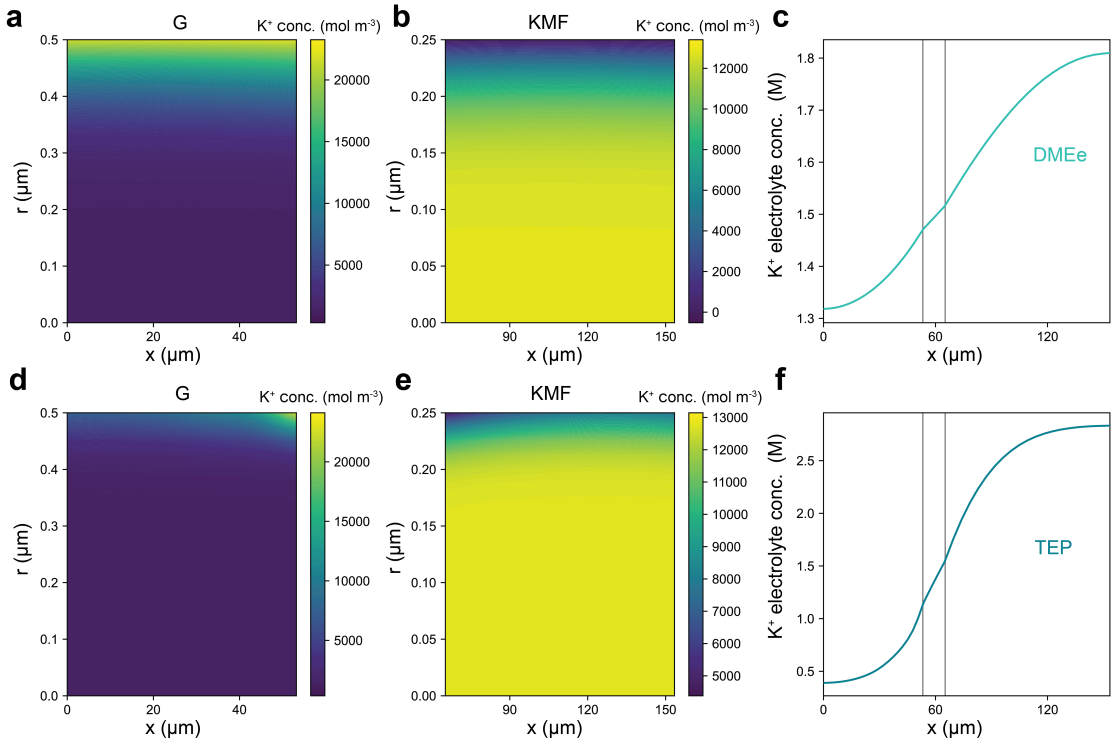


Figure 5.4 K-ion particle and electrolyte concentrations from DFN simulations at 5C. Concentration of K^+ in the graphite anode particles within the particles (r dimension) and across the electrode (x dimension), and K^+ concentration in the electrolyte in the DMEe or TEP electrolyte K-ion cell after 5C charge once upper cut-off voltage is reached. The cells are $K_2Mn[Fe(CN)_6]$ (KMF) | 2m KFSI TEP or 2m KFSI DME | graphite (G) (**a**) K^+ concentration in the graphite anode particles in the DMEe cell. (**b**) K^+ concentration in the KMF cathode particles in the DMEe cell. (**c**) K^+ electrolyte concentration across the DMEe cell (**d**) K^+ concentration in the graphite anode particles in the TEP cell. (**e**) K^+ concentration in the KMF cathode particles in the TEP cell. (**f**) K^+ electrolyte concentration across the TEP cell

Figure 5.4 also compares the K^+ particle concentrations within the active material particles and across the electrodes at the end of the 5C charge. In the

TEP cell significant potassiation has only occured at the surface of the graphite particles closest to the KMF cathode with the same for the KMF cathode with only those particles nearest the graphite having experienced depotassiation from the very surface. This contrasts with the DMEe cell, as across both electrodes the surfaces of the particles have experienced almost identical levels of potassiation and depotassiation even those nearest the current collectors. This again shows the significantly faster electrolyte transport of the DMEe electrolyte, enabling greater accessible capacity compared to the TEP cell. Nevertheless in the DMEe cell the KMF cathode particle surfaces across the electrode reach a K^+ concentration of 0 mol $m^{-}3$ which explains the significant increase in positive electrode concentration and reaction overpotential causing the upper cut-off voltage to be reached (Figure 5.3f). This occurs because K^+ cannot diffuse fast enough through the KMF particle to replenish the surface for charge transfer reaction. When the upper cut-off voltage is reached $\sim$ 80% of the KMF cathode is still essentially fully potassiated, demonstrating the critical KMF K^+ transport limitations from the slow $\widetilde{D}_{\mathrm{KMF}}$.

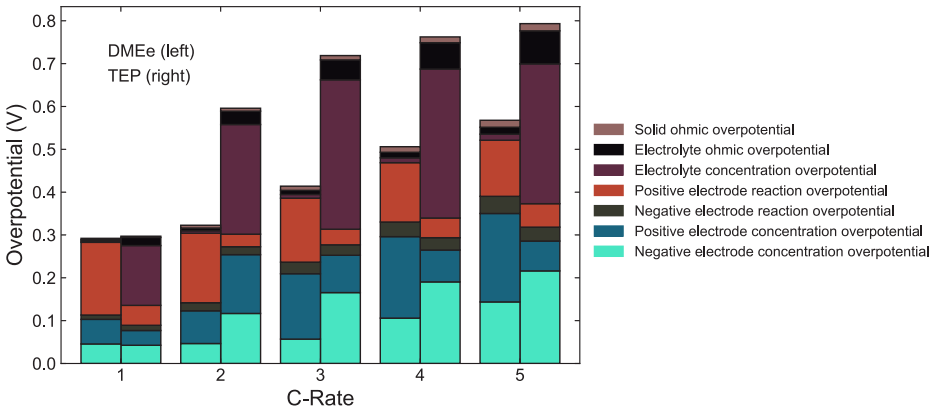


Figure 5.5 Final overpotential components when the upper cut-off voltage is reached with increasing C-Rate for the two K-ion chemistries in commercial LG M50 cylindrical cell format. The K-ion cells are $K_2Mn[Fe(CN)_6]$ (KMF) | | graphite (G) with the 2 m KFSI DME (DMEe) electrolyte (left) or 2 m KFSI TEP (TEP) electrolyte (right)

Exploring the model DMEe K-ion chemistry further, where the electrolyte concentration overpotentials are not the limiting factor in determining rate, Figure 5.3f shows the largest overpotential components at 5C are the negative and positive electrode concentration overpotentials with similar magnitudes. This reflects the

transport limitations within the particles as the most significant factor limiting high-rate performance as shown in Figure 5.4a and b, Initially, the graphite concentration overpotential is most significant, yet, after SOC ~ 0.25 the KMF concentration overpotential becomes more dominant reflecting the KMF leaving the two-phase OCV plateau between $0.75 < x < 0.95$ (Figure 4.14a), approaching the apparently undistorted phase at $0.4 < x < 0.75$ and thus the surface OCV increasing more rapidly. Outside of the KMF OCV plateau region the difference between the OCV at the KMF particle surface K^+ concentration, $U(c^{s}_{KMF,K^+})$, compared to the OCV at the bulk KMF K^+ concentration, $U(c_{KMF,K^+})$, is larger, driving greater concentration overpotentials, η_c. Thus at this point during charging, with decreasing KMF K^+ concentration, $\eta_{c,KMF} = U(c_{KMF,K^+}) - U(c^{s}_{KMF,K^+})$ becomes larger than $\eta_{c,g} = U(c_{g,K^+}) - U(c^{s}_{g,K^+})$ causing the KMF concentration overpotentials to start dominating over the graphite.

The positive electrode reaction overpotential is the third largest overpotential contribution at 5C after the concentration overpotentials (Figures 5.3f 5.5), significantly larger than the negative reaction overpotential throughout the charge reflecting the slower $j_{0,KMF}$ than $j_{0,g}$, despite the smaller KMF particles and greater surface area for reaction. Interestingly, Figure 5.5 shows at lower rates < 3C the positive electrode reaction overpotential is the dominant overpotential contribution limiting accessible capacity, again underlining the importance of investigating the slow kinetics of the KMF cathode. It is also important to note the charge-transfer kinetics are a function of the electrolyte as well as the electrode. Therefore, given j_{k0} was characterised for these materials in KFSI:TEP in Chapter 4, this may also be a factor in the slow kinetics experienced by the KMF, again reinforcing the need to develop and evaluate new K-ion electrolytes. The electrolyte and solid ohmic overpotentials are very small contributions. However, the electronic conductivity of the KMF was not formally investigated in this work and the electronic conductivity of LFP was used in the model[248]. As mentioned, PBAs exhibit low electronic conductivity[1,51] like LFP[250], which often requires carbon coating. Therefore, it was considered a reasonable assumption for the KMF in an electrode to share similar

LFP properties, however, the KMF electronic conductivity should be investigated and characterised to understand more accurately what limitation this may cause in KIB rate performance.

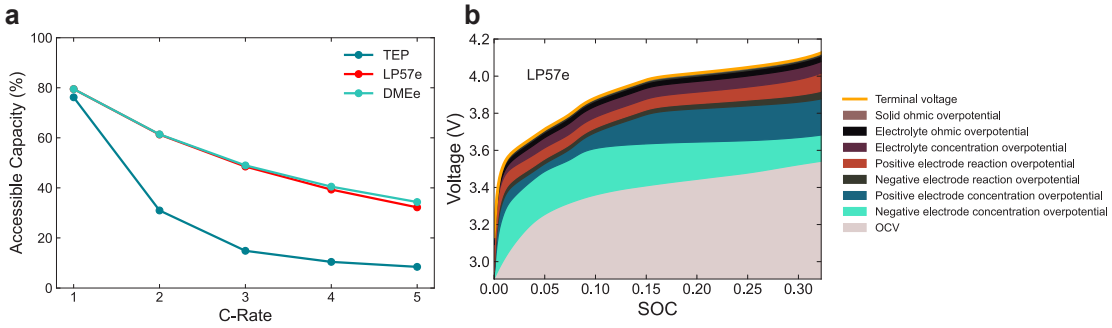


Figure 5.6 Additional DFN comparison with same K-ion cell with third electrolyte: a hypothetical electrolyte case using the characterised electrolyte properties of the commercial Li-ion electrolyte 1M LP57[123] to simulate K-ion performance with a LP57 equivalent (LP57e) electrolyte. Full-cell DFN simulations of three K-ion cells with different electrolytes in commercial LG M50 cylindrical cell format. The state-of-the-art modelled K-ion cell is $K_2Mn[Fe(CN)_6]$ (KMF) | | graphite (G) with 1) LP57e electrolyte 2) 2m KFSI TEP electrolyte[171] (denoted as TEP), or 3) 2m KFSI:DME electrolyte[170] (DMEe). The cell energy is 7.3 Wh. NP ratios were kept constant at 1.1 with constant electrode porosities, and properties for all chemistries. Modelled using PyBaMM[194] at 20°C (**a**) Accessible capacities at increasing C-rate (**b**) LP57e cell overpotential components during a 5C charge. Reproduced from Dhir *et al.*[171]

As the DMEe electrolyte transport properties are fast, an additional comparison was made with another hypothetical electrolyte, this time using an electrolyte with the properties of the commercial Li-ion electrolyte LP57 fully characterised by Landesfeind *et al.*[123] (Figure 5.6). 1 M LP57 was used as another benchmark indicating current Li-ion commercial electrolyte performance. Figure 5.6a shows using this hypothetical equivalent LP57 (LP57e) electrolyte results in very little difference with the DMEe electrolyte at 5C rate (32% vs. 34% accessible capacity, respectively), despite the larger LP57e electrolyte concentration and ohmic overpotentials (Figure 5.6b vs. Figure 5.3f). These larger overpotentials are caused by the salt diffusivity and ionic conductivity of 1 M LP57 being around half that of 2 m KFSI:DME at 20°C[123,170]. This shows that it makes negligible difference if a K-ion electrolyte is developed with the fast transport properties of DMEe or with the average transport properties of LP57e, as the electrode material properties

are rate limiting not the electrolyte for both, emphasising the need to also focus on electrode material optimisation in conjunction with electrolyte development. Unlike the electrolyte limitations, the active material transport and kinetic limitations can be mitigated through smaller particle sizes however, this necessitates a particularly high stablility electrolyte.

5.3.3 Comparison with LFP Lithium-ion

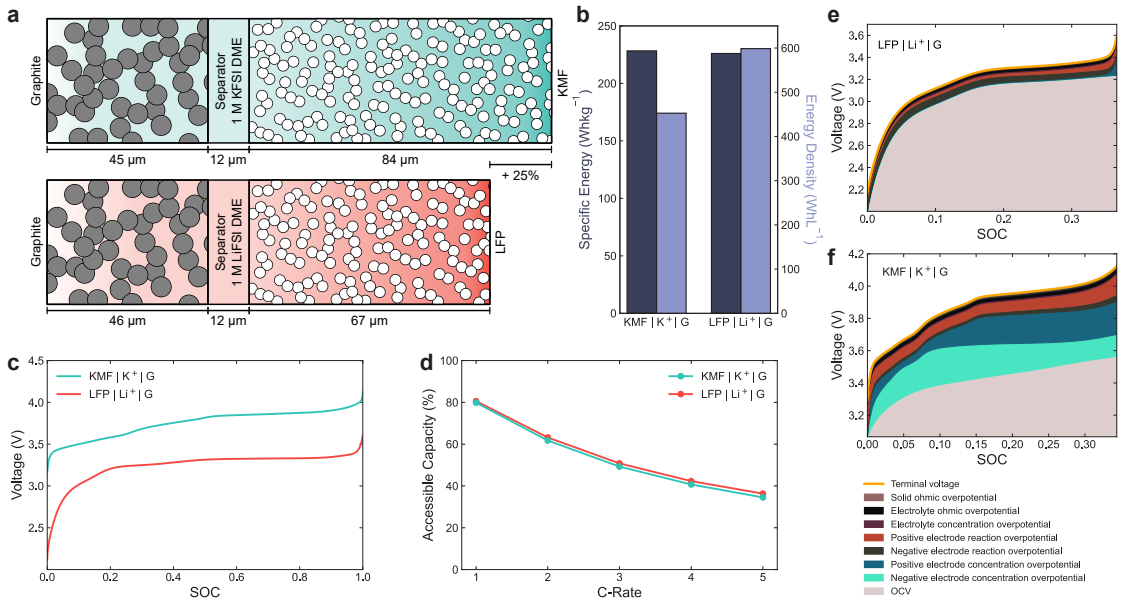


Figure 5.7 K-ion and LFP Li-ion full cell simulations. Doyle-Fuller-Newman (DFN) simulations of K-ion and LFP Li-ion full-cells in commercial LG M50 21700 cylindrical cell format at 20°C. The modelled K-ion and Li-ion cells are $K_2Mn[Fe(CN)_6]$ (KMF) | 1 M KFSI DME | graphite (G) and $LiFePO_4$ (LFP) | 1 M LiFSI DME | graphite (G), respectively. The composition-dependent electrolyte properties are from[170]. The cells are matched in energy at 7.3Wh by adjusting electrode thicknesses. NP ratios were kept constant at 1.1 with constant electrode porosities for both chemistries. Modelled using PyBaMM[194]. The LFP material parameters were taken from the PyBaMM 'Prada2013' parameter set[247,248]. LFP particle size was taken from BatPaC 5.1 and used for the cathode particle size for both chemistries[105]. (**a**) Schematic of simulated cell geometries (**b**) Energy density and specific energy of the two chemistries at the stack level using the stack-level technoeconomic model developed and used in the Introduction described in Section 2.1[1] (**c**) Simulated galvanostatic profiles for the K-ion and Li-ion cells (**d**) Accessible capacities at increasing C-rate (**e**) Overpotential components during a 5C charge (1C = 1.91 mA cm^{-2} and 2.24 mA cm^{-2} for the for the K-ion and LFP Li-ion cells, respectively). Reproduced from Dhir *et al.*[171]

Since the LFP LIB is the Li-ion chemistry that K-ion would be competing with[1], an LFP model in the same LG M50 21700 cylindrical cell was also simulated for

comparison. For fair comparison the total energy of the K-ion and LFP cell was matched at 7.3 Wh by adjusting the electrode thicknesses, and the particle sizes for each chemistry's cathode and anode materials were kept constant between the chemistries. 1M KFSI and LiFSI in DME electrolytes were used for the K-ion and LFP Li-ion cell, respectively for additional fair comparison and because both electrolytes were fully characterised over concentration using the same techniques and identical conditions in Chapter 3[170]. Again for the K-ion cell the half-cell OCV profiles for the graphite anode and KMF cathode determined in Chapter 4 were implemented (Figure 4.5a and 4.14a, respectively). NP ratios of 1.1 and electrode porosities were kept constant for both chemistries. Both the cathode materials particle sizes were kept constant as 500 nm, the commercial LFP particle size from BatPaC 5.1[105] and the same graphite particle sizes utilised for both chemistries (1 µm) for fair comparison. For this comparison energy-cell porosities were used rather than the power-cell porosities used in the previous K-ion TEP comparison models. The TEP model required higher porosities for the model to run due to the slow TEP transport. The porosities used here were 0.25 for the negative electrode and 0.335 for the positive electrode for both chemistries as found in a teardown analysis of the LG M50 cell[113]. Full details of the model parameters used in the LFP DFN simulations are detailed in Table A.4. The K-ion parameters are the same detailed in A.3 with the updated porosities, electrode thicknesses and 1M electrolyte concentration.

Figure 5.7a depicts the K-ion and Li-ion LFP full cells being modelled, with their corresponding thicknesses to match the energies of the cells, showing the KMF cathode is 25% thicker than LFP to match the total cell energies of 7.3 Wh. This is primarily due to the low bulk density of the KMF compared to LFP ($2.22\,\mathrm{g\,cm^{-3}}$ vs. $3.45\,\mathrm{g\,cm^{-3}}$, respectively[105]), limiting the energy density of the K-ion cell. Figure 5.7b compares the specific energy and energy density of the two chemistries at stack level based on their theoretical capacities and simulated galvanostatic profiles (Figure 5.3c) using the stack-level technoeconomic model developed and used in the Introduction described in Section 2.1[1]. The results show the K-ion chemistry

actually displays a comparable specific energy to the LFP chemistry (1% higher) though a significantly lower energy density (24% lower), again due to the lower KMF bulk density, showing K-ion is competitive particularly where mass is a more critical constraint than space. Figure. 5.7c displays the DFN simulated galvanostatic profiles during 1C charge of the two full cells, demonstrating the significantly higher operational voltage of the KIB, which enables it to be competitive particularly in specific energy, despite the lower theoretical specific capacities of the K-ion anode and cathode materials compared to the LFP cell (279 vs. 372 mA h g^{-1} for K and Li graphite, respectively and 155 vs. 170 mA h g^{-1} for KMF and LFP, respectively). Finally, Figure 5.7d shows the K-ion cell displays very similar rate performance to the LFP Li-ion cell (35% vs. 37% at 5C, respectively), indicating K-ion appears to be competitive with LFP, should a suitable electrolyte be developed.

Typically, when DFN modelling of Li-ion cells is conducted, characterised properties are tuned, estimated and calibrated for the simulation to match commercial galvanostatic cycling data[111,112,164,246,248,251]. $\widetilde{D}$ is a critical parameter which is often tuned higher than the values characterised experimentally to provide reasonable simulation values or model convergence[113,164]. The $\widetilde{D}_{\mathrm{LFP}}$ used in the LFP model is from estimation and tuning to experimental data[248], being around two to three orders of magnitude higher than an apparent median $\widetilde{D}_{\mathrm{LFP}}$ from GITT or EIS results in other studies[252,253]. The same is true for $\widetilde{D}_{\mathrm{g,Li^+}}$ which was tuned to be an order of magnitude higher than the value determined experimentally for simulations to match the experimental galvanostatic profile[113]. Therefore, given the conservative K-ion median $\widetilde{D_k}$ assumptions, it is possible that K-ion could exhibit superior rate performance to LFP from these results.

Exploring this further, Figure 5.7e and f plots the overpotential components over SOC for both chemistries during a 5C charge until the upper cut-off voltage is reached, again beyond which metal plating could start to occur[30]. First, it is clear that the K-ion cell can experience larger overpotentials before reaching the upper cut-off voltage due to the KIB OCV profile having a more gradual increase compared to that of the LFP Li-ion cell. One of the most significant reasons for

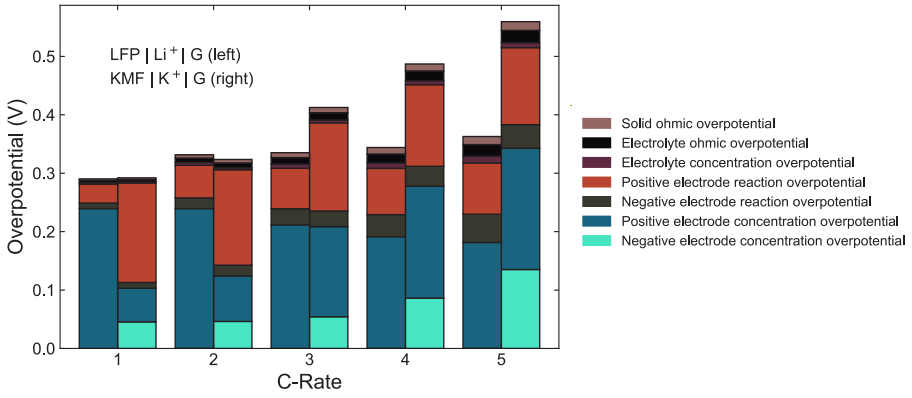


Figure 5.8 Final overpotential components for the two chemistries when the upper cut-off voltage is reached. The two chemistries are the 1) K-ion cell $K_2Mn[Fe(CN)_6]$ (KMF) | 1M KFSI DME | graphite (G) (right) and 2) the Li-ion cell LFP | 1M LiFSI DME | graphite (G) (left) with increasing C-Rate)

this is the higher intercalation potential of K^+ compared with Li^+ into graphite ($\sim$ 0.3 V and 0.1 V, vs. K^+/Li^+, respectively)[1]. Figure 5.8 plots the final overpotential components with increasing C-rate showing the overpotential contributions for the two chemistries more clearly, showing for the K-ion cell at the high rates >3C the electrode concentration overpotentials are the most significant. The negative electrode concentration overpotential is substantially higher for the K-ion cell compared to LFP cell where it is negligible at all rates and this is primarily due to $\widetilde{D}_{g,K^+}$ being almost three orders of magnitude lower than $\widetilde{D}_{g,Li^+}$ in the model, though $\widetilde{D}_{g,Li^+}$ was tuned higher as noted[113]. Figure 5.9a and d shows the Li^+ and K^+ concentration in the graphite anodes at the end of the 5C charge, showing no concentration gradient throughout the Li graphite particle, demonstrating the fast Li^+ transport and $\widetilde{D}_{g,Li^+}$, whereas there is a clear concentration gradient within the K graphite particles. Further work should also reanalyse $\widetilde{D}_{g,Li^+}$ using the Kang-Chueh GITT approach for a better comparison.

However, Figure 5.8 shows the most significant final overpotential contribution for both chemistries when the upper cut-off voltage is rached at high rates >3C is the positive electrode concentration overpotential. Despite the smaller particles for the positive electrodes $\widetilde{D}_{KMF}$ and $\widetilde{D}_{LFP}$ are similar and significantly lower than their respective graphite diffusivities (over four times for the K-ion and almost four orders

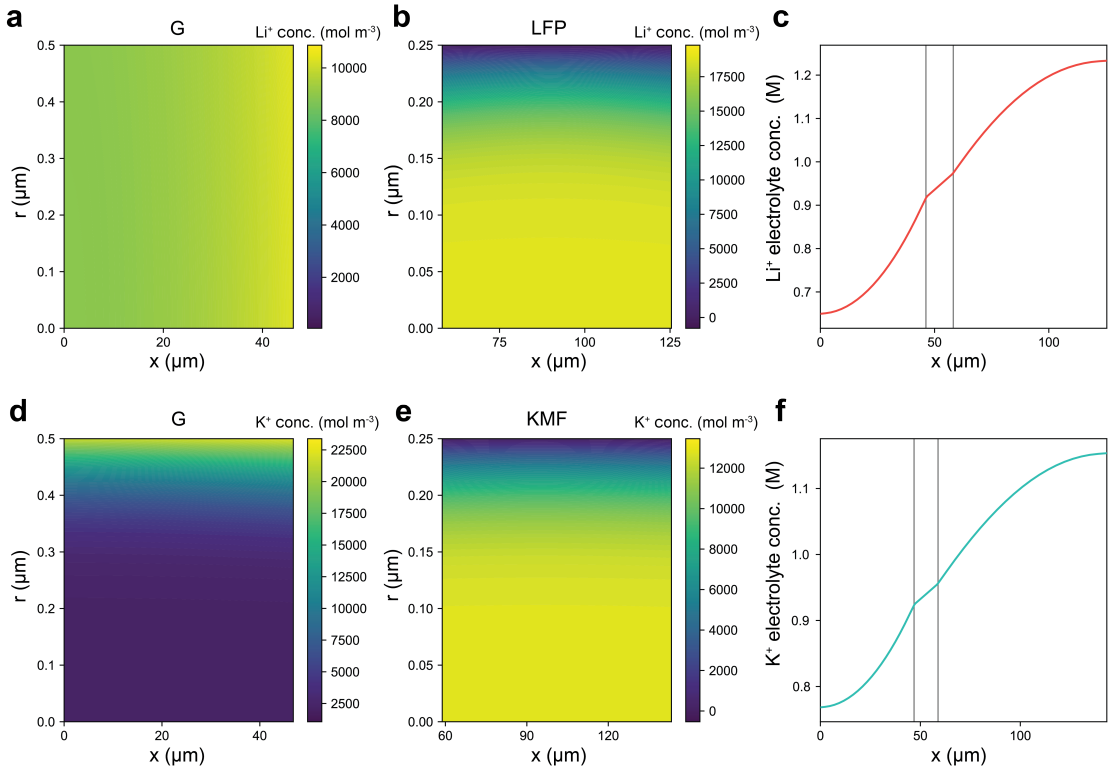


Figure 5.9 K-ion and LFP particle and electrolyte concentrations from DFN simulations. Concentration of Li^+/K^+ in the graphite anode particles within the particles (r dimension) and across the electrode (x dimension), and Li^+/K^+ concentration in the electrolyte. The modelled K-ion and Li-ion cells are $K_2Mn[Fe(CN)_6]$ (KMF) | 1 M KFSI DME | graphite (G) and $LiFePO_4$ (LFP) | 1 M LiFSI DME | graphite (G), respectively. (**a**) Li^+ concentration in the graphite anode particles. (**b**) Li^+ concentration in the LFP cathode particles. (**c**) Li^+ electrolyte concentration across the cell (**d**) K^+ concentration in the graphite anode particles. (**e**) K^+ concentration in the KMF cathode particles. (**f**) K^+ electrolyte concentration across the cell

for the Li-ion cell), and therefore, are the critical limitation in the rate capability of these cells. This is evidenced in Figure 5.9 by the Li^+ and K^+ concentration reaching zero at the particle surface in the LFP and KMF particles, respectively during the 5C charge. This shows the transport is too slow from within the particles to replenish the Li^+ and K^+ at the particle surface, thus being the reason for the significant increase in positive electrode concentration overpotential just before the upper voltage cut-off is reached in both chemistries (Figures 5.7e and f). This also explains the growth in positive electrode reaction overpotential for both chemistries, particularly near the end of the charge, as the particle surface concentration approaches zero j_{k0} drops as shown in the Butler-Volmer equation and profiles (Equation 1.15 and Figures 4.9a

and 4.18a), slowing the reaction kinetics and thus causing the increase in reaction overpotential. For the both the K-ion and LFP cell the final positive electrode reaction overpotential is significantly larger than the negative electrode reaction overpotential at all rates reflecting the slower average $j_{0,\mathrm{LFP,Li^+}}$ and $j_{0,\mathrm{KMF,K^+}}$ than $j_{0,\mathrm{g,Li^+}}$ and $j_{0,\mathrm{g,K^+}}$. At 5C in the LFP cell the negative reaction overpotential is greater for most of the charge than the positive reaction overpotential (Figure 5.7e), which becomes dominant as the LFP surface concentration approaches zero, reflecting the graphite kinetics are slower and initially limiting during the early SOC. It is also interesting to note that throughout the charge until the the significant growth near the end the positive electrode concentration overpotential is negligible for the LFP cell (Figure 5.7e). This is due to the almost constant OCV for the LFP cathode whilst in its large two-phase plateau region resulting in a very small difference between $U(c_{\mathrm{LFP,Li^+}})$ and $U(c^s_{\mathrm{LFP,Li^+}})$ with increasing changing surface concentration compared to that between $U(c_{\mathrm{KMF,K^+}})$ and $U(c^s_{\mathrm{KMF,K^+}})$, resulting in minimal positive electrode concentration overpotentials in the LFP cell during the charge until the concentration at the LFP particle surface approaches zero, which is not in the plateau region, resulting in a significant change in $U(c^s_{\mathrm{LFP,Li^+}})$, thus a significant increase in concentration overpotential.

The electrolyte concentration overpotential is a small contribution for both cells due to the fast transport of the DME electrolytes[170], though the electrolye concentration gradient in the K-ion cell is smaller than the Li-ion cell reflecting the faster transport of KFSI:DME compared to LiFSI:DME (Figures 5.9c and f). And again the electrolyte and solid ohmic overpotentials are very small contributions, with the electronic conductivity in the solid domains not limiting compared to the solid ionic transport, though again with the KMF electronic conductivity requiring further investigation.

Modelling Limitations

Though these models provide an indicative understanding of K-ion behaviour in commercial cell formats, these K-ion models are still provisional and are limited

by several aspects, some which have already been mentioned, and some which are inherent in the DFN model. First, the LFP model and K-ion model are not completely comparable, with the LFP model parameters tuned for simulations to match galvanostatic cycling data[113,248,251], whereas the K-ion model has been built purely from a bottom-up approach. Key properties such as the solid-state diffusivities are tuned up considerably for Li-ion models to match the galvanostatic cell cycling data, achieve model convergence, and achieve more realistic simulations as mentioned[113,164]. However, the same cannot currently be conducted for the K-ion cell there is no current electrolyte provides viable coulombic efficiencies, therefore, electrolyte decomposition, and its associated interfacial impedances, add overpotential contributions which prevents there being a comparable galvanostatic profile for the DFN. Another key limitation is that the DFN model simulates active material particles as one-dimensional spheres, and all particle surface is considered electrochemically active. The results from Chapter 4 show this is not the case for KMF or graphite in particular, however, to DFN model graphite with only the edge plane active area accounted for would mean changing the surface area per unit volume in the DFN electrodes. This could be done by increasing the particle size or scaling down the j_{k0}. Increasing the particle size also affects the diffusion length so is cannot be used, and scaling j_{k0} caused the model to have challenges converging. Therefore, the j_{k0} characterised was directly used, which therefore, means the active surface area could be considered an overestimate in this model meaning the graphite reaction overpotential may be underestimated. This underlines the importance of validation and tuning parameters, however, as this is difficult for K-ion as mentioned, this model is considered a bottom-up model based on fundamental property characterisation. There is also the assumption of the Bruggeman coefficients being set to the theoretical value of 1.5 for packed spheres, matching the geometry of the DFN model, however, again in reality the particle shapes are more complex, with alternative consequences for the tortuosity and transport efficiency in the electrodes. Another key limitation is that thermal effects have been neglected. At high-rates, thermal effects are highly important. Real cells, such as the real cylindrical LG M50 considered in this work,

are sufficiently large to form significant temperature gradients throughout, and as the electrochemical properties and parameters are highly temperature dependent, a thermal model would need to be solved at each point within the 3D cell, though this would add considerable computational complexity. Lumped thermal models may incorporate thermal effects without the level of computational intensity[110]. Processes such as diffusivities, reaction kinetics and ionic conductivity are highly temperature dependent and these effects have been neglected in this isothermal model. However, significant further property characterisation at other temperatures is required to determine Arrhenius relationships for these properties for K-ion. Finally, general limitations of the DFN model have been well documented such as the one-dimensional cell scale and one-dimensional particle scale neglecting effects of the three-dimensional cell geometry or non-spherical particles[109,110]. However, higher fidelity models incorporating microstructure and 3D geometry are far more computationally expensive.

5.4 Conclusion

KFSI:TEP is the current leading electrolyte for the K-ion research community using low loading in coin cells. However, the full-cell K-ion modelling in a commercial cell format demonstrates this electrolyte is unsuitable for even moderately high charge rates using realistic electrode thicknesses and loading due to its slow transport. Therefore, an electrolyte with faster transport properties must be developed for K-ion batteries. Utilising the transport properties of KFSI:DME (DMEe) shows promising results for K-ion fast-charging. However, it is important to recognise that there is no current low-cost electrolyte which provides this performance and practical stability for KIBs. All current K-ion electrolytes suffer impractically low initial coulombic efficiencies to be used in a commercial cell. The DMEe model has been developed to see what the rate capability of K-ion could be in realistic cell formats if a suitable electrolyte is developed which provides both a stable SEI for the graphite anode and stability at the high operating voltages of the KMF cathode[1] with the fast transport properties of KFSI:DME[170]. This model should

now support researchers in understanding the rate performance potential of K-ion, as well as understanding what the rate limitations are. The sluggish reaction kinetics and lower diffusivity in the KMF cathode requires nanosized particles to match the apparently faster kinetics of the graphite anode and achieve high rate performance, as is the case with LFP for LIBs. However, this increased surface area also exacerbates parasitic reactions and thus increases electrolyte consumption, decreasing coulombic efficiencies unless the electrolyte is exceptionally stable. This is particularly challenging at the high operating voltages of the KMF. The slow charge-transfer kinetics of the KMF must also be investigated, and optimisations explored. Nevertheless, this work again shows the electrolyte is the most critical barrier to realising commercially-viable fast-charging KIBs. Achieving high stability and faster transport electrolytes must now be the priority in K-ion research. This model can help guide the K-ion research community to develop optimised K-ion materials and electrolytes to realise fast-charging KIBs.

Overall, the modelling draws three critical conclusions. First, an electrolyte with faster transport properties than the leading research KFSI:TEP electrolyte is required to realise the potential fast-charging capabilities of K-ion. Second, if an electrolyte is developed with transport comparable with KFSI:DME or even LP57, the electrode active material transport becomes limiting in rate capability, not the electrolyte. To address the low $\widetilde{D}_{\mathrm{KMF}}$ and $\widetilde{D}_{\mathrm{g}}$ requires smaller particle sizes, making electrolyte stability even more important to maintain high coulombic efficiencies. The slower $j_{0,\mathrm{KMF}}$ than $j_{0,\mathrm{g}}$ reiterates the importance for researchers to focus on understanding the charge-transfer kinetics of the KMF cathode and improving them to match the faster kinetics at the graphite anode. Finally, should a stable electrolyte be developed, K-ion appears competitive with LFP Li-ion in rate capability. Though according to the model smaller graphite particle sizes are required, which again this increased surface area exacerbates parasitic reactions, resulting in increased absolute SEI formation during the formation cycle resulting in lower coulombic efficiencies.

Nevertheless, this remains a provisional DFN K-ion model with multiple simplifications and limitations as outlined. This model provides an indication of potential K-ion rate capability and material and electrolyte limitations, yet the model must be optimised, validated and developed with further characterisations, cell development, and modelling.

6 Conclusion and Future Work

6.1 Conclusion

Potassium-ion batteries (KIBs) are emerging as a promising alternative chemistry to lithium-ion batteries (LIBs) due to their significantly reduced dependency on critical minerals. The fact K^+ can reversibly intercalate into the graphite electrodes used in LIBs presents a major advantage over Na-ion, and the larger size of K^+ appears promising for faster electrolyte transport and charging rates due to its lower charge density. This thesis focuses on understanding the potential of K-ion batteries for fast-charging through a combination of fundamental property characterisation and full-cell modelling. Characterising these critical fundamental transport, kinetic and thermodynamic properties provides an understanding of the underlying material and electrolyte rate limitations as well as facilitates the development of novel materials and electrolytes. Since there is no current electrolyte which provides practical coulombic efficiencies, the full-cell modelling enables the potential rate performance of K-ion in commercial cell formats to be evaluated. In this thesis these fundamental rate-determining properties were characterised and the first full-cell DFN K-ion model developed, thus providing significant insight into the potential rate capability and the fundamental rate limitations of K-ion batteries. Following is a brief summary of the key results and conclusions.

In Chapter 3 the ionic transport and thermodynamic properties of a K-ion electrolyte were characterised for the first time, the model system characterised being the KFSI:DME electrolyte. The same properties were characterised in the same conditions for the Li-ion equivalent for comparison. To apply the most accurate electrolyte characterisation techniques, a K metal preparation protocol was developed which enabled sufficient stability for electrolyte characterisation. The results show the salt diffusivity and cation transference number of the KFSI:DME electrolyte is significantly higher than that of the LiFSI electrolyte for all concentrations below 2 m. This means significantly reduced concentration gradient formation, reducing concentration overpotentials, and thus faster ion transport. Slow electrolyte ion transport is one of the critical limitations for Li-ion fast charging, therefore, this is a promising result for K-ion fast-charging. The thermodynamic factor behaviour with concentration appears to indicate weaker solvent and ion-ion interactions of K^+ compared to Li^+. Provisional DFN simulations of K-ion and Li-ion graphite half-cells, using the electrolyte property relationships characterised here and the OCV profiles, demonstrates superior charging rates for the K-ion cell due to the combination of faster K-ion electrolyte transport and the ability of K graphite to experience larger overpotentials than Li graphite. Overall this work evidences for the first time that the larger K^+ size and lower charge density, and thus weaker solvent and ion-ion interactions does result in faster ion transport in K-ion electrolytes, which is promising for fast-charging.

In Chapter 4 the effective solid-state diffusivities $\widetilde{D_k}$ and exchange current densities j_{k0} of the leading K-ion electrode materials, graphite and KMF, were characterised for the first time. Through synthesising highly homogeneous and non-agglomerated KMF particles the electrochemically active surface area S, which is one of the most significant sources of error in $\widetilde{D_k}$ characterisation, was determined more accurately. The state-of-the-art Kang-Chueh GITT methodology and analysis was applied to characterise $\widetilde{D_k}$ more accurately for both materials. The results show the median $\widetilde{D}_{\mathrm{KMF}}$ is over four times lower than $\widetilde{D}_{\mathrm{g}}$ and $j_{0,\mathrm{KMF}}$ is an order of magnitude lower then $j_{0,\mathrm{g}}$. Therefore, the KMF cathode exhibits slower ionic

transport and particularly slower reaction kinetics than the graphite anode. This highlights the sluggish kinetics of the KMF is a critical area that cathode material research must focus on understanding and improving, in order to match the kinetics of the graphite anode.

In Chapter 5 all of the characterised critical rate-determining properties from the previous chapters were combined to conduct the first full-cell DFN modelling of a KIB. Multiple electrolyte cases were explored showing that the current leading K-ion electrolyte in the research community, KFSI:TEP, has too slow transport to be used at even moderate rates in commercial electrode thicknesses. Using an electrolyte with the properties of KFSI:DME or LP57 show that the electrode materials are rate limiting. To mitigate the slower solid-state diffusivity and charge transfer kinetics requires smaller particles, similar to LFP cathodes. However, this means electrolyte stability becomes even more important to maintain high coulombic efficiencies. Modelling LFP Li-ion for comparison shows, if a stable K-ion electrolyte is developed, K-ion appears competitive with LFP Li-ion in terms of rate capability. Overall the work of this chapter yet again emphasises the electrolyte is the most critical component to realising commercially-viable fast-charging KIBs, and development of a highly-stable, fast transport electrolyte is crucial.

Overall this thesis provides significant insights into the fundamental properties of K-ion electrolytes and electrode materials, as well as a deeper understanding of the fast-charging potential of KIBs and their material and electrolyte rate limitations. The results and insights generated can help guide the K-ion research community to focus on these limiting areas, and thus support the development of optimised materials and electrolytes to realise commercially-viable fast-charging KIBs. Given the uncertainty and risk surrounding the future supply of Li-ion critical minerals, I hope the results of this thesis can facilitate the development of KIBs as a supporting and more sustainable energy storage and electrification technology in the path to decarbonisation and climate change mitigation.

6.2 Future work

This research provides the foundation for multiple promising research fronts.

First, despite the improved stability through the K metal preparation protocol developed here, K metal remains too reactive to be a completely stable and reliable reference electrode. Therefore, to improve the accuracy of all electrochemical characterisation and evaluation of K-ion electrode materials the development of a reference electrode with a stable potential, which is chemically inert, should be prioritised. Exploring alloys which could also be used as a more stable counter electrode and even enable improved electrolyte characterisation could be particularly promising.

Second, since utilising the Kang-Chueh GITT enables significantly more accurate characterisation of D_k, it should be applied to other leading K-ion, Li-ion and Na-ion materials. Currently the Kang-Chueh GITT has not been applied to many Li-ion materials or any Na-ion electrode materials. Characterising $\widetilde{D}_\mathrm{k}$ for Li graphite would be a particularly interesting comparison, to understand whether $\widetilde{D}_\mathrm{k}$ of K graphite is truly slower than Li graphite as it appears from reported values using conventional GITT and other methods.

Building on the $\widetilde{D}_\mathrm{k}$ characterisation of the K-ion materials, the Kang-Chueh GITT could be extended to account for the contributions of parasitic currents to determine the Faradaic current more accurately and thus more accurately characterise $\widetilde{D}_\mathrm{k}$. By repeating pulses at the same stoichiometry at different current magnitudes, the parasitic current could be separated. Further, attempting to make dense, electrolyte-impenetrable pellets of the leading K-ion materials could be attempted to improve S estimation and ensure $\widetilde{D}_\mathrm{k}$ limitation.

In addition, Zsoldos *et al.* recently reported application of the Atlung Method for Intercalant Diffusion (AMID) to characterise D_k where S is not required and instead capacity is used to determine D_k[120]. Exploring this method on the leading K-ion electrode materials could also be interesting to compare against the Kang-Chueh methodology. Another area is to also explore and apply phase-field modelling and the multiphase work of Bazant *et al.*[117,118], accounting for phase changes, and

applying to the leading K-ion materials which are multiphase. This could possibly elucidate further insight into whether the effective diffusivity limitations are more due to transport or phase boundary movement. Finally, nonlinear EIS should be explored to investigate whether access to higher harmonics can enable more accurate characterisation of R_{ct} and hence j_{k0}. Nonlinear EIS has been used to successfully characterise Butler-Volmer charge-transfer coefficients, therefore, applying nonlinear EIS to characterise these coefficients for the leading K-ion battery materials would provide greater insight into the directional electrode material charge transfer kinetics, particularly important for the KMF material where they are significantly slower than the graphite. Greater understanding could help to develop material modifications to improve the KMF kinetics.

To further extend the accuracy of the KIB DFN model, accurate characterisation of the KMF electronic conductivity should be investigated. Since PBAs exhibit poor electronic conductivity, accurately characterising the electronic conductivity of KMF would enable more accurate determination of KMF rate capability and limitations. As mentioned, there is no viable electrolyte which produces practical coulombic efficiencies for K-ion, making any calibration or validation of the DFN K-ion model against galvanostatic cycling data difficult. However, there are degradation models of SEI growth[110,254] which could be adapted in combination with EIS measurements to try and capture some of the electrolyte decomposition reactions in the DFN model thus making some calibration and validation possible. Exploring the use of lumped thermal models together with characterisation at different temperatures could also improve modelling accuracy.

Finally, evaluating other K-ion electrolytes including additives utilising the characterisation methodologies utilised in this thesis will support K-ion electrolyte development. While also evaluating other electrolyte combinations for the KMF cathode material or modifications to the KMF cathode material itself such as dopants or surface coatings using the characterisation methodologies of this thesis to attempt to understand and improve the KMF charge-transfer kinetics. Conducting further fundamental characterisation and modelling will contribute to the development and

optimisation of novel K-ion materials and electrolytes, and ultimately support the realisation of viable KIBs.

Appendices

A
Appendix

Table A.1: Example graphite R1 and R2 values from EIS analysis

x	**R1**	**R2**	**RT (R1+R2)**
0	3405	1215	4620
0.09	6141	985	7127
0.18	5317	1016	6332
0.27	3997	1045	5042
0.36	3131	1049	4180
0.45	3166	1056	4222
0.55	3568	1072	4640
0.64	2791	1063	3854
0.73	2579	1056	3635
0.82	2528	1056	3584
0.91	2374	1065	3439
1.00	4042	1212	5254

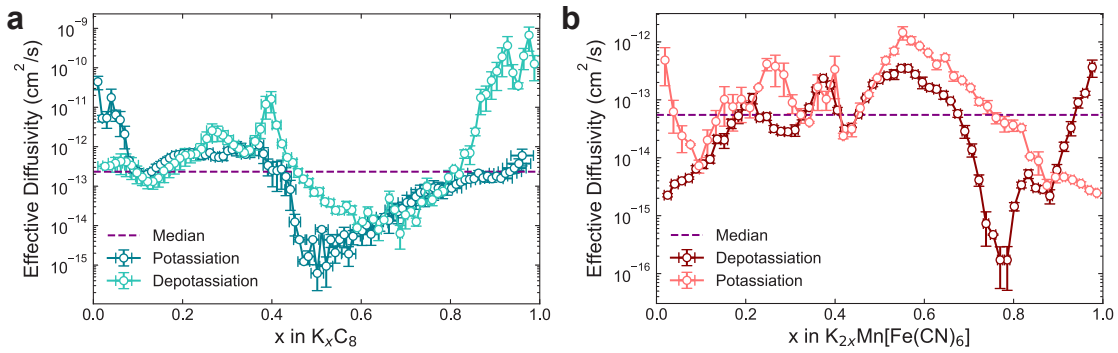


Figure A.1 Median diffusivities used in the modelling (**a**) graphite (**b**) KMF. Adapted from Dhir *et al.*[171]

Table A.2: Example KMF R1 and R2 values from EIS analysis

x	R1	R2	RT (R1+R2)
0.02	995	1301	2296
0.09	1015	440	1456
0.24	1039	259	1298
0.39	1039	499	1538
0.54	1052	346	1398
0.70	539	429	968
0.85	390	530	920
1.00	3142	865	4007

Table A.3: K-ion DFN modelling parameters

Parameter	Value	Unit	Reference
Cell Parameters			
Current collector thickness	16	µm	[113]
Current collector conductivity	3.6914×10^5	S cm^{-1}	[113]
Current collector density	2700	kg m^{-3}	[113]
Negative electrode thickness	53.319	µm	This work
Separator thickness	12	µm	[113]
Positive electrode thickness	88.224	µm	This work
Electrode height	6.52	cm	[113]
Electrode width	1.58	m	[113]
Negative Electrode Parameters			
Electronic Conductivity	2.15	S cm^{-1}	[113]
Maximum concentration	23301	mol m^{-3}	This work
Diffusivity, $\widetilde{D}_{\mathrm{g}}$	2.32×10^{-13} (Figure A.1a)	cm^2 s^{-1}	This work
OCV	Figure 4.5a	V	This work
Porosity	0.35	—	[105]
Active material volume fraction	0.65	—	
Particle radius	500	nm	
Bruggeman coefficient (electrolyte)	1.5	—	[113]
Bruggeman coefficient (electrode)	1.5	—	[113]
Electrons in reaction	1	—	
Charge-transfer coefficient, α_a	0.5	—	
Exchange current density, $j_{0,\mathrm{g}}$	Equation 1.15 and Figure 4.9	A cm^{-2}	This work
Density	2239	kg m^{-3}	[255]
Positive Electrode Parameters			
Electronic Conductivity	3.38×10^{-3}	S cm^{-1}	[248]
Maximum concentration	12875	mol m^{-3}	This work
Diffusivity, $\widetilde{D}_{\mathrm{KMF}}$	5.5040×10^{-14} (Figure A.1b)	cm^2 s^{-1}	This work
OCV	Figure 4.14a	V	This work
Porosity	0.35	—	[105]
Active material volume fraction	0.65	—	
Particle radius	250	nm	
Bruggeman coefficient (electrolyte)	1.5	—	[113]
Bruggeman coefficient (electrode)	1.5	—	[113]
Electrons in reaction	2	—	
Charge-transfer coefficient, α_c	0.5	—	
Exchange current density, $j_{0,\mathrm{KMF}}$	Equation 1.15 and Figure 4.18a	A cm^{-2}	This work
Density	2221	kg m^{-3}	This work

Table A.3: (Continued) K-ion DFN modelling parameters

Separator Parameters			
Porosity	0.47	—	[113]
Bruggeman coefficient (electrolyte)	1.5	—	[113]
Density	397	kg m^{-3}	[113]
Electrolyte Parameters - KFSI TEP			
Initial concentration	1.75 (2 molal)	mol L^{-1}	
Cation transference number, t_+^0	0.351	—	[171]
Thermodynamic factor, χ_M	6.477	—	[171]
Salt diffusivity, D	3.727	m^2 s^{-11}	[171]
Ionic conductivity, κ	3.053	mS cm^{-1}	[171]
Electrolyte Parameters - KFSI DME			
Initial concentration	1.57 (2 molal)	mol L^{-1}	
Cation transference number, t_+^0	Section 3.3.5	—	This work[170]
Thermodynamic factor, χ_M	Section 3.3.5	—	This work[170]
Salt diffusivity, D	Section 3.3.5	m^2 s^{-1}	This work[170]
Ionic conductivity, κ	Section 3.3.5	mS cm^{-1}	This work[170]
Model Parameters			
Lower voltage cut-off	2.85	V	This work
Upper voltage cut-off	4.125	V	This work
Initial negative electrode concentration	22396	mol m^{-3}	This work
Initial positive electrode concentration	100	mol m^{-3}	This work
Initial temperature	293.15	K	

Table A.4: LFP Li-ion DFN modelling parameters

Parameter	Value	Unit	Reference
Cell Parameters			
Negative current collector thickness	12	µm	[113]
Positive current collector thickness	16	µm	[113]
Negative current collector conductivity	5.8411×10^5	S cm^{-1}	[113]
Positive current collector conductivity	3.6914×10^5	S cm^{-1}	[113]
Negative current collector density	8960	kg m^{-3}	[113]
Positive current collector density	2700	kg m^{-3}	[113]
Negative electrode thickness	46.2	µm	This work
Separator thickness	12	µm	[113]
Positive electrode thickness	67.2	µm	This work
Electrode height	6.52	cm	[113]
Electrode width	1.58	m	[113]
Negative Electrode Parameters			
Electronic Conductivity	2.15	S cm^{-1}	[113]
Maximum concentration	30555	mol m^{-3}	[113]
Diffusivity, $\widetilde{D}_{\mathrm{g}}$	3.14×10^{-10}	cm^2 s^{-1}	[113]
OCV	Function	V	[113]
Porosity	0.25	—	[113]
Active material volume fraction	0.75	—	
Particle radius	500	nm	
Bruggeman coefficient (electrolyte)	1.5	—	[113]
Bruggeman coefficient (electrode)	1.5	—	[113]
Electrons in reaction	1	—	
Charge-transfer coefficient, α_a	0.5	—	
Exchange current density, Function	A cm^{-2}	[113]	
Density	2239	kg m^{-3}	[105]
Positive Electrode Parameters			
Electronic Conductivity	3.38×10^{-3}	S cm^{-1}	[248]
Maximum concentration	22806	mol m^{-3}	[248]
Diffusivity, $\widetilde{D}_{\mathrm{KMF}}$	5.9×10^{-14}	cm^2 s^{-1}	[248]
OCV	Function	V	[248]
Porosity	0.335	—	[105]
Active material volume fraction	0.665	—	
Particle radius	250	nm	
Bruggeman coefficient (electrolyte)	1.5	—	[113]
Bruggeman coefficient (electrode)	1.5	—	[113]
Electrons in reaction	1	—	[248]
Charge-transfer coefficient, α_c	0.5	—	
Exchange current density, $j_{0,\mathrm{LFP}}$	Function	A cm^{-2}	[247,248]
Density	3450	kg m^{-3}	[105]

Table A.3: (Continued) LFP Li-ion DFN modelling parameters

Separator Parameters			
Porosity	0.47	—	[113]
Bruggeman coefficient (electrolyte)	1.5	—	[113]
Density	397	kg m^{-3}	[113]
Electrolyte Parameters - LiFSI DME			
Initial concentration	1	mol L^{-1}	
Cation transference number, t_+^0	0.352	—	This work[170]
Thermodynamic factor, χ_M	Section 3.3.5	—	This work[170]
Salt diffusivity, D	Section 3.3.5	m^2 s^{-1}	This work[170]
Ionic conductivity, κ	Section 3.3.5	mS cm^{-1}	This work[170]
Model Parameters			
Lower voltage cut-off	2	V	[248]
Upper voltage cut-off	3.6	V	[248]
Initial negative electrode concentration	24749.6	mol m^{-3}	[248]
Initial positive electrode concentration	86.7	mol m^{-3}	[248]
Initial temperature	293.15	K	

References

1. Dhir, S. *et al.* Outlook on K-Ion Batteries. *Chem* **6,** 2442–2460 (2020).
2. IPCC. *AR6 Synthesis Report: Climate Change 2023* tech. rep. (2023).
3. IPCC. *Climate Change 2022 Mitigation of Climate Change Working Group III Contribution to the Sixth Assessment Report of the Intergovernmental Panel on Climate Change Summary for Policymakers* tech. rep. (2022).
4. IEA. *Net Zero Roadmap: A Global Pathway to Keep the 1.5 °C Goal in Reach* tech. rep. (2023).
5. IEA. *CO2 Emissions in 2022* tech. rep. (2022).
6. IEA. *Annual grid-scale battery storage additions, 2017-2022* 2023.
7. International Transport Forum OECD. ITF Transport Outlook 2023 (2023).
8. IEA. Global EV Outlook 2023: Catching up with climate ambitions (2023).
9. IEA. Global EV Outlook 2022 (2022).
10. BloombergNEF. *Lithium-Ion Battery Pack Prices Hit Record Low of $139/kWh* 2023.
11. Benchmark Mineral Intelligence. *Global cell prices fall below $100/kWh for first time in two years* 2023.
12. IEA. *Critical Minerals Market Review 2023* 2023.
13. IEA. *The Role of Critical Minerals in Clean Energy Transitions* 2021.
14. Frith, J. T. *et al.* A non-academic perspective on the future of lithium-based batteries. *Nature Communications 2023 14:1* **14,** 1–17 (2023).
15. Bibra, E. M. *et al.* Global EV Outlook 2022: Securing Supplies for an Electric Future. *IEA* (2022).
16. IEA. *Prohibition of the export of nickel ore* 2023.
17. Amnesty International. *Democratic Republic of Congo: "This is what we die for": Human rights abuses in the Democratic Republic of the Congo power the global trade in cobalt* 2016.
18. Banza Lubaba Nkulu, C. *et al.* Sustainability of artisanal mining of cobalt in DR Congo. *Nature Sustainability* **1,** 495–504 (2018).
19. Hosaka, T. *et al.* Research Development on K-Ion Batteries. *Chemical Reviews,* acs.chemrev.9b00463 (2020).
20. Sada, K. *et al.* Challenges and Prospects of Sodium-Ion and Potassium-Ion Batteries for Mass Production. *Advanced Energy Materials,* 2302321 (2023).

21. Tapia-Ruiz, N. *et al.* 2021 roadmap for sodium-ion batteries. *Journal of Physics: Energy* **3,** 031503 (2021).

22. Xiao, A. W. *et al.* The case for fluoride-ion batteries. *Joule* **5,** 2823–2844 (2021).

23. US Geological Survey. *Mineral Commodity Summaries 2023* tech. rep. (2023).

24. Roberts, S. *et al. The re-emergence of sodium ion batteries: Testing, processing, and manufacturability* 2018.

25. Jian, Z. *et al.* Carbon Electrodes for K-Ion Batteries. *Journal of the American Chemical Society* **137,** 11566–11569 (2015).

26. Komaba, S. *et al.* Potassium intercalation into graphite to realize high-voltage/high-power potassium-ion batteries and potassium-ion capacitors. *Electrochemistry Communications* **60,** 172–175 (2015).

27. Matsuda, Y. Behavior of Some Ions in Mixed Organic Electrolytes of High Energy Density Batteries. *Journal of The Electrochemical Society* **128,** 2552 (1981).

28. Hosaka, T. *et al.* KFSA/glyme electrolytes for 4 V-class K-ion batteries. *Journal of Materials Chemistry A* **8,** 23766–23771 (2020).

29. Li, M. *et al.* Fast Charging Li-Ion Batteries for a New Era of Electric Vehicles. *Cell Reports Physical Science* **1,** 100212 (2020).

30. Tomaszewska, A. *et al.* Lithium-ion battery fast charging: A review. *eTransportation* **1,** 100011 (2019).

31. Jagger, B. *et al.* Solid electrolyte interphases in lithium metal batteries. *Joule* **7,** 2228–2244 (2023).

32. Abe, T. *et al.* Solvated Li-Ion Transfer at Interface Between Graphite and Electrolyte. *Journal of The Electrochemical Society* **151,** A1120 (2004).

33. Barthel, J. *et al.* The Temperature Dependence of the Properties of Electrolyte Solutions. III. Conductance of Various Salts at High Concentrations in Propylene Carbonate at Temperatures from 45°C to + 25°C. *Berichte der Bunsengesellschaft für physikalische Chemie* **83,** 911–920 (1979).

34. Marcus, Y. Are ionic stokes radii of any use? *Journal of Solution Chemistry* **41,** 2082–2090 (2012).

35. Hosaka, T. *et al.* Highly concentrated electrolyte solutions for 4 V class potassium-ion batteries. *Chemical Communications* **54,** 8387–8390 (2018).

36. Bie, X. *et al.* A novel K-ion battery: hexacyanoferrate(ii)/graphite cell. *Journal of Materials Chemistry A* **5,** 4325–4330 (2017).

37. Xue, L. *et al.* Low-Cost High-Energy Potassium Cathode. *Journal of the American Chemical Society* **139,** 2164–2167 (2017).

38. Fiore, M. *et al.* Paving the Way toward Highly Efficient, High-Energy Potassium-Ion Batteries with Ionic Liquid Electrolytes. *Chemistry of Materials* **32,** 7661 (2020).

39. Deng, T. *et al.* Layered P2-Type K0.65Fe0.5Mn0.5O2 Microspheres as Superior Cathode for High-Energy Potassium-Ion Batteries. *Advanced Functional Materials* **28,** 1800219 (2018).
40. Wang, X. *et al.* Earth Abundant Fe/Mn-Based Layered Oxide Interconnected Nanowires for Advanced K-Ion Full Batteries. *Nano Letters* **17,** 544–550 (2017).
41. Kim, H. *et al.* Investigation of Potassium Storage in Layered P3-Type K0.5MnO2 Cathode. *Advanced Materials* **29,** 1702480 (2017).
42. Lin, X. *et al.* K3V2(PO4)2F3 as a robust cathode for potassium-ion batteries. *Energy Storage Materials* **16,** 97–101 (2019).
43. Chihara, K. *et al.* KVPO4F and KVOPO4 toward 4 volt-class potassium-ion batteries. *Chemical Communications* **53,** 5208–5211 (2017).
44. Kim, H. *et al.* A New Strategy for High-Voltage Cathodes for K-Ion Batteries: Stoichiometric KVPO 4 F Potassium-Ion Batteries (2018).
45. Mathew, V. *et al.* Amorphous iron phosphate: Potential host for various charge carrier ions. *NPG Asia Materials* **6** (2014).
46. Hosaka, T. *et al.* Polyanionic Compounds for Potassium-Ion Batteries. *The Chemical Record* **19,** 735–745 (2019).
47. Ma, J. *et al.* Endowing CuTCNQ with a new role: A high-capacity cathode for K-ion batteries. *Chemical Communications* **54,** 5578–5581 (2018).
48. Jian, Z. *et al.* Hard Carbon Microspheres: Potassium-Ion Anode Versus Sodium-Ion Anode. *Advanced Energy Materials* **6,** 1501874 (2016).
49. Hironaka, Y. *et al.* P2- and P3-KxCoO2 as an electrochemical potassium intercalation host. *Chemical Communications* **53,** 3693–3696 (2017).
50. Rajagopalan, R. *et al.* Advancements and Challenges in Potassium Ion Batteries: A Comprehensive Review. *Advanced Functional Materials,* 1909486 (2020).
51. Hurlbutt, K. *et al.* Prussian Blue Analogs as Battery Materials. *Joule* **2,** 1950–1960 (2018).
52. Eftekhari, A. *et al. Potassium Secondary Batteries* 2017.
53. Wu, X. *et al.* Highly Crystallized Na2CoFe(CN)6 with Suppressed Lattice Defects as Superior Cathode Material for Sodium-Ion Batteries. *ACS Applied Materials and Interfaces* **8,** 5393–5399 (2016).
54. Jiang, L. *et al.* Building aqueous K-ion batteries for energy storage. *Nature Energy* **4,** 495–503 (2019).
55. He, G. *et al.* Crystallite Size Control of Prussian White Analogues for Nonaqueous Potassium-Ion Batteries. *ACS Energy Letters* **2,** 1122–1127 (2017).
56. You, Y. *et al.* Subzero-Temperature Cathode for a Sodium-Ion Battery. *Advanced Materials* **28,** 7243–7248 (2016).

57. Moritomo, Y. *et al.* Glucose-treated manganese hexacyanoferrate for sodium-ion secondary battery. *Energies* **8,** 9486–9494 (2015).

58. Recham, N. *et al.* Preparation and characterization of a stable FeSO4F-based framework for alkali ion insertion electrodes. *Chemistry of Materials* **24,** 4363–4370 (2012).

59. Yamamoto, H. *et al.* Synthesizing higher-capacity hard-carbons from cellulose for Na- and K-ion batteries. *Journal of Materials Chemistry A* **6,** 16844–16848 (2018).

60. Jian, Z. *et al.* Hard-Soft Composite Carbon as a Long-Cycling and High-Rate Anode for Potassium-Ion Batteries. *Advanced Functional Materials* **27,** 1700324 (2017).

61. Wang, L. *et al.* TiS2 as a high performance potassium ion battery cathode in ether-based electrolyte. *Energy Storage Materials* **12,** 216–222 (2018).

62. Bin, D. S. *et al.* Engineering Hollow Carbon Architecture for High-Performance K-Ion Battery Anode. *Journal of the American Chemical Society* **140,** 7127–7134 (2018).

63. Share, K. *et al.* Role of Nitrogen-Doped Graphene for Improved High-Capacity Potassium Ion Battery Anodes. *ACS Nano* **10,** 9738–9744 (2016).

64. Xiong, H. *et al.* Carbon-polytetrahydrofuran double-coated Na3V2(PO4)2F3 submicron-composite as high-energy/power cathode material for sodium metal battery. *Journal of the Electrochemical Society* **165,** A746–A756 (2018).

65. Zhang, W. *et al.* Phosphorus-Based Alloy Materials for Advanced Potassium-Ion Battery Anode. *Journal of the American Chemical Society* **139,** 3316–3319 (2017).

66. Niu, X. *et al.* Amorphous FeVO4 as a promising anode material for potassium-ion batteries. *Energy Storage Materials* **22,** 160–167 (2019).

67. Lei, K. *et al.* High K-storage performance based on the synergy of dipotassium terephthalate and ether-based electrolytes. *Energy and Environmental Science* **10,** 552–557 (2017).

68. Dong, S. *et al.* Novel Potassium-Ion Hybrid Capacitor Based on an Anode of K2Ti6O13 Microscaffolds. *ACS Applied Materials and Interfaces* **10,** 15542–15547 (2018).

69. Wei, Z. *et al.* Fabrication of Hierarchical Potassium Titanium Phosphate Spheroids: A Host Material for Sodium-Ion and Potassium-Ion Storage. *Advanced Energy Materials* **8,** 1801102 (2018).

70. Zhang, H. *et al.* Graphite as anode materials: Fundamental mechanism, recent progress and advances. *Energy Storage Materials* **36,** 147–170 (2021).

71. Zhao, J. *et al.* Electrochemical Intercalation of Potassium into Graphite. *Advanced Functional Materials* **26,** 8103–8110 (2016).

72. Wang, L. *et al.* Rhombohedral Prussian white as cathode for rechargeable sodium-ion batteries. *Journal of the American Chemical Society* **137,** 2548–2554 (2015).

73. Liu, C. *et al. Understanding electrochemical potentials of cathode materials in rechargeable batteries* 2016.

74. Jian, Z. *et al.* Hard Carbon Microspheres: Potassium-Ion Anode Versus Sodium-Ion Anode. *Advanced Energy Materials* **6,** 1501874 (2016).

75. He, H. *et al.* Tuning nitrogen species in three-dimensional porous carbon via phosphorus doping for ultra-fast potassium storage. *Nano Energy* **57,** 728–736 (2019).

76. Luo, W. *et al.* Electrochemically expandable soft carbon as anodes for Na-ion batteries. *ACS Central Science* **1,** 516–522 (2015).

77. Kim, H. *et al.* A New Strategy for High-Voltage Cathodes for K-Ion Batteries: Stoichiometric KVPO 4 F Potassium-Ion Batteries (2018).

78. McCulloch, W. D. *et al.* Potassium-Ion Oxygen Battery Based on a High Capacity Antimony Anode. *ACS Applied Materials and Interfaces* **7,** 26158–26166 (2015).

79. Huang, J. *et al.* Bismuth Microparticles as Advanced Anodes for Potassium-Ion Battery. *Advanced Energy Materials* **8,** 1703496 (2018).

80. Wang, C. *et al.* Potassium perylene-tetracarboxylate with two-electron redox behaviors as a highly stable organic anode for K-ion batteries. *Chemical Communications* **55,** 1801–1804 (2019).

81. Dong, Y. *et al.* Ti3C2 MXene-Derived Sodium/Potassium Titanate Nanoribbons for High-Performance Sodium/Potassium Ion Batteries with Enhanced Capacities. *ACS Nano* **11,** 4792–4800 (2017).

82. Han, J. *et al.* Exploration of K2Ti8O17 as an anode material for potassium-ion batteries. *Chemical Communications* **52,** 11274–11276 (2016).

83. Okoshi, M. *et al.* Theoretical analysis of interactions between potassium ions and organic electrolyte solvents: A comparison with lithium, sodium, and magnesium ions. *Journal of the Electrochemical Society* **164,** A54–A60 (2017).

84. Kubota, K. *et al.* Towards K-Ion and Na-Ion Batteries as "Beyond Li-Ion". *The Chemical Record* **18,** 459–479 (2018).

85. Amara, S. *et al.* Comparative Study of Alkali-Cation-Based (Li + , Na + , K +) Electrolytes in Acetonitrile and Alkylcarbonates. *ChemPhysChem* **20,** 581–594 (2019).

86. Wang, M. *et al.* Synthesis and electrochemical performances of Na3V2(PO4)2F3/C composites as cathode materials for sodium ion batteries. *RSC Advances* **9,** 30628–30636 (2019).

87. Yamamoto, T. *et al.* Physicochemical and Electrochemical Properties of K[N(SO2F)2]-[N-Methyl-N-propylpyrrolidinium][N(SO2F)2] Ionic Liquids for Potassium-Ion Batteries. *Journal of Physical Chemistry C* **121,** 18450–18458 (2017).

88. Zhang, T. *et al.* Sodium ion batteries particles: Phase-field modeling with coupling of Cahn-Hilliard equation and finite deformation elasticity. *Journal of the Electrochemical Society* **165,** A1997–A2007 (2018).

89. Hui, J. *et al.* Achieving Fast and Efficient K+ Intercalation on Ultrathin Graphene Electrodes Modified by a Li+ Based Solid-Electrolyte Interphase. *Journal of the American Chemical Society* **140,** 13599–13603 (2018).

90. Komaba, S. *et al.* Fluorinated ethylene carbonate as electrolyte additive for rechargeable Na batteries. *ACS Applied Materials and Interfaces* **3,** 4165–4168 (2011).

91. Hosaka, T. *et al.* Development of KPF6/KFSA Binary-Salt Solutions for Long-Life and High-Voltage K-Ion Batteries. *ACS Applied Materials and Interfaces* **12,** 34873–34881 (2020).

92. Deng, L. *et al.* Defect-free potassium manganese hexacyanoferrate cathode material for high-performance potassium-ion batteries. *Nature Communications 2021 12:1* **12,** 1–9 (2021).

93. Liu, S. *et al.* An Intrinsically Non-flammable Electrolyte for High-Performance Potassium Batteries. *Angewandte Chemie International Edition* **59,** 3638–3644 (2020).

94. Deng, L. *et al.* A Nonflammable Electrolyte Enabled High Performance K0.5MnO2Cathode for Low-Cost Potassium-Ion Batteries. *ACS Energy Letters* **5,** 1916–1922 (2020).

95. Nelson, P. A. *et al. Modeling the Performance and Cost of Lithium-Ion Batteries for Electric-Drive Vehicles, Third Edition* tech. rep. (2019).

96. Hesse, H. *et al.* Lithium-Ion Battery Storage for the Grid—A Review of Stationary Battery Storage System Design Tailored for Applications in Modern Power Grids. *Energies* **10,** 2107 (2017).

97. Mauger, A. *et al. Olivine positive electrodes for li-ion batteries: Status and perspectives* 2018.

98. Billaud, J. *et al.* β-NaMnO2 : A High-Performance Cathode for Sodium-Ion Batteries. *Journal of the American Chemical Society* **136,** 17243–17248 (2014).

99. Vaalma, C. *et al. A cost and resource analysis of sodium-ion batteries* 2018.

100. LME. *London Metal Exchange: Lithium prices* 2020.

101. Firouzi, A. *et al.* Monovalent manganese based anodes and co-solvent electrolyte for stable low-cost high-rate sodium-ion batteries. *Nature Communications* **9,** 1–10 (2018).

102. Bauer, A. *et al.* The Scale-up and Commercialization of Nonaqueous Na-Ion Battery Technologies. *Advanced Energy Materials* **8,** 1702869 (2018).

103. Ahn, D. *et al.* Variations of the Electrochemical Properties of LiMnO with Synthesis Conditions. *Journal of The Electrochemical Society* **147,** 874 (2000).

104. Barnhart, C. J. *et al.* On the importance of reducing the energetic and material demands of electrical energy storage. *Energy and Environmental Science* **6,** 1083–1092 (2013).

105. Nelson, P. A. *et al. Modeling the Performance and Cost of Lithium-Ion Batteries for Electric-Drive Vehicles, Fifth Edition* tech. rep. ANL/CSE-19/2 (Argonne National Laboratory (ANL), Argonne, IL (United States), 2023).

106. Dahn, J. R. *et al.* Importance of coulombic efficiency measurements in R & D efforts to obtain long-lived li-ion batteries. *Electrochemical Society Interface* **25,** 75–78 (2016).

107. Lagadec, M. F. *et al.* Characterization and performance evaluation of lithium-ion battery separators. *Nature Energy* **4,** 16–25 (2019).

108. Doyle, M. *et al.* Modeling of galvanostatic charge and discharge of the lithium/ polymer/insertion cell. *Journal of the Electrochemical Society* **140,** 1526–1533 (1993).

109. Wang, A. A. *et al.* Review of parameterisation and a novel database (LiionDB) for continuum Li-ion battery models. *Progress in Energy* **4,** 032004 (2022).

110. Brosa Planella, F. *et al.* A continuum of physics-based lithium-ion battery models reviewed. *Progress in Energy* **4,** 042003 (2022).

111. Ecker, M. *et al.* Parameterization of a Physico-Chemical Model of a Lithium-Ion Battery. *Journal of The Electrochemical Society* **162,** A1836–A1848 (2015).

112. Ecker, M. *et al.* Parameterization of a Physico-Chemical Model of a Lithium-Ion Battery II. Model Validation. *Journal of The Electrochemical Society* **162,** A1849–A1857 (2015).

113. Chen, C.-H. *et al.* Development of Experimental Techniques for Parameterization of Multi-scale Lithium-ion Battery Models. *Journal of The Electrochemical Society* **167,** 080534 (2020).

114. Zülke, A. *et al.* Parametrisation and Use of a Predictive DFN Model for a High-Energy NCA/Gr-SiOx Battery. *Journal of The Electrochemical Society* **168,** 120522 (2021).

115. Newman, J. *Electrochemical Systems, 3rd Edition* enus (2004).

116. Suthar, B. *et al.* Numerical Simulation of Intercalation-Induced Stress in Li-Ion Battery Electrode Particles. *Journal of The Electrochemical Society* **154,** A910 (2007).

117. Bazant, M. Z. Theory of chemical kinetics and charge transfer based on nonequilibrium thermodynamics. *Accounts of Chemical Research* **46,** 1144–1160 (2013).

118. Zhao, H. *et al.* Learning heterogeneous reaction kinetics from X-ray videos pixel by pixel. *Nature* **621,** 289–294 (2023).

119. Kang, S. D. *et al.* Galvanostatic Intermittent Titration Technique Reinvented: Part I. A Critical Review. *Journal of The Electrochemical Society* **168,** 120504 (2021).

120. Zsoldos, E. *et al.* How to Measure Solid State Lithium-ion Diffusion using the Atlung Method for Intercalant Diffusion. *Journal of The Electrochemical Society* **170,** 040511 (2023).

121. Hou, T. *et al.* Composition-dependent thermodynamic and mass-transport characterization of lithium hexafluorophosphate in propylene carbonate. *Electrochimica Acta* **332,** 135085 (2020).

122. Bergstrom, H. K. *et al.* Interfacial Effects on Transport Coefficient Measurements in Li-ion Battery Electrolytes. *Journal of The Electrochemical Society* **168,** 060543 (2021).

123. Landesfeind, J. *et al.* Temperature and Concentration Dependence of the Ionic Transport Properties of Lithium-Ion Battery Electrolytes. *Journal of The Electrochemical Society* **166,** A3079–A3097 (2019).

124. Nyman, A. *et al.* Electrochemical characterisation and modelling of the mass transport phenomena in LiPF6-EC-EMC electrolyte. *Electrochimica Acta* **53,** 6356–6365 (2008).

125. Valoen, L. O. *et al.* Transport Properties of LiPF[sub 6]-Based Li-Ion Battery Electrolytes. *Journal of The Electrochemical Society* **152,** A882 (2005).

126. Lundgren, H. *et al.* Electrochemical Characterization and Temperature Dependency of Mass-Transport Properties of LiPF 6 in EC:DEC. *Journal of The Electrochemical Society* **162,** A413–A420 (2015).

127. Lundgren, H. *et al.* Characterization of the Mass-Transport Phenomena in a Superconcentrated LiTFSI:Acetonitrile Electrolyte. *Journal of The Electrochemical Society* **162,** A1334–A1340 (2015).

128. Steinrück, H.-G. *et al.* Concentration and velocity profiles in a polymeric lithium-ion battery electrolyte. *Energy & Environmental Science* (2020).

129. Fawdon, J. *et al.* Characterising lithium-ion electrolytes via operando Raman microspectroscopy. *Nature Communications* **12,** 1–9 (2021).

130. Wang, A. A. *et al.* Potentiometric MRI of a Superconcentrated Lithium Electrolyte: Testing the Irreversible Thermodynamics Approach. *ACS Energy Letters* **6,** 3086–3095 (2021).

131. Bazak, J. D. *et al.* Mapping of Lithium-Ion Battery Electrolyte Transport Properties and Limiting Currents with In Situ MRI. *Journal of The Electrochemical Society* **167,** 140518 (2020).

132. Diederichsen, K. M. *et al.* Promising Routes to a High Li+ Transference Number Electrolyte for Lithium Ion Batteries. *ACS Energy Letters* **2,** 2563–2575 (2017).

133. Bruce, P. G. *et al.* Steady state current flow in solid binary electrolyte cells. *Journal of Electroanalytical Chemistry and Interfacial Electrochemistry* **225,** 1–17 (1987).

134. Ma, Y. *et al.* The Measurement of a Complete Set of Transport Properties for a Concentrated Solid Polymer Electrolyte Solution. *Journal of The Electrochemical Society* **142,** 1859–1868 (1995).

135. Ehrl, A. *et al.* Determination of Transport Parameters in Liquid Binary Electrolytes: Part II. Transference Number. *Journal of The Electrochemical Society* **164,** A2716–A2731 (2017).

136. Xu, K. Navigating the minefield of battery literature. *Communications Materials 2022 3:1* **3,** 1–7 (2022).

137. Wang, A. A. *et al.* Shifting-reference concentration cells to refine composition-dependent transport characterization of binary lithium-ion electrolytes. *Electrochimica Acta* **358,** 136688 (2020).

138. Wang, A. A. *et al.* Current-driven solvent segregation in lithium- ion electrolytes Current-driven solvent segregation in lithium-ion electrolytes. *Cell Reports Physical Science,* 101047 (2022).

139. Mistry, A. *et al.* Do we need an accurate understanding of transport in electrolytes? *Joule* **0** (2021).

140. Harned, H. S. *et al.* A CONDUCTANCE METHOD FOR THE DETERMINATION OF THE DIFFUSION COEFFICIENTS OF ELECTROLYTES. *Annals of the New York Academy of Sciences* **46,** 267–284 (1945).

141. Newman, J. *et al.* Restricted diffusion in binary solutions. *AIChE Journal* **19,** 343–348 (1973).

142. Ehrl, A. *et al.* Determination of Transport Parameters in Liquid Binary Lithium Ion Battery Electrolytes. *Journal of The Electrochemical Society* **164,** A826–A836 (2017).

143. Landesfeind, J. *et al.* Comparison of Ionic Transport Properties of Non-Aqueous Lithium and Sodium Hexafluorophosphate Electrolytes. *Journal of The Electrochemical Society* **168,** 040538 (2021).

144. Wang, A. A. *et al.* Potentiometric MRI of a Superconcentrated Lithium Electrolyte: Testing the Irreversible Thermodynamics Approach. *ACS Energy Letters* **6,** 3086–3095 (2021).

145. Orazem, M. E. *et al.* Electrochemical Impedance Spectroscopy. *Electrochemical Impedance Spectroscopy,* 1–523 (2008).

146. Wang, S. *et al.* Electrochemical impedance spectroscopy. *Nature Reviews Methods Primers 2021 1:1* **1,** 1–21 (2021).

147. Peng, L. *et al.* Self-assembled LiNi1/3Co1/3Mn1/3O2 nanosheet cathodes with tunable rate capability. *Nano Energy* **17,** 36–42 (2015).

148. Cui, S. *et al.* Optimized Temperature Effect of Li-Ion Diffusion with Layer Distance in Li(NixMnyCoz)O2 Cathode Materials for High Performance Li-Ion Battery. *Advanced Energy Materials* **6,** 1501309 (2016).

149. Li, Z. *et al.* Towards understanding the rate capability of layered transition metal oxides LiNiyMnyCo12yO2. *Journal of Power Sources* **268,** 106–112 (2014).

150. Tsai, P. C. *et al.* Single-particle measurements of electrochemical kinetics in NMC and NCA cathodes for Li-ion batteries. *Energy & Environmental Science* **11,** 860–871 (2018).

151. Li, i. *et al.* Characterization of Electronic and Ionic Transport in Li1-xNi0.33Mn0.33Co0.33O2 (NMC333) and Li1-xNi0.50Mn0.20Co0.30O2 (NMC523) as a Function of Li Content. *Journal of The Electrochemical Society* **163,** A1512 (2016).

152. Wu, S.-L. *et al.* High Rate Capability of Li(Ni 1/3 Mn 1/3 Co 1/3)O 2 Electrode for Li-Ion Batteries. *Journal of The Electrochemical Society* **159,** A438–A444 (2012).

153. Weppner, W. *et al.* Determination of the Kinetic Parameters of Mixed-Conducting Electrodes and Application to the System Li3Sb. *Journal of The Electrochemical Society* **124,** 1569–1578 (1977).

154. Wen, C. J. *et al.* Thermodynamic and mass transport properties of "LiAl". *Materials Research Bulletin* **15,** 1225–1234 (1979).

155. Komayko, A. I. *et al.* Resolving the Seeming Contradiction between the Superior Rate Capability of Prussian Blue Analogues and the Extremely Slow Ionic Diffusion. *Journal of Physical Chemistry Letters* **13,** 3165–3172 (2022).

156. Han, B. C. *et al.* Electrochemical modeling of intercalation processes with phase field models. *Electrochimica Acta* **49,** 4691–4699 (2004).

157. Ahn, S. *et al.* Chemical Origins of a Fast-Charge Performance in Disordered Carbon Anodes. *ACS Applied Energy Materials* (2023).

158. Jia, M. *et al.* Re-understanding the galvanostatic intermittent titration technique: Pitfalls in evaluation of diffusion coefficients and rational suggestions. *Journal of Power Sources* **543,** 231843 (2022).

159. Zhu, Y. *et al.* Galvanostatic intermittent titration technique for phase-transformation electrodes. *Journal of Physical Chemistry C* **114,** 2830–2841 (2010).

160. Levi, M. D. *et al.* The application of electroanalytical methods to the analysis of phase transitions during intercalation of ions into electrodes. *Journal of Solid State Electrochemistry* **11,** 1031–1042 (2007).

161. Smith, R. B. *et al.* Multiphase Porous Electrode Theory (2017).

162. Markevich, E. *et al.* Comparison between potentiostatic and galvanostatic intermittent titration techniques for determination of chemical diffusion coefficients in ion-insertion electrodes. *Journal of Electroanalytical Chemistry* **580,** 231–237 (2005).

163. Hallemans, N. *et al.* Electrochemical impedance spectroscopy beyond linearity and stationarity—A critical review. *Electrochimica Acta* **466,** 142939 (2023).

164. O'Regan, K. *et al.* Thermal-electrochemical parameters of a high energy lithium-ion cylindrical battery. *Electrochimica Acta* **425,** 140700 (2022).

165. Fraggedakis, D. *et al.* Theory of coupled ion-electron transfer kinetics. *Electrochimica Acta* **367,** 137432 (2021).

166. Lian, H. *et al.* Modeling lithium plating onset on porous graphite elec- trodes under fast charging with hierarchical multiphase porous electrode theory. *ChemRxiv. Preprint.* (2023).

167. Dokko, K. *et al.* High-rate lithium deintercalation from lithiated graphite single-particle electrode. *Journal of Physical Chemistry C* **114,** 8646–8650 (2010).

168. Swamy, T. *et al.* Electrochemical Charge Transfer Reaction Kinetics at the Silicon-Liquid Electrolyte Interface. *Journal of The Electrochemical Society* **162,** A7129–A7134 (2015).

169. Kirk, T. L. *et al.* Nonlinear Electrochemical Impedance Spectroscopy for Lithium-Ion Battery Model Parameterization. *Journal of The Electrochemical Society* **170,** 010514 (2023).

170. Dhir, S. *et al.* Fundamental investigations on the ionic transport and thermodynamic properties of non-aqueous potassium-ion electrolytes. *Nature Communications* **14,** 3833 (2023).

171. Dhir, S. *et al.* Characterisation and Modelling of Potassium-ion Batteries. *Research Square - preprint* (2024).

172. Zhang, W. *et al.* Approaching high-performance potassium-ion batteries via advanced design strategies and engineering. *Science Advances* **5** (2019).

173. Pramudita, J. C. *et al.* An Initial Review of the Status of Electrode Materials for Potassium-Ion Batteries. *Advanced Energy Materials* **7,** 1602911 (2017).

174. Liu, J. *et al.* On the characterization of battery electrolytes with polarization cells. *Electrochimica Acta* **167,** 357–363 (2015).

175. Thompson, S. D. *et al.* Differential Diffusion Coefficients of Sodium Polysulfide Melts. *Journal of The Electrochemical Society* **136,** 3362–3369 (1989).

176. Stewart, S. *et al.* Measuring the Salt Activity Coefficient in Lithium-Battery Electrolytes. *Journal of The Electrochemical Society* **155,** A458 (2008).

177. Newman, J. *Electrochemical Systems, 3rd Edition* en-us (2004).

178. Casteel, J. F. *et al.* Specific Conductance of Concentrated Solutions of Magnesium Salts in Water-Ethanol System. *Journal of Chemical and Engineering Data* **17,** 55–59 (1972).

179. Atkins, P. W. (W. *et al. Atkins' Physical chemistry* 371 (2017).

180. Yim, C.-H. *et al.* Connection between Phase Diagram, Structure and Ion Transport in Liquid, Aqueous Electrolyte Solutions of Lithium Chloride. *Journal of The Electrochemical Society* **165,** A547–A556 (2018).

181. Kang, S. D. *et al.* Galvanostatic Intermittent Titration Technique Reinvented: Part II. Experiments. *Journal of The Electrochemical Society* **168,** 120503 (2021).

182. Nickol, A. *et al.* GITT Analysis of Lithium Insertion Cathodes for Determining the Lithium Diffusion Coefficient at Low Temperature: Challenges and Pitfalls. *Journal of The Electrochemical Society* **167,** 090546 (2020).

183. Nikitina, V. A. *et al.* Metal-Ion Coupled Electron Transfer Kinetics in Intercalation-Based Transition Metal Oxides. *Advanced Energy Materials* **10,** 1903933 (2020).

184. Montella, C. Apparent diffusion coefficient of intercalated species measured with PITT: A simple formulation. *Electrochimica Acta* **51,** 3102–3111 (2006).

185. Montella, C. Discussion of the potential step method for the determination of the diffusion coefficients of guest species in host materials: Part I. Influence of charge transfer kinetics and ohmic potential drop. *Journal of Electroanalytical Chemistry* **518,** 61–83 (2002).

186. Levi, M. D. *et al.* Potentiostatic and Galvanostatic Intermittent Titration Techniques. *Characterization of Materials,* 913–932 (2012).

187. Vorotyntsev, M. A. *et al.* Spatially limited diffusion coupled with ohmic potential drop and/or slow interfacial exchange: a new method to determine the diffusion time constant and external resistance from potential step (PITT) experiments. *Journal of Electroanalytical Chemistry* **572,** 299–307 (2004).

188. Levi, M. D. *et al.* Application of a Novel Refinement Method for Accurate Determination of Chemical Diffusion Coefficients in Electroactive Materials by Potential Step Technique. *Journal of The Electrochemical Society* **152,** E61 (2005).

189. Malifarge, S. *et al.* Guidelines for the Analysis of Data from the Potentiostatic Intermittent Titration Technique on Battery Electrodes. *Journal of The Electrochemical Society* **164,** A3925–A3932 (2017).

190. Lazanas, A. C. *et al.* Electrochemical Impedance SpectroscopyA Tutorial. *ACS Measurement Science Au* **2023,** 162–193 (2022).

191. Urquidi-Macdonald, M. *et al.* Applications of Kramers-Kronig transforms in the analysis of electrochemical impedance data-III. Stability and linearity. *Electrochimica Acta* **35,** 1559–1566 (1990).

192. Weppner, W. *et al.* Electrochemical Methods for Determining Kinetic Properties of Solids. *http://dx.doi.org/10.1146/annurev.ms.08.080178.001413* **8,** 269–311 (2003).

193. Bard, A. J. *et al. Electrochemical Methods: Fundamentals and Applications* 156–225 (Wiley, 2001).

194. Sulzer, V. *et al.* Python Battery Mathematical Modelling (PyBaMM). *Journal of Open Research Software* **9,** 1–8 (2021).

195. Andersson, J. A. *et al.* CasADi: a software framework for nonlinear optimization and optimal control. *Mathematical Programming Computation* **11,** 1–36 (2019).

196. Vernon-Parry, K. Scanning electron microscopy: An introduction. *III-Vs Review* **13,** 40–44 (2000).

197. Goldstein, J. I. *et al. Scanning Electron Microscopy and X-Ray Microanalysis* (Springer US, Boston, MA, 1981).

198. Klug, H. *et al.* X-ray Diffraction Procedures: For Polycrystalline and Amorphous Materials, 2nd Edition. *Willey, New York, EUA,* 992 (1974).

199. Bragg, W. H. *et al.* The reflection of X-rays by crystals. *Proceedings of the Royal Society of London* **88,** 428–438 (1913).

200. Stevie, F. A. *et al.* Introduction to x-ray photoelectron spectroscopy. *Journal of Vacuum Science & Technology A: Vacuum, Surfaces, and Films* **38,** 63204 (2020).

201. Bruker. *Atomic Force Microscopy For Materials* 4–31 (2017).

202. Hosaka, T. *et al.* Potassium Metal as Reliable Reference Electrodes of Nonaqueous Potassium Cells. *The Journal of Physical Chemistry Letters* **10,** 3296–3300 (2019).

203. Xiao, N. *et al.* Reversible Dendrite-Free Potassium Plating and Stripping Electrochemistry for Potassium Secondary Batteries. *Journal of the American Chemical Society* **139,** 9475–9478 (2017).

204. Shkrob, I. A. *et al.* Why Bis(fluorosulfonyl)imide Is a "Magic Anion" for Electrochemistry. *The Journal of Physical Chemistry C* **118,** 19661–19671 (2014).

205. Le Pham, P. N. *et al.* Potassium-ion batteries using KFSI/DME electrolytes: Implications of cation solvation on the K+-graphite (co-)intercalation mechanism. *Energy Storage Materials* **45,** 291–300 (2022).

206. Wang, L. *et al.* Graphite as a potassium ion battery anode in carbonate-based electrolyte and ether-based electrolyte. *Journal of Power Sources* **409,** 24–30 (2019).

207. Aspinall, J. *et al.* EBSD-coupled indentation: nanoscale mechanics of lithium metal. *Materials Today Energy* **30,** 101183 (2022).

208. Hosaka, T. *et al.* 1,3,2-Dioxathiolane 2,2-Dioxide as an Electrolyte Additive for K-Metal Cells. *ACS Energy Letters* **4,** 3643–3649 (2021).

209. Nečas, D. *et al.* Gwyddion: An open-source software for SPM data analysis. *Central European Journal of Physics* **10,** 181–188 (2012).

210. Fairley, N. *et al.* Systematic and collaborative approach to problem solving using X-ray photoelectron spectroscopy. *Applied Surface Science Advances* **5,** 100112 (2021).

211. Caracciolo, L. *et al.* XPS Analysis of K-based Reference Compounds to Allow Reliable Studies of Solid Electrolyte Interphase in K-ion Batteries. *ACS Applied Energy Materials* **4,** 11693–11699 (2021).

212. Ai, W. *et al.* Electrochemical Thermal-Mechanical Modelling of Stress Inhomogeneity in Lithium-Ion Pouch Cells. *Journal of The Electrochemical Society* **167,** 013512 (2020).

213. Xu, S. *et al.* Evolution of Dead Lithium Growth in Lithium Metal Batteries: Experimentally Validated Model of the Apparent Capacity Loss. *Journal of The Electrochemical Society* **166,** A3456–A3463 (2019).

214. Li, L. *et al.* Understanding High-Rate K+-Solvent Co-Intercalation in Natural Graphite for Potassium-Ion Batteries. *Angewandte Chemie International Edition* **59,** 12917–12924 (2020).

215. Liu, J. *et al.* Unraveling the Potassium Storage Mechanism in Graphite Foam. *Advanced Energy Materials* **9,** 1900579 (2019).

216. Popovic, J. Review—Recent Advances in Understanding Potassium Metal Anodes. *Journal of The Electrochemical Society* **169,** 030510 (2022).

217. Allgayer, F. *et al.* Comparing the Solid Electrolyte Interphases on Graphite Electrodes in K and Li Half Cells. *ACS Applied Energy Materials* **5,** 1136–1148 (2022).

218. Zhang, P. *et al.* Insight into the effect of lithium-dendrite suppression by lithium bis(fluorosulfony)imide/1,2-dimethoxyethane electrolytes. *Electrochimica Acta* **277,** 116–126 (2018).

219. Raccichini, R. *et al.* Ion Speciation and Transport Properties of LiTFSI in 1,3-Dioxolane Solutions: A Case Study for Li-S Battery Applications. *Journal of Physical Chemistry B* **122,** 267–274 (2018).

220. Zhang, Q. *et al.* Boosting the Potassium Storage Performance of Alloy-Based Anode Materials via Electrolyte Salt Chemistry. *Advanced Energy Materials* **8,** 1703288 (2018).

221. Pitzer, K. S. Activity Coefficients in Electrolyte Solutions. *Activity Coefficients in Electrolyte Solutions* (2018).

222. Zhang, X. *et al. Comprehensive Insights into Electrolytes and Solid Electrolyte Interfaces in Potassium-Ion Batteries* 2021.

223. Asenbauer, J. *et al.* The success story of graphite as a lithium-ion anode material – fundamentals, remaining challenges, and recent developments including silicon (oxide) composites. *Sustainable Energy & Fuels* **4,** 5387–5416 (2020).

224. Min, X. *et al.* Potassium-ion batteries: outlook on present and future technologies. *Energy Environ. Sci* **14,** 2186 (2021).

225. Xu, W. *et al.* Exploring the Limits of the Rapid-Charging Performance of Graphite as the Anode in Lithium-Ion Batteries. *Journal of The Electrochemical Society* **169,** 010531 (2022).

226. Coelho, A. A. TOPAS-Academic, version 6. *Coelho Software: Brisbane* (2016).

227. Murbach, M. D. *et al.* impedance.py: A Python package for electrochemical impedance analysis. *Journal of Open Source Software* **5,** 2349 (2020).

228. Igarashi, D. *et al.* Effect of crystallinity of synthetic graphite on electrochemical potassium intercalation into graphite. *Electrochemistry* **89,** 433–438 (2021).

229. Levi, M. D. *et al.* Diffusion coefficients of lithium ions during intercalation into graphite derived from the simultaneous measurements and modeling of electrochemical impedance and potentiostatic intermittent titration characteristics of thin graphite electrodes. *Journal of Physical Chemistry B* **101,** 4641–4647 (1997).

230. Yang, H. *et al.* Evaluation of Electrochemical Interface Area and Lithium Diffusion Coefficient for a Composite Graphite Anode. *Journal of The Electrochemical Society* **151,** A1247 (2004).

231. Persson, K. *et al.* Lithium Diffusion in Graphitic Carbon. *J. Phys. Chem. Lett* **1,** 19 (2010).

232. Oswald, S. *et al.* Novel Method for Monitoring the Electrochemical Capacitance by In Situ Impedance Spectroscopy as Indicator for Particle Cracking of Nickel-Rich NCMs: Part I. Theory and Validation. *Journal of The Electrochemical Society* **167,** 100511 (2020).

233. Onuma, H. *et al.* Phase evolution of electrochemically potassium intercalated graphite. *Journal of Materials Chemistry A* **9,** 11187–11200 (2021).

234. Sayavong, P. *et al.* Dissolution of the Solid Electrolyte Interphase and Its Effects on Lithium Metal Anode Cyclability. *Journal of the American Chemical Society* **145,** 12342–12350 (2023).

235. Zhuo, Z. *et al.* Breathing and oscillating growth of solid-electrolyte-interphase upon electrochemical cycling. *Chemical Communications* **54,** 814–817 (2018).

236. Liang, H. J. *et al.* Staging Na/K-ion de-/intercalation of graphite retrieved from spent Li-ion batteries: in operando X-ray diffraction studies and an advanced anode material for Na/K-ion batteries. *Energy & Environmental Science* **12,** 3575–3584 (2019).

237. Zhuang, Q. *et al.* An electrochemical impedance spectroscopic study of the electronic and ionic transport properties of LiCoO2 cathode. *Chinese Science Bulletin* **52,** 1187–1195 (2007).

238. Wang, C. *et al.* Electrochemical impedance study of initial lithium ion intercalation into graphite powders. *Electrochimica Acta* **46,** 1793–1813 (2001).

239. Srout, M. *et al.* Insights into the Importance of Native Passivation Layer and Interface Reactivity of Metallic Lithium by Electrochemical Impedance Spectroscopy. *Small* **19,** 1–10 (2023).

240. Boyle, D. T. *et al.* Transient Voltammetry with Ultramicroelectrodes Reveals the Electron Transfer Kinetics of Lithium Metal Anodes. *ACS Energy Letters* **5,** 701–709 (2020).

241. Schmalstieg, J. *et al.* Full Cell Parameterization of a High-Power Lithium-Ion Battery for a Physico-Chemical Model: Part I. Physical and Electrochemical Parameters. *Journal of The Electrochemical Society* **165,** A3799–A3810 (2018).

242. Costard, J. *et al.* Three-Electrode Setups for Lithium-Ion Batteries. *Journal of The Electrochemical Society* **164,** A80–A87 (2017).

243. Hertle, J. *et al.* Miniaturization of Reference Electrodes for Solid-State Lithium-Ion Batteries. *Journal of The Electrochemical Society* **170,** 040519 (2023).

244. Cattermull, J. *et al.* K-Ion Slides in Prussian Blue Analogues. *Journal of the American Chemical Society* **145,** 19 (2023).

245. Cattermull, J. *et al.* Structural complexity in Prussian blue analogues. *Materials Horizons* **8,** 3178–3186 (2021).

246. Farkhondeh, M. *et al.* Mathematical Modeling of Commercial LiFePO 4 Electrodes Based on Variable Solid-State Diffusivity. *Journal of The Electrochemical Society* **159,** A177–A192 (2011).

247. Kashkooli, A. G. *et al.* Representative volume element model of lithium-ion battery electrodes based on X-ray nano-tomography. *Journal of Applied Electrochemistry* **47,** 281–293 (2017).

248. Prada, E. *et al.* A Simplified Electrochemical and Thermal Aging Model of LiFePO 4 -Graphite Li-ion Batteries: Power and Capacity Fade Simulations. *Journal of The Electrochemical Society* **160,** A616–A628 (2013).

249. Menne, S. *et al.* The synthesis and electrochemical characterization of bis(fluorosulfonyl)imide-based protic ionic liquids. *Chemical Communications* **51,** 3656–3659 (2015).

250. Liu, Y. *et al.* Formation of size-dependent and conductive phase on lithium iron phosphate during carbon coating. *Nature Communications* **9,** 1–8 (2018).

251. Prada, E. *et al.* Simplified Electrochemical and Thermal Model of LiFePO 4 -Graphite Li-Ion Batteries for Fast Charge Applications. *Journal of The Electrochemical Society* **159,** A1508–A1519 (2012).

252. Prosini, P. P. *et al.* Determination of the chemical diffusion coefficient of lithium in LiFePO4. *Solid State Ionics* **148,** 45–51 (2002).

253. Tang, K. *et al.* Kinetic analysis on LiFePO4 thin films by CV, GITT, and EIS. *Electrochimica Acta* **56,** 4869–4875 (2011).

254. Edge, J. S. *et al.* Lithium ion battery degradation: what you need to know. *Physical Chemistry Chemical Physics* **23,** 8200–8221 (2021).

255. SEC Carbon. *Fine Powder https://sec-carbon.com/eng/fine_powder.html* 2012.